DEVELOPMENT OF AN INDUCTION MOTOR CONDITION MONITORING TEST RIG AND FAULT DETECTION STRATEGIES

by

Mpendulo Dlamini

Thesis submitted to the Department of Electrical Engineering, University of Cape Town, in fulfilment of the requirements for the degree of

MSc Electrical Engineering

University of Cape Town

January 2014

DECLARATION

This dissertation is submitted to the Department of Electrical Engineering, University of Cape Town, in complete fulfilment of the requirements for the degree of Master of Science in Electrical Engineering. It has not been submitted before for any degree or examination at this or any other university. I know the meaning of plagiarism and declare that all the work in the document, save for that which is properly acknowledged, is my own.

Signed: _____ Date: _____

DEDICATION

To Mom, Dad, Sindiswa Dlamini Maseko, Kwena Maseko and Dimakatso Ntema

Thank you for your endless love and support. Your encouragement and belief in me has been motivating and inspirational. Know that I look up to you as a friend.

ACKNOWLEDGEMENTS

My sincere thanks and gratitude extends to my supervisor, Dr P.S Barendse for all his encouragement and inspiration. His patience and sincerity has made him a highly admirable mentor to me. I also thank my co-supervisor, Prof M.A Khan, for all his words of guidance and support throughout this thesis.

Also, thanks to Mr C. Wozniak and Mr P. Titus, your continuous and valued support in the Machines Laboratory is indispensable.

I would like to thank the administration staff of Electrical Engineering Department at the University of Cape Town for their outstanding kindness and goodwill.

I am also grateful for the support received from my friends and colleagues in the AMES research group. To Mr Otshepeng Moraka , Mr Jacques De La Bat and Mr Philip von Platen, I thank you for your willingness to provide assistance, despite having your own stress. Your practical knowledge in the labs has been truly invaluable. To Mr Akrama Khan, Mr Oladapo Ogidi, Mr Ramzi Solomon, Mr Hossein Dehnavifard and Mr Daleel Lilla, you have brought much light and laughter. Even during the difficult times-your positive attitude towards life and its challenges is truly inspirational.

EXECUTIVE SUMMARY

Induction motors are electromechanical devices known to be the workhorse of industrial applications. Nowadays, there is a trend towards using inverter-fed induction motors in industry applications. With an increased emphasis towards energy conservation and lower costs, the use of inverters has grown exponentially [**1**]. Induction motors are highly reliable although they are susceptible to various types of faults. Such faults can be catastrophic and cause production downtime. It is therefore important to detect them at an early stage. Condition monitoring and fault detection of induction motors have become an important area of research and many techniques have been applied. The introduction of inverter-fed motors has produced significant problems in the detection of these faults, requiring further investigation in order to overcome various challenges, example such as increased noise injection.

This thesis sets out to develop an induction motor condition monitoring test rig to experimentally simulate the common faults associated with induction motors and to develop strategies for detecting these faults that employ signal processing techniques. Literature on basic concepts of induction motors and inverter drives, the phenomena of common faults associated with induction motors, the condition monitoring systems were intensively reviewed.

The frequency and time-frequency domain signal processing techniques are used in this thesis are discussed. Spectral analysis based on the Fourier transform is used for the fault detection of stationary (steady-state) signals, whilst Wavelet transforms are used for the detection of non-stationary (transient) signals. Two of the most prominent parameters; current and vibration were used for fault detection. The fault detection strategies rely on the presence of a fault signature. Experiments were conducted on the developed test rig, which allows for practical implementation of the faults. Data was acquired during steady state and startup transient operation of a grid connected and inverter-fed motor. The vibration and current signals gathered from the experiments are then analysed to detect the presence of fault signatures.

The results of applying the fault detection strategies are presented. Final conclusions are drawn on the capabilities of these strategies to detect the common faults in grid and inverter-fed motors.

TABLE OF CONTENTS

LIST OF FIGURES

LIST OF TABLES

LIST OF SYMBOLS

f_1	Power supply frequency (in Hertz)
n_s	Synchronous speed (in revolutions per minute)
n_r	Rotational speed (in revolutions per minute)
p	Number of pole pairs.
s	Per unit slip
f_2	Frequency at which the voltage and current are induced in the rotor circuit
T	Sampling period (in seconds)
F_s	Sampling frequency (in Hertz)
N	Number of samples
t	Time (in seconds)
n	Sample point
f	Frequency (in hertz)
ω	Frequency (in radians)
a	Contraction or dilation
b	Translation
d_j	Detail space
a_n	Approximation space
l	Decomposition level
N_l	The data length of the decomposition level
N_{lw}	The data length of the decomposition level with boundary effect
$2fL$	Twice line frequency
$1X, 2X$	One times rotational speed , two times rotational speed
f_r	Rotational frequency
Z	Number of rolling elements
α	Angle of contact
D	Arc diameter
d	Rolling element diameter
R	The number of rotor slots

NOMENCLATURE

EPRI	Electric Power Research Institute
IEEE	Institute of Electrical and Electronic Engineers
MCC	Motor control centre
MCSA	Motor Current Signature Analysis
FFT	Fast Fourier Transform
MFS – MG	Machinery Fault Simulator – Magnum
MMF	Magnetomotive force
VFD	Variable frequency Drives
DC	Direct current
AC	Alternating current
FOC	Field oriented control
DTC	Direct torque control
SVC	Sensor-less vector control
PWM	Pulse width modulated
ORNL	Oak Ridge National Laboratory
AI	Artificial intelligence
STFT	Short time Fourier transforms
ADC	Analogue-to-digital converter
DTFT	Discrete-time Fourier Transform
DFT	Discrete Fourier transform
PSD	Power spectral density
WVD	Wigner-Ville distribution
WT	Wavelet transforms
CWT	Continuous Wavelet transforms
DWT	Discrete Wavelet transforms
WPD	Wavelet packets decomposition
WHs	Winding harmonics
PSHs	Principal slot harmonics
IEPE	Internal Electronic Piezoelectric
FBPO	Ball pass frequency outer race
PBPI	Ball pass frequency inner race

PVA	Park's Vector Approach.
EPVA	Extended Park's Vector Approach
NI	National Instrument
AI	Analogue Input
AO	Analogue Output
DAQ	Data acquisition
VI	Virtual Instrument

1. INTRODUCTION

1.1 Background

Induction motors are electro-mechanical devices used in most industrial applications for the conversion of power from electrical to mechanical form. Thus, these are regarded as the workhorse of industry. The general applications for these motors include pumps, conveyors, machine tools, presses and packaging equipment. Some of these applications are in hazardous locations, operating under harsh environments. The major advantages of these motors are that they are highly reliable, require low maintenance, and have relatively high efficiency. Furthermore, the wide range of power ratings, which is from hundreds of watts to megawatts, satisfies the production needs of most industrial processes. A growing number of induction motors operate using inverter drives. In this case, the motor is not directly connected to the power grid but inverter-fed. The inverter provides voltage of variable amplitude and frequency in order to vary the mechanical speed.

However, induction motors are susceptible to many types of faults in industrial applications. A motor fault that is not detected at an early stage may become catastrophic and the induction motor may suffer severe damage. Thus, undetected motor faults cascade into motor failure, which in turn may cause production shutdowns. Such shutdowns are costly, in terms of production time, maintenance cost and wasted raw materials. Common faults occurring in electrical motor drive systems can be classified as follows:

Electrical faults: stator winding short circuit, broken rotor bar, broken end-ring, and inverter faults.

Mechanical faults: rotor eccentricity, bearing faults, shaft misalignment, load faults: unbalance, gearbox fault or general failure in the load part of the drive.

These faults can be summarised in Table 1-1. This table presents the surveys conducted by the Motor Reliability Working Group of the IEEE-IAS which surveyed 1141 motors [**2**] and the Electric Power Research Institute (EPRI) which surveyed 6312 motors [**3**]. According to these surveys, most failures are due to bearing and winding faults.

Table 1-1: Percentage failure by component

Failed Component	Percentages of failures (%)	
	IEEE-IAS	EPRI
Bearing related	44	41
Windings related	26	36
Rotor related	8	9
Others	22	14

Several alternatives have been used in industry to prevent severe damage to induction motors. Scheduled maintenance is implemented to verify the integrity of the motor, lubrication problems, bearing conditions, stator winding and rotor cage integrity. However, most maintenance is performed with the motor the de-energised, which implies production shutdown. Redundancy is one method to prevent production shutdowns, but not induction motor failure. Employing redundancy requires two sets of equipment including the induction motors; the first set operates unless there is failure where the second set takes over. This solution is not feasible in many industrial applications due to physical space and high cost limitations [**4**].

Monitoring and failure detection improves the reliability and availability of the existing system. Since the various faults degrade relatively slowly, there is a potential for fault detection at an early stage. This avoids sudden and total failures which have serious consequences. In the context of condition monitoring it is important to differentiate fault detection from fault diagnosis. Fault detection is the decision if the fault is present or not, while fault diagnosis provides more information about the root cause of the failure or localisation of the failure. This information can be used to minimise downtime and to schedule adequate maintenance action. There are generally two approaches for monitoring and fault detection in electric motors:

Model based approach: A dynamic model is used in parallel to the real process. Identical inputs are used in comparing the model outputs to those of the real process.

Signal analysis approach: No dynamic model of the real process is required; the fault detection is based on measured quantities.

The major disadvantage of the model based approach is the need for an accurate dynamic model [**5**]. A signal analysis approach is chosen in this work, hence the fault detection and diagnosis is only based on processing and analysis of the measured signal.

1.2 Problem Statement

The studies of induction motor behaviour during abnormal conditions due the presence of the fault and the possibility to detect these abnormal conditions have been a challenge to electrical engineers. There are many condition monitoring techniques available including axial flux, temperature, chemical, noise and vibration monitoring; although these require expensive sensors or specialised tools. Vibration monitoring is, however, the most established and commonly used approach for detecting mechanical faults.

The basic quantities associated with electromechanical plants, such as current and voltage are readily measured by tapping into the existing voltage and current transformers that are already installed as part of the protection system. As a result, current monitoring is non-invasive and can be implemented in the motor control centre (MMC) room remotely from the motors being monitored [**6**]. A technique called 'Motor Current Signature Analysis (MCSA) is based on stator current monitoring of induction motors; therefore it is not very expensive.

Both vibration analysis and MCSA are commonly based on Fourier transform in particular the Fast Fourier Transform (FFT) since it easy to implement and represents the spectra understandably. However, the FFT methods suffer in reliably detecting faults during light loading, inverter-fed and transient conditions that are commonly experienced in industry. Generally, the majority of research on this subject is focused towards the detection of faults in motors directly supplied from the grid. However, in industrial applications, a growing number of these motors are inverter-fed. The inverter switching operation affects the harmonic content of the current. Thus, it becomes more difficult and demanding to detect faults in inverter-fed motors using MCSA.

There is therefore a need for reliable fault detection strategies for electrical and mechanical faults in grid or inverter-fed motors.

1.3 Research Questions

The research presented in this thesis focuses on the detection of electrical and mechanical faults in low voltage induction motors by measuring non-invasive signals; motor current and vibration.

In this regard, several questions have been formulated, this includes:

1. If a fault is introduced in isolation to other faults, can the conventional techniques reliably detect fault components in ac grid connected motors at different loading conditions under steady state conditions using current and vibration signals?

2. When these conventional techniques are applied to inverter-fed motors under steady conditions, can they detect fault components, and how does the inverter influence these components?
3. Can these faults be detected under transient conditions for grid connected and inverter-fed motors?
4. Which techniques are better suited for electrical and mechanical faults.
5. How do these distinguish between harmonics introduced by the grid and the motor related faults.

1.4 Objectives of the Research

1. Thorough literature review of condition monitoring techniques for induction motors.
2. In order to perform accurate and reliable analysis, the installation of the motors and measurement of their signals needs to be reliable. Therefore the second objective of this research is to develop an induction motor condition monitoring test rig that is capable of: implementing a particular fault in isolation to other faults, and that can capture measured signals in an accurate and repeatable manner.
3. Stator current and machine vibration signals contain unique fault frequency components that can be used to detect various faults associated with induction motors. Therefore the third objective of this research is to validate that the conventional techniques can detect the faults associated with a grid supplied induction motor under steady state conditions using motor current and vibration signals.
4. To explore the applicability of these techniques for inverter-fed motors.
5. To examine more recent time-frequency signal processing techniques for identifying faults under startup transient conditions for grid and inverter-fed motors

1.5 Scope and Limitations of Report

This study is limited to the detection of inter-turn faults, broken rotor bars, bearing outer and inner race faults and dynamic eccentricities under steady and startup transient conditions for grid connected and inverter-fed induction motors. The condition monitoring signals used for the detection of the faults are limited to stator current and vibration signals on the drive end of the induction motor. The limitations of the study also include the use of one type of load; namely servomotor operating as a generator. The effect of different types of load is therefore not considered. The effect of voltage supply unbalance is not considered even though efforts are made to use a balanced supply.

1.6 Organisation of the Thesis

The remainder of this thesis is structured as follows:

Chapter 2 presents a literature review of condition monitoring techniques for induction motors where the basic description of the physical phenomena related to induction motors, inverter drives and the common faults experienced in induction motors are discussed. Furthermore, the condition monitoring parameters are identified.

Chapter 3 introduces the signal processing techniques used for detecting faults using current and vibration signals. The frequency domain and time-frequency domain signal processing techniques are discussed.

Chapter 4 presents the monitoring methods and frequency domain fault characteristics associated with the current and vibration signals.

Chapter 5 describes the development of the Machinery Fault Simulator – Magnum (MFS – MG) experimental setup used to implement the fault conditions experimentally. The setup of the test motors and load are also presented. The experimental methodology and baseline conditions are also presented in the chapter.

Chapter 6 presents and discussed the experimental results for the faulted scenarios under steady state conditions, whereby these are compared to the healthy motor.

Chapter 7 presents and discussed the experimental results for the faulted scenarios under transient conditions, whereby these are compared to the healthy motor.

Chapter 8 finally draws conclusions on the capabilities of these strategies to detect the common faults in grid and inverter-fed motors.

2. LITERATURE REVIEW OF CONDITION MONITORING TECHNIQUES FOR INDUCTION MOTORS

2.1 Introduction

This chapter presents a literature review of condition monitoring for induction motors. The basic description of the physical phenomena related to induction motors, inverter drives, and the common faults experienced in induction motors are discussed, as well as the commonly monitored parameters in induction motors.

2.2 Induction Motor

Induction motors are the most commonly used electrical machines in industry because of the low cost and rugged construction. The rating these machines vary widely (i.e. few watts to megawatts). The small single phase motors are used in household applications, such as blenders, lawn mowers and washing machines, while large three phase induction motors are used in pumps, fans, compressors and paper mills. In this thesis three phase induction motors will be considered. These motors can operate as motors or generators. An induction motor contains a stator and rotor mounted on bearings, and the rotor is separated from the stator by an air-gap. The stator and rotor windings carry an alternating current. This current is supplied to the stator winding directly while supplied to the rotor winding through induction [**7**] [**8**].

2.2.1 Construction Features of Induction Motors

Induction motors have uniform air-gaps unlike the DC motors. The stator is constructed of high grade steel laminations. The three phase windings are placed in slots cut on the inner surface of the stator frame. The rotor windings can either be squirrel cage or wound-rotor type. The squirrel cage rotors are embedded with copper or aluminium rods shorted on both ends by copper or aluminium rings. The wound rotors have a similar form of windings as the stator. The

terminals of the windings are connected to slip-rings [**7**]. The squirrel cage motors are more rugged and economical compared to the wound-rotor motors. The windings on the stator and rotor (wound-rotor type) are distributed over several slots to improve the magnetomotive force (MMF) waveform and to create a smooth torque output developed by the machine. The MMF is a measure of the strength of the magnetic field, it is proportional to the number of turns in the coil and current that flows through this coil. The measure of MMF in a coil is ampere-turns. A current flowing in a distributed winding results in essentially a sinusoidally space distribution of MMF. If balanced three phase currents flow through these three-phase distributed windings, a constant rotating magnetic field of constant speed and amplitude is produced in the air gap and this will induce current in the rotor circuit to produce torque [**7**].

2.2.2 Principle of Operation

The rotor circuit can be left open or closed circuited depending on the mode of operation. In standstill the rotor circuit is considered an open circuit, if the three phase windings are connected to a three phase supply; a rotating magnetic field is produced in the air gap which rotates at synchronous speed n_s

$$n_s = \frac{120}{p} f_1 \qquad (2\text{-}1)$$

Where frequency f_1 is the power supply frequency and p is the number of pole pairs. Voltages are induced in both the stator and rotor windings at the same frequency f_1 due to the rotating magnetic field. Under running operation the rotor circuit is closed, the induced voltages in rotor produces rotor currents that produce its own field which interacts with that of the air-gap magnetic field to produce a torque. The rotor will rotate in the direction of magnetic field in a manner such that the relative speed between the rotor windings and rotating decreases. The rotor, under steady state conditions will rotate at speed n_r which is less than the synchronous speed n_s of the rotating field in the air gap [**7**]. The difference in speed between rotor and synchronous speed is referred to as slip s.

$$s = \frac{n_s - n_r}{n_s} \qquad (2\text{-}2)$$

The voltage and current in the rotor circuit are induced at frequency f_2

$$f_2 = sf_1 \tag{2-3}$$

In conventional squirrel cage motors, at full load conditions the slip and current are low but the power factor and the efficiency are high. However, during direct-on line startup conditions the torque and power factor are low but the current is high. These starting currents are in the order of 500 to 800% of the full load current. If the load requires a large starting torque, the motor will accelerate slowly. This will cause the starting currents to flow for a longer period of time, thereby creating overheating and damage to the insulation. In the Figure 2-1, a typical torque speed characteristic curve of an induction motor is shown.

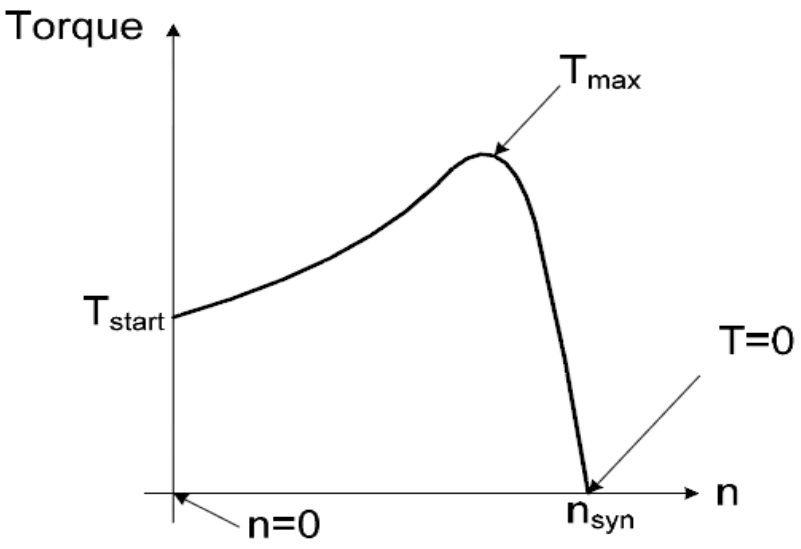

Figure 2-1: A typical induction motor torque-speed (torque-slip) characteristic curve [4]

2.2.3 Inverter-fed Induction Motors

As previously mentioned, the speed of the rotating magnetic field is directly related to the voltage frequency applied to the windings. Variable Speed Drives (VSD) or Inverter Drives, used to control the speed and torque of the motor, can produce variable frequency; thus variable voltage waveforms. When these waveforms are applied to the stator windings there is a shift of

the torque-speed curve shown earlier, maintaining a constant pull out torque and the same slop of the linear operation of the curve. In this manner, the motor speed is proportional of the applied frequency generated by the inverter drive, as shown in Figure 2-2.

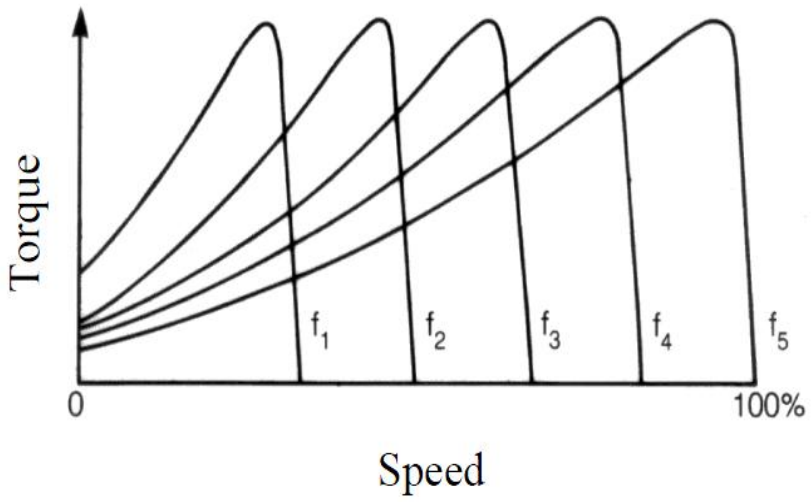

Figure 2-2: Torque-speed curve of an induction motor when supplied by an inverter [9]

The AC power supplied by the grid is rectified to produce DC power then inverted to form AC at the designated frequency. The inverter can produce either step wave or pulse width modulated (PWM) current that simulates the current power at variable frequencies. The output wave of the PWM drive is not a sinusoidal waveform but a series of constant amplitudes. The amplitude of each pulse is the DC voltage, and the pulse width depends on the desired output voltage [**10**]. The current waveform of the motor contains additional harmonics. The harmonic characteristics are a function of the number of pulse or rectifiers in the inverter drive [**11**].

2.2.3.1 Torque and speed capabilities

Speed control by means of frequency (and voltage) allows the inverter-fed motor to operate below and above rated speed. At low frequency (speed), where the air-gap flux is kept constant, the stator voltage magnitude decreases approximately in proportion to the frequency from its rated value down to very low values. If this flux is maintained constant; the motor can deliver its rated torque. Beyond the rated frequency, the voltage applied to the stator is kept at its rated value while the frequency is increased; which results in a reduced voltage and frequency ratio, hence a reduced air-gap. However, in this case the rated torque cannot be maintained [**8**].

2.2.3.2 Control strategies

The inverter-drive can have the following control strategies: Vector or field oriented control (FOC), Scalar control constant volts per Hertz, Sensor-less vector control (SVC) and direct torque and flux control (DTC). This thesis is focused on scalar constant volts per hertz control.

Scalar control mode can operate either in an open or closed loop. The closed loop gives better performance compared to open loop, since a speed sensor is used to correct the deviations between the reference value and the real value in order to obtain accurate control of speed and faster torque perturbation response. The most commonly used scalar control method is the open loop constant Volts/Hz control. This method yields low performance compared to the aforementioned control strategies, although it is easily implemented. The fundamental idea of the scalar control is to keep a constant ratio between the voltage and frequency applied to the induction motor. This constant ratio Volts/Hz results in a constant air-gap flux and therefore constant torque for constant magnitude of the stator and rotor current for operating frequency from zero to the rated frequency. The motor frequency and torque are based on reference values [**4**].

2.3 Common Types of Faults Associated with Induction Motor

Induction motors are frequently exposed to non-ideal or detrimental operating environments. These circumstances include: insufficient lubrication, inadequate cooling, frequent start/stops conditions, and overload. During these conditions the motor is subjected to undesirable stresses, which makes the motor susceptible to faults or failure. According to surveys the majority of the faults in induction motors can be broadly classified as follows: stator faults, rotor cage failures (broken rotor bars/end-rings), air-gap irregularities and bearing failures. These faults account for more than 90% of the induction failures **[6], [12] – [19]**. These common faults can be categorized into two groups: electrical and mechanical faults. Electrical faults include stator and rotor faults, while mechanical faults include bearing faults and air-gap eccentricities.

2.3.1 Stator Faults

The stator faults can be classified as lamination or frame fault (ground or circulation current) and stator winding faults. According to surveys, stator winding faults account for 30 - 40% of all electrical failures [**6**], [**12**], [**16**] - [**19**]. Stator winding faults can either be turn-to-turn (short circuit within the same phase) or other phase combinations (phase-to-phase, phase to ground and or three phase faults) as illustrated in Figure 2-3.

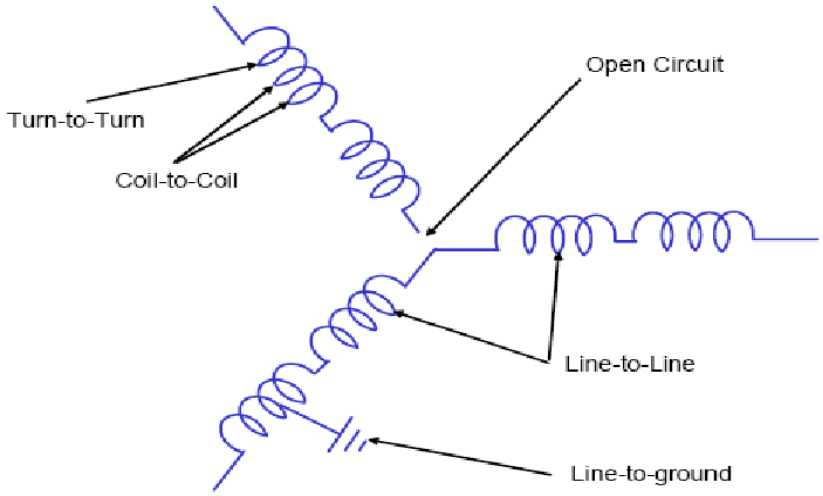

Figure 2-3: Various types of stator winding faults [6]

Most of the phase faults are characterised by high fault currents, which facilitate detecting them, whereas turn-to-turn faults (particularly with lower number of faulted windings) are characterised with lower fault current levels, which make these faults difficult to detect [**20**]. Many of these faults are caused by a combination of various stresses acting up on the stator, which can be categorised as: thermal, electrical, mechanical and environmental [**6**], [**17**], [**18**].

Thermal stresses are the most recognised causes for insulation degradation and ultimate motor failure. These can be categorised into three types: aging, cycling and overloading. As a rule of thumb, for every 10°C increase in temperature; the insulation life is halved due to thermal aging. Winding failure will occur irrespective of the degree of thermal aging if the other stresses mentioned above increase. The effect of temperature on thermal aging can be reduced to prolong thermal life by reducing the operating temperature or increasing the insulation class of winding material used. Thermal overloading occurs due to variation of the applied voltage, unbalanced phase voltages, obstructed ventilation and higher ambient temperature. As a rule of thumb, for every 3.5% voltage unbalance the winding temperature increases by 25% in phase with the highest current. Cycling gives expansion and contraction in the insulation system resulting in a weakening effect [**6**], [**18**].

Electrical stresses resulting in winding faults can be classified into dielectric, tracking, corona and voltage transients. Tracking occurs in motors operating above 600V resulting in ground faults since the winding insulation system is not completely protected from the environment. Transient gaseous ionisation in the insulation system where the voltage exceeds the critical levels on motors operating above 5kV range results in corona. Transient voltage conditions

caused by line-to-line, repetitive re-striking, open and closing of breakers, rapid bus transfer, capacitor switching and lightning, reduce the winding life [**18**].

Mechanical stresses that accelerate the degradation of insulation include coil movement and rotor striking the stator. The current in the stator windings produce a force on the coils that is proportional to the square of the current. This force is maximal under starting cycle or transient overloads, causing the coils to vibrate at twice the line frequency in both the radial and tangential directions. This movement causes damage to insulation. The rotor can strike the stator due to a number of reasons, such as shaft deflection, air-gap eccentricities and broken rotor bars. If the strike occurs during the starting cycle, the force of the rotor can cause the stator laminations to puncture the insulation, whereas during full speed steady operation it can cause premature grounding of the coil in the stator slots [**6**], [**18**].

Environmental stresses include contamination of foreign material and condensation. The presence of foreign material can result in reduced heat dissipation causing adverse effects on the winding insulation. Thus it is crucial to restrict foreign particles from interacting with the surface of the motor. Condensation development can lead to grounding in the slot. This can be prevented by drying out the windings using space heaters during the off cycle [**6**], [**18**].

2.3.2 Rotor Cage Faults

Broken rotor bars account for more than 5% of the electric motor failure of induction motors **[12] - [16].** There are numerous reasons for rotor bars and end rings breakages, these include:

- magnetic stresses caused by electromagnetic stresses;
- thermal stresses due to abnormal operating duty including imbalance and overload conditions;
- inadequate casting, fabrication procedures or overloading;
- contamination and abrasion due to poor operating conditions; and
- lack of maintenance.

As a result of the reasons mentioned above; the rotor bars may be damaged and simultaneously an unbalance condition may occur. Rotor asymmetries result in asymmetrical distribution of rotor currents. An incipient broken rotor bar aggravates exponentially in time as excessive current flow is concentrated on adjacent bars instead of the broken bar, which propagates electrical stresses to adjacent areas. This progressively deteriorates the rotor part and degrades the motor's overall performance and shortens its lifetime [**12**], [**19**].

2.3.3 Bearing Faults

Bearing faults account for 40% of induction motor failures [**12**], [**14**], [**15**]. A majority of induction motors use ball or rolling element bearings, which consist of an inner and outer ring with a set of rolling elements placed in raceways rotating inside these rings [**15**], [**21**]. Most of the bearings' industrial facilities operate in non-ideal conditions and are subjected to:

- excessive loading which usually causes premature failures;
- overheating due to temperatures in excess of 204.4 ℃ can anneal the ball and ring material. The result of loss in hardness reduces the bearing capacity causing early failure. In extreme cases the balls and rings will deform. The increase in temperature can also degrade or destroy the lubricant;
- brinelling which occurs when the loads exceed elastic limit of the ring material;
- contamination due to dirty work areas, tools, fixtures, hands and grinding operations;
- corrosion resulting from exposure to corrosive fluids or a corrosive atmosphere;
- lubrication failures typically caused by restricted lubricant flow and excessive temperatures that degrade the lubricant properties; and
- misalignment caused by exceeding the alignment tolerances. The misalignment results in rises of temperatures of the bearings.

Bearing faults or defects can be classified as: outer race, inner race, rolling element and cage defects as depicted in Figure 2-4

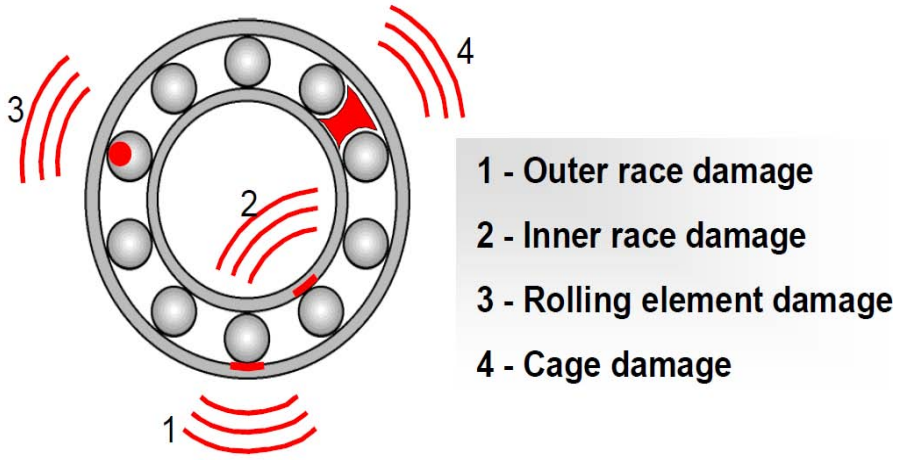

Figure 2-4: Various types of bearing faults [22]

2.3.4 Air-Gap Eccentricities

Air-gap eccentricities are conditions that occur when there is a non-uniform distance between the rotor and stator in the air-gap. Generally, there are three types of eccentricity: static, dynamic and mixed as displayed in Figure 2-5

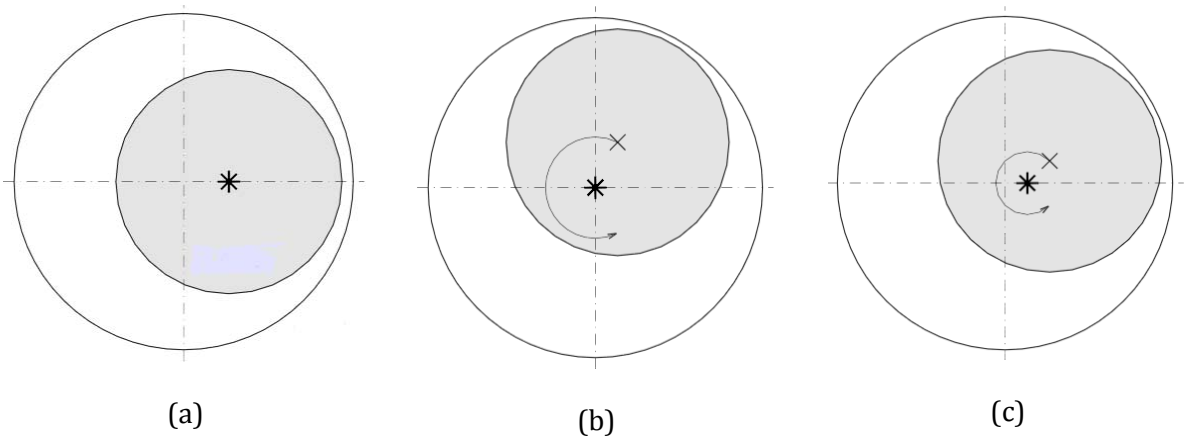

Figure 2-5: Schematic representation of (a) Static eccentricity (b) Dynamic eccentricity (c) Mixed eccentricity. X denotes the rotor geometrical center. The rotor rotational centre is denoted by * [5]

In static eccentricity the rotor geometrical centre is identical to the rotational centre but displaced with respect to the stator geometrical centre. The point of minimal gap length is stationary with respect to stator. This type of eccentricity is caused by misalignment of the rotor axis within the stator. This condition may be attributed to manufacturing tolerances, an oval stator core, incorrect bearing positioning or bearing wear. In dynamic eccentricity the rotor geometrical centre is different from the rotational centre. The rotational centre is identical to the stator geometrical centre. The point of minimal gap is moving with respect to the stator. This type can also be caused by manufacturing tolerances, bearing wear and bent shaft or flexible shaft. Mixed eccentricity is a combination of both static and dynamic eccentricity. The rotor geometrical centre, rotor rotational centre and stator geometrical centre are different. The point of minimal gap is also moving with respect to the stator. The major risk of these eccentricities is mechanical contact of the rotor and stator, which would result in damage for the machine [**5**], [**12**].

2.4 Need for Conditioning Monitoring

Condition monitoring is a continuous evaluation process of the health of the plant and equipment through its service life. It is essential to detect faults while they are still developing; this is referred to as incipient failure detection. The incipient fault detection of motor failure provides a safe operating environment. Using a comprehensive condition monitoring scheme for continuous assessment of the induction has become increasingly important. By condition

monitoring induction motors; adequate warning to imminent failure can be provided to the operator, which ,makes it possible to schedule future maintenance and repair work. This can reduce down time and optimise the maintenance schedule.

2.5 Condition Monitoring Parameters

The condition parameters or symptoms for determining various faults in induction machines recognised by *International Standards Organization* are displayed in Table 2-1. The most prominent parameters used include: current, vibration, temperature and axial flux [**23**]. These prominent parameters can be categorised as: invasively (Axial flux) and non-invasively (noise, vibration and current) monitored parameters.

Table 2-1: Various parameters used to detect faults in induction motors [23]

Machine type: Electric motor	Symptom or parameter change												
Examples of faults	Current	Voltage	Resistance	Partial discharge	Power	Torque	Speed	Vibration	Temperature	Coast down time	Axial flux	Oil debris	Cooling gas
Rotor windings	•				•	•	•	•	•		•		•
Stator windings	•							•	•		•		•
Eccentric rotor	•							•			•		
Brush(es) fault	•	•			•	•			•				
Bearing damage	•					•		•	•	•		•	
Insulation deterioration	•	•	•	•									•
Loss of input power phase	•	•						•			•		
Unbalance								•					
Misalignment								•					

• Indicates symptom may occur or parameter may change if fault occurs.

2.5.1 Noise Monitoring

Noise monitoring is a non-invasive method that determines the health of an induction motor. It is monitored using microphones mounted near the machine. The noise signal is then converted to an electrical signal. The quality and the noise source are analysed on the noise spectrum. Each fault in a rotating machine produces distinctive characteristics that can be compared to

reference ones in-order to perform fault detection and diagnosis. However, it is not an accurate way to detect a fault given that background noise from other machines can influence the noise measurement [**24**].

2.5.2 Axial flux Monitoring

Axial flux leakage is a result of stator and rotor currents on the machine extremities; in the coil ends and the rotor end rings. Axial flux can always be detected even with symmetrical supply due to the effect of imperfections in the production process. Therefore, the axial flux can be a good indicator of an induction motor's health. However, the measurement is invasive since a search coil is wound around an end-turn in front of the machine. The coil is perpendicular to the machine and shaft. The search coil measures the sum of the flux from stator winding and flux from the rotor winding [**25**], [**26**].

2.5.3 Temperature Monitoring

Temperature or thermal measurement involves bulk temperature measurement or parameter estimation. Researchers have developed two thermal models to categorise electric machines: the finite element analysis model and the lumped parameter thermal model. The finite element analysis model handles heat conduction problems more accurately and is well suited for steady state or transient problems of large machines where asymmetries are a common feature but are computationally intensive [**6**], [**27**], [**28**]. The lumped parameter thermal model is the most popular for temperature estimation. It is composed of different thermal resistors and capacitors [**6**], [**29**], The lumped parameter model can be derived in two methods:

1. the dimensional information and the thermal properties of the materials used in the design and the heat transfer coefficients; and
2. by measuring the temperature at different locations of the machine, which can be easily adaptable to motors of different frame sizes [**29**],[**30**], [**31**].

In a turn-to-turn fault described earlier, the temperature rises in the region of the fault; however, this might be too slow to detect the incipient fault before it progresses to a more severe fault [**32**] .

2.5.4 Vibration Monitoring

Vibration analysis is the most established technology and the most tangible. Almost all machines vibrate, and the connection between these vibrations and the machine condition is that both are easily measured and interpreted. The major benefit of vibration monitoring is that different mechanical processes within the machine (eg. imbalances, gear-mesh, bearing faults) all produce energies at different frequencies. Separating these different frequencies from one

another through spectrum analysis enables a whole new level of detail to be seen [**33**]. The monitoring and frequency analysis will be discussed later.

2.5.5 Current Monitoring

Motor Current Signature analysis (MCSA) is an electric machinery technology developed by the Oak Ridge National Laboratory (ORNL). It exploits the intrinsic ability of the electric motors and generators to act as transducers by using non-intrusive current clamps. The motor current provides the means of detecting small variations in time dependent loads and speed variation generated anywhere within the electro-mechanical system, which converts them into revealing signatures that can be used to determine equipment degradation and incipient failures [**34**], [**35**]. There are numerous applications of using MCSA on equipment health published among the nuclear-generation, industrial and defense industries. In motor applications the stator current is monitored for detection of different faults in induction motors. The monitoring methods and fault frequency analysis will be discussed later.

2.6 Concluding Remarks

In conclusion, the basic concepts of the induction motor and inverter drive have been presented. The four common types of faults associated with induction motors were identified and categorized into electrical and mechanical faults. These common faults have also been described. Furthermore, the most prominent parameters used to detect these faults, namely motor current and vibration have also been identified and discussed briefly. Their measurement methods and frequency analysis will be discussed later. The next chapter presents the signal processing techniques commonly used for motor current and vibration time signals.

3. SIGNAL PROCESSING TECHNIQUES FOR INDUCTION MOTORS

3.1 Introduction

This chapter presents the commonly used signal processing techniques for the condition monitoring of induction motors. Continuous advancements of these signal processing techniques and related monitoring instrumentation is necessary for effective and reliable fault detection. The signals measured correspond to the physical measured quantities of the motor drive system. In the context of this work two types of signals are considered; vibration and current, which can be distinguished depending on their origin. The origin of these signals is a rotating machine, thus these are generally periodic. The frequency domain and time-frequency domain techniques for processing such time periodic signals are discussed.

3.2 Fault Detection Techniques

The most common fault detection techniques used for electric motors are shown in Figure 3-1. These fault detection techniques can be categorised into three: artificial intelligence based techniques, standard digital techniques and advanced digital signal processing techniques. Artificial intelligence (AI) is the study of the system conditions through the use of computational models. The AI tools solve practical engineering problems which require human intelligence. The standard signal processing techniques such as: DFT, FFT and STFT are most widely used for fault detection and condition monitoring of electric machines in the last fifteen decades. The standard digital techniques have been applied the frequency domain, assuming a stationary signal, and in the joint time-frequency domain for non-stationary signals. In the frequency domain, Fourier methods are commonly applied to transform the signal to the frequency domain for further analysis [**36**]. Advanced signal processing techniques, such as wavelet algorithms are applied for localising and identifying short time dynamic phenomena.

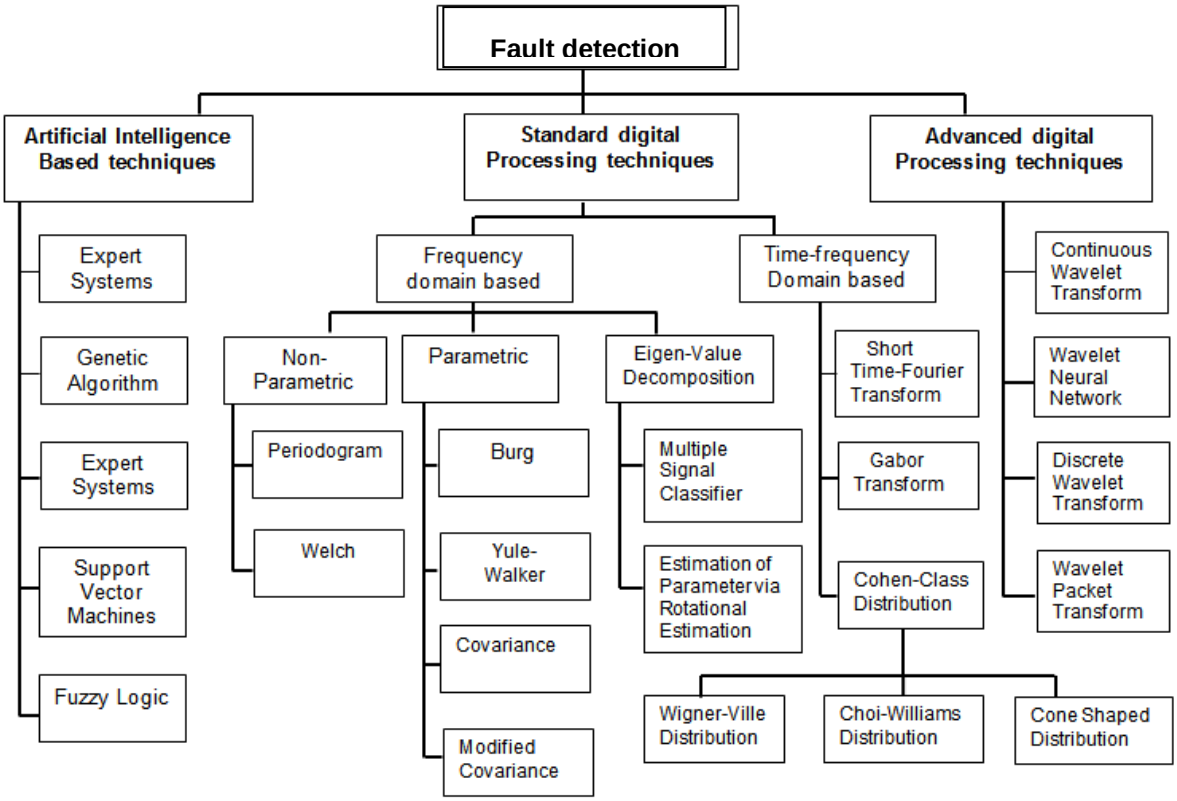

Figure 3-1: The common fault diagnostic technique for electric machines [36]

Signal processing is one of the most important methods used in fault detection that aims to find a simple and effective transform of the original signal. The important information contained in the signal can be shown and the dominant features can be extracted for fault detection.

3.3 Signal Classification

Various signals may be encountered; hence it is useful to classify these signals according to certain properties. The type of signal and property are important for appropriate choice of signal analysis and processing method. Certain signal processing techniques will be effective for a certain class of signals. Signals can be classified as deterministic and non-deterministic, as illustrated in Figure 3-2.

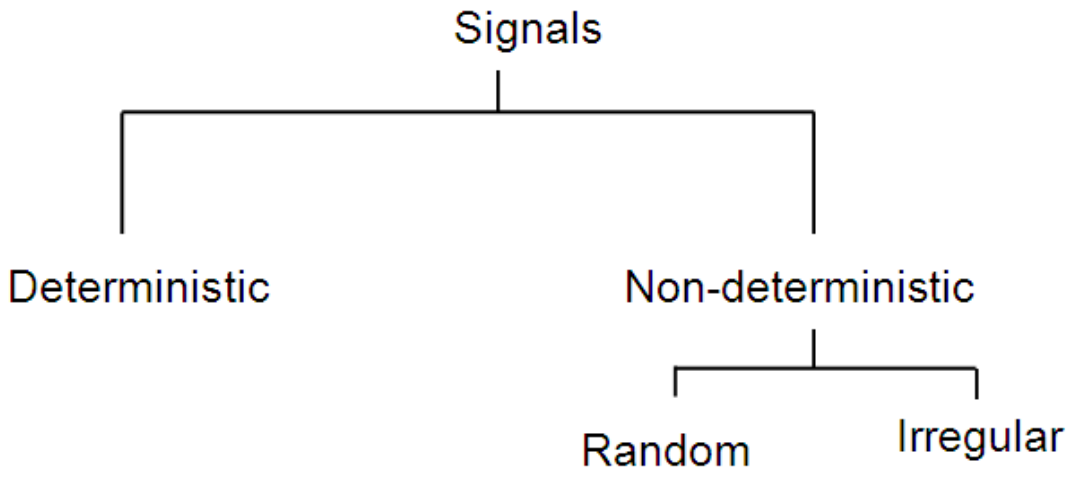

Figure 3-2: Signal Classification diagram

Deterministic signals are described by analytical expressions at all times. They can be predicted for arbitrary times and can often be reproduced arbitrarily. Non-deterministic signals are either random or irregular. Random signals cannot be described by analytical expressions but are statistically or stochastically describable. These are often considered disturbing; thus in order to make measurement and analysis representable, reduction of the random character is necessary. An example of a random signal is Gaussian noise, which is a stochastic process commonly used to model measurement noise. Irregular signals cannot be statistically or stochastically describable [**5**], [**37**].

3.4 Signal Conditioning and Sampling

A continuous time signal $x(t)$ is defined at any given point of time. Often the time signal has to be pre-filtered before sampling to avoid aliasing. This is achieved through a low pass filter design that can decrease the alias to an acceptable level. The discrete signal $x[n]$ is a sampled version of the continuous time signal $x(t)$ when acquired through a data acquisition system or digitising oscilloscope. The sampling period is then equal to T, and the sampling frequency $F_s = 1/T$. In practice, sampling is implemented using an analogue-to-digital converter (ADC). The continuous time signal has to be sampled at a rate greater than twice the maximum frequency contained in the signal. This is a result of the fundamental theorems of signal processing known as the Shannon sampling theorem [**38**]. Real-world signals are not expressed as continuous signals $x(t)$ but rather as discrete time signals $x[n]$. Therefore in this chapter the discrete expressions will also be presented.

3.5 Fourier Transform

The Fourier transform allows periodic and non-periodic continuous time signals to be described in terms of frequency content given by sinusoidal components. The Fourier transform $X(f)$ of a continuous time $x(t)$ is commonly defined as [**38**]:

$$X(f) = \mathfrak{F}\{x(t)\} = \int_{-\infty}^{\infty} x(t)e^{-j2\pi ft}\, dt \qquad (3\text{-}1)$$

In general $X(f)$ is complex valued function of the continuous frequency variable f, and thus inorder to specify $X(f)$, it is necessary to display the magnitude function $|X(f)|$and the angle function $< X(f)$. Equation (3-1) is known as the analysis or forward equation since it extracts the frequency information from the time domain signal [**12**].

3.5.1 Discrete Fourier Transform

The discrete counter part of the Fourier transform is the discrete-time Fourier Transform (DTFT). The DTFT is of a discrete time signal $x[n]$ is a function of a continuum of frequencies, and unlike the continuous case, the DTFT is always periodic with period 2π any other interpretation is inconsistent. A transform of a discrete-time signal that is a function of a finite number of frequencies is called a discrete Fourier transform (DFT). The DFT can be viewed as "discretization in frequency" of the DTFT. The discrete Fourier transform $X[k]$ of the sampled signal $x[n]$, where $k = 0, 1, \ldots N-1$ is given by:

$$X[k] = \sum_{n=0}^{N-1} x[n]e^{-j\left(\frac{2\pi}{N}\right)kn} \qquad (3\text{-}2)$$

The direct evaluation of $X[k]$ requires N^2 multiplications, which can result in a great deal of computation if N is large. However, using a fast Fourier transform (FFT) algorithm to compute $X[k]$ requires an order of $(Nlog_2N)/2$ multiplications. This is a significant decrease in the N^2 multiplications required in DFT computation, thus the FFT is a computational efficient method for determining the DFT of $x[n]$ [**38**].

3.6 Analytical Signal

3.6.1 Properties

The real and imaginary parts of Fourier transform $X(f)$ can be expressed as:

$$X(f) = \mathfrak{R}\{x(t)\} = \int_{-\infty}^{\infty} x(t)\cos(2\pi f t)dt \tag{3-3}$$

$$X(f) = \mathfrak{J}\{x(t)\} = -\int_{-\infty}^{\infty} x(t)\sin(2\pi f t)dt \tag{3-4}$$

This suggests the following symmetry of $X(f)$ [**5**]

$$\mathfrak{R}\{X(-f)\} = \mathfrak{R}\{X(f)\} \tag{3-5}$$

$$\mathfrak{J}\{X(-f)\} = -\mathfrak{J}\{X(f)\} \tag{3-6}$$

This relationship shows that the values of the Fourier transform with respect to the negative frequencies can be deduced from the values of the positive frequencies. The negative frequencies of $X(f)$ contain no additional information if the values of the positive frequencies are known. The disadvantage of omitting the negative frequencies in real valued signals would result in the large bandwidth being divided into two. This is realised using analytical signals. A signal $z(t)$ is considered an analytical signal if the Fourier transform is zero for negative frequencies [**5**].

$$Z(f) = 0 \text{ for } f < 0 \tag{3-7}$$

In general, $z(t)$ will be a complex signal.

3.6.2 Hilbert Transform

Now considering how a real signal $x(t)$ is transformed into the corresponding analytical signal $z(t)$. The Hilbert transform techniques are useful for analysing instantaneous frequency

content of a signal. The Hilbert transform $y(t) = H\{x(t)\}$ of the signal $x(t)$ is obtained using the following expression [**39**]

$$y(t) = \frac{1}{\pi}\int_{-\infty}^{\infty} \frac{x(\tau)}{\tau - t} d\tau \tag{3-8}$$

where the principle value of the integral is used. Thus, the complex analytical signal $z(t)$ is obtained from both $x(t)$ and y(t)

$$z(t) = x(t) + jy(t) \tag{3-9}$$

$$z(t) = x(t) + jy(t) \tag{3-10}$$

The envelope $E(t)$of the analytical signal is given as:

$$E(t) = |x(t) + jy(t)| \tag{3-11}$$

Now the discrete version of the Hilbert transform of the sampled signal $x[n]$ is given by [**39**].

$$y[n] = \frac{1}{N}\sum_{k=0}^{N-1}\left\{\frac{X_r[k]sin2\pi kn}{N} - \frac{X_j[k]cos2\pi kn}{N}\right\} \tag{3-12}$$

It follows that the discrete analytical signal $z[n]$ can be expressed as:

$$z[n] = x[n] + jy[n] = x[n] + jH_d\{x[n]\} \quad (3\text{-}13)$$

The instantaneous magnitude of the analytical signal reflects how much energy changes with time. The fundamental component is therefore shifted to the DC value, and can be removed from the magnitude of the analytical signal by subtracting the mean. This results in a signal $q[n]$ given by Equation (3-14), which shows oscillations close to the fundamental [**40**].

$$q[n] = abs\big(hilbert(x)\big) - mean\,(abs\big(hilbert(x)\big)) \quad (3\text{-}14)$$

3.7 Frequency Domain Based Signal Analysis Techniques

The standard techniques based on the frequency domain are discussed in this section. These techniques consider the sampled signal $x[n]$ as a stationary random signal containing some level of noise and for which the first and second order moment statistics do not change with time (Wide sense stationary). A typical sinusoidal sampled stationary signal is displayed in Figure 3-3.

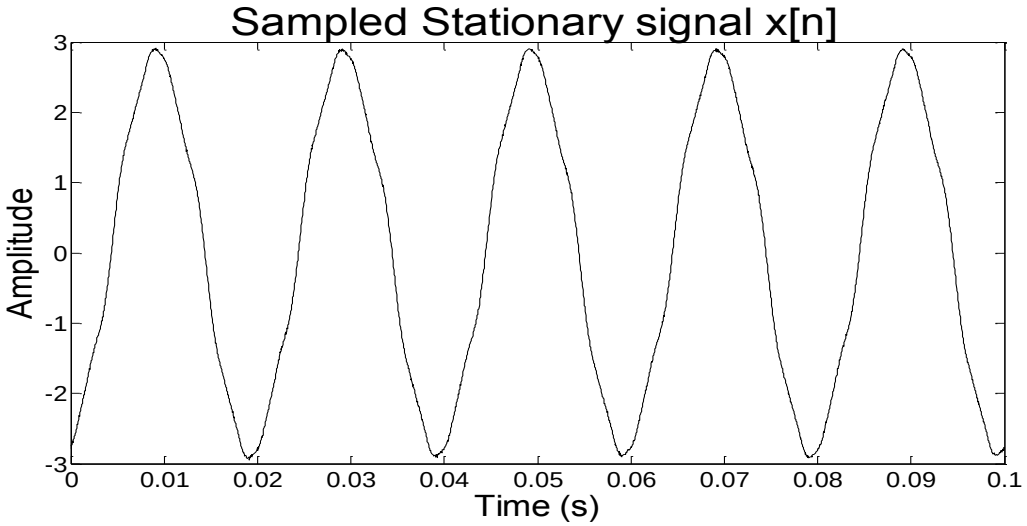

Figure 3-3: A typical sampled stationary signal

The sampled signal is a realisation of a random process characterised by its mean and variance in relation to the true spectrum. Spectrum estimation methods can be broadly categorised into

three methods: non-parametric, parametric and eigen-decomposition methods [**41**] - [**44**]. Non-parametric methods do not assume a specific underlying model for the observed process and the estimates are based directly on the signal itself.

Parametric methods estimates are based from a signal that is assumed to be an output of a linear system driven by white noise. These methods first estimate parameters (coefficient) of the linear system that hypothetically generates the signal. Further discussion of these methods can be found in **[42] – [45]**. The eigen-decomposition (High frequency resolution) methods generate frequency components based on eigen-analysis or eigen-decomposition of the autocorrelation matrix of the input signal into noise and signal subspaces. The signals components are considered as a set of sinusoids corrupted by additive white noise [**41**]. Further discussions of these methods can be found in [**46**].

Some researchers have applied parametric and eigen-decomposition methods for fault feature extraction using parametric methods in [**47**] and eigen decomposition methods in [**48**], [**49**]. The major advantage of these methods is that short data records are used; however, they require large computational time and strongly depend on the choice of parameters. This thesis is focused on non-parametric methods, thus the techniques used to enhance the spectral estimation of the non-parametric method are further discussed.

3.7.1 Windowing

Spectral leakage is an undesired phenomena when the power of the original signal data leaks out over the entire frequency range instead of being concentrated at the points of interest. Spectral leakage produces amplitude bias and may mask the presence of weak signals and prevent their detection. The quality of a signal can be improved by multiplying the signal data with a suitable window function $w[n]$.

$$y[n] = x[n] \cdot w[n] \tag{3-15}$$

The simplest window is called the rectangular window. Other window functions shown in Figure 3-4, have been devised to achieve better sidelobe levels than those of a rectangular window. Decreasing the sidelobe levels reduces the amplitude bias (the difference between the true value and the expected value), although this can be achieved only by broadening the window's mainlobe frequency response thus leading to a reduction in spectral resolution. A trade-off between mainlobe width and level of sidelobe suppression must be established [**43**].

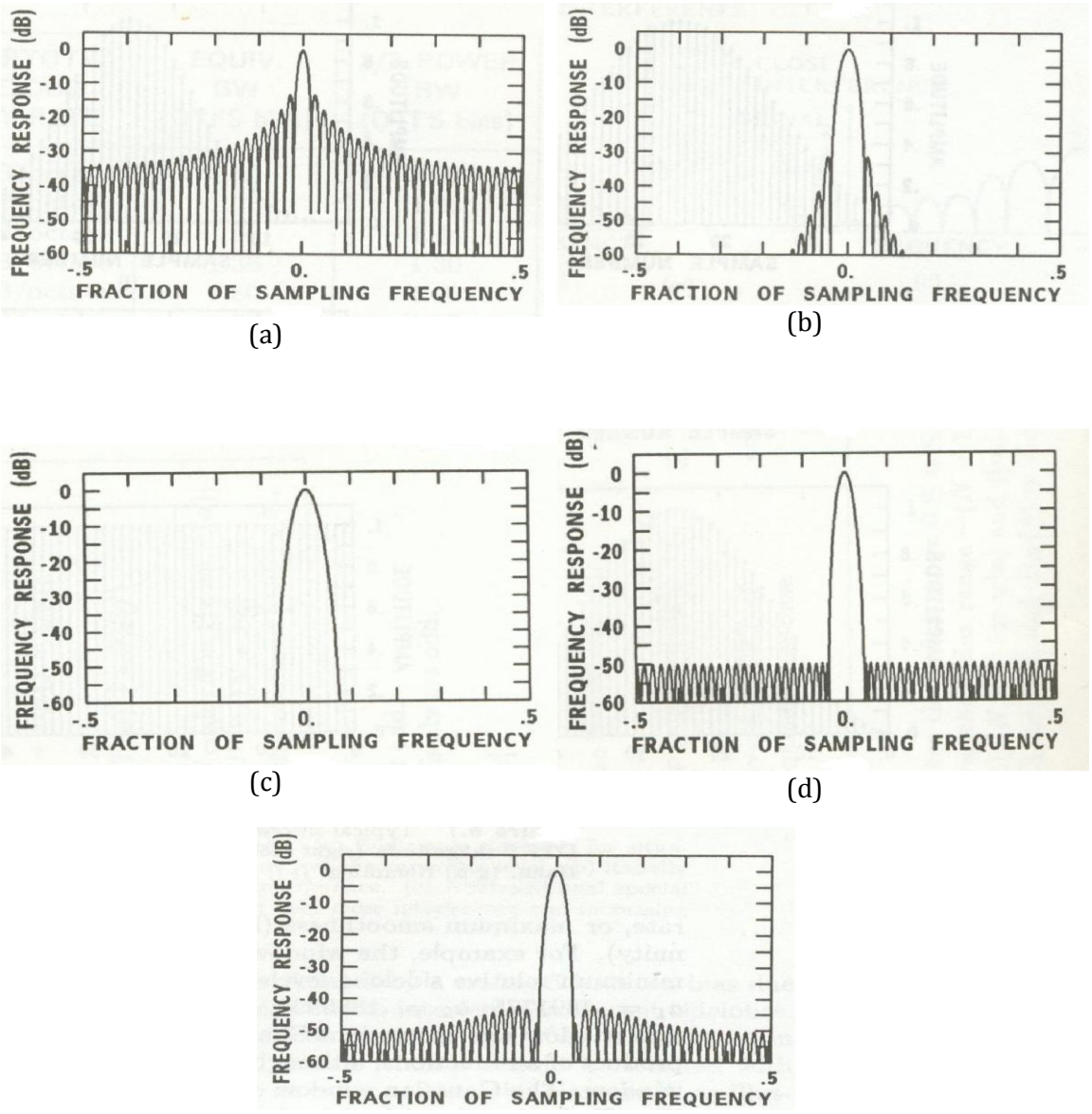

Figure 3-4 : a) Some of the window functions a) Rectangular b) Hann c) Nuttall d) Chebyshev (equiripple) e) Hamming window [43]

The frequency resolution is indicated by mainlobe frequency bandwidth. There are two measures used to quantify the mainlobe bandwidth: The half power bandwidth which is 3 dB from the peak response and equivalent bandwidth. The sidelobe behaviour is quantified using two measures:

- peak sidelobe level, which indicates how well a window suppresses leakage; and
- sidelobe decay rate, which indicates the rate at which the sidelobes closest to the main lobe fall off.

The characteristic of some windows are presented in Table 3-1.

Table 3-1: Some characteristics of window functions

WINDOW NAME	HIGHEST SIDELOBE LEVEL	ASYMPTOTIC SIDELOBE DECAY RATE	EQUIVALENT BAND WIDTH (DTFS bins)	½ - POWER BAND WIDTH (DTFS bins)
Rectangle	-13.3 dB	-6 dB/octave	1.00	0.89
Triangle	-26.5 dB	-12 dB/octave	1.33	1.28
Hann	-31.5 dB	-18 dB/octave	1.50	1.44
Hamming	- 43 dB	-6 dB/octave	1.36	1.30
Nuttall (r=3)	-98 dB	-6 dB/octave	1.80	1.70
Gaussian	-42 dB	-6 dB/octave	1.39	1.33
Chebyshev	-50 dB	0 dB/octave	1.39	1.33

The window selection process is determined by the trade-off between the bias due to the interferers in nearby sidelobes versus bias due to interferers in distant sidelobes. A Chebyshev window is suitable for close and distant interferences shown in Figure 3-5a). A rapidly decaying sidelobe window such as the Hann is suitable for distant strong interference as shown in Figure 3-5b). A window with low adjacent sidelobes such as the Hamming is suitable for very close interference and increasing sidelobes in Figure 3-5. In the field of fault detection of induction motors via motor current and vibration signals, the most popular is the Hann also known as the Hanning window [**50**], [**51**].

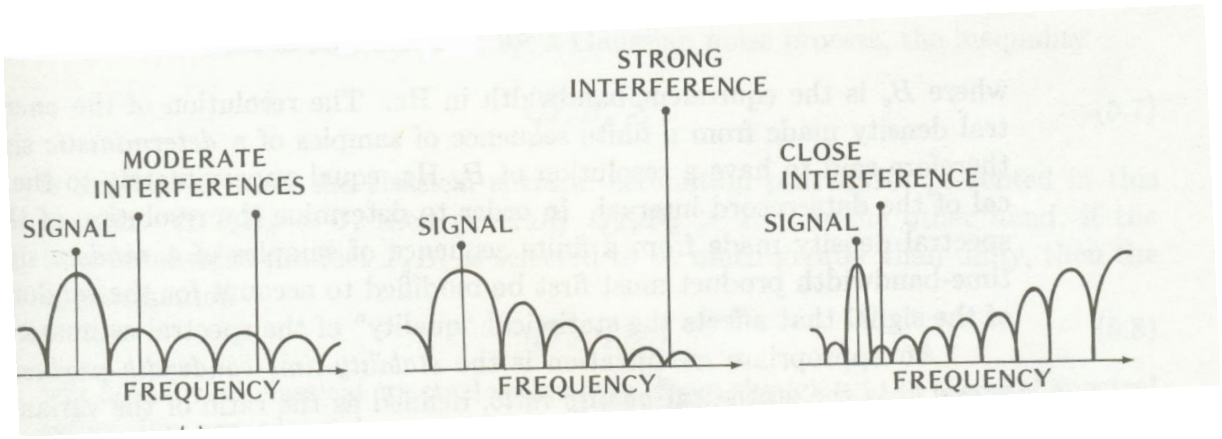

(a) (b) (c)

Figure 3-5: The criteria used for window selection [43]

3.7.2 Zero Padding

A common tool for increasing the frequency resolution of FFT is zero padding the sampled signal by augmenting it with zeros, to obtain a denser frequency grid when applying DFT. Augmenting the signal $x[n]$ with $M-N$ zeros (of course $M > N$) assumes that a new signal $y[n]$ is created

$$y[n] = \begin{cases} x[n], & n = 0, \dots\dots, N-1, \\ 0, & n = N, \dots\dots, M-1. \end{cases} \quad (3\text{-}16)$$

If the FFT of $y[n]$ is computed, an implicit assumption is made that $y[n]$ is periodic with period M. As more and more zeros are appended to the signal, the periodicity assumption will more and more resemble the assumption that the signal is zero outside the sampled range. Thus, zero padding the signal shifts the FFT assumption (periodicity) to the truncated DTFT assumption (the signal is zero outside the sampled range). However, no further information about the signal is gained. Zero padding is merely shifting from one assumption to another [**52**].

3.7.3 Power Spectral Density Estimation

In practice, the signal data is bound to contain some level of noise where the sensitivity of the signal to noise ratio of the classical spectral estimation technique reduces its performance and can make detection of fault frequency components difficult. The noises can be simply minimised by averaging the power spectral density (PSD) spectra [**12**]. The PSD of $x[n]$ can be computed

directly and indirectly. The direct approach evaluates the squared magnitude of the FFT of the data set followed by averaging; these PSD estimates are collectively known periodograms. The indirect approach performs an autocorrelation of the signal data set followed by the FFT to estimate the PSD are collectively termed as correlogram methods. The periodogram is the simplest to compute and is given as

$$p[k] = \frac{1}{N}\left|\sum_{n=0}^{N-1} x[n]e^{-j\left(\frac{2\pi}{N}\right)kn}\right|^2 \quad k = 0, 1, \dots N-1 \qquad (3\text{-}17)$$

The periodogram is an asymptotically unbiased estimator. However, as $\rightarrow \infty$; the variance does not tend towards zero, thus it not a consistent estimator. It is necessary to average the power estimate of many outputs to cause the variance to decrease [**42**]. There are three types of basic averaging schemes considered by Marple in [**43**] to be robust for many signal class:

1) the method of Daniell smooths the periodograms by averaging them over adjacent frequency bins:
2) the method of Bartlett averages multiple periodograms produced from segments of the original sequence; and
3) the method of Welch extends the Bartlett approach of overlapping segments and introduces data windowing.

The Welch PSD is the commonly used method in practical applications of spectral analysis and condition monitoring [**53**].

3.8 Time-Frequency Domain Based Signal Analysis Technique

The time-frequency domain analysis is the most popular method for analysing non-stationary signals. Some of the standard methods for analysing such signals include the Wigner-Ville distribution (WVD) and the short time Fourier transforms (STFT). These methods perform mapping of a one dimensional signal $x(t)$ to a two dimensional function of the time and frequency $TFR(x: t, \omega)$, and therefore are able to provide a true time-frequency representation of signal $x(t)$ [**54**]. But each of these methods have shortcomings. The WVD has good concentration of time-frequency plane but support areas of the signal do not overlap each other, thus interference appears on the time-frequency plane. Improvement methods such as the Choi-Williams and cone-shaped distribution have been proposed to overcome these shortcomings;

however, reduction of interference results in loss of time-frequency concentration. The problem with STFT technique is that it provides constant resolution for all frequency since it uses the same window with constant width for the analysis the whole signal. This means that if a good frequency resolution using windows is desired, this would compromise the time resolution. Furthermore, there are no orthogonal bases existing for the STFT, thus it is difficult to obtain a fast and effective algorithm to calculate the STFT [**54**].

More recent development in non-stationary signal analysis has been use of the Wavelet transforms (WT). The WT can be used for multi-scale analysis of a signal through dilation and translation in order to extract the time-frequency of a signal more effectively. In this section the signal $x(t)$ is considered non-stationary and the WT technique is discussed further this section. A typical sampled non-stationary signal $x[n]$ is displayed in Figure 3-6.

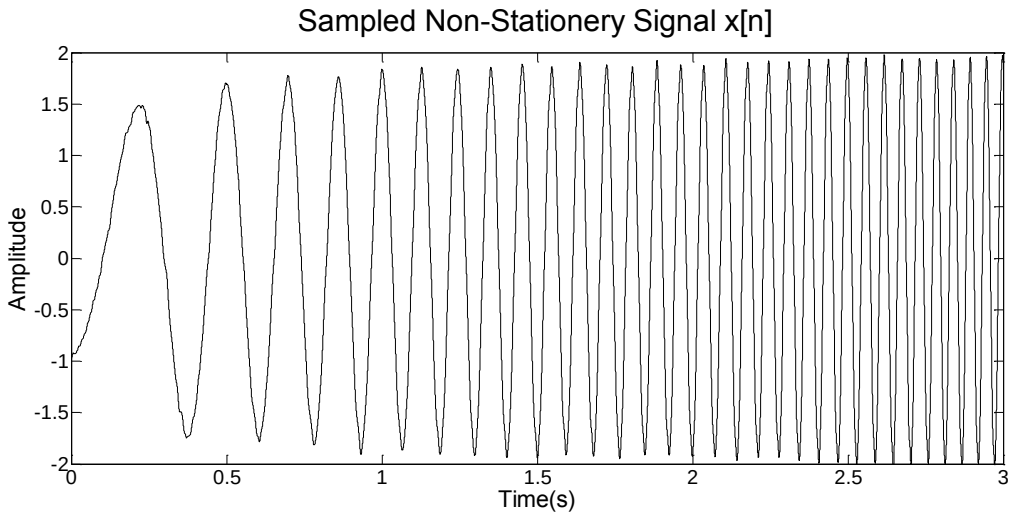

Figure 3-6: A typical sampled non-stationary signal

3.8.1 Wavelet Transform

3.8.1.1 Continuous Wavelet transform

The continuous wavelet transform (CWT) of $x(t)$ is a time-scale method of signal processing that can be defined as the sum over all time of the signal multiplied by the shifted, scale version of the wavelet function $\psi(t)$ is given by

$$T(a,b) = \frac{1}{\sqrt{a}} \int_{-\infty}^{\infty} x(t)\psi^*\left(\frac{t-b}{a}\right) dt \qquad (3\text{-}18)$$

Where $\psi^*(t)$ denote the complex conjugates of the mother wavelet $\psi(t)$. The parameter a represents the scale (contraction or dilation) index which is the reciprocal of frequency and is the distance between the centre of the wavelet function and its crossing on the time axis. The parameter b is the shift (translation); it governs the movement of the wavelet function along the time axis. In Figure 3-7a) the contraction and dilation of a Mexican Hat wavelet function on the time axis is illustrated, while in Figure 3-7b) the translation of the Mexican Hat wavelet function on the time axis from b_1 via b_2 to b_3 is illustrated. In CWT, the mother wavelet is dilated and translated continuously on a real number system.

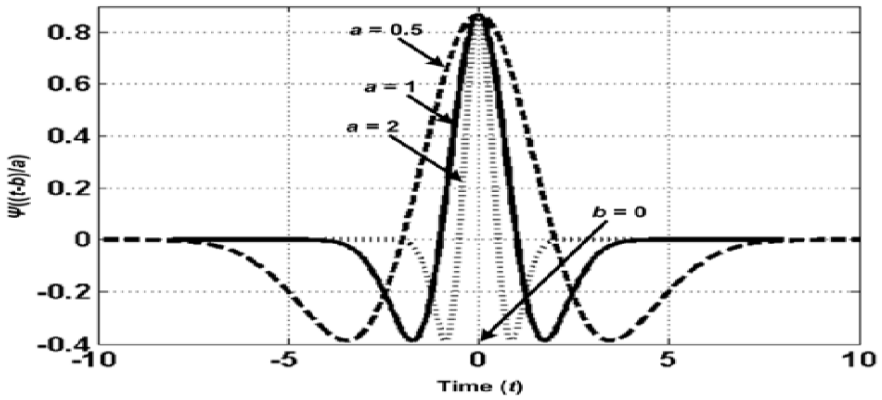

(a)

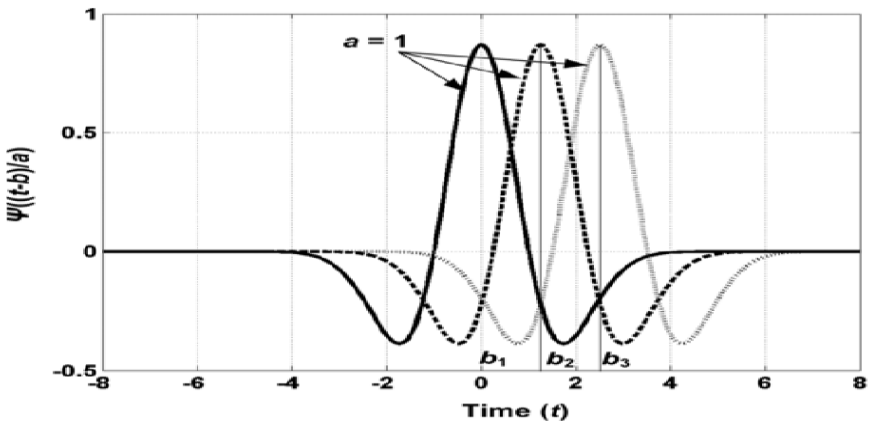

(b)

Figure 3-7: a) The contraction of the Mexican Hat wavelet b) and the dilation [36]

3.8.1.2 Discrete Wavelet transform

The Wavelet Series was introduced as a sampled version of CWT for implementation on the computer, but required a considerable amount of resources. It also suffered redundancy when attempting to reconstruct the signal. The discrete wavelet transform (DWT) was introduced to overcome the shortcomings of the Wavelet Series [**55**]. The DWT reduces computational time and is much easier to compute. The most common discretisation is dyadic, given by

$$DWT(j,k) = \frac{1}{\sqrt{2^j}} \int_{-\infty}^{\infty} x(t)\psi^* \left(\frac{t - 2^j k}{2^j} \right) \tag{3-19}$$

Where a and b are replaced by 2^j and $2^j k$ respectively. An efficient way of implementing this is using filter schemes which was developed by Mallat in 1988 [**54**], [**55**].

3.8.1.3 One stage filtering: approximation and detail

For many signals, the low frequency content is the important part, which gives the signal identity, while the high frequency contents impart flavour. In wavelet analysis, the approximations are the high-scale, low frequency components of the signal. The details are the low-scale, high frequency components. The most basic filter process is depicted in Figure 3-8. The original sampled signal $x[n]$ passes through two complementary filters and emerges as two signals. If this operation is applied on a real signal digitised signal such as $x[n]$, twice as much data is obtained. To overcome this problem down-sampling is introduced [**56**].

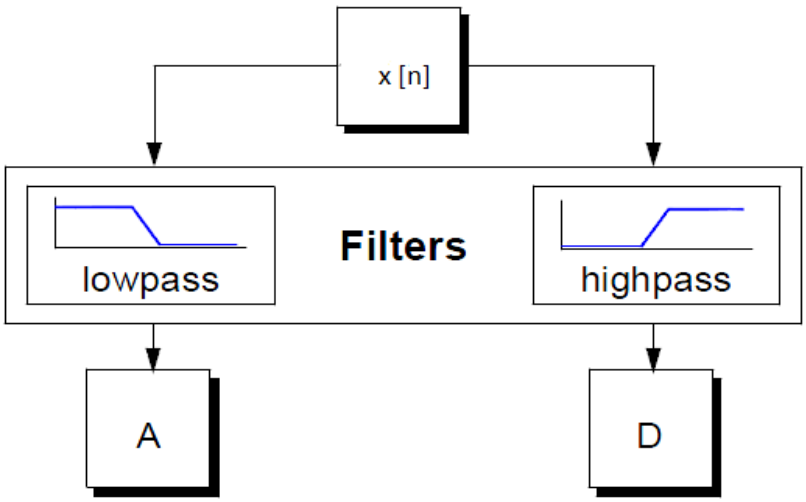

Figure 3-8: The most basic filter process [56]

3.8.1.4 Multiple level decomposition

The wavelet decompositions process can be iterative, with successive approximations being decomposed in turn, such that the signal is decomposed into lower resolutions components as shown in Figure 3-9.

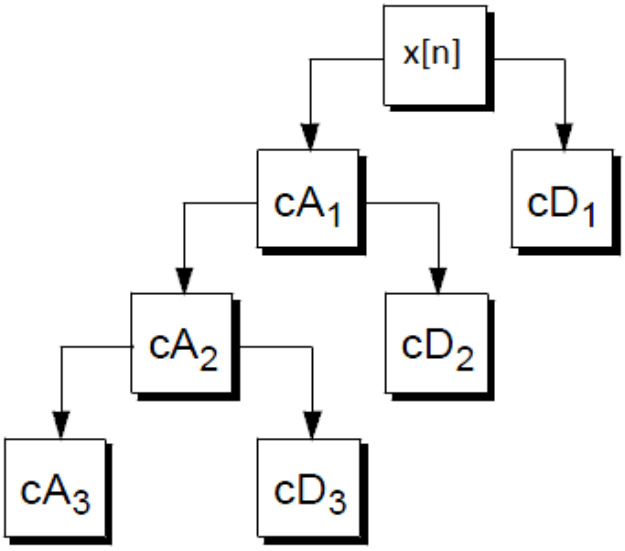

Figure 3-9: Iterative wavelet decomposition [56]

If F_s (in samples per second) is the sampling frequency used to capture the signal $x[n]$, then the detail space d_j contains information concerning the signal components whose frequencies are included in the interval.

$$f(D_j) \in \left[2^{-(j+1)} \cdot F_s,\ 2^{-j} \cdot F_s\right] \tag{3-20}$$

The approximation space a_n includes low frequency components of the signal belong to the interval.

$$f(A_n) \in \left[\ 0, 2^{-(n+1)} \cdot F_s\right] \tag{3-21}$$

The decomposed components can be reconstructed or synthesised to obtain the original signal without loss of information using inverse discrete Wavelet transforms (IDWT). Since the wavelet decomposition process involves filtering and down-sampling; the reconstruction process involves up-sampling and filtering [**56**].

3.8.1.5 Wavelet packets decomposition

Wavelet packets decomposition (WPD) offers a more complex and flexible analysis since the detail spaces d_j as well as the approximation spaces a_n are decomposed further, as shown in Figure 3-10a). A single WPD gives a lot of bases where the best representation of the signal with respect to the objectives can be looked for. The reiterative decomposition of the spaces is represented in a binary tree, shown in Figure 3-10b), where the nodes are labelled by their *Depth j* (a dilation factor) and *node number k* (frequency scale).

It has been proven that there are more than $2^{2^{j-1}}$ different wavelet packet orthonormal bases included in the wavelet binary tree of *Depth j*. Each of these packets has a limited time as well as frequency support. Using WPD redundancy is added to the transformation by expanding each packet repeatedly. The time-frequency representation obtained is a matrix containing the wavelet packets coefficients for all the Depths and Nodes. If signal $x[n]$ has length M, then the total number of Depth is $(1 + \log_2 M)$. The maximum number of one Depth is M. The coefficients are equal to the original signal at *Depth 0.* The Depths and Nodes corresponding to particular fault frequencies can be examined [**57**].

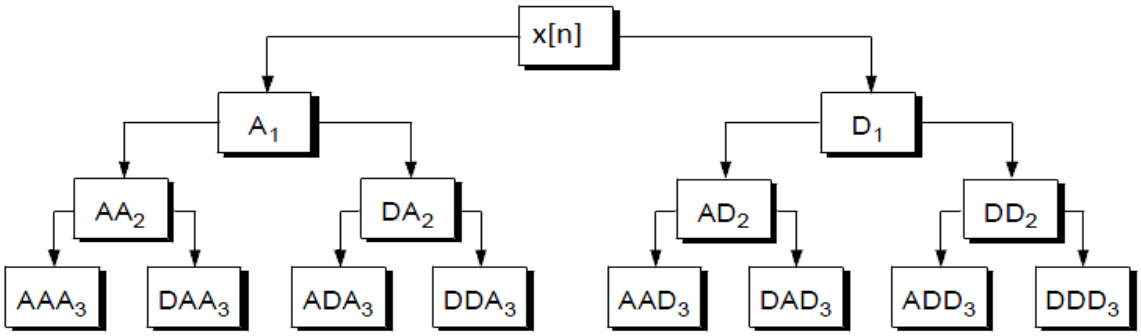

(a)

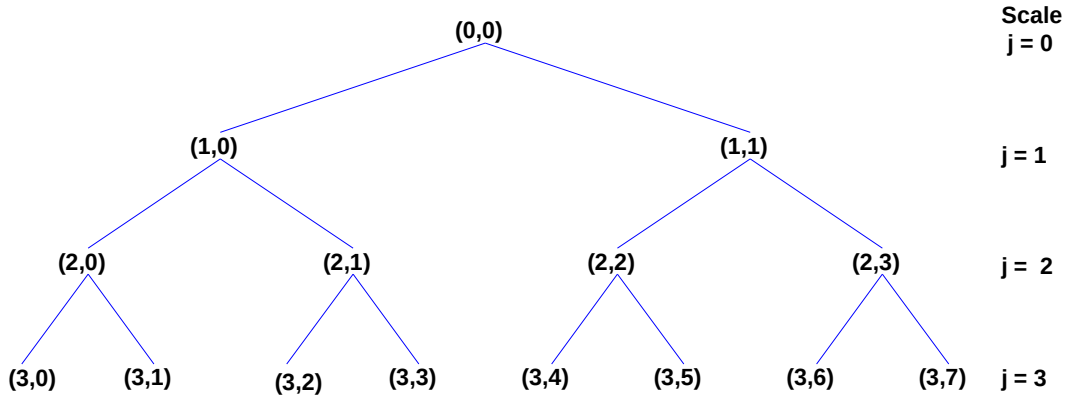

(b)

Figure 3-10: a) WPD process b) binary tree

3.8.1.6 Selection of mother wavelet

There are several wavelets with different functions with different mathematical properties that have been developed. The wavelets include infinite support wavelets, such as Gaussian, Mexican Hat, Morlet and Meyer, and wavelets with compact support, such as the Haar, Daubechies, Coiflet, Symlets and Biorthogonal. Some of these wavelets functions are displayed in Figure 3-11.

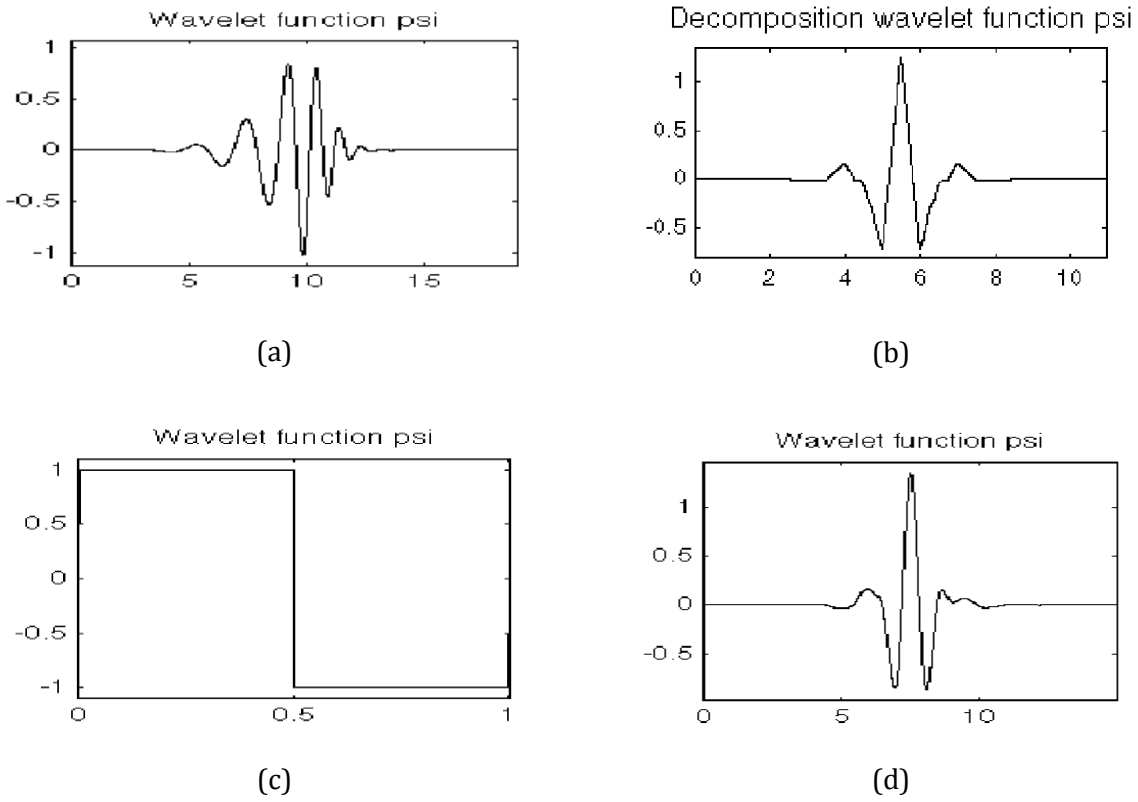

Figure 3-11: Some wavelet functions a) Daubechies 10 b) Biorthogonal c) Haar d) Symlets [56]

In some fields of science, some families show better results for particular applications. In the case of compactly supported wavelets there are higher order mother wavelets (with a large number of coefficients) and lower-order mother wavelets. Lower order wavelets result in overlap between adjacent frequency bands. The Daubechies mother wavelet is commonly used in the DWT to analyse induction motor faults [**58**] - [**61**].

3.8.1.7 Specification of decomposition level

The number of decomposition levels is determined by the frequency components at frequency f to be traced. The lower the frequency level to be extracted, the higher the number of decompositions levels. [**59**]. The decomposition level l is given by [**61**]

$$l = integer\left[\frac{\log\left(\frac{F_s}{f}\right)}{\log(2)}\right] \tag{3-22}$$

The data length N_l of the decomposition level l is given

$$N_l = \frac{N}{2^l} \tag{3-23}$$

3.8.1.8 Decomposition Energy

Energies related to the decomposition signal for each approximation coefficient E_j^A and each detail coefficient E_j^D can be computed by [**61**]

$$E_j^A = \sqrt{\frac{1}{N_{lw}} \sum_{i=1}^{N_{lw}} (Aj)^2[i]} \tag{3-24}$$

$$E_j^D = \sqrt{\frac{1}{N_{lw}} \sum_{i=1}^{N_{lw}} (Dj)^2[i]} \tag{3-25}$$

Where $j = 1, \ldots\ldots, l$ and N_{lw} is the data length of the decomposition level without the boundary effect. In DWT, the boundary distortion effect is a result of the finite data length convolution.

3.9 Concluding remarks

This chapter presented some of the frequency and time-frequency domain techniques which may be used for fault detection in induction motors. They can analyse time periodic signals such as the current and vibration signals of the motor. Demodulation of such signals using the Hilbert transform to remove the fundamental component was discussed. The frequency domain techniques are a two dimensional representation of the frequency and magnitude or phase of the signal, and are suitable for stationary analysis of the signal. The non-parametric frequency domain technique based on the Fourier transform was discussed in detail. Methods to enhance the spectral estimation of this technique such as windowing, zero-padding and power density estimation were discussed. Zero padding increases density of samples in the transform domain while the window function reduces the spectral leakage. The Hann window is a popular choice in the field of condition monitoring. The signal to noise ratio is increased by averaging several power spectral density. The Welche method is the commonly used PSD estimator in the field of condition monitoring.

The time-frequency domain techniques are a three dimensional representation of time, frequency and magnitude of the signal, and are suitable for non-stationary signals. The DWT wavelet transform extracts the time-frequency information of the signals more effectively than the other techniques.

The next chapter discusses the measurement techniques of these types of signals, and the application of these signal processing techniques to detect the characteristics of these faults.

4. CURRENT AND VIBRATION MONITORING AND FAULT CHARACTERISTICS OF INDUCTION MOTORS

4.1 Introduction

The most commonly monitored parameters or signals in condition monitoring; current and vibration, as already mentioned in chapter 2, will be discussed further in this chapter. These parameters indicate a fault condition by either an increase or decrease in the overall value or by some change in characteristic value. For such parameters, simple measurements of overall values may not be sufficient to reveal a fault condition. As a result, spectral and phase (in the case of vibration) measurements may be required to reveal changes attributed to faults. The accuracy required for condition monitoring parameters is not as absolute as the one required for performance measurement. The monitoring methods and frequency domain fault characteristics of these two signals is discussed in this chapter.

4.2 Current Monitoring

4.2.1 Types of frequency harmonic in the current

In the stator current of every induction motor there are two types of frequency harmonics that are always present: the winding harmonics (WHs) and the principal slot harmonics (PSHs). The important ones for a three phase induction motor are: the first order WH (also called the fundamental component), the fifth order (WH5), and seventh order (WH7). The frequency of the n order is WH (WHn) is proportional to the fundamental supply frequency f_1 [**62**]. For inverter-fed motors there are additional harmonics in the current based on the number of pulses due to the switching as expressed in section 2.2.3.

4.2.2 Current monitoring instrumentation

It is possible to obtain information about the health and the integrity of an induction motor through the monitoring and analysis of the electrical signature, as mentioned previously. The instrumentation system usually consists of the following items according to [**63**]:

- A current transformer (CT) to sense the signal
- A resistive shunt across the output of the CT. These CTs are usually available with internal shunts.
- An MCSA instrument to produce the current spectrum or signature

The current measurements can be collected by measuring the secondary side of a current transformer (CT) or around the motor cable using a clip on current transformer. Usually only one current signal of one motor phase is analysed for its current frequency content. The reason for this is that, the rotating flux waves produced by the different faults cut all three stator phase windings; thus the corresponding currents are induced in each of the three phases. High frequency response range is required for the CTs to cover the frequency range of components that can be induced due to different faults mechanism and also to cater for inverter-fed induction motor drives. The frequency domain based methods of the line current are generally known as motor current signature analysis (MCSA) [**63**].

However, the CT specifications have not yet been documented by the *International Standards Organisation* in [**64**].

4.3 Vibration monitoring

4.3.1 Classification of Vibration

All machines under normal operation produce oscillation motion such as vibration. There are two types of vibration - benign and serious vibration.

4.3.1.1 Benign vibration

Benign vibrations are characteristics of regular operating conditions. Examples of benign vibrations are as follows:

- blade passing frequency;
- 120Hz (100Hz for 50Hz AC supplies) motor hum frequency. The motor noise associated with the vibrations of the core and windings due to the MMF is at this frequency;
- pure tone from motors driven by VFD;
- gearmesh frequencies; and
- broadband turbulence from pumps or fans.

The amplitude will vary from machine to machine and is a measure of the quality of manufacturing and load condition. Increase in normal levels advocates a reason for investigation but not for alarm [**65**].

4.3.1.2 Serious vibration

Serious vibration cause accelerated wear and premature failure. The serious vibrations can be categorised into two: forced and natural. The corrective actions of these two serious vibrations are totally different. Forced vibrations are caused by mechanical (misalignment, unbalance, worn bearing, bent rotor etc.) and electrical (shorted turns, rotor cage faults, etc) defects. These defects can be corrected by alignment, balancing or changing the faulty component, whereas natural vibrations are caused by a structural effect, where the structure behaves like a mechanical amplifier to sensitive frequencies. Symptoms of natural vibrations are:

- abnormally high amplitudes of vibrations;
- strongly directional vibrations;
- variation of vibration amplitude; and
- rumbles during coast up and coast down of motor.

There are three main tests used to verify resonance: impact or hammer test on the major components to determine their natural frequencies, variable shaker, and coast-up and down test. Thus, corrective measures involve changing the speed, adding damping, changing the natural frequency of the responding part, dynamic absorber and reducing source input [**65**].

4.3.2 Vibration Monitoring Methods

4.3.2.1 Types of vibration signals

The commonly measured vibration signals are: displacement, velocity and acceleration. The vibration amplitude versus frequencies of these three signals are illustrated in Figure 4-1.

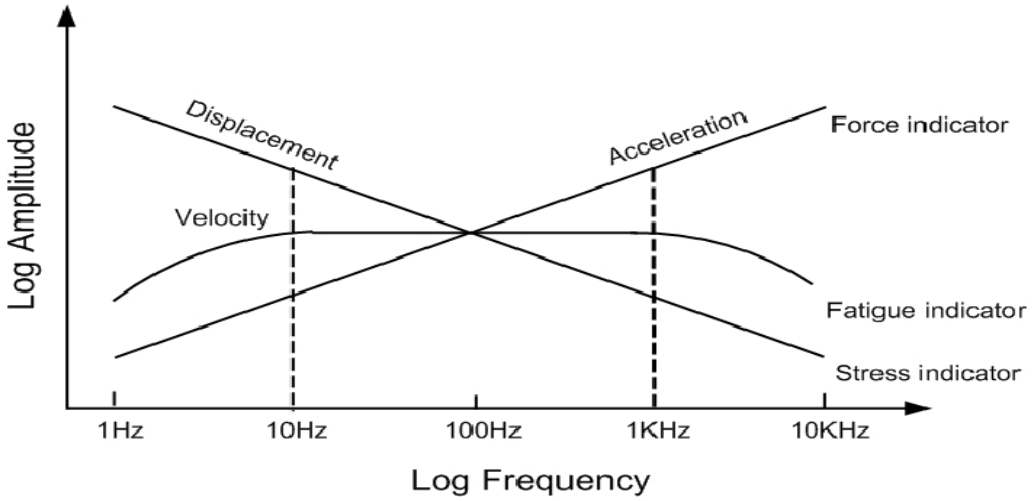

Figure 4-1: Amplitude versus frequency plot of the vibration signals [66]

Displacement measures the distance that the moving component has moved relative to a fixed reference and it indicates stress. It is a predominate factor at low speeds $1200rpm$ (below $20Hz$). Velocity measures the instantaneous rate of change of the displacement and it indicates fatigue. The amplitude is constant throughout all frequencies, and as a result it is preferred for condition monitoring where the amplitude has the same meaning at all frequencies, which simplifies the interpretation of the severity and establishing the alarm limits. Velocity is generally used between $10Hz$ ($600rpm$) and $1kHz$ ($60{,}000rpm$). Acceleration measures the instantaneous rate of change of velocity and it indicates force. It is a predominate factor at high speeds $60{,}000rpm$ ($1kHz$) [**66**].

4.3.2.2 Types of measuring sensors

In general there are three categories of vibration sensors based on their electrical outputs: displacement sensors, velocity sensors and accelerometers. Each sensor type serves a specific purpose and is restricted by inherent constraints [**66**]. Displacement sensors, such as proximity switches and strain gauges are non-contact and measure shaft movement or displacement relative to the probes itself. Velocity sensors, such as tachogenerators, unlike the displacements sensors, have contact with the moving components to measure the motion. Accelerometer sensors are usually classified into two: Piezoelectric (PE) and Piezoresistive (PR) accelerometers.

The PE accelerometers are the most widely used for testing and measurement [**67**] compared to the PR accelerometers since they provide a wide frequency range and are available in wide range of sensitivity, size and weight. There are two subdivisions of the PE accelerometer: the

basic charge mode piezoelectric and the voltage mode internal electronic piezoelectric (IEPE) accelerometers. The basic charge mode PE requires use of special low noise cables (which tend to be expensive compared to the standard commercial coaxial cable and charge amplifiers), thus IEPE type is preferred.

These vibration sensors need to be attached to the surface of the machines. The merits and demerits of these device types can be summarised in Table 4-1. In the field of vibration monitoring the PE accelerometer is the most commonly used, which permits the vibration signal to be converted to either a velocity or displacement signal [**33**], [**66**], [**68**], [**69**].

Table 4-1: Summary of vibration sensors

Measuring device	**Advantages**	**Disadvantages**
Proximity sensors	Measures shaft static position. Measures dynamic motion. Simple calibration. Rugged and reliable construction. Excellent response in the operating range. Suitable for installation of harsh environment.	Sensitive to imperfection of the surface. Sensitive to material properties. Shaft surface must be conductive. Low signal response at high speeds (rpm) External power source is required Sensitive to interference from near proximity probes
Velocity sensors	No external power supply is required Powerful signal output is required Easy to use	Limited frequency range Wear of moving parts is potential for failure Mounting orientation is essential Bulky size
Accelerometers (PE)	Easy attachment Wide Frequency range Light weight Many configurations High acceleration applications High temperature applications Solid-state electronics with rugged construction	Frequency changes based on mounting technique External power supply source is required Double integration sometimes suffers low noise Can't measure shaft vibration

4.3.2.3 Mounting methods of sensors

The location and mounting of the sensor is critical to capturing the desired information. Proximity sensors tend to be located by the machinery manufacturers and are mostly correctly located. Velocity sensors and accelerometers are usually located by the user; hence these require proper orientation and secure installation to achieve optimal results. The mounting methods used can affect the final frequency response of the sensor. Depending on the mounting configuration the frequency can be limited as indicated in Table 4-2. This provides some indication of the frequency ranges for different mounting methods [**68**]

Table 4-2: Mounting method used for sensors and their corresponding frequency ranges

Mounting Method	**Frequency range**
Hand-held probe tip	500Hz – 1000Hz
Using a magnetic base	1500Hz – 2000Hz
Stud Mounting	5000Hz – 10000Hz
Use of Adhesive on base	4000Hz – 5000Hz

4.3.2.4 Sensor location and axis orientation

The sensor location depends on the particular machine and specific parameter to be measured. In general, sensors should be located at or near the bearings. There are three axis orientations for mounting the sensors shown in Figure 4-2.

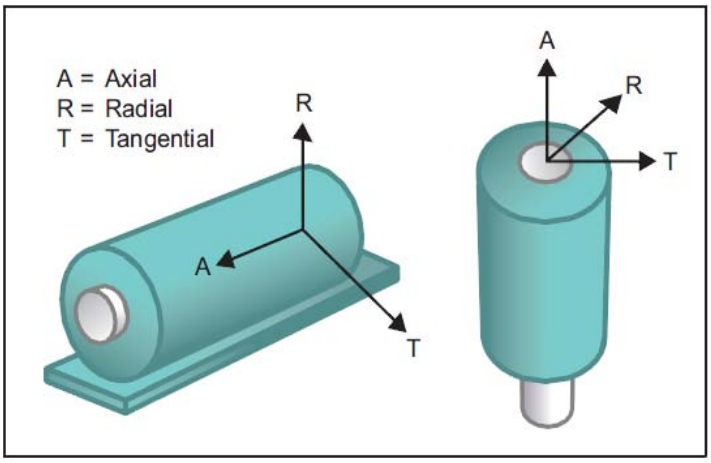

Figure 4-2: Sensor axis orientation

The vibration monitoring methods are in accord with the *International Standards Organisation* in [**68**].

4.4 Characteristics of Common Faults during Steady State

The monitoring methods of the current and vibration signals have been discussed in the previous sections. The causes of the common faults associated with induction motors, discussed in 2.3, normally have a mechanical origin that affects the magnetic field. An unbalanced magnetic field causes unbalanced electrically induced forces in the motor. In conducting fault analysis, the analysis is based on the line frequency (50/60Hz), the frequency at which the AC power is supplied to the motor and the rotational speed (slip). In the case of inverter-fed motors, the operating frequency of the drive must be known. In vibration analysis, the one times line frequency may be present, especially if the natural frequency is at the line frequency since machine faults produce additional frequency harmonics or an increase in existing ones in the stator current or vibration signals. Spectral analysis of these harmonics is therefore an obvious approach used for fault detection. The basic spectral analysis of these signals is based on the Fourier transform referred to as the classical technique. The spectral characteristics, in accordance with the *International Standards Organisation*, associated with the four most common faults in induction motors are discussed.

4.4.1 Shorted Stator Windings Faults

Stator turn fault in an AC symmetrical machine causes a large circulating current to flow and as a result it generates excessive heat in the shorted windings. If the heat which is proportional to the square of the currents exceeds the limiting value complete failure may occur. The stator faults progress from an incipient stage to a very advanced stage in a matter of seconds, thus detecting one or two turns, in stator coil, a pre-planned shutdown can be arranged [**6**]. Previous

studies have shown that the following equation gives harmonic components in the air-gap flux waveform are functions of shorted turns [**12**], [**64**]:

$$f_{st} = f_1\left(\frac{n}{p}(1-s) \pm k\right) \qquad (4\text{-}1)$$

Where the harmonic components at frequencies f_{st} , due to the shorted windings, are a function of the supply frequency f_1, integers $n = 1,2,3,..$, integers $k = 1,3,5,..$, p is the pole-pairs, and s is the per unit slip. These rotating flux waves can induce corresponding current components in the stator winding. The detection of the shorted turns using MCSA is based on detecting the harmonic components given by (4-1). Using vibration analysis, the shorted stator windings (electrical phase problems) cause an unbalance force at twice line frequency $2f_L$ and multiples with modulation at rotor speed. This generates high vibrations at twice line frequency predominantly in the radial direction as illustrated in Figure 4-3 [**33**].

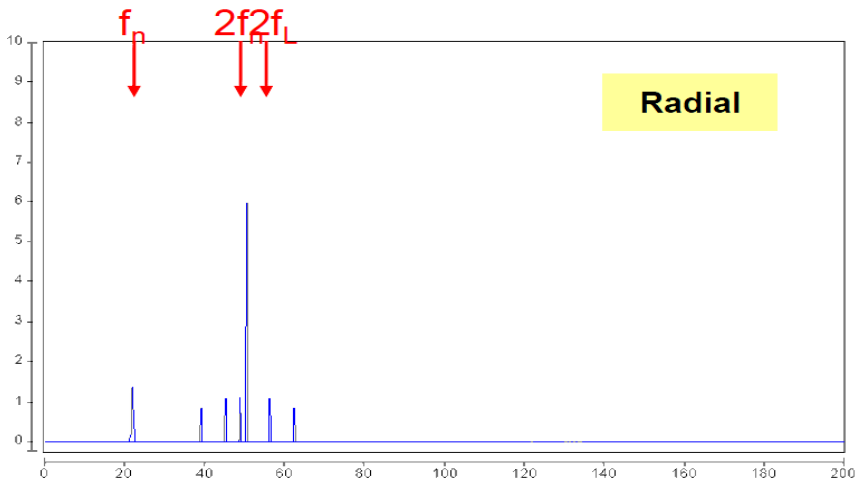

Figure 4-3 : A typical vibration spectrum for a motor with shorted windings or laminations [22]

4.4.2 Rotor Winding Cage Defects

The currents in the rotor cage produce a three phase magnetic field, which contains the same number of poles as the stator field but is rotating at slip frequency with respect to the rotor. If a rotor asymmetry occurs, there is a backward resultant rotating field at slip frequency with respect to the forward rotating rotor. This asymmetry is a result of broken or breaks on the shorting rings, thus preventing current flow. As a result, the field around that area will not exist.

Hence the force applied to that side of the rotor would be different from the other side of the rotor. Rotor asymmetries result in current harmonic components induced in the stator winding. The result of backward rotating field induced additional frequency harmonics seen as sidebands to the fundamental harmonic component at frequencies given by:

$$f_{brb} = (1 \pm 2ks) f_1 \qquad (4\text{-}2)$$

Where f_{brb} is the broken rotor frequency harmonic, s is the rotor per unit slip, f_1 is the supply frequency and $= 1,2,3,..$. Among these components, those normally used in industrial environment for the detection of rotor asymmetries are the twice slip frequency sideband components appearing around the supply frequency given by [left side harmonic (negative) and right side harmonic (positive sign)] [**59**], [**64**], [**70**]:

$$f_{sb} = (1 \pm 2s) f_1 \qquad (4\text{-}3)$$

Detecting the frequency components in the line current is the most common method of detecting defected rotors; however vibration analysis can be employed. Using vibration analysis the unbalance force created rotates at one times rotational speed (frequency) and is modulated by slip frequency times the number of poles. The electrical imbalance can create significant vibration levels at one and two times rotational frequencies predominate in the radial direction on the vibration spectrum. A typical vibration spectrum illustrating this is shown in Figure 4-4. The one times rotational frequency is the fundamental component. Since this problem is not interactive with the line frequency, a spectral line at $50Hz$ may not be present [**71**].

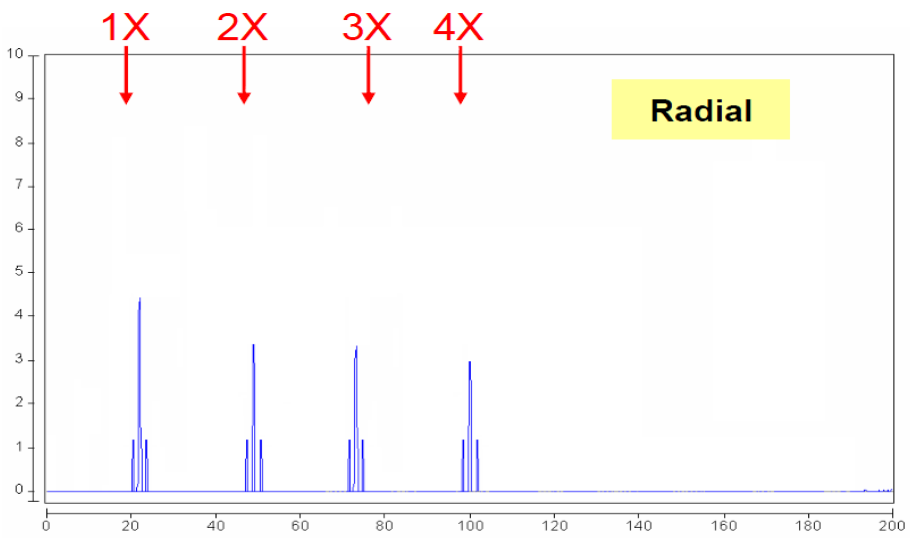

Figure 4-4: A typical vibration spectrum of a motor with broken rotor bars [22]

4.4.3 Bearing Defects

Machine vibration due to bearing faults can be considered as slight rotor displacement, which may result in eccentricities. The mechanical oscillations due to bearing faults change the air-gap symmetry and machine inductance like eccentricity faults. The single point bearing fault presented in section 2.3.3 produces specific fault frequencies in the machine vibration. The two most common ways to determine single point defects are by motor current analysis and vibration. These frequencies are a function of the bearing size, type and location of the defect. The bearing fault frequencies include: ball pass frequency outer race F_{BPO}, ball pass frequency inner race F_{BPI}, ball spin frequency F_{BS} and fundamental train frequency F_{TT}. These are given by [**72**], [**73**]:

$$
\begin{aligned}
F_{BPO} &= \frac{Z \cdot n_r}{2 \cdot 60}\left(1 - \frac{d}{D}cos\alpha\right) \\
F_{BPI} &= \frac{Z \cdot n_r}{2 \cdot 60}\left(1 + \frac{d}{D}cos\alpha\right) \\
F_{BS} &= \frac{D \cdot n_r}{d \cdot 60}\left(1 - \left[\frac{d}{D}cos\alpha\right]^2\right) \\
F_{TT} &= \frac{n_r}{2 \cdot 60}\left(1 + \frac{d}{D}cos\alpha\right)
\end{aligned}
\tag{4-4}
$$

There are five parameters that must be known in-order to determine the fault frequencies, indicated in Figure 4-5.

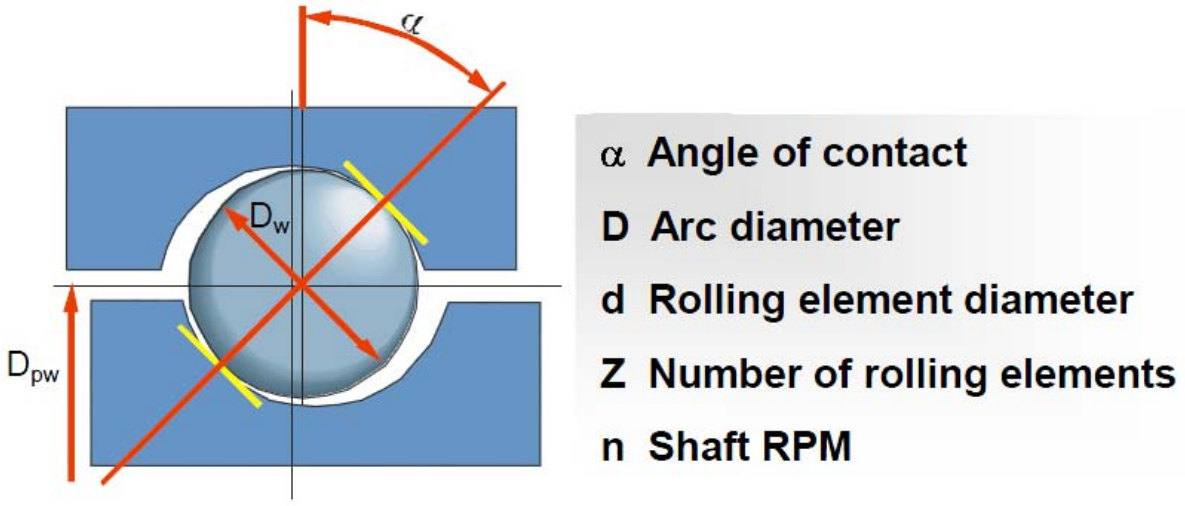

Figure 4-5: Ball bearing geometry and parameters [22]

The inner and outer bearing faults given in equation (4-5) can be approximated by the following formulas if the number of balls Z is between $6-12$, where the rotational frequency is f_r [**64**]:

$$F_{BPI} = 0.6 \cdot Z \cdot f_r$$
$$F_{BPO} = 0.4 \cdot Z \cdot f_r \qquad (4\text{-}5)$$

In motor current analysis, the variations of machine inductances attributed to bearings faults are reflected to line current in terms of current harmonics, which are indicators of bearing faults due to the mechanical oscillation in the air-gap [**12**]. This leads to harmonics at the following bearing frequencies f_{bng} in line current [**12**]:

$$f_{bng} = |f_1 \pm m f_v| \qquad (4\text{-}6)$$

Where f_1, is the supply frequency and f_v is one of the characteristic frequencies expressed by equation (4-4) and (4-5). Detecting the inner F_{BPI} harmonic components is more challenging on the current spectrum [**73**].

In vibration analysis, in the case of single-point bearing defects only one of the four characteristics frequencies given in equation (4-4) and (4-5) would show up. The collision of the bearings at the point of contact; results in shock waves that excite the natural frequencies. The natural frequencies modulate the fault frequencies. Detecting a single point faults in the inner race is more challenging since the fault moves in and out of the static load zone when the inner race is constantly moving. Thus the inner race is not only modulated by the natural frequencies but also the shaft rotational speed. The fault harmonics occur in a group near the natural resonance harmonic, each group containing a peak is separated by the shaft rotational frequency harmonic. The frequency spacing F_{sp} from any harmonic peak in one group to another peak in another group is given by equation (4-10) where $m = 0, \pm 1, \pm 2$.

$$F_{sp} = \pm F_{BPI} + mf_r \qquad (4\text{-}7)$$

The typical vibration spectrums of a motor with an inner and an outer bearing race fault is displayed in Figure 4-6a) and b) respectively.

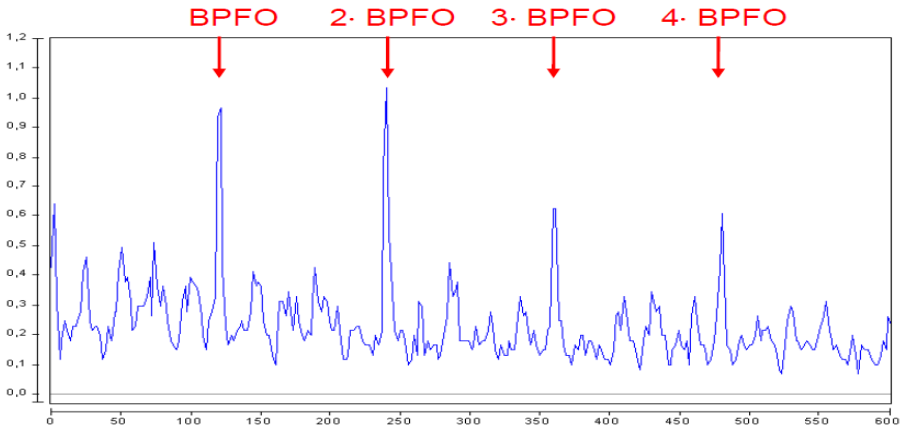

(a)

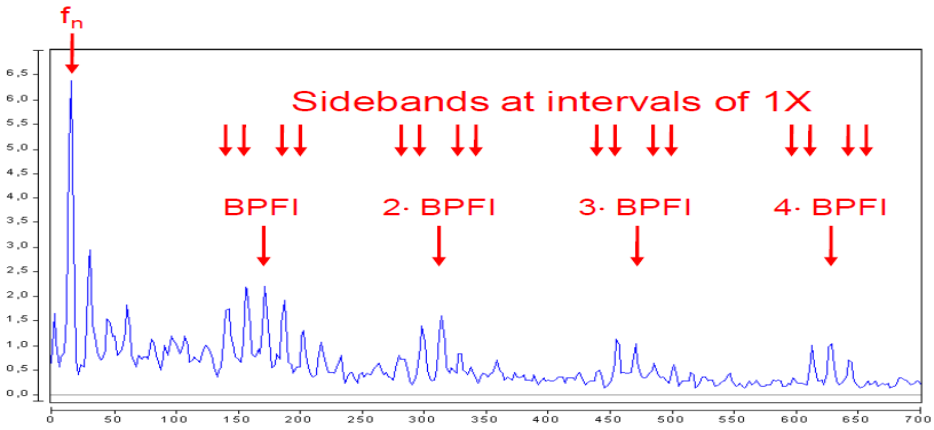

(b)

Figure 4-6: A typical vibration spectrums of a motor with bearing faults (a) Outer race fault (b) inner race fault [22]

4.4.4 Dynamic Eccentricities

When there is an eccentricity in the air-gap the flux density of the motor is affected. The flux density affects the current indirectly and the vibration directly. Hence the vibrations are a very dependable means of detecting the eccentricity. Varying inductances cause an imbalance in the magnetic flux within the air-gap that results fault harmonics in the line current, which can be identified in the frequency spectrum [**12**]. The flux density in the air-gap of an induction motor is due to the interaction of the MMF and permeance. While the MMF is a function of the time and space harmonics, the permeance is the function of the rotor, stator slots and eccentricity. The high stator current components arising out of the static, dynamic and mixed eccentricities are at frequencies given by [**64**]:

$$f_{ecc1} = \left[R\left(\frac{1-s}{p}\right) \pm n_{ws}\right] f_1 \pm \left[f_1\left(\frac{1-s}{p}\right)\right] \qquad (4\text{-}8)$$

Where f_{ecc1} are the frequencies of the harmonic components which are a function of the air-gap eccentricity, f_1 is again the supply frequency, R is the number of rotor slots, $n_{ws} = 1, 3, 5, etc$ (integer 1 corresponds to the fundamental component in the MMF waveform, integer 3 – 3rd harmonic etc), s is the rotor per unit slip and finally p is the pole pair. In the case of dynamic eccentricities variance in flux can yield to induced stator current components at frequencies given by:

$$f_{ecc2} = f_1 \pm m f_r \tag{4-9}$$

Where f_{ecc2} are the frequencies of the stator current harmonics due to changes in the air-gap, the harmonic number $m = 1, 2, 3$ and f_r is again the rotational speed. In the mechanical vibration spectrum the dynamic eccentricity components at frequencies f_{lv} given by:

$$f_{lv} = 2f_1 \pm f_r \tag{4-10}$$

The twice line frequency vibrations are a result of the changes in the magnetic attraction between the rotor and stator at twice the line frequency. The varying magnetic forces cause small dimensional changes in the iron material, leading to vibrations. The $2f_1$ ($2f_L$) component is also expected to rise. A typical vibration spectrum of a motor with an eccentric rotor is shown in Figure 4-7.

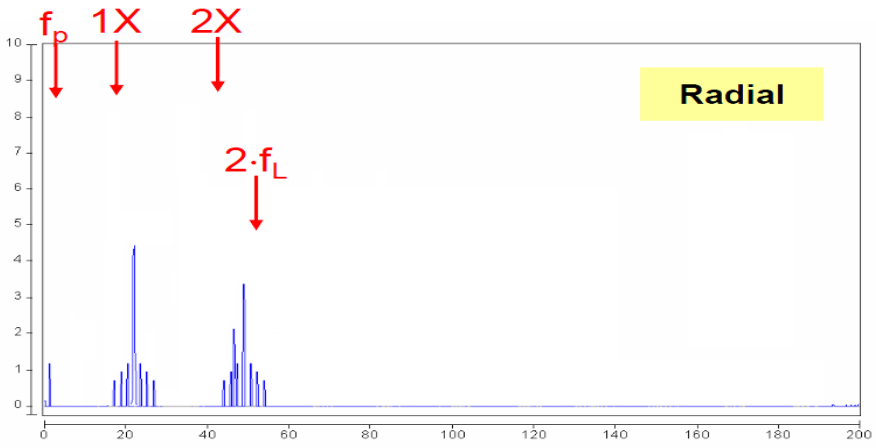

Figure 4-7: A typical vibration spectrum for a motor with eccentric rotor [22]

4.5 Characteristics of Common Faults during Transient State

In the previous section the frequency domain characteristics of the fault harmonics associated with the common faults were discussed. However, if the induction motor is operating under varying operating fundamental frequency or fluctuating load conditions, the harmonic

components are time-varying since they depend on the supply frequency and/or rotational speed. If the variations are slow during the observation interval the classical spectral estimation can be applied. However, when variations are faster; signal processing methods for non-stationary signals are applied.

As a result of the advances in Wavelet theory and the optimisation of the different modes (CWT, DWT, WPD) in the last decade, authors have tried to overcome the limitations of classical technique by proposing wavelet based methods on the analysis of non-stationary signals. For MCSA, the current demanded by the machine during startup transient operation has been investigated in [**59**], [**60**], [**62**], [**74**]. This technique is referred to as transient motor current signature analysis (TMCSA). This can be seen as an extension of the conventional MCSA technique, since it is based on the extraction and identification of the characteristic current components used by MCSA, but in the transient regime. Thus it can be used to analyse currents during start-up and for any transients involving changes in slip. Some researchers have applied DWT successfully to the startup current to detect the presence of broken rotor bars in [**59**], [**60**] [**75**], [**76**], [**77**].

The main idea underlying this alternative methodology is tracking the characteristics transient evolution of the fault related to the left side harmonic (LSH) component. A qualitative pattern rising in high level DWT signals shown in Figure 4-8 was proven to be a good indicator of the fault, provided that the length of the start-up is long enough. However, very little work has been done for the other common faults in [**75**],[**62**].

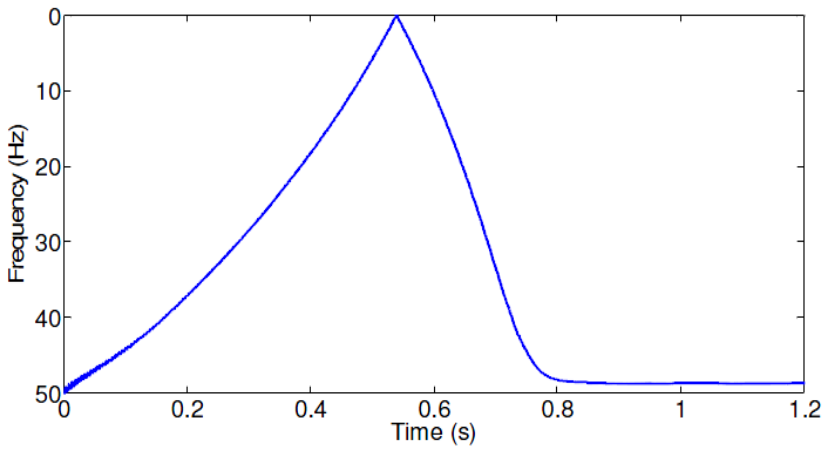

Figure 4-8: The evolution pattern of the LSH during a direct on line startup transient [74]

The energy evaluation detail coefficients of the known bandwidth using DWT during steady and startup has also been explored by authors [**61**], [**78**]. Detection of rotor and air-gap eccentricities under transient conditions using WPD has been investigated in [**57**]. Authors have also investigated DWT for detecting mechanical faults using vibration analysis during startup in [**79**], [**80**] .

4.6 Characteristics of PVA and EPVA

4.6.1 Park's Vector Approach

In three phase motors, a two dimensional representation can be used to describe the three phase induction motor phenomena. A suitable one is based on the current Park's Vector Approach (PVA). The main phase variables (i_a, i_b, i_c) are functions of the currents Park's Vector components (i_d, i_q) given by

$$i_d = \sqrt{\frac{2}{3}}\, i_a - \sqrt{\frac{1}{6}}\, i_b - \sqrt{\frac{1}{6}}\, i_c \tag{4-11}$$

$$i_q = \sqrt{\frac{1}{2}}\, i_b - \sqrt{\frac{1}{2}}\, i_c \tag{4-12}$$

Under ideal conditions, the three phase currents lead to a Park's vector with the following components

$$i_d = \sqrt{\frac{6}{2}}\, I_{max} \sin(\omega t) \tag{4-13}$$

$$i_d = \sqrt{\frac{6}{2}}\, I_{max} \sin(\omega t - \frac{\pi}{2}) \tag{4-14}$$

Where the maximum value of the supply phase current is I_{max}, the supply frequency is ω and t is the time constant. Its representation is a circular pattern centred at the origin [**6**]. If a machine contains a fault or asymmetry, a circular pattern will appear irregular. This technique

can be used to detect induction motor malfunctions, such as unbalance supply voltages and the common faults mentioned in 2.3.

4.6.2 Extended Park's Vector Approach

An advanced implementation of the Park's Vector known as the Extended Park's Vector Approach (EPVA) was developed in order to analyse the spectral components of the motor current. In ideal conditions the EPVA spectrum will not contain any spectral components at twice the supply. During an asymmetrical condition caused by a fault or unbalance voltage supply, a spectral component at twice that of the supply frequency will appear and the magnitude is related to the severity of the fault. [**11**], [**64**], [**81**]. This method is applicable to motors directly supplied from the grid and inverter-fed motors.

4.7 Concluding remarks

In this chapter, the methods for monitoring current and vibration signals were discussed. Current transformers (CTs) are usually used to sense the current signal in current montoring. Vibration monitoring is more mature and established technique for detecting faults. In vibration monitoring, the velocity is the preferred signal used to quantify the level of vibration since the amplitude is constant throughout all frequencies. The accelerometers are usually used to measure vibration. The acceleration can be integrated to obtain the velocity signal. The Internal Electronic Piezoelectric (IEPE) accelerometers are widely used to measure the accelerations. The mounting location and method are critical for measuring capturing results, a stud mounting method least affects the final frequency response; thus it is preferred.

The characteristics of the fault harmonic components under steady state analysis based on the classical spectral estimation technique were discussed. These characteristics are well defined in the *International Standards* for current and vibration. The operation of the induction motor affects the detection of the fault harmonics; therefore under varying load condition and transient operations, the classical technique cannot be employed. The characteristics of these fault harmonics have been investigated in the startup transient regime using DWT but mainly for the broken rotor bar faults. The characteristics of the PV and EPVA of the motor current have also been discussed. These characteristics only indicate an asymmetry in the machine but do not indicate the type of fault.

The next chapter discusses the developments of the experimental setup and methodology to experimentally simulate these common faults.

5. THE DEVELOPMENT OF AN INDUCTION MOTOR CONDITION MONITORING TEST RIG AND EXPERIMENTAL METHODOLOGY

5.1 Introduction

The four common faults associated with induction motors were implemented on the Machinery Fault Simulator - Magnum (MFS – MG). Various faults can be introduced individually or jointly in a controlled environment. The MFS - MG is a tool focused to train maintenance personnel in the area of predictive maintenance. However, there are limiting factors of the MFS-MG for the purpose of this research. This chapter describes the development of MFS – MG experimental setup to meet the needs of research. The data acquisition hardware and software, and power supply configurations are developed. The setup of the test motors and loads are also discussed. Experimental methodology and validation of baseline conditions are also presented in the chapter. The goal is to develop the MFS- MG such that a single fault can be introduced and to minimise the influence of the mechanical drive on the fault detection. Secondly, to develop an experimental methodology that can be accurately repeated to obtain measurements.

5.2 The MFS – MG test rig

5.2.1 The General Setup

The MFS – MG is designed to be both versatile and easy to operate. The simulator is constructed with a split bracket bearing housing a sliding shaft, rotors with a split collars ends, couplings, pulleys, a multiple belt tensioning and gearbox mounting mechanism, and reciprocating system as shown in Figure 5-1, all of which are designed to be easily removed and replaced between experiments. Different types of faults that can be implemented are:

- misalignment in all three planes, both angular and parallel;
- unbalancing in single plane, multiple planes, and overhung;
- different types of bearing faults;

- eccentricity, rotor rubs and bent shaft;
- mechanical looseness and soft foot;
- belt tension and gearbox problems; and
- reciprocating mechanism with and without defects.

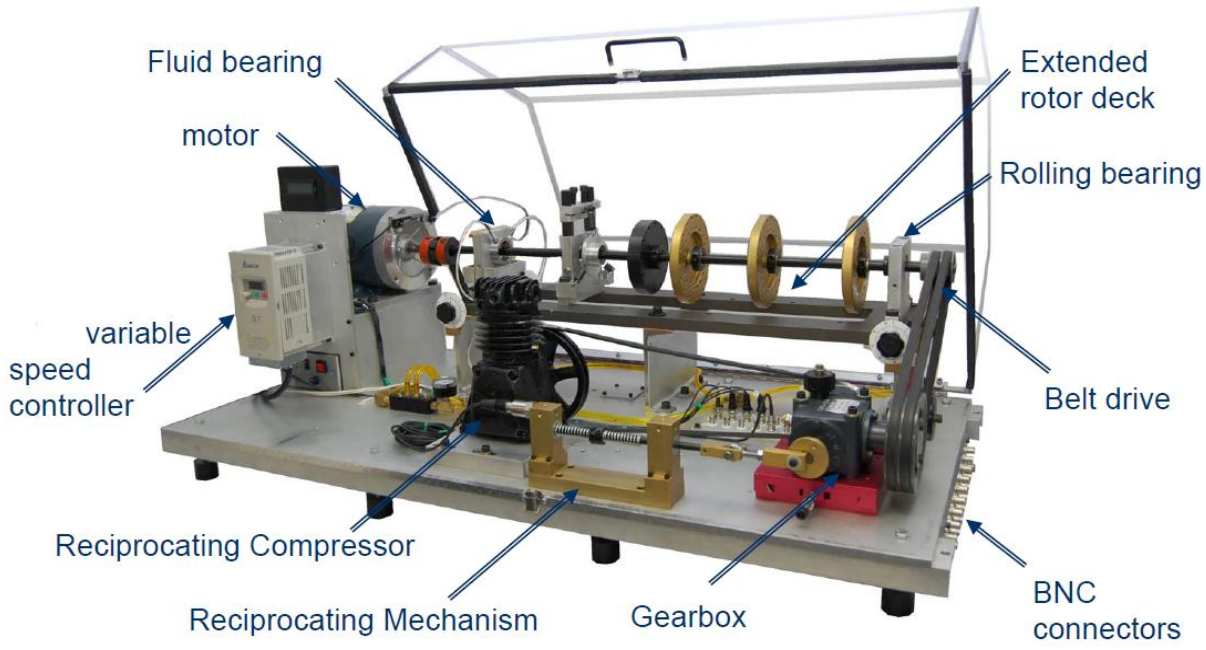

Figure 5-1: An image of the Machinery Fault Simulator - MG

The MFS – MG is driven by a three phase 250W induction motor via inverter-drive. Test induction motors with seven types of defects can be fitted in:

- rotor unbalance;
- rotor misalignment;
- bowed rotor;
- faulted bearings;
- broken rotor bars;
- stator winding faults; andvoltage unbalance & single phasing.

All seven motors have identical motor details listed in Table 5-1

Table 5-1: Induction motor details

Parameter	**250W motor**
Voltage (V)	190
Frequency (Hz)	50
Number of poles	2
Full load current (A)	1.85
No load current (A)	0.7
Full load speed (rpm)	2930
Full load torque (Nm)	1.03
Locked rotor torque (Nm)	4.06

The induction motor can be loaded using several load types, such as: a centrifugal pump with and without defects, an air compressor with and without defects, and a gearbox with and without a defect loaded using a magnetic clutch (brake) mounted at the rear of the gearbox with an adjustable load torque setting in the range of $0.06 - 1.13\ Nm$. Each motor and load type is attached with a magnetic base to mount a vibration sensor. A tachometer sensor is attached above the shaft of the motor to provide speed; this speed is displayed on a digital display and can be fed to a data acquisition system. To eliminate the variables in the machine drive setup introduced by multiple components such as pulleys and belt on the drive train system, direct drive installation of the loads is considered, as shown for a compressor in Figure 5-2.

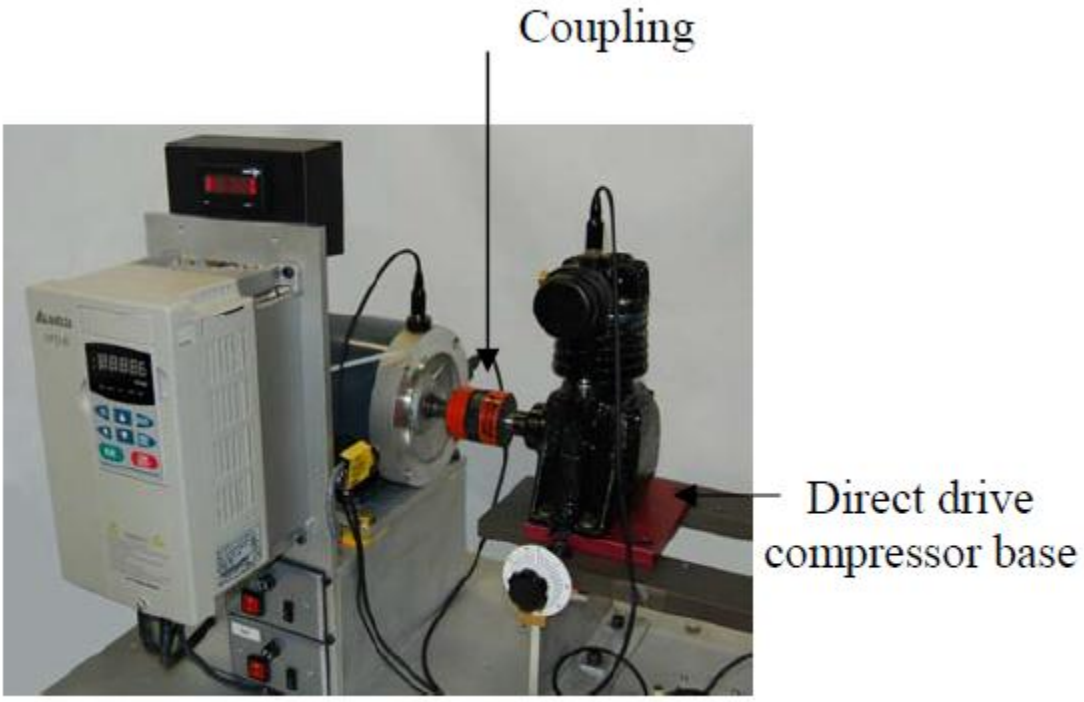

Figure 5-2: A directly coupled compressor

5.2.2 Limitations of the MFS – MG

The MFS - MG contains a 'breakout' box on the right hand side with 16 BNC connectors for connecting the vibration sensors to a data acquisition system. However, the setup does not allow for current measurement required for motor current signature analysis, as discussed in previous chapters. Secondly, the induction motor is inverter-fed; which introduces additional complexities, as discussed in section 2.2.3. To understand the motor current signatures attributed to different faults, an AC grid connected induction motor needs to be considered first. The load torque of the motor during operation is constant and to change the load torque requires the motor to stop in order to adjust the magnetic brake (in the case of gearbox and magnetic brake load), thus prohibiting simulation of continuous and transient load change operations of the motor.

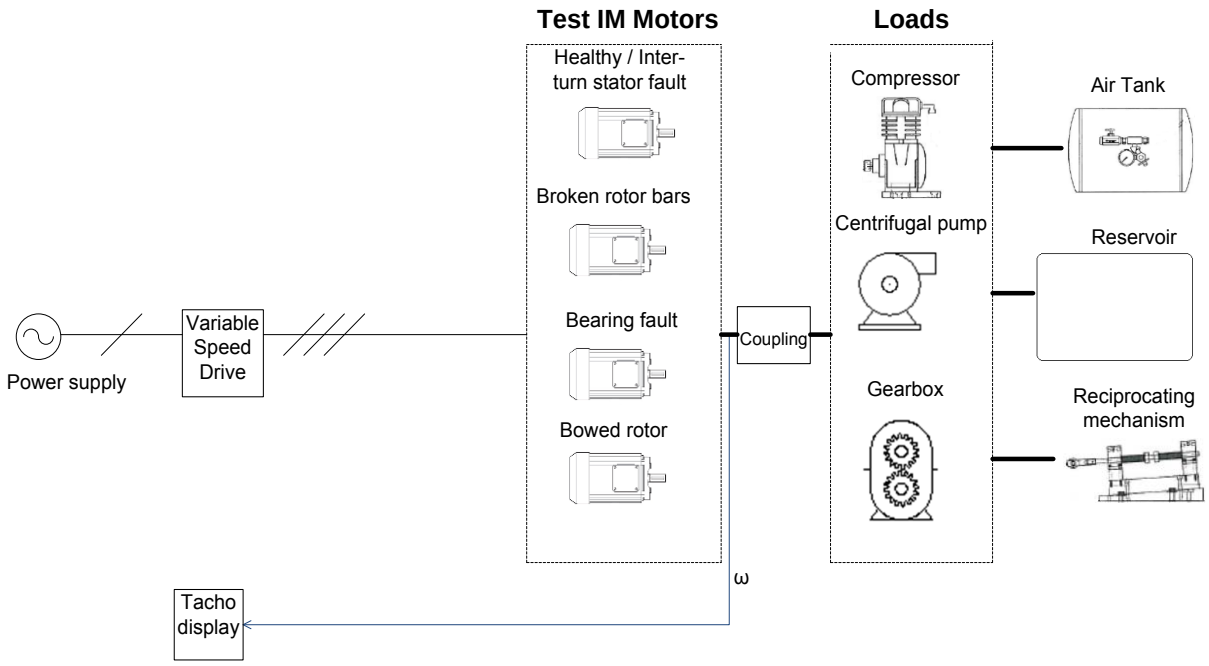

Figure 5-3: Schematic of the MFS-MG before modifications

5.2.3 Development of the MFS test rig for condition monitoring

The objectives for modifying the MFS – MG were to address the limitations mentioned in the section above. The motor power supply was modified such that the motor could be grid connected, via a variac supply or inverter-fed. The measuring instrumentation, namely signal conditioning hardware, data acquisition hardware and software required to capture the relevant signals such as: current, voltage, vibration, speed and the fundamental operating frequency was also developed, and a detailed discussion of these items follows later in this chapter. To simulate continuous load changes of the motor during operation, the induction motor was mechanically coupled to a permanent magnet servo motor. The operation and loading methods of the servo motor are discussed later in this chapter. The control circuitry was developed such that fault implementation can be conducted in an efficient and safe manner. The schematic diagram of the modified setup is shown in Figure 5-4. The instrumentation and control circuitry for the modified test rig was integrated into a motor control panel (See Appendix C for control circuit).

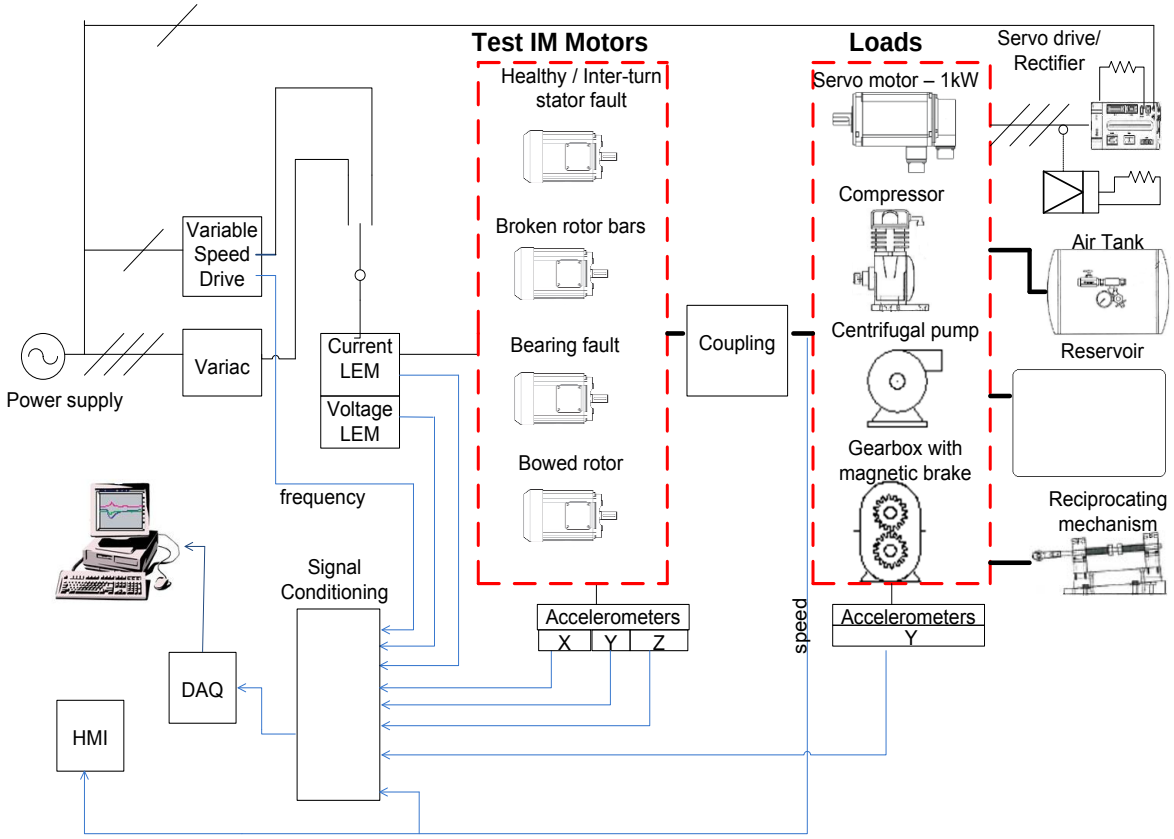

Figure 5-4: Schematic diagram after modifications

5.3 Development of the Measuring Instrumentation

The previous section gave an overview of the developments of the MFS-MG test rig. In this section the development of the measuring instrumentation will be discussed.

5.3.1 Current and Voltage Sensor

The current and voltage of the motor are measured using LEM modules. The *LA 25 NP* is used for current measurement and the *LV 25-P* is used for voltage. Each phase contains a current sensor. The line-to-line voltage is measured; therefore each line voltage has a sensor. These types of sensors provide the necessary isolation from the power circuit. The current and voltage sensors used have the following important features: good range of linear operation with linearity better than 0.2 %, the response time for the sensors is less than 1 μs and 40 μs for current and voltage sensor respectively, which is fast enough to acquire transients. The current sensor has a wide frequency bandwidth, $0 - 150\ kHz$, which is desired for inverter-fed motors to allow for the high switching frequencies. The current sensor primary current measuring range is 0 to $\pm\ 36A$. The startup current of the induction for direct on line (DOL) started motors can be in the order of 500 to 800% of the rated current as expressed in section 2.2.2, which is

within the measuring range of the sensor. The measuring range for the voltage sensor is 0 to $\pm 400V$, thus it is capable of measuring the supply voltage of the induction motor as indicated in Table 5-1. The current and voltage LEM sensors are fitted on a PC board as shown in Figure 5-5.

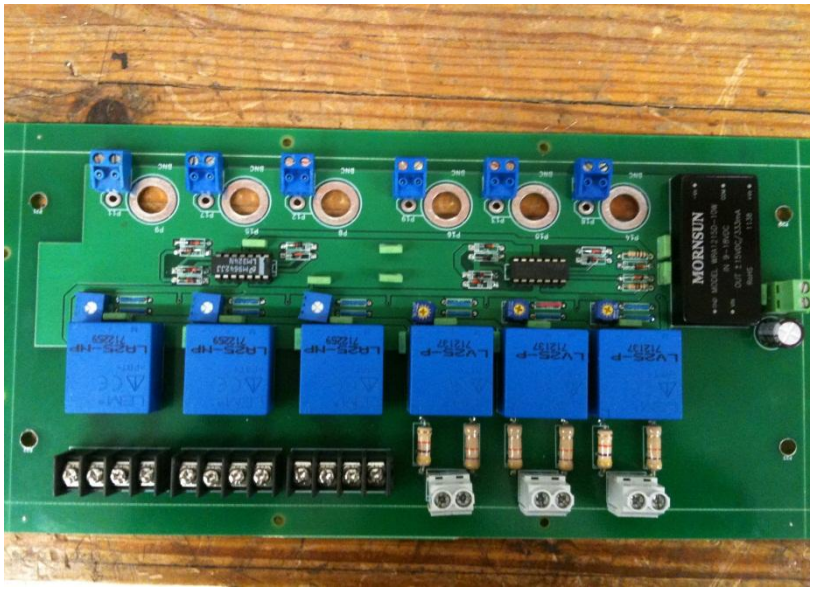

Figure 5-5: The PC board with a current and voltage LEM sensor

The current signals from the current LEM sensors are converted to voltage signals using a 200 $k\Omega$ shunt variable resistor, which allows for the output voltage to be calibrated. The voltage range was calibrated such that start-up currents measured by the sensor can be within the voltage ranges on the input of the DAQ system $\pm 10V$. The outputs of these transducers serve as the inputs to the low pass filters.

5.3.2 Vibration Sensor

Four general purposes, ceramic shear Internal Electronic Piezoelectric (IEPE) accelerometers were used to measure vibration for the reason discussed in section 4.3.2. Some of the performance features are indicated in Table 5-2. Three of these accelerometers were placed on the drive end of the induction motor to obtain vibration acceleration in three directions X (tangential), Y (radial) and Z (axial) as described in section 4.3.2, and a single accelerometer was placed in Y (radial) direction of the load .

Table 5-2: The IEPE accelerometer details

Performance parameter	Performance value
Sensitivity (±10 %)	10.0mV/g (1.02 mV/(m/s^2))
Measurement Range	±4900 m/s^2 pk
Frequency Range (±5 %)	0.5 to 10000 Hz
Frequency Range (±10 %)	0.3 to 15000 Hz
Resonant Frequency	≥50 kHz
Broadband Resolution (1)	0.005 m/s^2 rms

The stud mounting method is ideal for obtaining high frequencies as discussed in section 4.3.2. However, the test structure mounting surfaces are curved and rough, thus the surface was not adequately prepared for this type of mounting method. As a result, the stud mounting method via an adhesive mounting base, as shown in Figure 5-6 was employed. The adhesive base is manufactured of "hard coated" aluminium to provide electrical isolation to eliminate ground loops and to reduce electrical interference that may be propagating from the surface of the test motor [**82**]. The accelerometer is stud mounted on the flat side of the adhesive base, which is attached on the surface of the induction motor using adhesives.

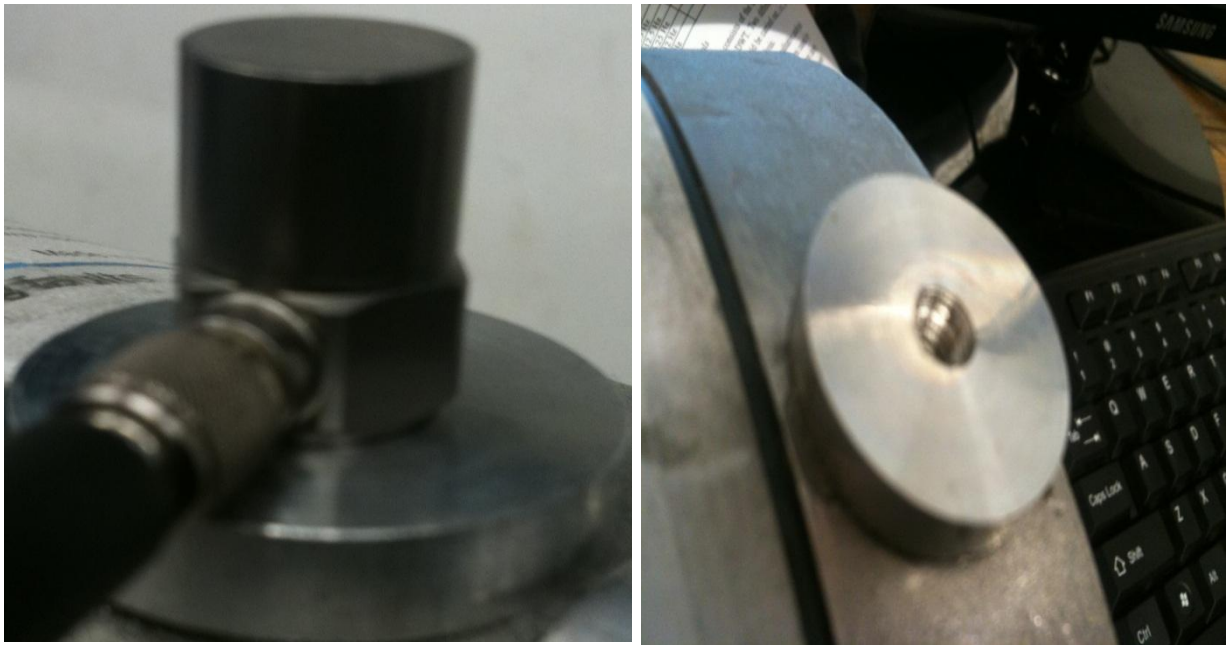

Figure 5-6: Mounting method for the accelerometers

5.3.3 Speed Sensors

The rotational speed of the motor can be measured using a digital tachometer or a pulse encoder. These sensors are presented below.

5.3.3.1 Digital tachometer

The tachometer sensor is positioned on the drive end of the induction motor which has an LCD display as shown in Figure 5-7, whereby a one pulse per revolution analogue signal is generated. The conditioning of this signal is discussed later in this chapter.

(a) (b)

Figure 5-7: a)The positioning of the tachometer sensor b) The LCD display of the tachometer

5.3.3.2 Pulse encoder

When the servo motor is used to load the induction motor, the speed is obtained from a 20 bit incremental encoder attached at the non-drive end of the servo motor as shown in Figure 5-8. The number of pulses per revolution obtained from the encoder ranges from $200 - 1280000$ $pulse/rev$, which can be configured in the servo drive in parameter editor $P1 - 72$ (See Appendix A). To achieve maximum resolution during transient conditions it was set to 1280000 $pulse/rev$. The pulses are fed into the drive via a $CN2$ connector (see Servo drive manual). The drive programme calculates the speed and displays it on the *Human interface (HMI);* alternatively, an analogue voltage signal is obtained ranging from $0 - 8V$ which is fed into the data acquisition system.

Figure 5-8: The location of the pulse encoder on the servo motor

5.3.4 Fundamental Operating Frequency

The fundamental frequency is obtained from the induction motor inverter drive. The inverter is configured to output an analogue voltage signal ranging from $0 - 10V\ DC$; this corresponds to the output frequency of the drive, and is achieved by setting the inverter drive parameter to $P - 150$ (refer to Appendix A). The conditioning of this signal is discussed later.

5.4 Signal Conditioning and Data Acquisition Hardware Devices

The instrumentation used to obtain the signals were discussed in the previous section. This section discusses the signal conditioning hardware, data acquisition hardware and software required for these signals.

5.4.1 Current and Vibration Signal Conditioning

5.4.1.1 Current and voltage signal

The current signals are converted to voltages as mentioned in section 5.3.1. To reduce the alias of the measured signals to an acceptable level as discussed in section 3.4, a first stage analogue low pass resistor capacitor (RC) filter is used to reject frequencies outside the range of interest. The primary goal of the filter is to prevent aliasing. The circuit diagram of the filter is shown in Figure 5-9. The cut-off frequency of the filter is determined by the resistor and capacitor combination. The 100 $k\Omega$ resistor potentiometer is implemented to provide an adjustable cut-off frequency. The two operational amplifiers (741) in the low pass filter circuit buffer and provide isolation to the signal. The sampling frequency (which is discussed later) used is $25.6kHz$, and as a result the cut-off frequency in this application is selected to be $12kHz$ which is approximately $0.46 \cdot F_S$.

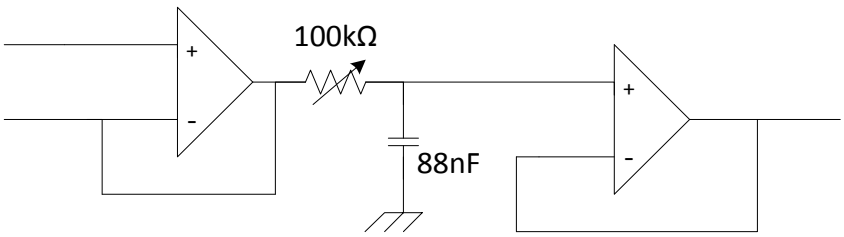

(a)

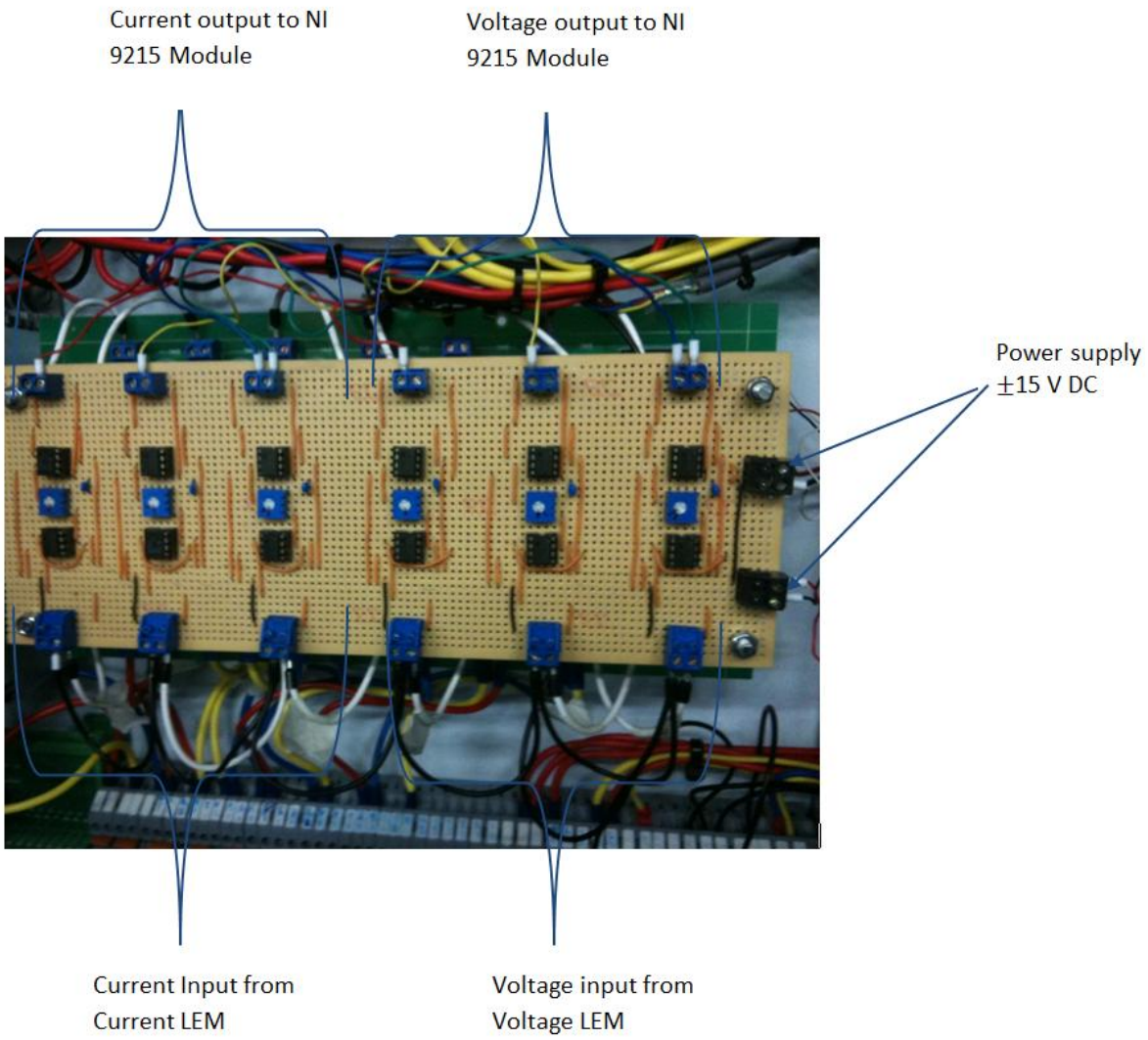

(b)

Figure 5-9: a) Antialiasing filter circuit b) The image of the antialiasing in the control panel

The output analogue voltage signals of the filter are fed to the input ports of the national instrument NI 9215 modules. These modules provide four differential analogue input channels with a $\pm 10\,V$ input range. Each channel contains $AI+$ and $AI-$ terminal for positive and negative voltage signals respectively. Each of the modules contains a common terminal COM that is internally connected to the isolated ground reference of the module. The single end voltage from the filter channel, the positive voltage signal is connected to $AI+$ terminal and the negative voltage signal to $AI-$terminal. To keep a common mode voltage, the ground signal is connected to the COM terminal as shown in Figure 5-10.

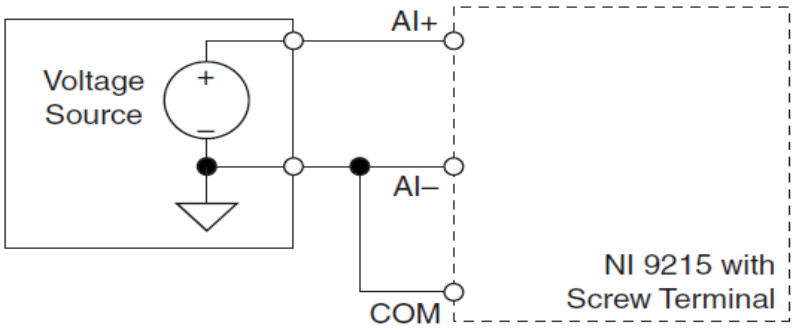

Figure 5-10: Connecting a single-end voltage signal of the input signal to the NI 9215 module [83]

The *NI* 9215 module protects each channel from overvoltage. The incoming voltage signals are buffered and conditioned by an instrumentation amplifier and then sampled by a 16 bit analogue to digital converter (ADC) as shown in Figure 5-11.

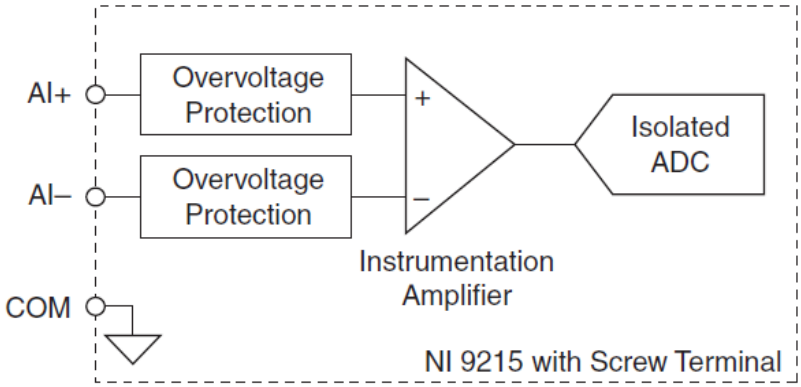

Figure 5-11: Input circuitry for one channel on the NI 9215 module [83]

5.4.1.2 Vibration signal

The voltage signals obtained from the accelerometer sensors are fed into the input ports of the national instrument *NI* 9234 module. This module differs from the *NI* 9215 module used for voltage measurement, since it provides DC excitation for accelerometers and contains anti-aliasing filters. It provides four BNC analogue input channels with $\pm 5\,V$ input range. Each channel contains a $AI+$ and $AI-$ terminal. The centre pin of the connector $AI+$provides DC excitation to the IEPE sensor on a per channels basis and enables the positive input signal, while the shell of the connector $AI-$ provides the return path of the DC excitation and the signals

ground reference. To avoid picking up the ground noises, a floating connection is used as shown in Figure 5-12. The $AI-$ shell is protected against accidental contact with overvoltages [**84**].

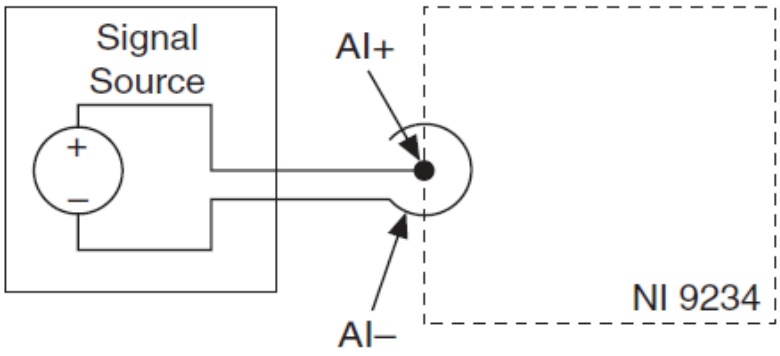

Figure 5-12: Connecting a Floating Signal Source in NI 9234 module [84]

A combination of digital and analogue filtering is used in the card to ensure accurate representation of in-band signals while rejecting out-of band signals. The pass-band of the digital filters is determined by the sampling rate. The frequency range of the pass-band is $0.45 \cdot F_s$. The stopband filters attenuates the signals above the stop-band and the frequency range is $0.55 \cdot F_s$. The alias free bandwidth is the ability to reject the frequencies above the stop band, which is equal to $0.45 \cdot F_s$ [**84**]. The ADC used in the module is 24 bits delta-sigma.

5.4.2 Signal Conditioning of the speed

For the digital tachometer, pulse per revolution (5 *V TTL*) measurement is acquired. The speed or rate can be determined in two ways from the TTL signal. In the first method, the *TTL* signal can be fed directly to *NI* 9215 module. Using *LabView* coding, the pulses contained in the *TTL* signal are counted for a given period of time, and then pulses are divided by the period to obtain the rate. In the second method, the frequency of the pulses in the *TTL* signal is converted to a voltage that is linear with input frequency (See Appendix C for circuit). The voltage output can then be fed into the channel of the *NI* 9215 module. The second method was used to determine speed.

For the pulse encoder, the analogue voltage signal is related to the speed obtained from the servo drive is fed directly into the *NI* 9215 module. For servo load applications, the speed obtained from the encoder is preferred since it is more accurate compared to the one obtained from the tachometer.

The voltage signal obtained from the encoder is fed into the *NI* 9215 module in a similar manner as the voltage signals for the motor voltages and currents, but is connected as a floating differential signal.

5.4.3 Fundamental Operating Frequency Signal

The output voltage related to the fundamental operating frequency obtained from the inverter is fed into the *NI* 9215 module in a similar manner as the speed signal.

5.4.4 DAQ Hardware and Interfacing Software

The modules; *NI* 9215and *NI* 9234 described previously were inserted onto a *8 slot NI compaqDAQ – 9178 USB chassis*. The chassis contains four general purpose 32-bit built-in counters, which allow up to 7 hardware-time analogue I/O, digital I/O or counter operations to run simultaneously. This permits simultaneous acquisition of currents, voltages, vibrations speed, and fundamental operating frequency. Figure 5-13 illustrates the flow of the measured signals in the conditioning and NI DAQ hardware.

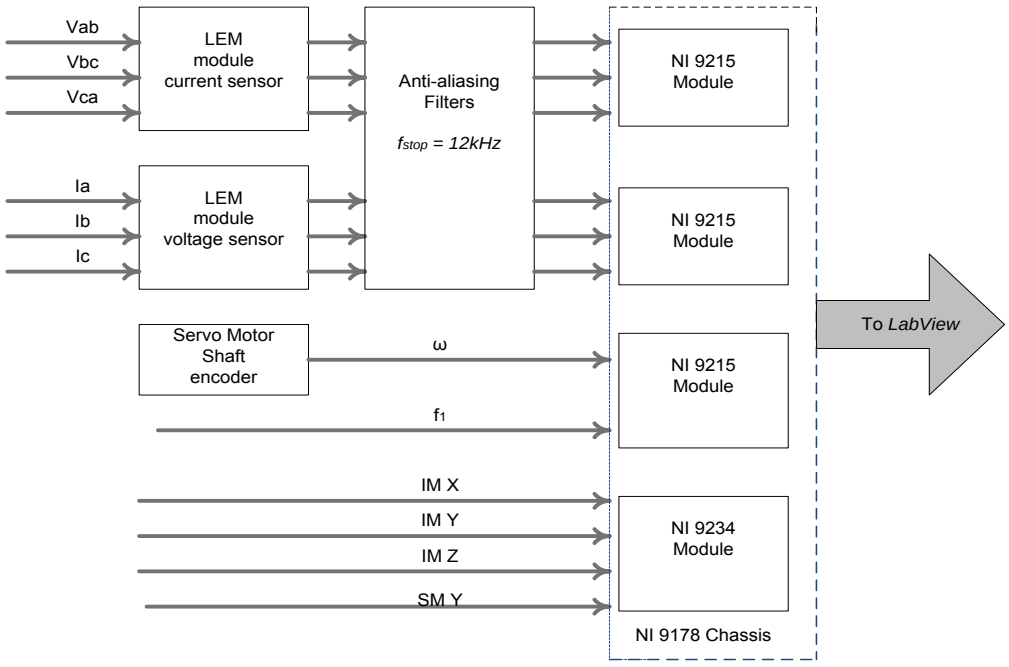

Figure 5-13: A flow chart showing the signal conditioning devices and the DAQ system

The NI DAQ system was used in conjunction with *NI-DAQmx driver software* to provide an interface for programming of the analogue inputs from the NI DAQ hardware device in the *LabView* environment. The *LabView (*short for Laboratory virtual instrument engineering

workbench) *2012 32bit* software was installed on the computer. This is a platform and development environment for a visual programming language from National Instruments. A LabView virtual instrument (VI) was created using a DAQ assistant to read and display the signals (see Appendix A). The DAQ assistant settings are configured according to the: input terminal connection, physical channel, type of measurement, scaling information of the DAQ hardware system. The configuration screen is displayed in Figure 5-14.

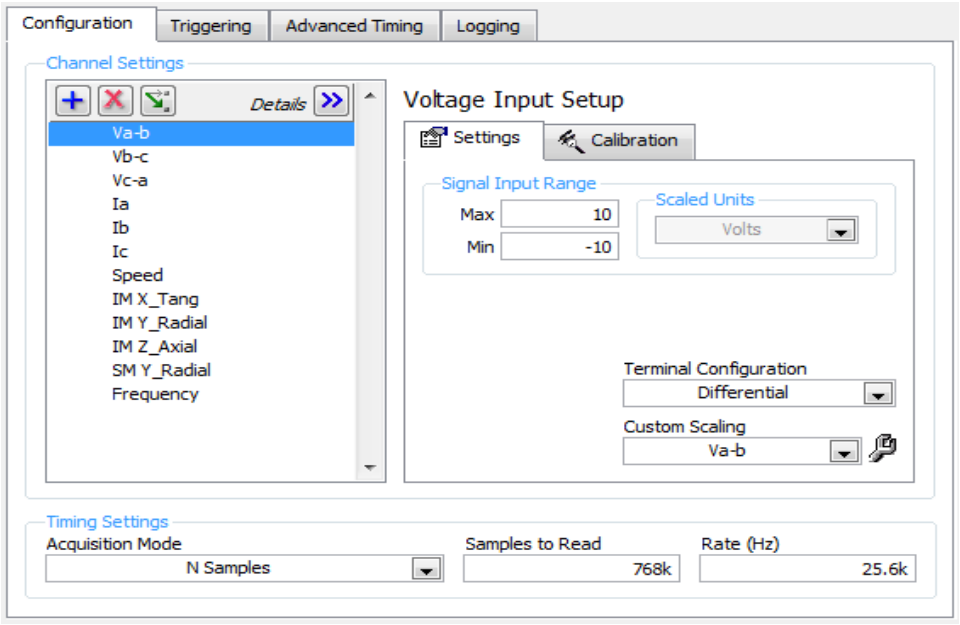

Figure 5-14: The *LabView* configuration screen for the DAQ Assistant

The voltage, current, speed and fundamental operating frequency related voltage signals are read as analogue voltage and then each scaled accordingly, while the vibration signals are acquired as acceleration in metre/second^2. The scaling factors were calculated and confirmed with the digital power analyser, tachometer and inverter frequency display accordingly.

5.4.4.1 Sampling rate and number selection on the DAQ software

Since the induction motor can be inverter-fed, the sampling procedure is more demanding due to the switching operation and multiple harmonics reflected in the current signals discussed in section 4.2. Although anti-aliasing filters have been implemented in the circuitry to reduce alias to an acceptable level, as discussed in section 3.4, oversampling is still required. The maximum sampling rate that each of the channels of the NI 9215 and NI 9234 modules are capable of 100 kHz and 51.2kHz respectively. Since all the signals are captured simultaneously, the ideal mutual sampling rate of the signals would be 51.2kHz . However, the two modules are not using

the same clock (due to the way in which the module circuitry is setup), so to obtain a specific sample rate (frequency) the main clock needs to be divided (usually by factors of 2). Since the two module types are setup to run in the same DAQ assistant task, a mutually acceptable clock rate to keep the samples synchronised is 25.6 kHz. Notice this sampling frequency is double the set cut-off frequency of the antialiasing filter described earlier. Ideally, a long sampling time is desired to obtain good frequency resolution; however, the MFS-MG is not designed to operate for more than 30s at a time when operating within 20% of the critical speeds and during severe fault conditions. Due to these operational constraints the sampling time is selected to 30s by reading 768k $Samples$. The acquired signals are written to an excel file and displayed on the front panel display charts in the *LabView* environment, as shown in the flow chart in Figure 5-15

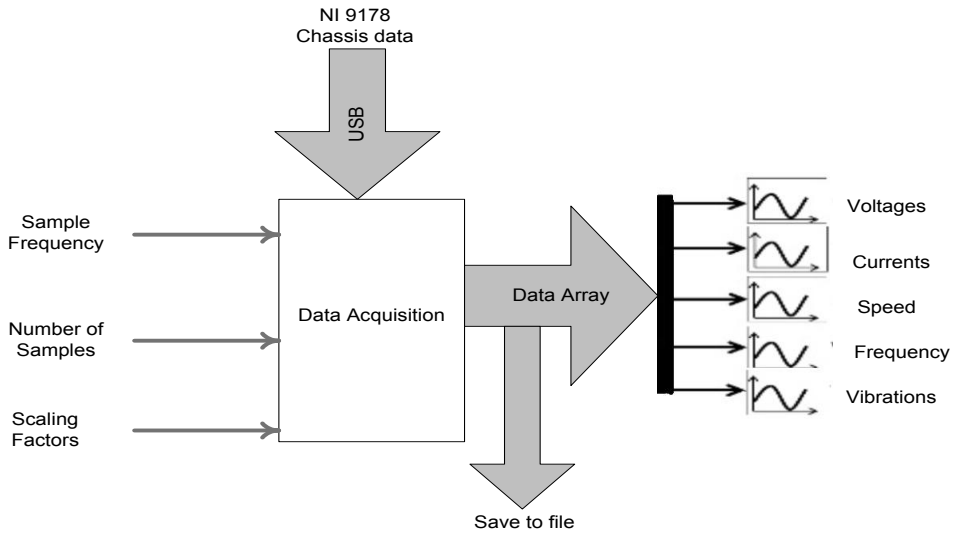

Figure 5-15: The flow shows the *LabView* environment, variables accessible to the user and the front panel display charts

5.5 Induction Motor Power Supply

The induction motor can be grid connected through a three phase variac supply or inverter-fed. The supply mode is selected through a selector switch that energises cross wired contactors (See Appendix C for details).

5.5.1 Grid Supply

The laboratory main power supply delivers a line voltage of $380\,V$ while the motor requires $190\,V$. So the purpose of variac is to supply the appropriate voltage, and to soft start the motor for steady state operation.

5.5.2 Inverter Supply

The variable speed drive (an inverter source) that powers the motor is the *AC Lenzo SMV frequency inverter* The control mode is configured to constant V/Hz control. The integration can be set to provide a linear ramp or an S-ramp during startup. The linear ramp maintains a constant (stepped) acceleration integrated over time while the S-ramp uses a linear ramp on the acceleration (i.e. the acceleration begins slowly and increases to the maximum acceleration rate). The voltage is varied with frequency to maintain a constant flux level as discussed in section 2.2.3. In the *PWM*, the triangular switching frequency (carrier frequency) used to modulate the voltage has a selectable range of carrier frequencies: $4, 6, 8\ and\ 10\ kHz$. The higher the switching frequency selection, the lower the motor noise; however, this increases the demands on sampling. Recall that the mutual sampling frequency that can be achieved is $25.6\ kHz$ as was discussed in section 5.4.4 and the sampling frequency must be at least twice the maximum frequency contained as mentioned in section 3.4. The switching frequency was selected to be $6kHz$, thus the switching frequency can be sampled more than four times using the sampling frequency. This is a good compromise between the injected noise and over sampling using the mutual sampling frequency. The other relevant settings of the drive are attached in Appendix A

5.6 The Setup of the Test Induction Motors

The faulted test motors used in this thesis contain the following defects: a stator winding fault, broken rotor, faulted bearings and bowed rotor. The setup of the test motors is discussed below.

5.6.1 Healthy motor and motor for simulating an Inter-turn stator fault

For simulating the inter-turn stator fault, the induction motor provides access to three points within the phase winding as shown in Figure 5-16. The stator winding of phase A have been tapped across the top and bottom terminal to enable 2 turns to be shorted, the voltage drop across these terminals is $12 - 13V$. The tapping across the top and middle terminal enables 4 turns to be shorted, and the voltage drop across these terminals is $25 - 27V$. The total resistance of phase A is approximately 10.3Ω. The resistance values across terminals corresponding to 2 and 4 turns are 3.4Ω and 4.1Ω respectively. These taps (turns) can be shorted through an external variable resistor. The fault condition can be controlled by a switch

placed within the fault circuit such that the fault can be switched in and out, refer to Appendix C for control circuit. When the resistor is switched out (disconnected), the motor operates like a healthy (normal) motor as the circuit is open.

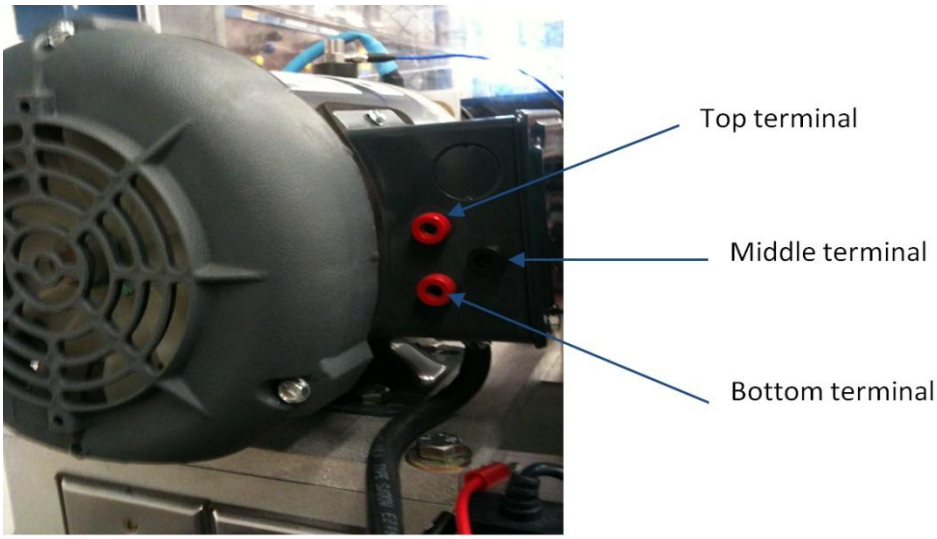

Figure 5-16: The motor for simulating an inter-turn fault

The impedance of the stator winding is changed by varying the $500W$, 100Ω variable resistor placed in parallel with the winding as shown in Figure 5-17, thus simulating the winding fault.

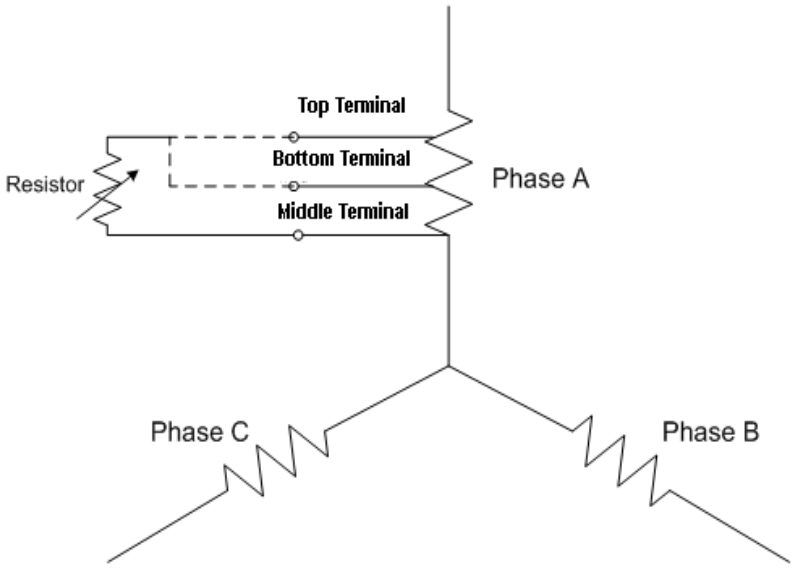

Figure 5-17: A circuit diagram for simulating an inter-turn fault

High resistance simulates an insulated winding while low resistance simulates a shorted winding. A low setting of the resistor allows for a large fault current hence increases fault severity. The limiting factor for the resistor setting is current capacity of the winding and

variable resistor. The maximum current capacity of the motor winding at locked rotor conditions is $8A$ and $20A$ for the resistor. Thus the resistance is critical in ensuring no permanent damage is caused to the motor winding or the resistor. The resistance R_f is set to 7Ω and then connected across the terminals corresponding 2 and 4 turns. The fault current I_{fault} is the current flowing through the resistor. The fault currents and voltages obtained across this resistor is shown in Table 5-3.

Table 5-3: Results of the fault current and voltage as a function of the resistance value

No. of shorted turns	$R_f(\Omega)$	$I_{fault}(A)$	$V_{fault}(V)$
2	7	2	12.92
4	7	4	26.34

5.6.2 Broken Rotor Bar Fault

The motor with the broken rotor bar fault has three cracked rotor bars. There are 34 rotor bars in the motor rotor.

5.6.3 Bearing Fault

The motor contains 6203 ball bearings fitted on the drive and non-drive end of the motor. The motor has been fitted with intentionally faulted bearings: one bearing with inner race fault and one bearing outer race fault.

5.6.4 Stator-Rotor Air Gap Eccentricity Fault

Dynamic eccentricities can be simulated using a motor with a bowed rotor. The bowed rotor motor consists of an intentionally bent rotor, the range to which the shaft is bent relative to the center is from 0.127 to 0.254mm, while ensuring that the rotor does not bind with the stator.

5.7 Setup of Induction Motor Loads

The loads can be directly connected in turn to the test induction motor. There are four different load types that can be directly connected: servo, gearbox with magnetic brake, centrifugal pump and air compressor. The setup of these loads is discussed below.

5.7.1 Servo Load

To load the induction motors continuously, a three phase, $1\ kW$, $220\ V\ AC$, $3000 rpm$ servo machine is coupled to the induction motor. The servo machine can be controlled in two ways: in

closed loop and open loop configuration. In both configurations, the servo machine operates as a generator.

5.7.1.1 Closed loop control

The servo motor is controlled through 1 kW AC servo drive. The servo motor can be operated in torque or speed mode. When generating, the servo machine is operated in torque mode. The induction motor drives the servo machine and torque is applied in reverse direction of the induction motor; this creates a regenerative braking effect and the regenerative power returns from the servo motor to the servo drive. This power is transmitted into the capacitor of the DC bus and causes in a voltage to rise. When the voltage rise is too high, the servo drive dissipates the extra energy in an external regenerative resistor with a capacity of 1 kW. The servo drive is interfaced through a human interface to display and control the torque and speed. It is configured not to exceed a power loading of 0.25 kW. The relevant configurations are displayed in Appendix A.

5.7.1.2 Open loop control

In open loop control the three phase terminals of the servo motor are rectified into a DC voltage. To vary the torque of the induction motor; a $500W$, 100Ω variable resistor is connected on to the DC side. Thus changing the DC current, changes the torque applied to the induction motor.

5.7.2 Gearbox with Brake

A gearbox with a magnetic brake (clutch) can be fitted to the system. The load torque is variable from 0 and $1.12Nm$. Further details and the operation procedure is available in MFS manual.

5.7.3 Centrifugal Pump

A centrifugal pump can be fitted to perform pump studies and simulate typical undesirable pump conditions, such as cavitation, improper clearances, and worn/damaged impeller. Due to convenience and safety, water is the media that is frequently used in the process. Further details and the operation procedure is available in MFS manual.

5.7.4 Air Compressor

An air compressor can be fitted to assess faults attributed by the compressor housing, valves and other components. Further details and the operation procedure is available in MFS manual.

5.8 Experimental Methodology

To ensure repeatability and correct operation of the induction motor and loads, the following procedure was adhered to. The experimentation involves working with fast rotating machinery,

thus extreme caution should be exercised when using the machinery fault simulator test rig. All the Machine laboratory rules should be strictly adhered to as well as the safety procedure specific to this experimentation. All four motors were tested, namely: the motor with inter-turn (it is also used as the healthy motor when the turns are not shorted), the motor with three broken rotor bars, the motor with bearing fault and the motor with bowed rotor described earlier. The servo machine is used to load the induction motors and is operated in the open loop control mode due to its simplicity.

5.8.1 Alignment of Motors

All the motors have alignment sockets which connect with pins on the alignment plate; this eliminates the need to perform shaft alignment each time the test motor is changed as shown in Figure 5-18. The alignment can be verified using the reverse dial indicator method. The procedure for verification of alignment using the reverse dial indicator is procedure is available in MFS manual.

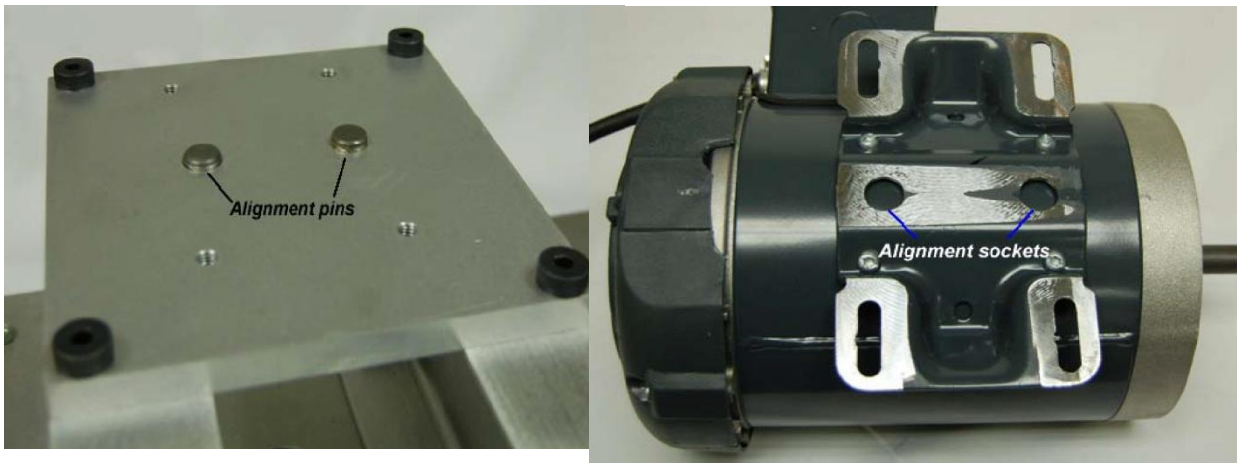

Figure 5-18: Inductor motor alignment pins and sockets

The servo motor is flange mounted on an adapter base attached to the test rig platform as illustrated in Figure 5-19

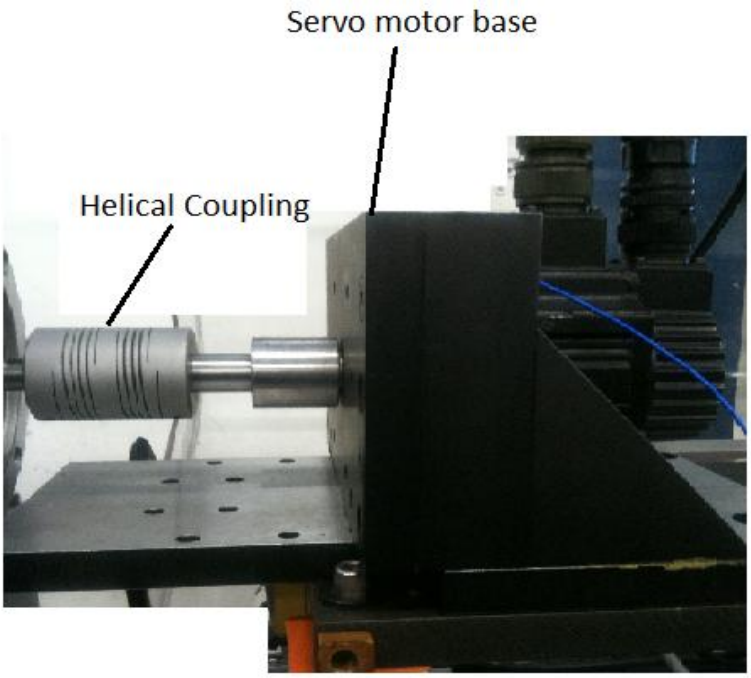

Figure 5-19: Servo motor and base mounting

The servo motor and base are fitted such that they are aligned with respect to the induction motor, which again eliminates the need to perform shaft alignment each time the test induction motor is changed. However, the shaft alignment can be validated using the procedure mentioned above. The induction motor and servo motor are coupled using helical coupling as shown in Figure 5-19.

5.8.2 Testing Methodology

The sampling time is set to 25.6 kHz and to obtain a 30s recording of each of the signals desired; 768$kSamples$ are collected by the data acquisition system as discussed previously in section 5.4.4

5.8.2.1 Disconnected motor

To obtain the voltages signals from the grid and inverter in the absence of the motor, the following methodology is carried out.

1. Ensure that the main isolator of the test rig is de-energised, then disconnect the motor plug from the supply socket.
2. To obtain the **grid voltage supply**, energise the main isolator then select the grid mode using the selector switch, press the start buttons on the control panel and on the variac supply. Adjust the variac knob until the voltage on the voltmeter reads 190V.

To obtain the **inverter voltage supply**, select the stop button on the control panel then select the inverter mode using the selector switch and then press start on the control panel. Ramp the inverter drive to $50Hz$.

3. Then run the *LabView VI* to record the voltage signals for $30s$ and then save.

5.8.2.2 Connected motor

Perform steps 2, depending on the motor voltage supply selected (grid or inverter-fed). For consistency, the motor to be tested is run for approximately $30mins$ to warm-up. Once the motor is warmed-up, the load level can be adjusted by varying resistance value of the resistor described in 5.7.1. The current flowing into the resistor is used to confirm the loading level. The load levels and current values are shown in Table 5-4.

Table 5-4: Loading levels and current flow into resistor

Loading (%)	**Torque (Nm)**	**Current (A)**
100	1.03	2.56
50	0.5	1.21
0	0.1	0

For each of the test motors the following procedure is repeated for each loading level. The procedure is applied to the steady state and transient operation of the grid connected and inverter-fed motor.

1. For **Steady state operation** of the **grid connected or inverter-fed** motor, run the *LabView VI* to record the signals for approximately $30s$ and then save.
2. For **Start-up transient operation** of the **grid connected** motor, adjust the variac knob to the setting of $190V$,
3. Start the *LabView VI* recording, after a period of $10s$; press the start buttons on the control panel and on the variac, then save when the recording is done.
4. For **Start-up transient operation** of the **inverter-fed** motor, start the *LabView VI* recording,
5. After a period of $10s$ and the motor is started from the control panel, by pressing the start button followed by the run button on the inverter drive.

5.9 Baseline Conditions

The motor current and vibration signals of the healthy motor, obtained from the transducers are discussed. Furthermore, the torque characteristics of the different motors operating at different load levels.

5.9.1 Supply Voltage

The induction motor as discussed in section 5.5 can be powered directly from grid or inverter-fed. To gain insight into the nature of these two different voltage supplies, the motor is first isolated with respect to the power supply and the voltage signals are obtained using the methodology described in section 5.8.2. In Figure 5-20, the grid and inverter voltage supply time plots are shown. Notice in the grid supply time plot, the voltage signals are sinusoidal, whereas in the inverter voltage supply time plot the voltage signals are non-sinusoidal and contain noise due to switching and harmonic expressed in section 2.2.3

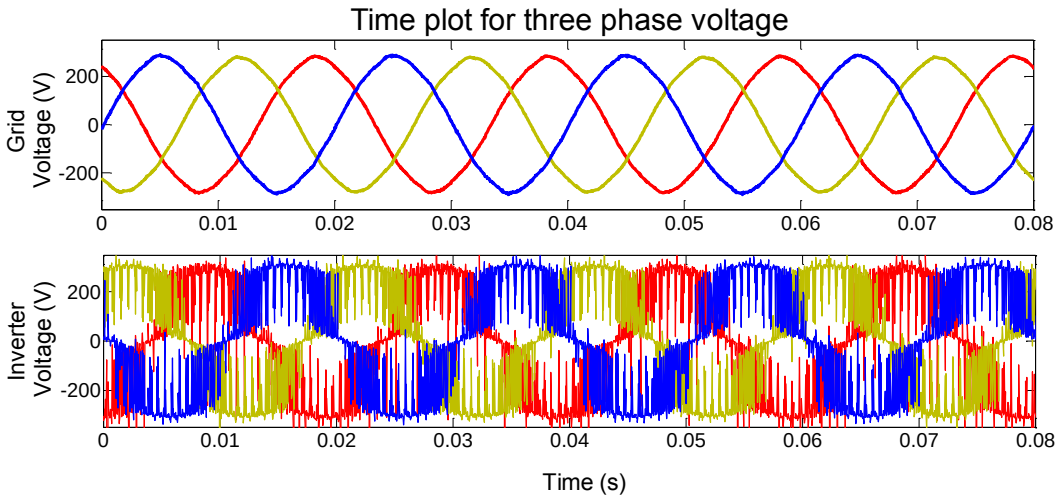

Figure 5-20: Grid and inverter voltage supply time plot before connecting the induction motor

5.9.2 Motor Current

The results of the measured current for the fully loaded healthy grid connected and inverter-fed motor during steady and transient start-up conditions are presented and discussed in the sections below

5.9.2.1 Steady state

The current signal time plots for the grid and inverter-fed motor during steady state conditions are shown in Figure 5-21. During this test, the speed and load remain constant. For the grid

connected motor, the current signals are steady and balanced. In the inverter-fed case, the current is also steady and balanced but also contain noise due to the switching of the drive. The baseline measurements are available in Appendix B. The frequency analysis of the currents will be discussed further in chapter 8.

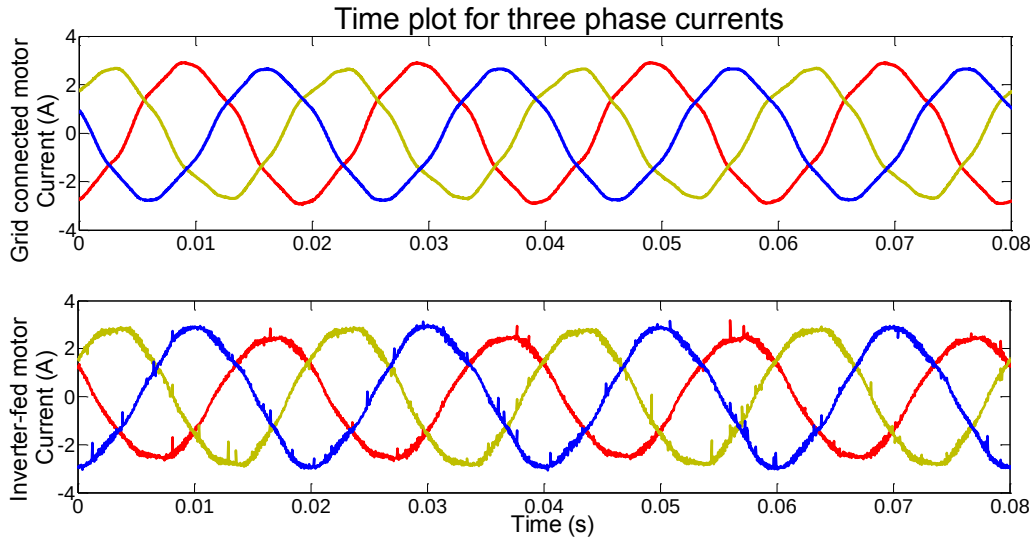

Figure 5-21: Time plots for the grid and inverter-fed motor three phase currents during steady state conditions

5.9.2.2 Transient state

The current plot for the grid and inverter-fed motor during transient start-up conditions are shown in Figure 5-22. Starting the motor by connecting the motor directly to grid supply; this will be referred to as direct on line (DOL) starting, results in high currents initially as expressed in section 2.2.2. The period of this transient is approximately $0.17s$. In the inverter-fed motor, the start-up current is low; it's between 0.5 to 1 times the rated motor current. The transient duration is governed by the S-ramp integration and acceleration time set on the inverter discussed in section 5.5.2, in this case a linear acceleration ramp and with an acceleration time of $8s$ is used.

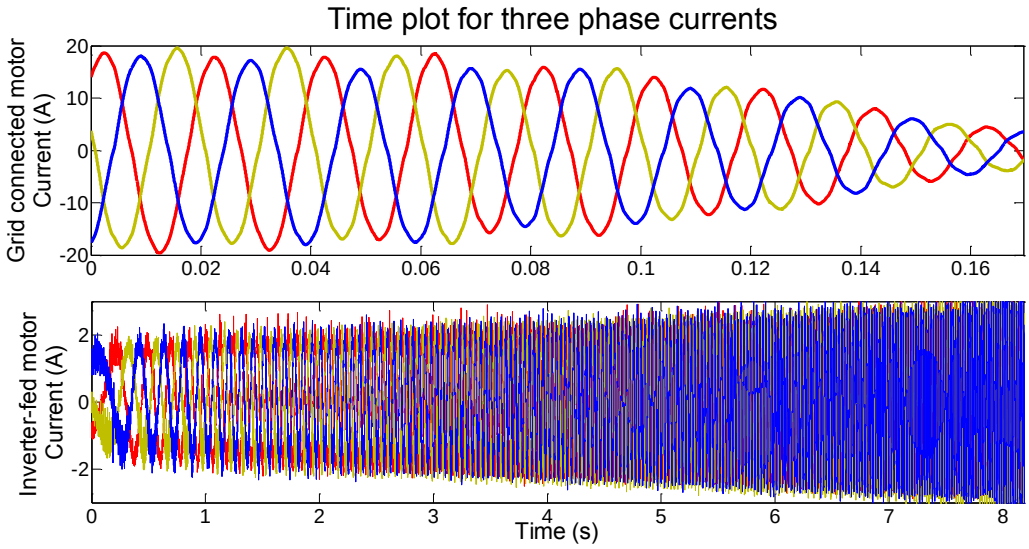

Figure 5-22: Time plots for the grid and inverter-fed motor three phase currents during transient startup conditions

5.9.2.3 Vibration

The baseline vibrations signals obtained from the accelerometers in the three different directions of the induction motor are displayed in Figure 5-23. The average vibration of the Tangential, Radial and Axial directions is 0.7×10^{-4}, 8.6×10^{-3} and 3.2×10^{-3} m/s^2 respectively. As expressed in section 4.3.2, vibration acceleration is often converted to vibration velocity for fault detection and diagnosis.

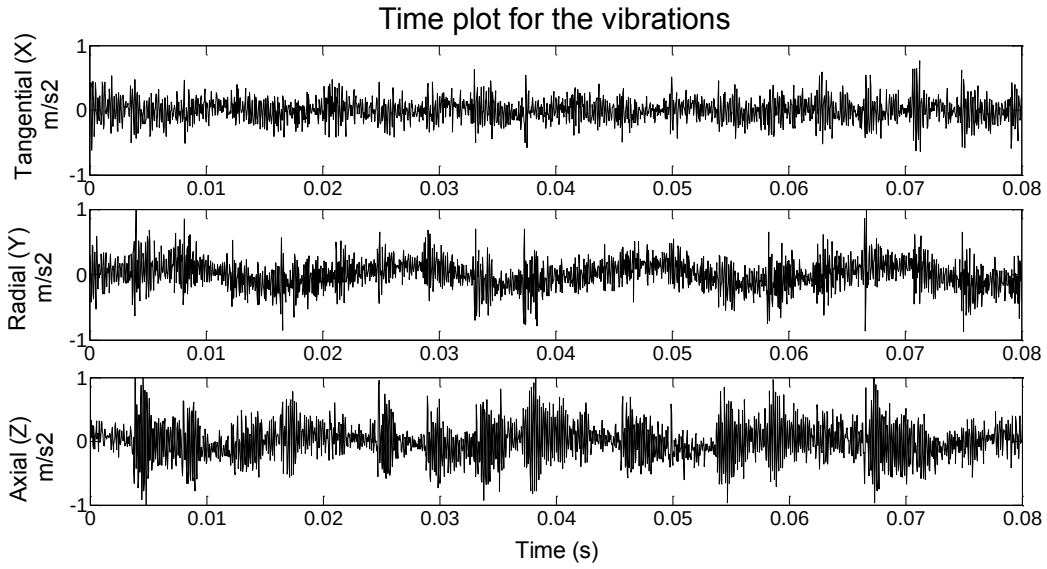

Figure 5-23: Time plots for the vibration acceleration in three directions

The overall vibration velocities of the motor under these conditions are displayed in Table 5-5. These are compared with the vibration criteria set in the *IS0 10816* (See Appendix A). According to this criterion, the MFS-MG induction motor is categorised as *Class I*, where these vibration velocities levels indicated are within the *Zone A* boundary. Hence these vibration levels are acceptable.

Table 5-5: The overall vibration for a healthy motor under full load

Types of Measuring Vibrations instrument	**Directions**	**Overall vibration RMS mm/s**
MFS vibration system	Tangential	3.808e-006
	Radial	5.1e-006
	Axial	4.782e-006

5.9.3 Torque versus Speed Characteristics

The torque versus speed characteristics for the different test motors for open loop control of the servo load are displayed in Figure 5-24, where speed is expressed as frequency. The standard deviations of the frequency (speed) under 100% and 50% load conditions are $0.05Hz$ $(3.25rpm)$ and $0.05Hz$ $(3.21rpm)$ respectively. The standard deviations of the torque at 100% and 50% load conditions for are 0.0078 and 0.0028 Nm respectively. Hence these test motors operate at approximately the same torque load point but at slightly different speeds.

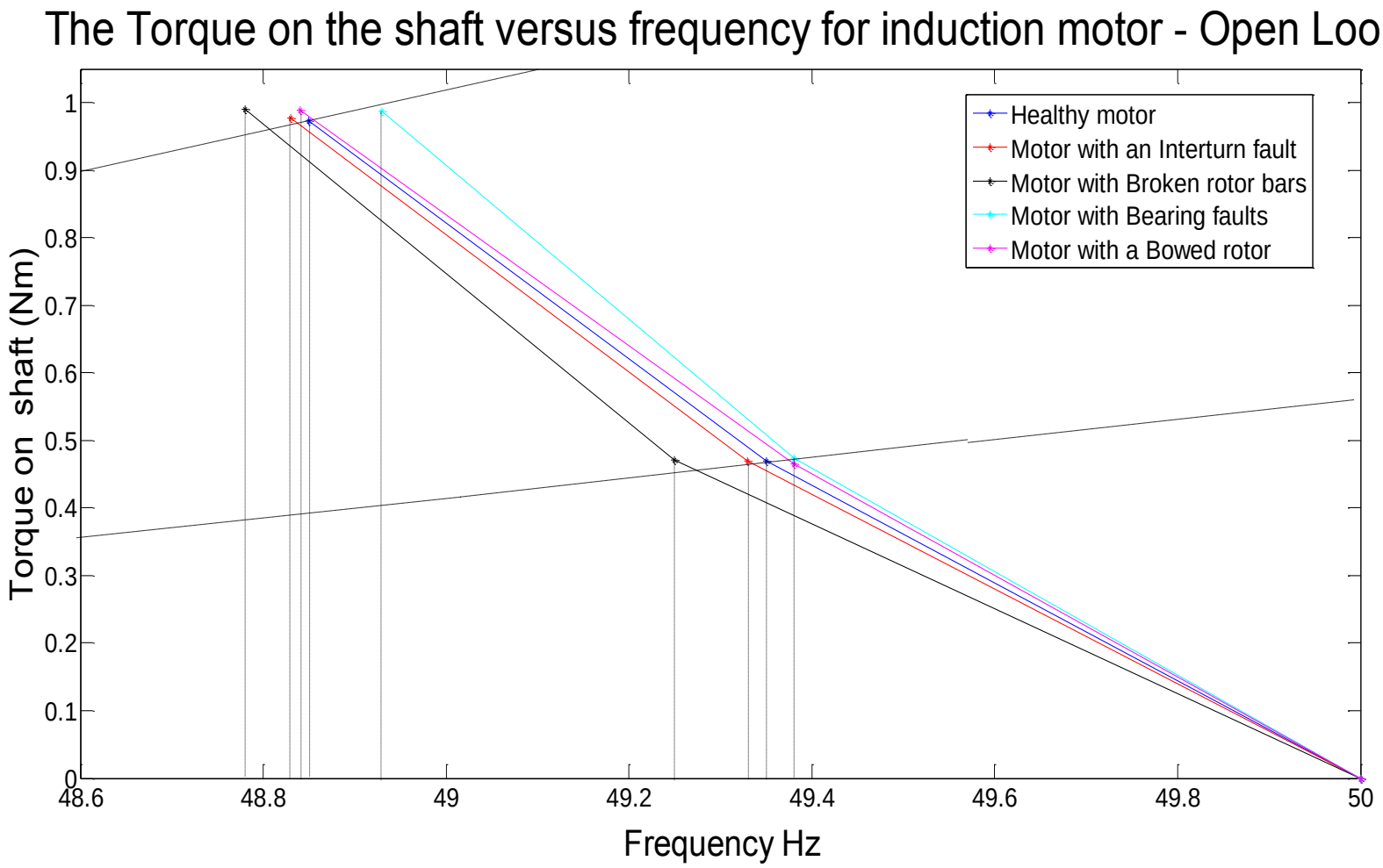

Figure 5-24: The torque versus frequency profile for the induction motors – closed loop

5.10 Concluding Remarks

This chapter discussed the developments of MFS – MG test rig used to test the motors with the common faults associated with induction motors. The signal measuring instrumentation, signal conditioning, data acquisition hardware and software, and power supply configurations were developed such that signals like: current, voltage, vibration, speed and fundamental operating frequency(for inverter-fed) could be accurately measured and captured for the fault detection of grid connected and inverter-fed motors. The setup of the test motors and loads were also discussed. In this research, the servo machine controlled in open loop mode is used to load the test motors. The experimental methodology to ensure repeatability and safe operation of the motor was also discussed. Lastly, the baseline voltage, current and vibration time signals were benchmarked for the healthy motor.

The next chapter presents and discusses the steady state fault detection strategy and results of detecting the faults under steady state conditions

6. RESULTS AND DISCUSSIONS OF DETECTING FAULTS UNDER STEADY CONDITIONS: USING FREQUENCY DOMAIN SIGNAL PROCESSING TECHNIQUES

6.1 Introduction

The common faults experienced in induction motors; inter-turn stator, broken rotor bar, bearing and dynamics eccentricity fault were implemented under steady conditions on the developed Machinery Fault Simulator test rig. Each of the fault conditions were operated under different load conditions and power supply configurations (grid connected and inverter-fed). The instrumentation and methodology of capturing the signals was discussed in chapter 5. This chapter presents the fault detection strategy used for each of the fault scenarios and discusses the experimented results. The results pertaining to each fault condition is compared to the healthy motor, which serves as the baseline condition.

The aim is to determine whether the fault characteristic frequency components discussed in chapter 4 are detected in both the current and vibration velocity frequency spectrum. The current and vibration velocity spectra normalised magnitudes are expressed in decibels and the frequency in hertz. Secondly, it is to establish which of the fault components is most prominent within the current or vibration spectra. The impact of loading, varying fault level (in inter-turn fault simulation), impact of the inverter and varying the fundamental operating frequency are explored to establish how these variables influence the detection of the fault components under a steady state conditions. Lastly, it is to determine whether the frequency domain techniques can confidently detect the faults. Figure 6-1 shows the flowchart of the various tests conducted on the MFS test rig, which will be analysed in the proceeding sections.

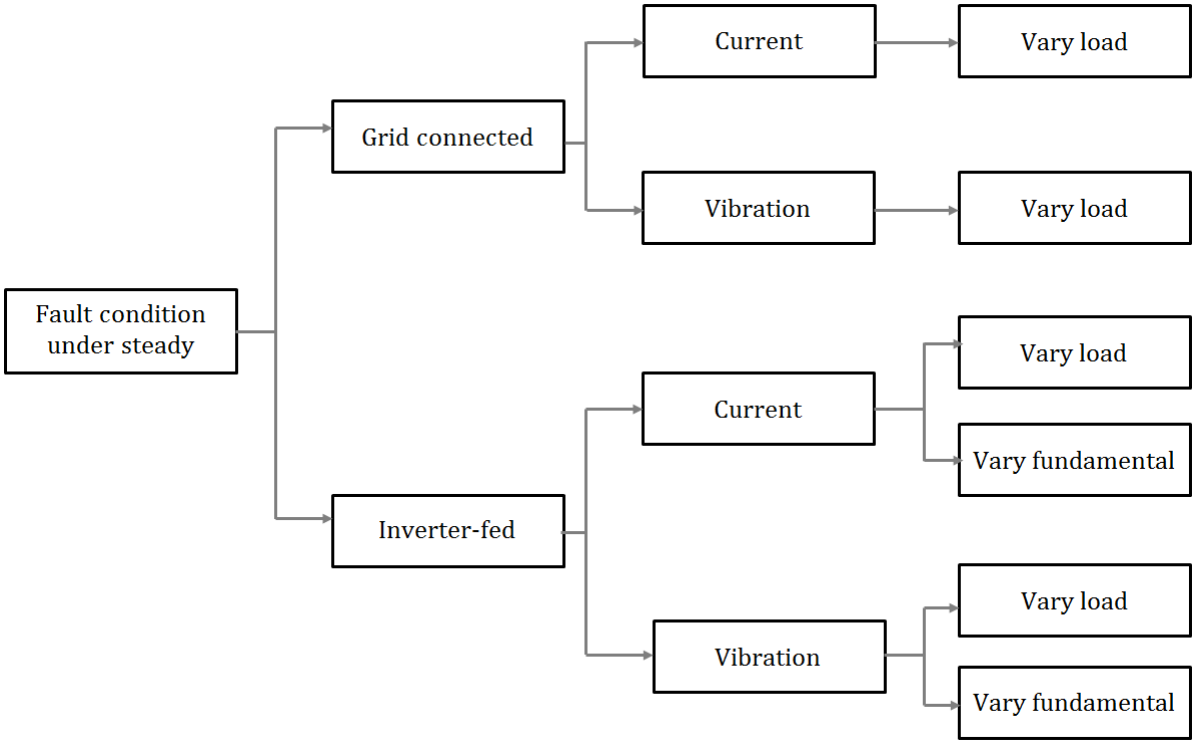

Figure 6-1: Flow chart for the experimental testing procedure

6.2 Fault detection strategy

The signals were acquired using the methodology discussed in section 5.8.2, all of which were sampled at a frequency of 25.6kHz whereby 768k *Samples* were acquired. These signals were processed in a *Matlab 2010* environment (see Appendix A). The fault detection strategy flow diagram is shown in Figure 6-2.

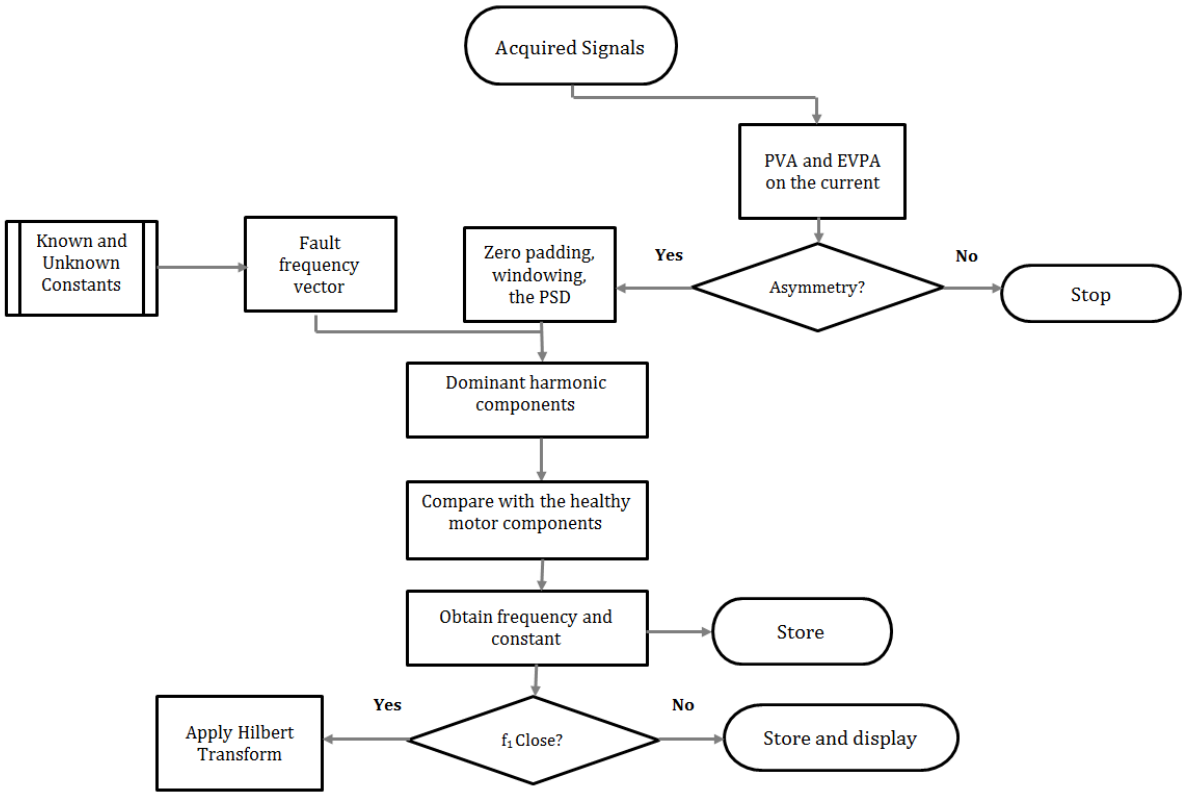

Figure 6-2: Fault detection strategy for steady state conditions

The PVA and EPVA techniques discussed in section 4.6 are applied to the current and voltage signals to observe the degree of asymmetry. The degree of asymmetry is compared to the healthy motor. If the degree of asymmetry is greater compared to the healthy motor; then the current and vibration velocity signals are zero padded, then multiplied by Hann window then a Welch PSD is applied. The reasons for choosing these methods, has been discussed in section 3.9. The detection of fault components is achieved using the fault characteristic equations discussed in section 4.4. However, these equations also have unknown constants (i.e. n and k), which poses a challenge in determining the fault frequencies using MCSA or vibration analysis (in some cases) since the fault harmonic components appear at fault frequencies where the unknown constants are one of the functions of these fault characteristic equations.

The frequency searching procedure adopted from [**85**] can be applied to the signals processing technique to obtain the fault harmonic components and frequencies. Assuming that the fault frequency band of a particular fault is decided upon; a vector of fault frequencies can be generated. All the dominant harmonic components in the current or vibration spectra corresponding to fault frequencies can be pursed. If one of these harmonic components exceeds the magnitude of the corresponding component of the healthy motor then it is focused on. The frequency of this component is obtained and the related constants are stored. For cases where

the fault component is closely located to the fundamental, the Hilbert transform described in section 3.6.2 is applied to the signal before applying the PSD to remove the fundamental component. The fault detection strategy diagram serves a process that can be implemented for practical fault detection. However, from here onwards the detection techniques (i.e. PSD and EPVA) will be analysed in isolation and will not follow the flow diagram.

6.3 Frequency analysis of supply voltages

The four faults discussed in this chapter are mostly reflected in phase A of the motor. Prior to connecting the motor, the Welch PSD is applied to voltage signal of phase A for both voltage supply configurations to analyse the frequency harmonic components already existing. The voltage spectrums of phase A for both supplies are displayed in Figure 6-3.

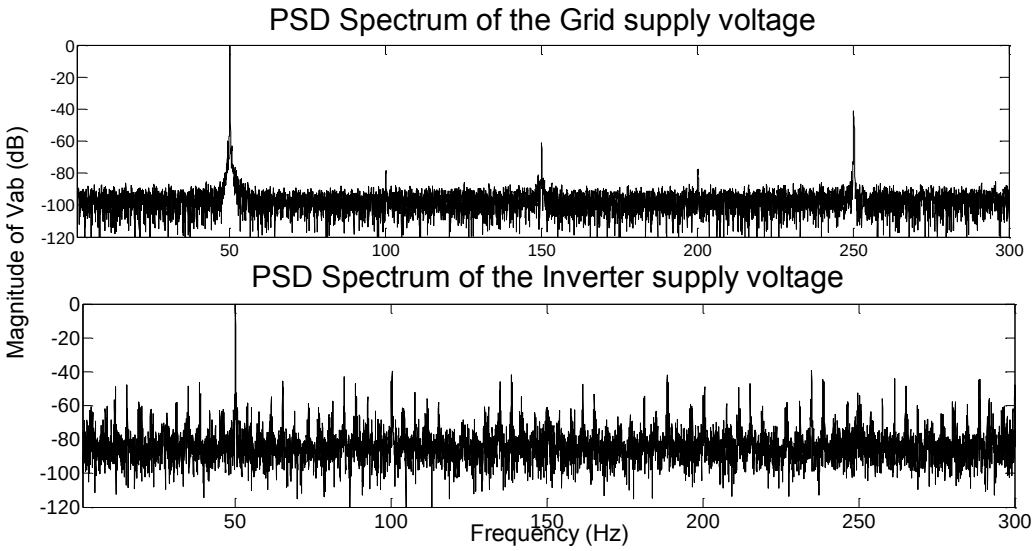

Figure 6-3: Phase A voltage frequency spectrum for the grid and inverter supply before connecting the induction motor

For the grid supply voltage, the first, third and fifth harmonics are clearly identifiable together with the second and forth harmonics which emerge due to the imperfections in the supply voltage, while in the inverter supply spectrum there are additional harmonics attributed to the switching operation discussed in section 2.2.3.

This exercise provides insight into the harmonics which would already be present due to the power supply, thus these harmonics maybe subtracted from the current spectrum when identifying the motor fault frequency components.

6.4 Detection of the Inter-turn fault

The motor is initially grid connected and the inter-turn fault is implemented in the manner described in section 5.6. The objective is to identify the components in the current and vibration spectra that are induced as a result the inter-turn fault (shorted turns) and are not due to any other problem or electro-mechanical drive characteristic. The inter-turn fault was introduced to phase A of the motor by shorting the turns as described in section 5.6.1, thus current analysis was performed for phase A. When four turns are shorted; the load conditions are kept constant. This has been considered for the different loading conditions (see Table in Appendix B). Under full load conditions, the current spectrum of the healthy motor and faulted motor (four turns shorted) is shown in Figure 6-4. The components that are indicative of an inter-turn fault are given by equation (4-1), however the most dominant component appeared at $196.2Hz$ where $k = 3$ and $n = 1$. The magnitude of this component is $-74.7\ dB$ for the motor with shorted turns, while the corresponding component on the healthy motor is $-93.4\ dB$.

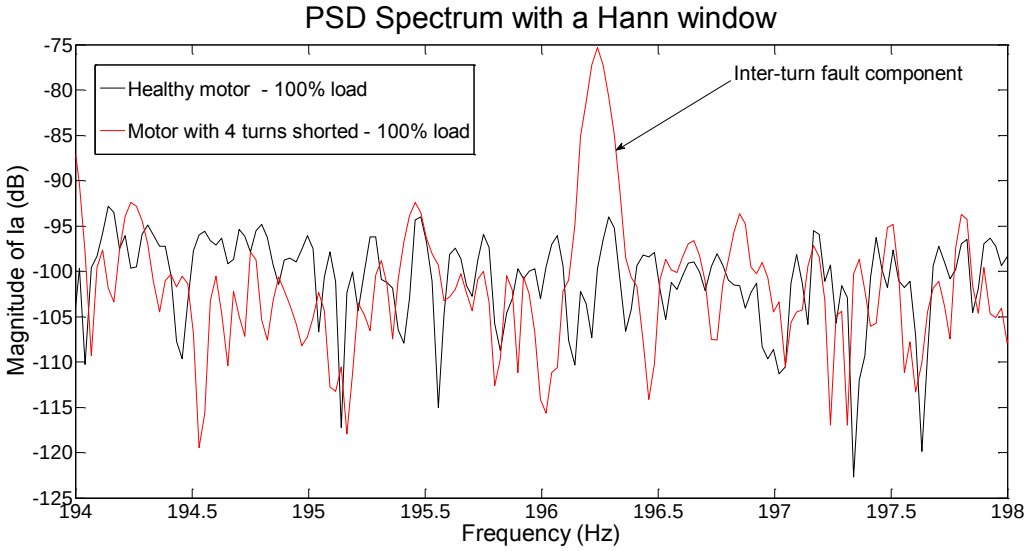

Figure 6-4: Current spectra for the grid connected; healthy motor and faulted motor(with 4 shorted turns) at 100% load conditions

Using vibration analysis, the inter-turn stator fault is indicated by an increase of the twice frequency component as discussed in section 4.4.1. All three directions were considered; however, the radial vibrations were the most prominent. The radial vibration velocity spectrum of the healthy motor and faulted motor is shown in Figure 6-5. The twice line frequency component located at $99.83\ Hz$ appears on the spectrum of the healthy motor due to the reasons expressed in section 4.3.1, the magnitude of this component increases for the faulted

motor from $-55.6\ dB$ to $-48.5\ dB$ due to the increase in the unbalance force attributed to the inter-turn fault discussed in section 4.4.1. Note that twice the rotational frequency is closely located to twice the line frequency component; this is typical for two pole machines but is not considered as an indicator for an inter-turn fault. The manifestation of the fault is more prominent on the current spectrum compared to the vibration velocity, since the magnitude of the fault component changes by $19.32dB$ in the current spectrum whereas in the vibration spectrum, the twice frequency component changes by $7.1dB$. This has also been evaluated for different loading conditions (see Table in Appendix B).

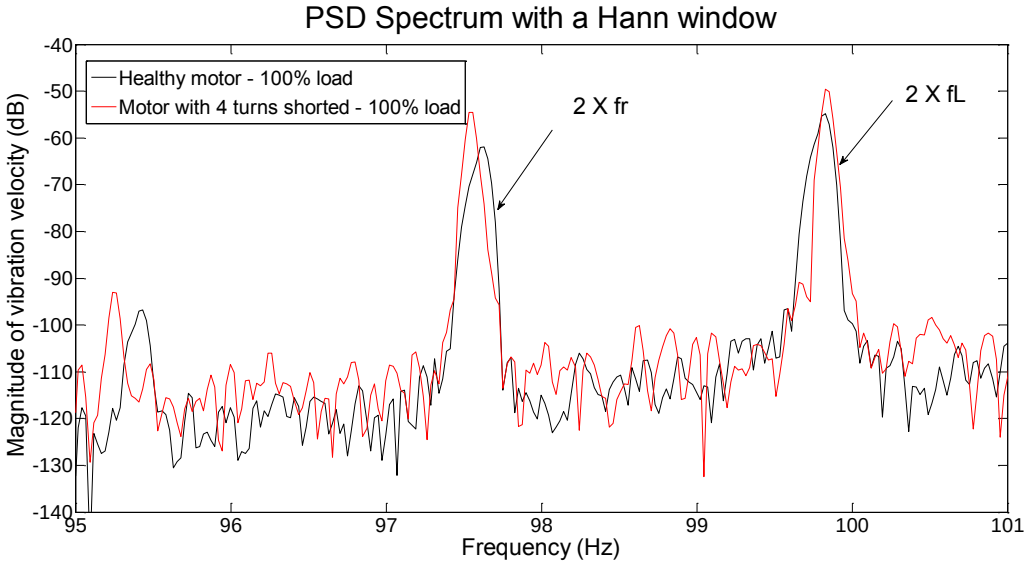

Figure 6-5: The vibration spectra for the grid connected; healthy motor and faulted motor (with 4 shorted turns) at 100% load conditions

6.4.1 Impact of varying the fault

The results in the previous section demonstrated that under extreme load and fault conditions the impact of shorting four turns prevailed more dominantly in the current compared to the vibration; thus from here on the current will be used. To establish the impact of the fault severity at full load within the current spectrum; the number of shorted turns is reduced to two turns. This has been also explored for the different loading conditions (see Appenidx B). Figure 6-6 shows the two fault conditions and the healthy motor yet again. The fault is evident at $196.8Hz$ for the motor with two shorted turns. However, the magnitude of fault component decreases from $-74.7\ dB$ (when four turns are shorted) to $-83.6\ dB$. This reduction of the magnitude is expected when the fault severity is reduced since the distribution of the stator MMF in the airgap is less affected because less of the stator current will be flowing through the

shorted turns [**86**]. The frequency location of the components deviates due to fluctuations in the speed during the signal acquistion. The standard deviation of the fault components is approximately 0.1 Hz $(6rpm)$.

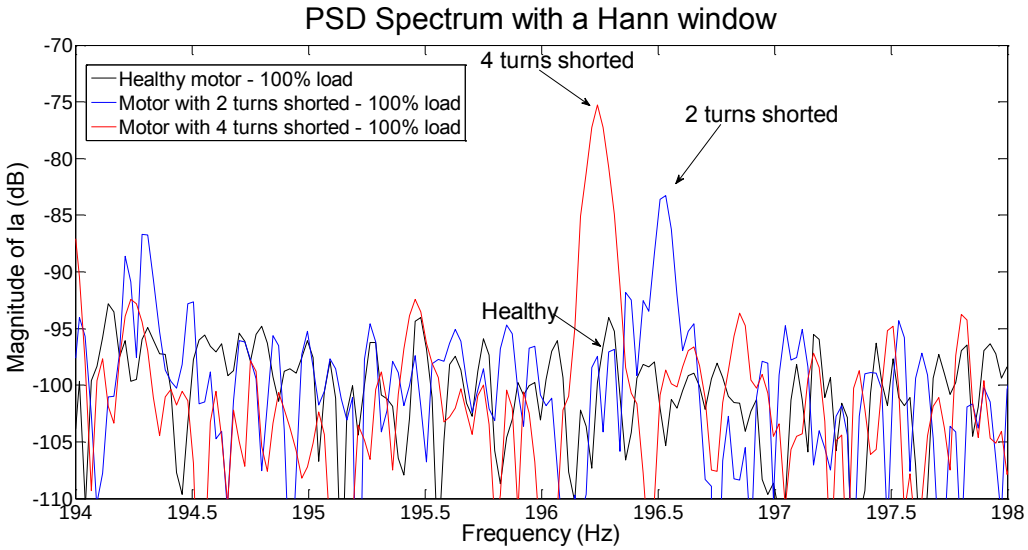

Figure 6-6: The current spectrum of a grid connected motor with an inter-turn fault with different fault levels under 100% load conditions

6.4.2 Impact of varying the load

In the previous section, the impact of varying the fault under full load condition was explored. The impact of varying the load under constant fault condition will now be considered for different fault severities. Figure 6-7 shows the current spectrum when four turns are shorted and the load is set to 100%, through 50% and 0%. As the load is reduced, the magnitude of inter-turn fault component is noticeably decreased from $(-74.7\,dB)$ through $(-76.7\,dB)$ to $(-78.8\,dB)$. However, it is important to note that the difference in magnitude of these components with four turns shorted as a function of load is less compared to the changes that occurr when the vary severity is reduced, since at any load condition it is the short turn effect that dominates [**87**]. The inter-turn fault frequency components are a function of slip; hence the deviation in frequency as the load is varied. The frequency location of this component deviates by $2.9Hz$ $(57.9rpm)$ between no load and full load.

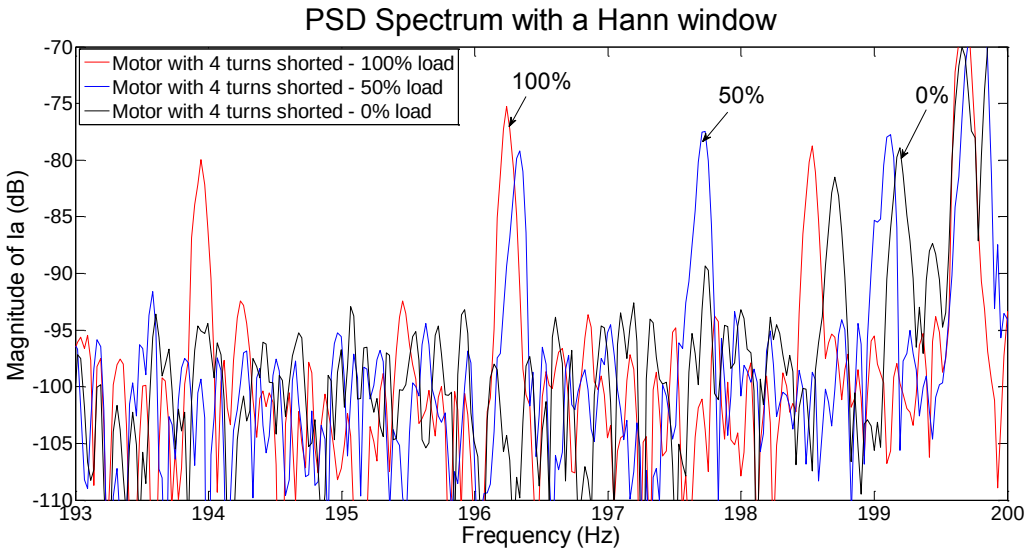

Figure 6-7: The current spectrums of a motor with 4 turns shorted under different load conditions

6.4.3 The impact of the inverter

The detection of the inter-turn fault in the grid connected motor was explored in the sections above; the inverter-fed motor has been considered to determine whether the inter-turn fault can still be detected. Four turns were shorted in the same manner described for the grid connected motor under constant load. At 100% loading; the fault component is clearly evident in the current spectrum of the grid connected motor with four turns shorted; however it is not noticeable in the inverter-fed motor current spectrum as illustrated in Figure 6-8, this is possibly due to additional components associated with the switching of the inverter that would mask the inter-turn component. The detection of the 2 ×line frequency vibration velocity component has also been explored, the results are shown in the Appendix B; however there was no significant difference here.

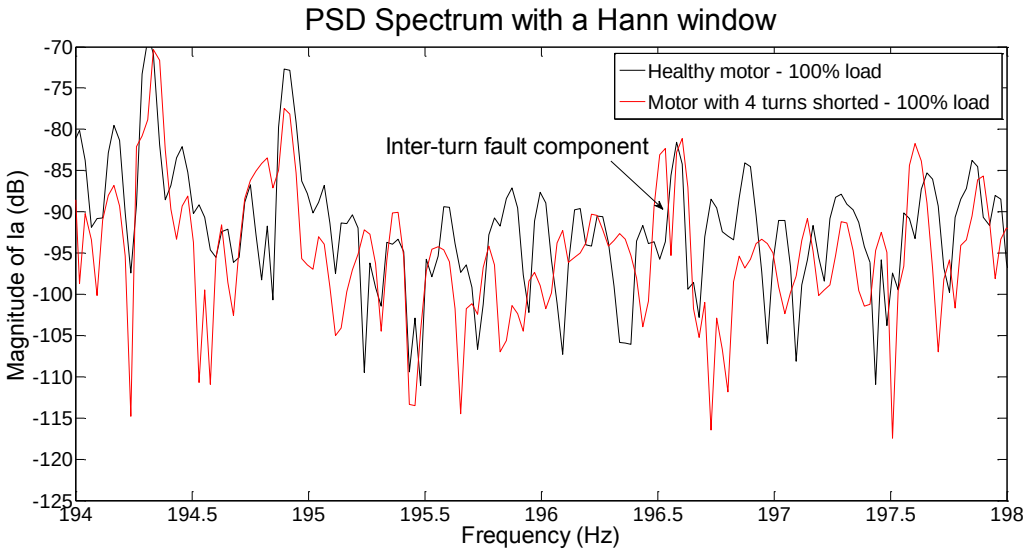

Figure 6-8: Inverter fed motor at a 50Hz fundamental frequency of 50Hz - Current spectrums of a healthy motor and faulted (motor with 4 shorted turns) under 100% load conditions

6.4.4 Extended Parks Vector Approach

It was shown in the previous sections that classical MCSA was capable of detecting the inter-turn fault for a grid connected motor. Reducing the fault level reduces the magnitude of the fault frequency components, while reducing the load condition also reduces magnitude but increases the frequency location of the component. Under the least extreme conditions; low fault level and load condition, the combination of these two effects can pose a challenge in detecting the inter-turn fault. In the inverter-fed motor, the inter-turn component was not evident due to the influence of the additional harmonics associated with inverters. The Park Vector and the EPVA techniques were employed to improve the fault detection capability in the cases where detection of the fault was difficult to achieve.

6.4.4.1 Grid supplied motor

The PVA and EPVA technique were initially applied to the grid supply voltage to gain insight into the degree of unbalance in the supply. Figure 6-9 shows a non-ideal circular trajectory of the PV for the supply voltage, which indicates that there is a slight imbalance in the voltage supply. In the EPVA spectrum of the supply voltage, the magnitude of the twice fundamental frequency component is $-44.31dB$.

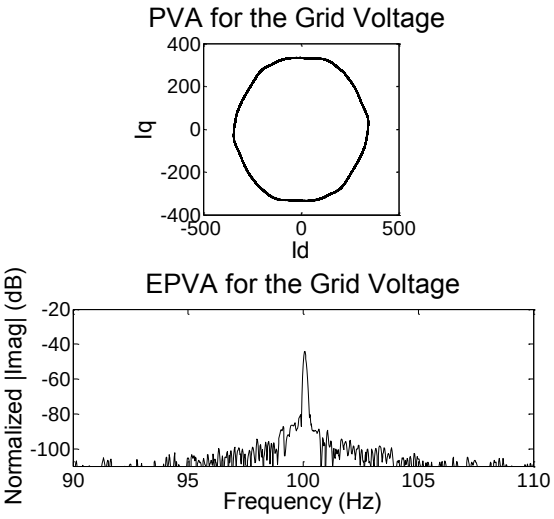

Figure 6-9: PVA and EVPA for the grid voltage

These techniques were applied to the current signal of the healthy motor under different loading to gain insight into the PVA and EPVA prior to fault implementation. In Figure 6-10, the PVA and EPVA for a healthy motor at 0 and 100% loading are shown. This results in elliptical PVs rather circular for both loading conditions. This demonstrates that there are asymmetries already prevalent in the machine. There is a noticeable difference in the magnitude of the ellipses at the two loading levels.This is expected the phase currents (i.e. i_a, i_b and i_c) differ in magnitude according to the load on the machine. The magnitude of the twice fundamental frequency components at 0 and 100% loading is respectively $-34.23dB$ and $-30.93dB$.

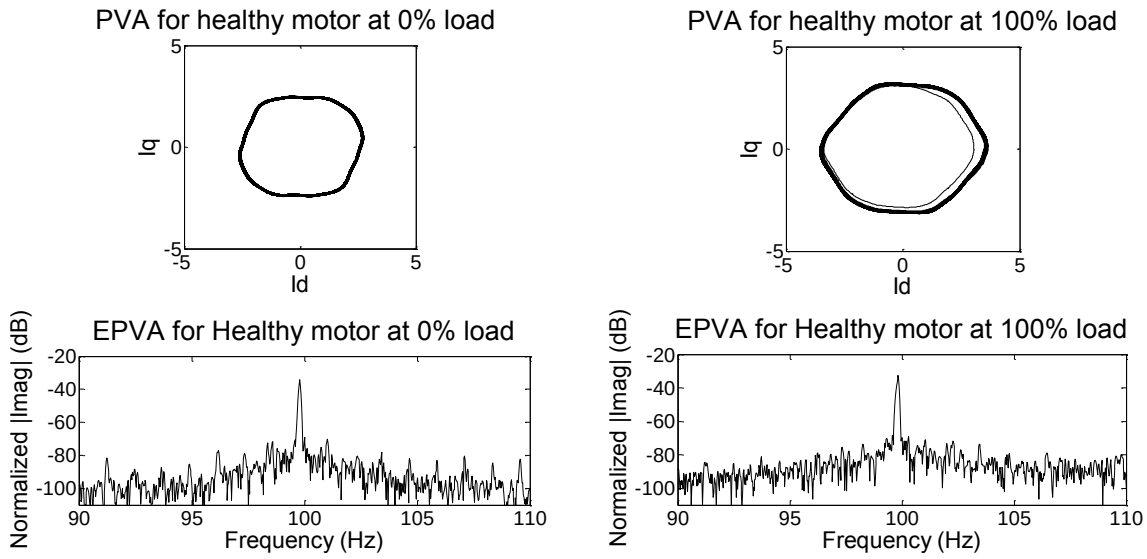

Figure 6-10: PVA and EPVA for healthy motor under 0% and 100% loading conditions

The impact of shorting two and four turns at different loading conditions was then considered. Figure 6-11 and Figure 6-12 shows the PVA and EPVA of a motor with two and four turns shorted respectively. Notice that the degree of elliptical obscurity in the PVs trajectory increases in magnitude as the fault severity increases. This is expected since increasing the fault severity increases the asymmetry between the three phases, thus increasing the negative sequence component in the current. In the EPVA spectrums, at 0% loading, the twice fundamental components when two and four turns are shorted is $-23.55dB$ and $-19.31dB$ respectively, while at 100% loading the magnitude of the components corresponds respectively to $-22.98dB$ and $-17.92dB$. The magnitude increase of these components is proportional to the severity of the fault.

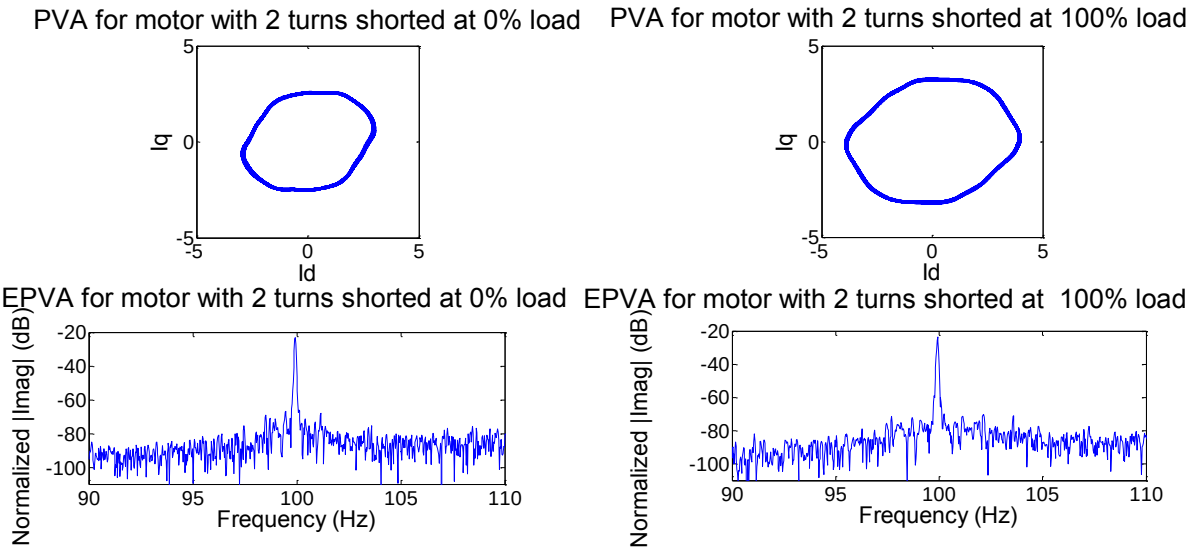

Figure 6-11: PVA and EVPA for a motor with 2 shorted at 0 and 100% loading

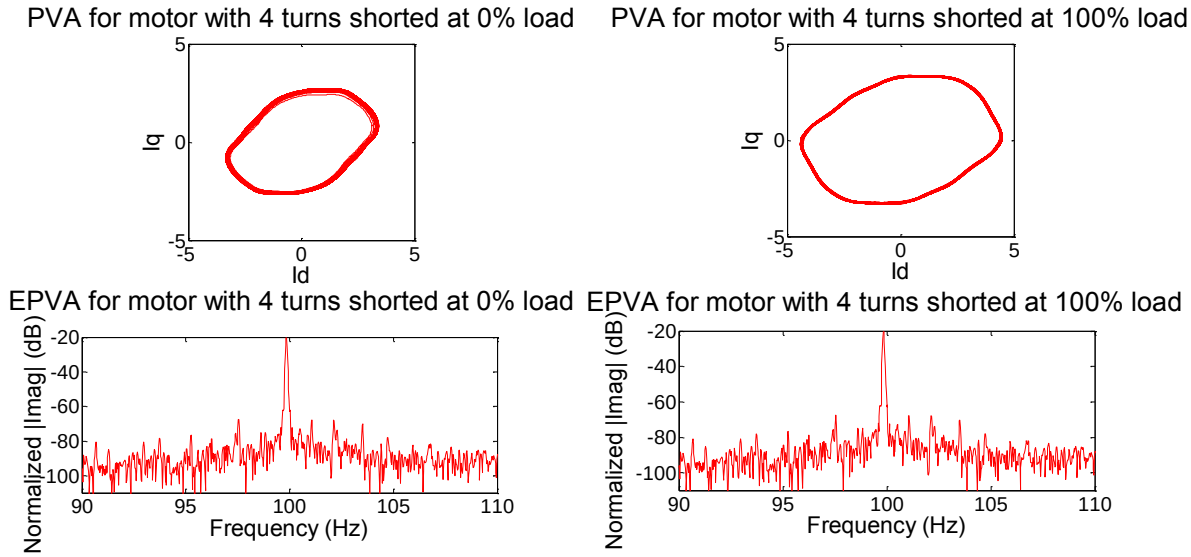

Figure 6-12: PVA and EVPA for a motor with 4 turns shorted at 0 and 100% loading

6.4.4.2 Inverter fed motor

Similar to the grid supplied motor, the PVA and EPVA techniques were applied to the inverter-fed motor. The fault severities and loading conditions, as with the grid connected motor were considered. In Figure 6-13, the results of the techniques applied to a healthy motor and a motor with four turns shorted at 100% loading conditions are shown. Likewise, the PV for the healthy motor is also elliptical but it also contains an element of noise due to the switching. When four turns are shorted, the degree of elliptical obscurity and magnitude is at a maximum. In the EPVA

spectrums, the magnitude of twice the fundamental frequency components for healthy and faulted are $-34.33dB$ and $-21.72dB$. These values are slightly lower than corresponding values of the grid supplied motor, which could suggest that inverter supply is slightly more balanced compared to grid supply.

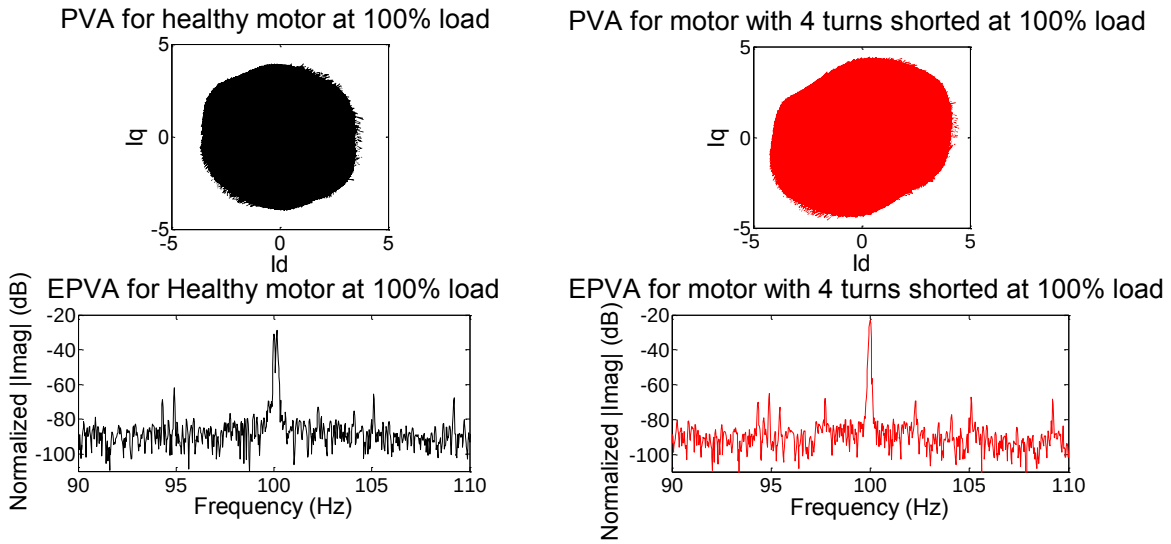

Figure 6-13: PVA and EPVA for inverter-fed healthy motor and motor with 4 turns shorted at 100% loading

6.4.5 Summary of inter-turn detection

A summary of the main findings for the preceding sections will now be presented. The impact of varying the fault severity and load conditions on a grid connected healthy and motor with shorted turns were explored; furthermore, the impact of the inverter and varying the operating fundamental on an inverter-fed motor was also explored. The results of the vibration analysis were not as promising as they were in the current analysis for this particular fault in the case of a grid connected motor. The impact of varying the severity affected the magnitude of the inter-turn fault component in the current spectrum more as compared to varying the load level. The impact of varying the load affects the frequency location of the inter-turn fault component. For an inverter-fed motor, the fault component was not detected due to the noise associated with the switching of the drive. Figure 6-14 summarizes the inter-turn fault detection for a grid connected motor using MCSA. The dashed grey line represents the boundary of the fault condition. The difference between the least extreme fault scenario (2 turns and 0% load) and the maximum loading condition of a healthy motor is approximately $3.9dB$.

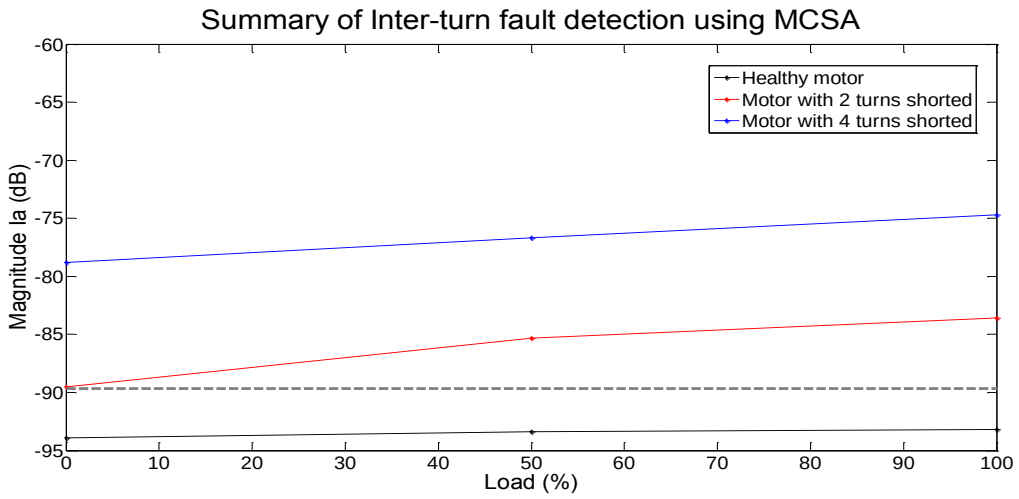

Figure 6-14: Summary of detecting an inter-turn fault on a grid connected motor using current

The PV technique provided some indication to the severity of the fault by observing the magnitude and degree of the PV trajectory. The degree of obscurity and magnitude of the PVs trajectory increased as the fault severity increased. The EPVA technique provided indication of the intensity of the fault by observing the magnitude of the twice fundamental frequency component. The magnitude of this component increased as the fault severity increased. The application of the EPVA to grid connected and inverter-fed motors under different load and fault conditions is summarized in Figure 6-15. In both supply configurations the magnitude of the EVPA increases with load and fault severities. The difference between the least extreme fault scenario (2 turns and 0% load) and the maximum loading conditions of a healthy motor for a grid connected and inverter-fed motor is respectively $-7.39dB$ and $0.7dB$. Thus, the inverter-fed motor requires caution under such conditions.

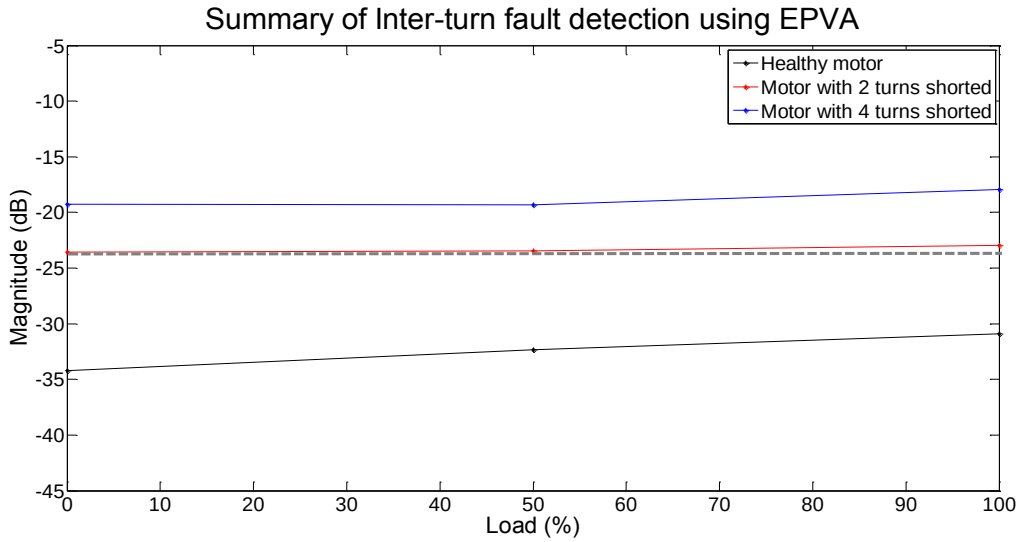

(a)

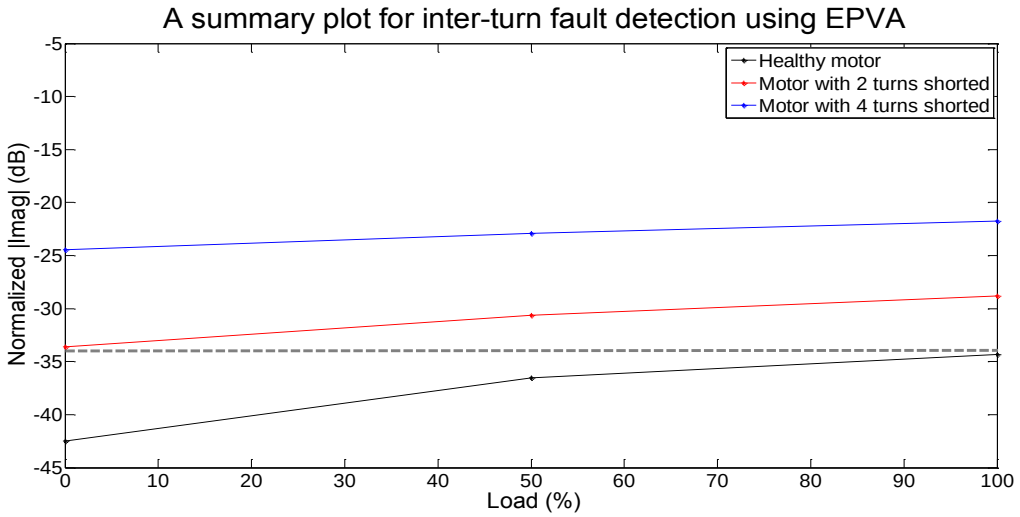

(b)

Figure 6-15: A summary of the application of the EPVA on a) a grid connected and b) an inverter-fed motor

6.5 Detection of broken rotor bar

The detection of broken rotor bars will be described, whereby the influence of the supply and load, and its sensitivity to the current and vibration signal will be explored. The motor with three broken rotor bars described in section 5.6.2 is used, which was initially grid connected. As with the previous section, the objective is to identify the components in the current and vibration spectra that are only a function of broken rotor bars. The 0% and 100% loading conditions of the healthy motor and faulted motor (with three broken bars) were first considered. The current of phase A was used due the reasons previously discussed. Figure 6-16 shows for phase A current spectrum of both motors for no load and full load conditions. The fundamental is linked to the supply frequency as expressed in section 4.4.2. Under no load conditions, the left side harmonic (LSH) and right side harmonic (RSH) of the healthy motor given by equation (4-3) appear at 49.40 Hz and 50.37 Hz respectively where k is equal to 1. The magnitude of these harmonics are $-47.00\ dB$ and $-46.9\ dB$ respectively, whereas on the motor with three broken rotor bars, these harmonics appear at 49.32 Hz and 50.51Hz. The LSH and RSH in the faulted motor increase by 7.15 dB and 6.94 dB respectively. The frequency variation of the harmonics between the healthy motor and motor with broken rotor bars is due to the different operating speeds of the healthy motor and faulted (motor with broken rotor bars) as described in section 5.9.3.

For the healthy motor, 100% loading, these harmonics appear at 47.77 Hz and 52.22 Hz respectively, with magnitudes of $-51.11\ dB$ and $-50.32\ dB$ respectively. For the faulted motor, the LSH and RSH appear at 47.29 Hz and 52.00 Hz respectively. The LSH and RSH in the faulted motor increase by 8.36 dB and 9.09 dB respectively.

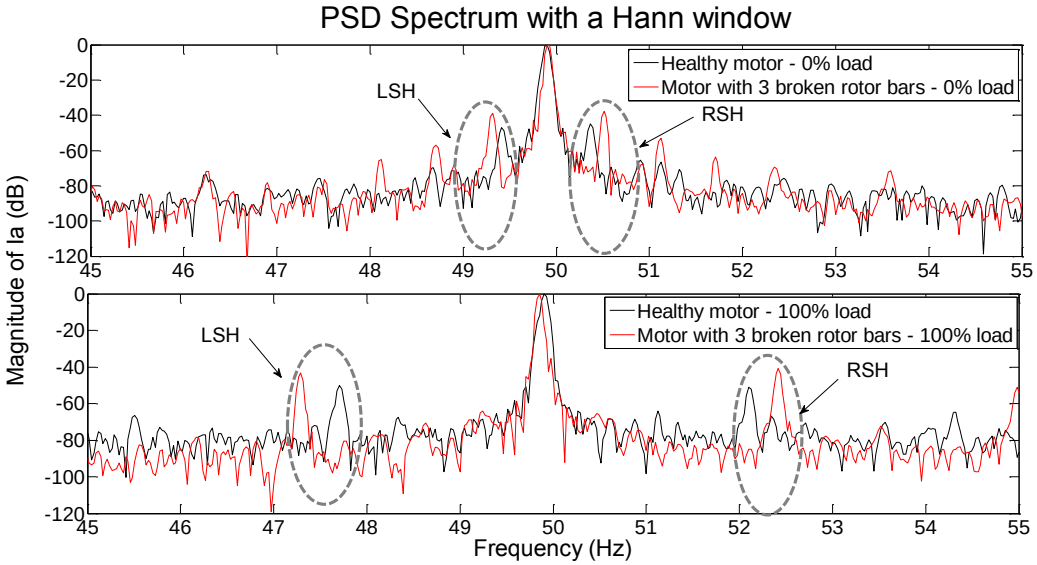

Figure 6-16: Current spectrums of a Grid supplied healthy motor and a motor with 3 broken rotor bars at 0 and 100% load conditions

Likewise, the vibration velocity spectrums of both motors for no load and full load conditions are shown in Figure 6-17. In vibration analysis all three directions were considered, although the radial vibrations were the most prominent. The fundamental is related to the rotational frequency of the motor as expressed in 4.4.2. At 0% load, the LSH and RSH of the healthy motor, explained in section 4.4.2, appear at 49.20 Hz and 50.13 Hz respectively. The magnitude of these components are $-44.31dB$ and $-38.19dB$ respectively. In the faulted motor these harmonics appear at 49.23 Hz and 50.37Hz respectively. The lower and upper sidebands in the fault motor increase by 6.43 dB and 6.05 dB respectively. At 100% loading, the LSH and RSH are respectively located at 46.6Hz and 50.13Hz are evident on the healthy motor spectrum, and the magnitude of these components are -53.52 and $-43.09dB$. The motor with the broken rotor bars, the LSH and RSH appear at 46.00 Hz and 51.13Hz respectively. Notice that the LSH and RSH respectively increase by 12.81dB and 7.09dB.

The LSHs are associated with rotor asymmetry, which was also evident in the healthy motor current and vibration spectra. This possibly means that the rotor is not perfect and there is some asymmetry due to inherent differences in the rotor bar to end ring joint. The impact of a broken rotor bar increased the magnitude of the LSHs and RSHs in the current and vibration spectrums. The frequency location of these side bands is slip dependant. At 0% loading, the

increase in the harmonics was more evident in the current spectrum. At 100% loading, the increase in the LSH was more prominent in the vibration compared to the current spectrum, whereas the RSH was more eminent on the current spectrum.

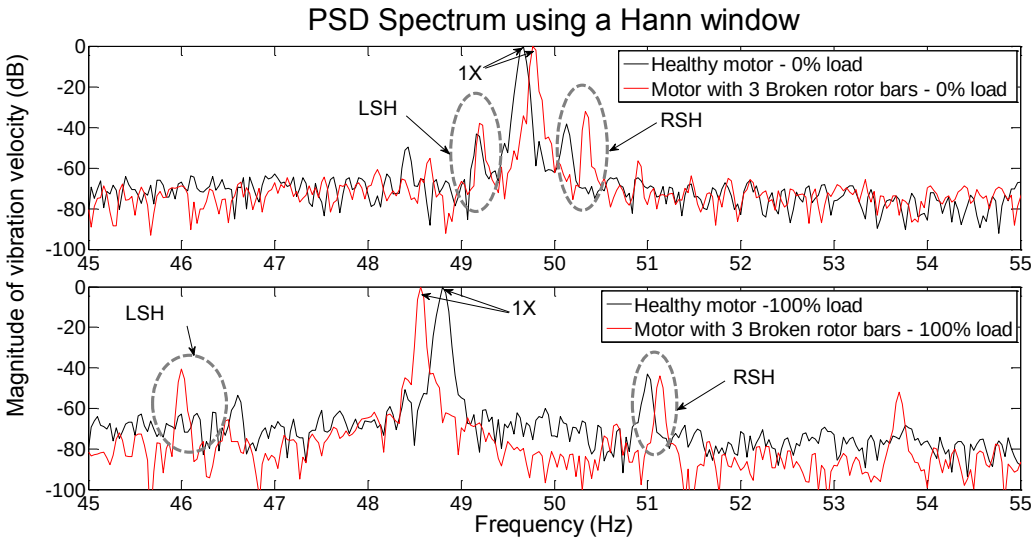

Figure 6-17: Vibration velocity spectrums of a Grid supplied healthy motor and a motor with 3 broken rotor bars at 0 and 100% load conditions

6.5.1 Impact of varying the load

The harmonics indicative of broken rotor bars were identified at 0 and 100% loading conditions. To examine the impact of varying the load, the load level was reduced from 100% through 50% to 0% load. The impact of varying the load on the faulted motor was investigated further. Figure 6-18 illustrates the impact of varying the load in the current spectrum. The fundamental frequency component deviates slightly by $0.11Hz$ due to the oscillations of the supply frequency. As the load is reduced, the LSH and RSH are located closer to the fundamental frequency due the decrease of slip as shown in Figure 6-18. This poses a challenge of detecting these sideband peaks under lightly load conditions since they may be masked by the fundamental component. The magnitudes of the LSH and RSH increase slightly by $3.3dB$ and $0.72dB$ respectively, as the load is reduced.

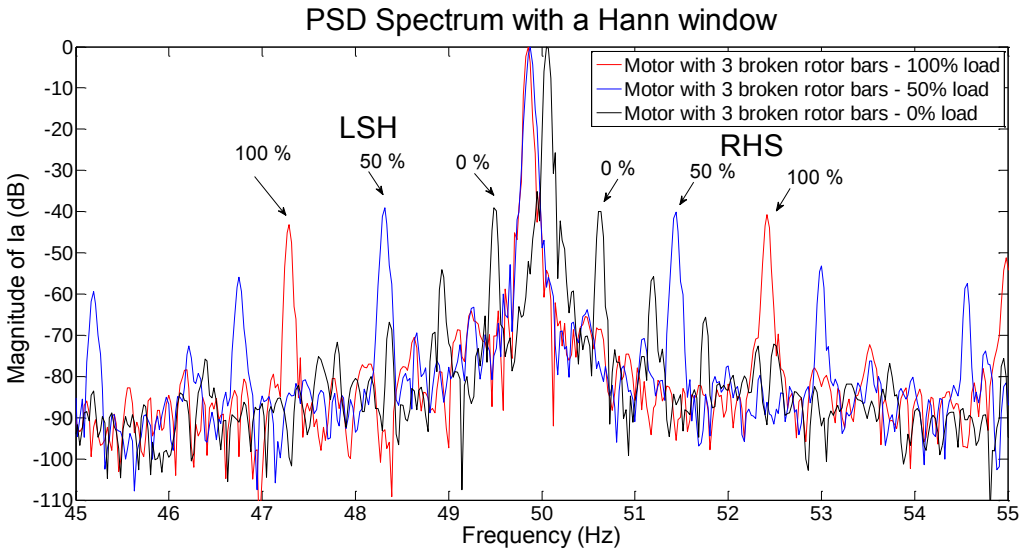

Figure 6-18: Current spectrums of a grid connected motor with 3 broken rotor bars at different load conditions

Similarly, in the vibration spectrum, as indicated in Figure 6-19, shows that as the load is reduced, the LSH and RSH move closer to the fundamental frequency (1 × vibration frequency). However, the fundamental component varies with the load condition. As the load is reduced the fundamental frequency increases in frequency due the increase in speed. The magnitudes of the LSH and RSH also increase by $11.33dB$ and $11.9dB$ respectively as the load is reduced.

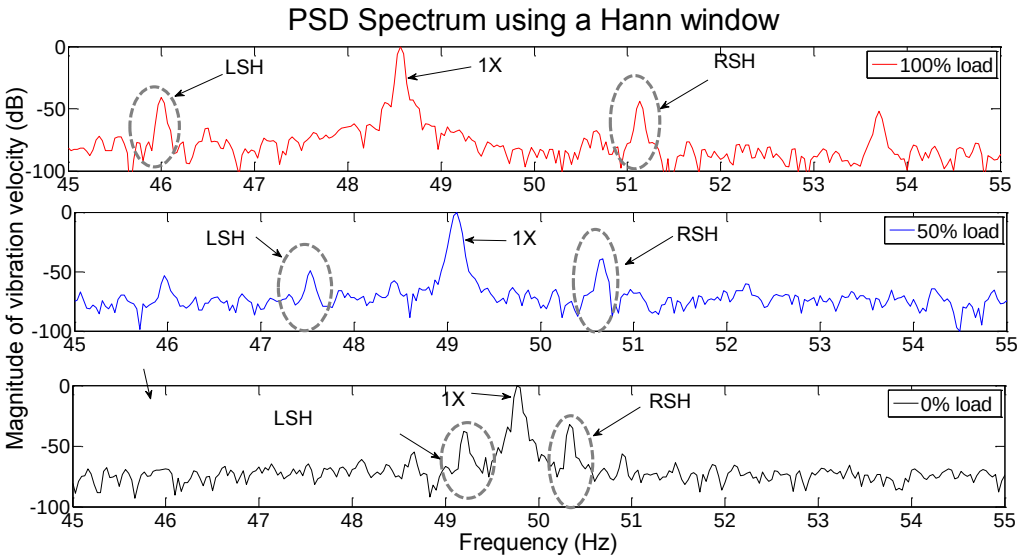

Figure 6-19: Vibration velocity spectrums of a grid connected motor with 3 broken rotor bars at different load conditions

6.5.2 Impact of the Hilbert transform

The influence of the fundamental component can create a challenge in the detection of the sideband peaks for lightly loaded conditions in both the current and vibration spectrums since the fault indicative harmonics are closely located to the fundamental component, which can mask them. Furthermore, in the vibration analysis, the fundamental component varies with speed of the rotor, thus increasing the number of variables. The Hilbert transform as described in section 3.6.2 is capable of removing the fundamental component.

The PSD is computed on the remaining signal, after the removal of the fundamental component in the manner explained in section 6.2. The application of a window function or the logarithmic scale is not critical since the spectral leakage is not an issue. The Hilbert transform was applied to the current signals to obtain the magnitude of the analytical signal for the three different loading conditions; the frequency spectrums are displayed in Figure 6-20. As loading is reduced, the fault harmonic component $2sf_1$ obtained from equation (4-3), is located closer to $0Hz$. The fault component is present in both the healthy motor and fault motor; however it is approximately 10 times larger for the faulted motor compared to healthy motor. The magnitude of the fault component on the faulted motor increases from 0.014 to 0.018 as the load is reduced from 100% through 50% to 0% load. This is an improvement to result of those previously discussed.

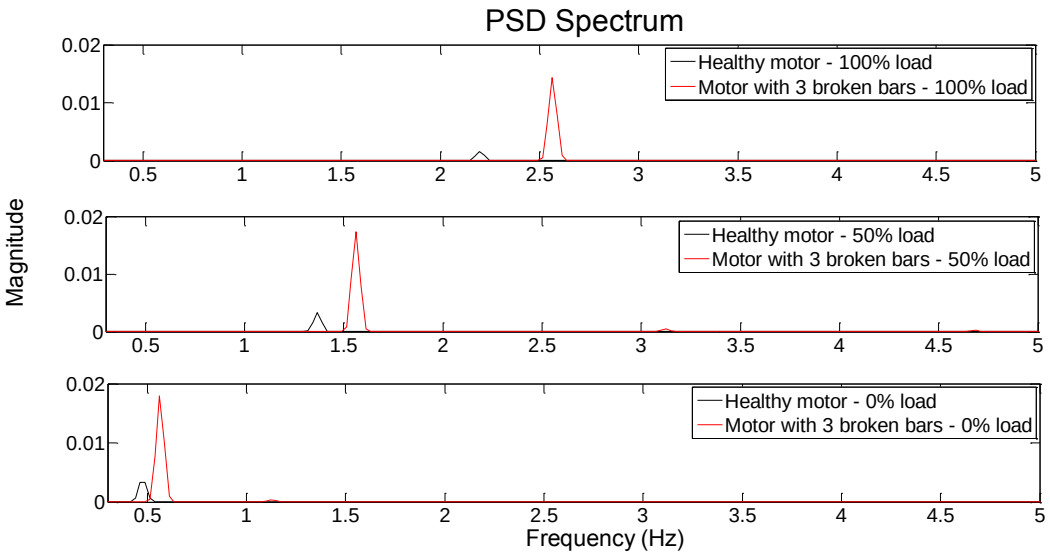

Figure 6-20: The spectrums of the Hilbert transform of current of a grid supplied motor with 3 broken rotor bars at different load conditions

Similarly, the same approach was applied on the vibration velocity signal of both motors under different loading conditions refer to Appendix B. Similarly, the fault component is present in both the healthy motor and fault motor vibration spectrum; however it is much larger for the faulted motor compared to healthy motor. The fault component on the vibration spectrum at light loading, for the faulted motor, is not as distinct as compared the current.

6.5.3 The impact of the inverter

The advantage in using the Hilbert transform for the broken rotor bar conditions has been illustrated and will be used the case of the inverter fed motor. The spectrum of the remaining current, after removing the fundamental, of an inverter-fed healthy motor and faulted motor under full load conditions is shown in Figure 6-21. Despite the complexity of the additional noise due to the switching frequency of the inverter, the fault component is still evident on the healthy and faulted motor current spectrums at 2.25 Hz and 2.46 Hz respectively. However, the magnitude difference is 0.0018 and 0.015 respectively, which is synonymous to the ones obtained for the grid connected motor.

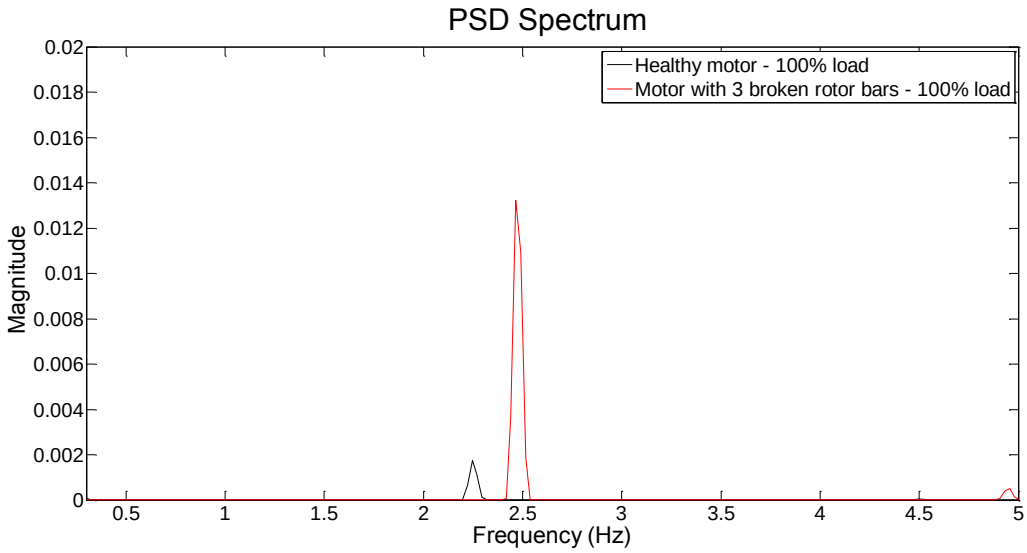

Figure 6-21: The spectrums of the Hilbert transform of current of an inverter-fed healthy motor and a motor with 3 broken rotor bars at 100% load conditions

The fault component was detected in the inverter-fed motors at $50Hz$ operating fundamental. Speed control by means of varying the fundamental frequency (and voltage), enables the motor to operate at speeds below the rated but also speeds above the rated as expressed in section 2.2.3. To evaluate the impact of varying the speed, the operating fundamental was adjusted to $40Hz$ and $60Hz$. Varying the fundamental at 100% loading is discussed here; however, the impact has been considered at different loads. When the fundamental was set to $40Hz$ as shown in Figure 6-22a), the fault components of the healthy and faulted motor are closer to $0Hz$ and the magnitude decreases slightly to 0.0017 and 0.014 respectively. The minimal decrease is expected since air-gap flux is kept constant given that the stator voltage magnitude decreases in proportion to the fundamental frequency.

When the fundamental frequency was set to $60Hz$ as shown Figure 6-22b), the fault components of the healthy and faulted motor are further from $0Hz$ compared when the fundamental frequency is $50Hz$ due to the increase of the fundamental frequency. However, notice the magnitude of components of the healthy motor and faulted motor decreases to $3.35e-008$ and 0.0018 respectively. This is due to the fact that the stator voltage is kept to its rated value, while the fundamental is increased; thus reducing the air-gap flux of the motor as discussed in section 2.2.3.

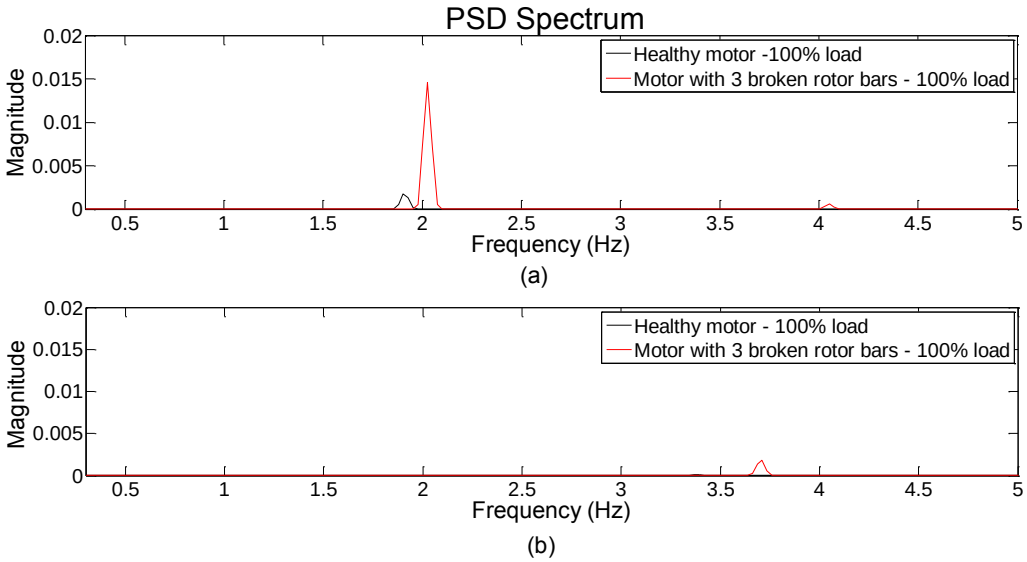

Figure 6-22: The spectrums of the Hilbert transform of current of an inverter-fed healthy motor and a motor with 3 broken rotor bars at 100% load conditions at fundamental frequency of a) 60Hz and b) 40Hz

6.5.4 Summary of broken rotor bar detection

A summary of the main findings for the preceding sections will now be presented. The impact of varying the load conditions and applying the Hilbert transform on a grid connected healthy and motor with three broken rotor bars were explored; furthermore, the impact of the inverter and varying the operating fundamental on an inverter-fed motor was also explored. For the grid connected motor, the classical technique is capable of detecting harmonics indicative of the broken rotor bars in both current and vibration velocity spectrums. However, at low loading conditions the detection of such peaks becomes a challenge since these are closely located to the fundamental. In the vibration spectrum, the fundamental is related to rotor speed which is an additional variance.

The Hilbert transform is capable of removing the fundamental frequency, which omits the use of the window function and logarithmic scale. Thus, the results of the Hilbert technique compared to the classical are more precise for detecting the fault component. For the inverter-fed motor, the impact of varying the fundamental alters the location of the components. At below rated speeds, the magnitude of the fault components is reduced slightly since that the air-gap flux is kept constant, whereas at beyond the rated speeds, where field weakening is applied, the magnitude of the component is reduced drastically because the air gap flux is reduced. This is expected since the magnetising component of the stator current establishes the air-gap, thus a change in the air-gap flux will affect the current magnitude.

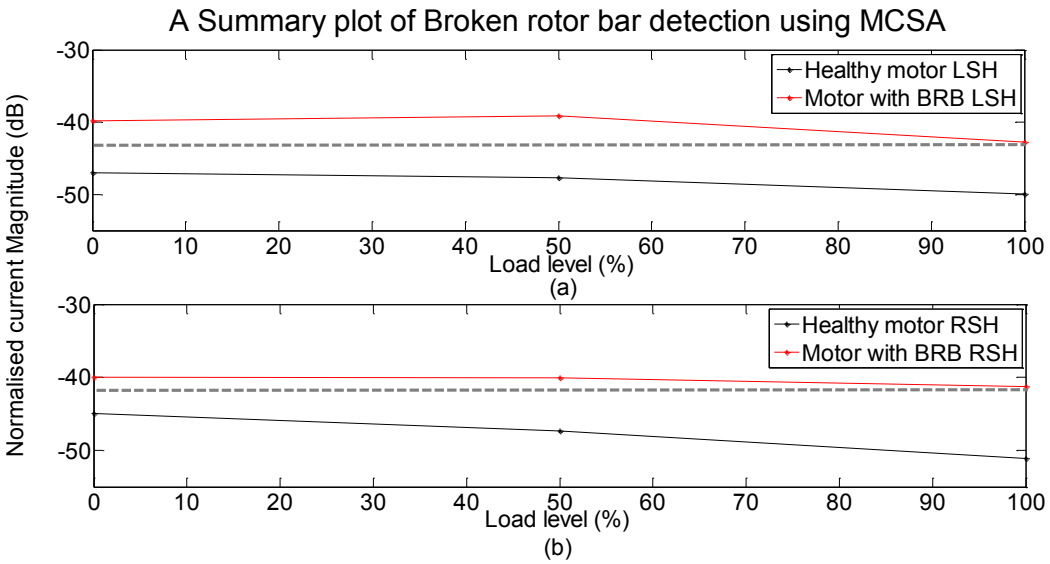

Figure 6-23: Summary of detecting broken rotor fault on a grid connected motor using current

Figure 6-23 summarizes the broken rotor bar detection for a grid connected motor using MCSA. The dashed grey line represents the boundary of the fault condition. The difference between the least extreme fault scenario (3 broken bars and 0% load) and the minimum loading condition of a healthy motor is approximately $7.15dB$ and $4.98dB$ for the LSH and RSH respectively.

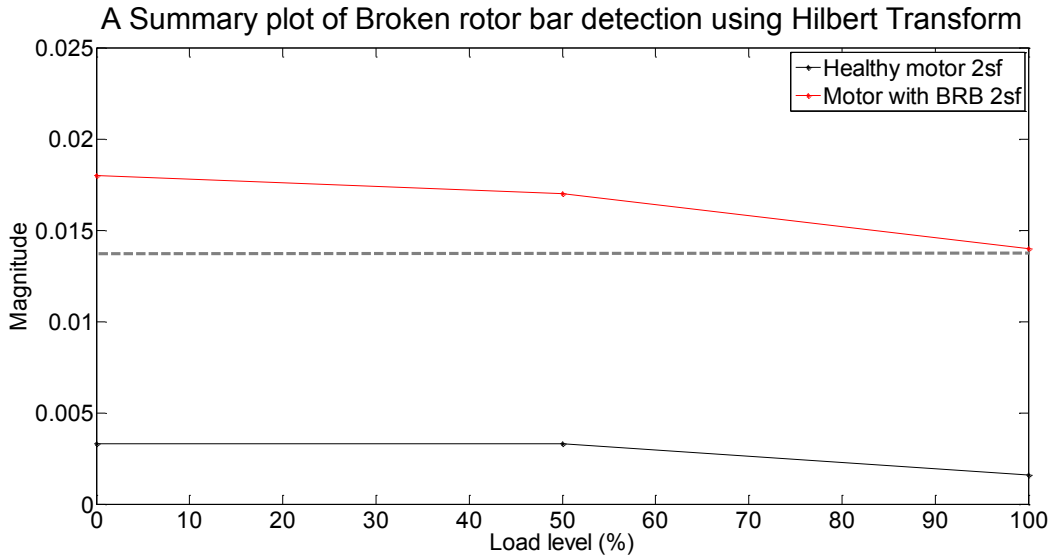

Figure 6-24: Summary of detecting broken rotor fault on a grid connected motor using the Hilbert transform

Figure 6-24 summarizes the broken rotor bar detection for a grid connected motor using the Hilbert transform. The difference between the least extreme fault scenario (3 broken bars and 0% load) and the minimum loading condition of a healthy motor is approximately 0.0147.

6.6 Detection of bearing faults

The detection of the bearing faults will now be described. The motor with faulted bearings (one bearing with inner race fault and one bearing with outer race fault) described in section 5.6.3 was used. As before, it is initially grid connected with the objective to identify the frequency components in the current and vibration spectrums associated with bearing faults. The 100% loading conditions of the healthy motor and motor with faulted bearings were first considered. The current of phase A is used due the reasons previously discussed. Figure 6-25 shows phase A current spectrums of both motors. At 100% loading, outer and inner race fault components given by equation (4-5) and (4-6) respectively appear only in the spectrum of the motor with faulted bearings. These were revealed at $201.3Hz$ and $291.1\,Hz$ where m is equal to 1 respectively. The magnitude of these outer race and inner race components are $-84.52\,dB$ and $-87.36\,dB$ respectively. Notice the inner race component is less prominent compared to the outer race.

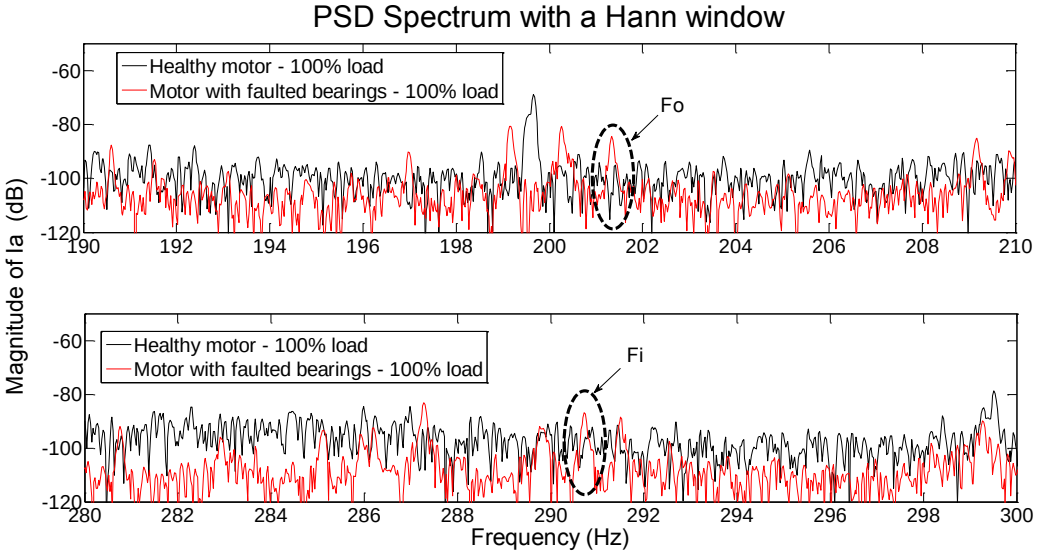

Figure 6-25: The current spectrums for healthy motor and motor that contains one bearing with outer race fault and one bearing with inner race fault under 100% loading conditions

In the vibration spectrum as shown in Figure 6-26, the difference is more pronounced. The outer and inner race fault components given by equation (4-5) are revealed at $151Hz$ and $241.1Hz$ for the outer and inner race faults respectively, where m (for the outer race fault) is equal to 0. These components, like in current analysis are only evident in the motor with faulted bearings. This is expected since the bearing faulted motor causes an eccentricity (dissymmetry) in the air-gap. The eccentricity causes a point of minimal air-gap resulting in an unbalance

magnetic pull existing in the direction of the minimum air-gap, which causes a much higher shaft vibration reflected in the magnitude of the bearing fault harmonic [**88**]. The magnitudes of the outer race and inner race components are $-74.92dB$ and $-78.79\ dB$ respectively. Again, the outer race fault component is more prominent compared to the inner race fault. The possible reason for this is that the fault on the inner race comes into the load zone once per revolution and the signal must travel through more structural interfaces before reaching the accelerometer location i.e. rolling element, across the oil film, through outer ring and bearing housing as also expressed in section 4.4.3. Thus, the transmission path is more difficult for the inner race fault which probably explains the lower magnitude of the inner race fault component compared to outer race [**89**].

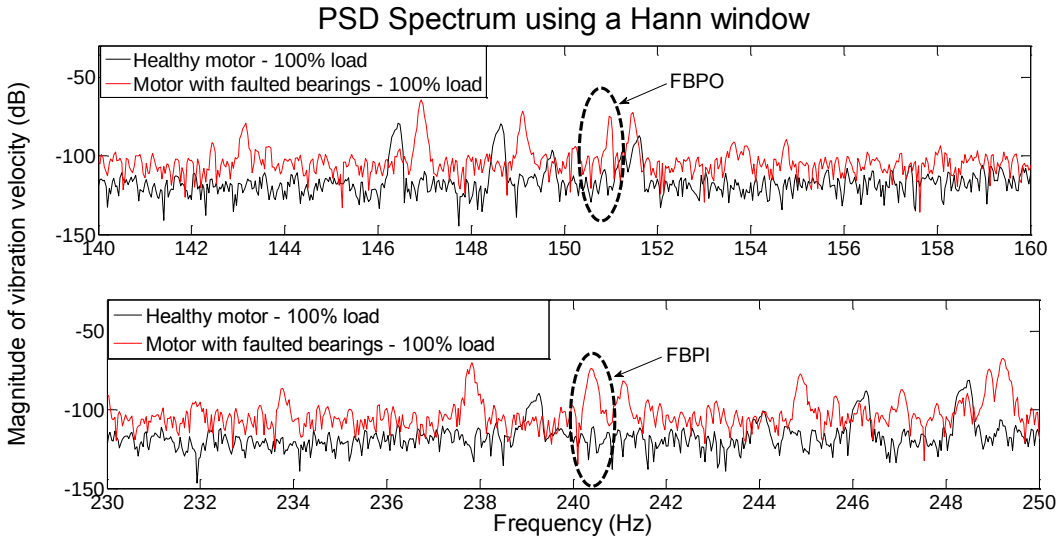

Figure 6-26: The vibration velocity spectrums for healthy motor and motor that contains one bearing with outer race fault and one bearing with inner race fault under 100% loading conditions

6.6.1 Impact of varying the load

The results presented above, showed that both outer and inner race fault components were prominent in the vibration spectrum compared to the current, therefore only the vibration will be considered from here on. The load was varied to explore the impact on the outer and inner race component on the vibration spectrum. The vibration velocity spectrum under varying load is shown in Figure 6-27. The location of the outer race fault component increases in frequency as the load is reduced from 100% through 50% to 0% load in Figure 6-27a. This is expected since these components are dependent on the rotor speed. The magnitude of the component reduces by $9.96\ dB$ as the load reduces from full to no load. The same phenomenon is experienced by the inner race fault component in Figure 6-27b, although the component

changes by 12.43 dB. The possible explain for this is that, under no load conditions, the decrease in temperature resulting from no load condition can alter the air-gap mechanically, which therefore reduces the air-gap dissymmetry and magnitude of the bearing fault components from full load condition [**90**] .

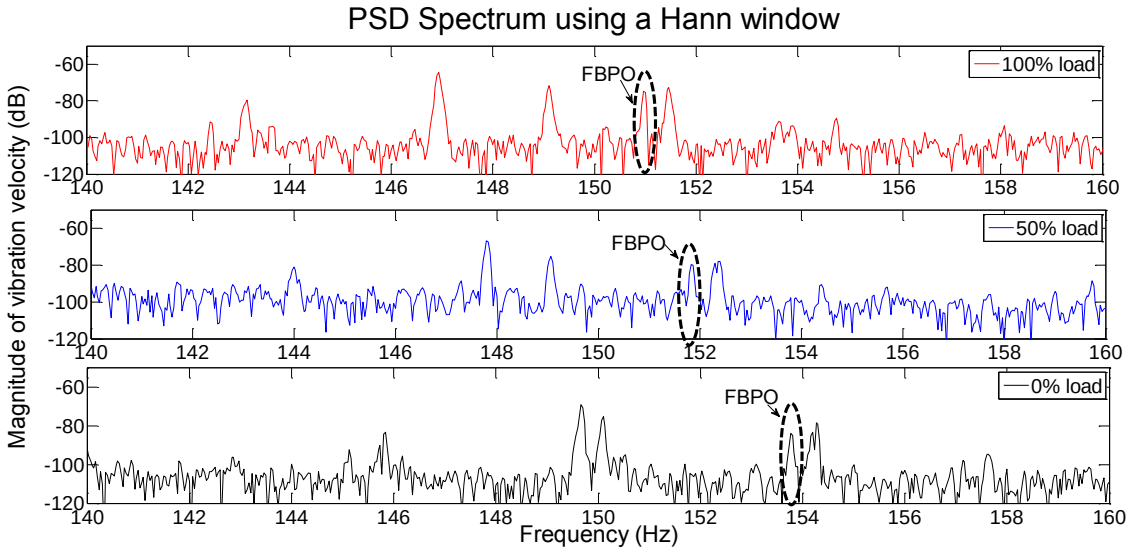

(a)

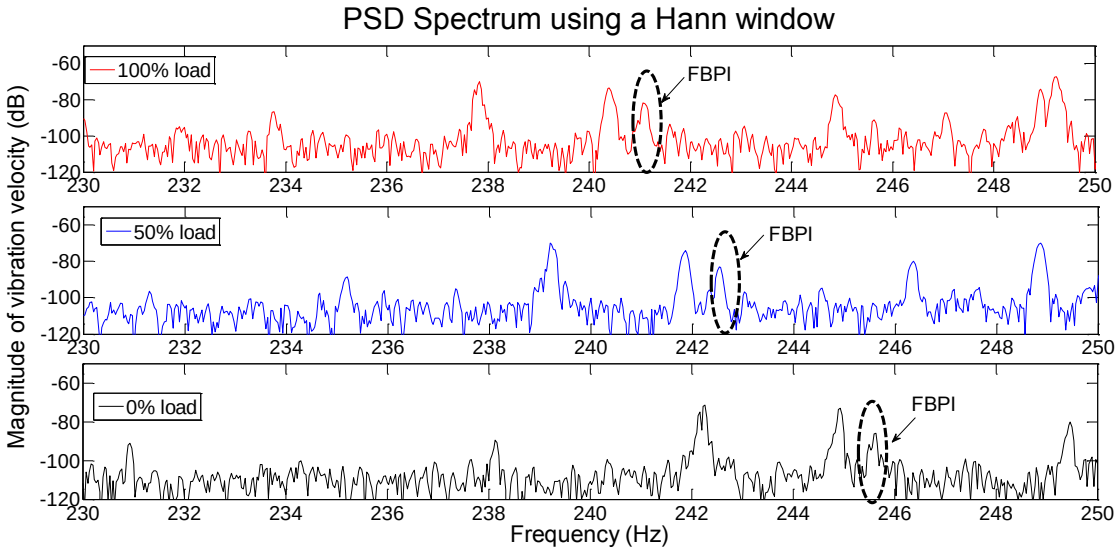

(b)

Figure 6-27: The vibration velocity spectrums for healthy motor and motor that contains one bearing with outer race fault and one bearing with inner race fault under different loading conditions a) Outer race b) Inner race

6.6.2 *The impact of the inverter*

The impact of the inverter on the detection of outer and inner race was considered, the results are available in Appendix B. The bearing fault components identified in the grid supplied motor were also evident in the vibration spectrums. The inverter has an insignificant effect on the detection of the inner and outer race components on the vibration spectrum; thus the results are similar to that of the grid connected motor. Varying the fundamental frequency only alters the frequency location due to dependency of the rotor speed.

6.6.3 *Summary of bearing faults*

In a grid supplied motor, under full load conditions the outer and inner race fault components were most prominent in the vibration analysis compared to current. The bearing fault components were only observed in the motor with faulted bearings. The fault components of the outer and inner race behaved in a similar manner. However, in both analyses the magnitude of the outer race component was more prominent than the inner race. When the load was decreased, the frequency location of the components increased with decrease in load as the fault frequencies are a function of the rotor speed. However, the magnitude of these components decreased as the load decreased. The results for the inverter-fed motor were synonymous to that of the grid connected motor. Figure 6-28 summarizes the bearing fault detection for a grid connected motor using vibration analysis. Since the components are only observed on the healthy motor.

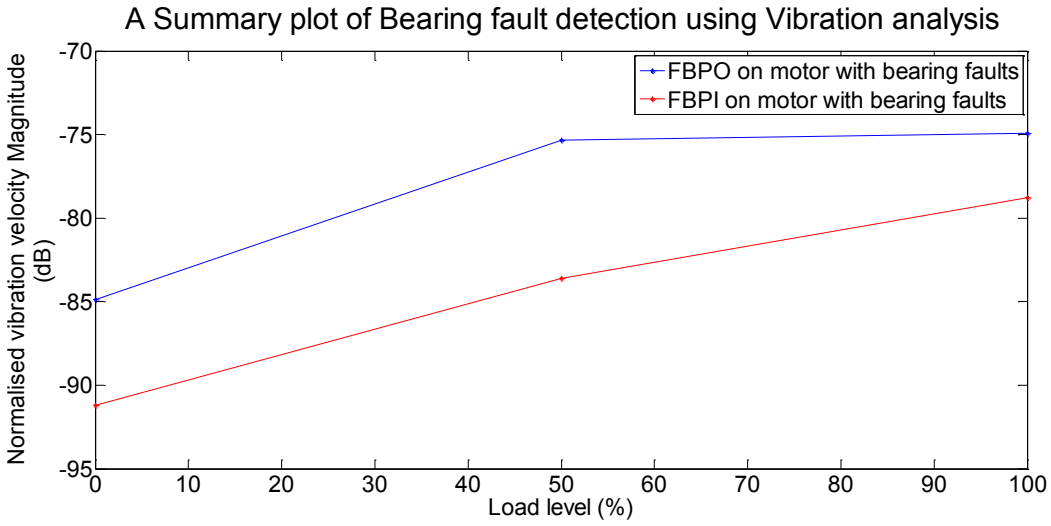

Figure 6-28: Summary of detecting bearing faults on a grid connected motor using vibration analysis

6.7 Detection of dynamic eccentricities

The motor with a bowed rotor described in section 5.6.4, was used to simulate dynamic eccentricities. The grid connected case is first considered with the objective to identify the components in the current and vibration spectrums that are only a function of dynamic eccentricity fault. The 100% loading condition of the healthy motor and motor with the bowed rotor were considered first. The current of phase A is used due the reasons previously discussed. Figure 6-29 shows current spectrums of both motors.

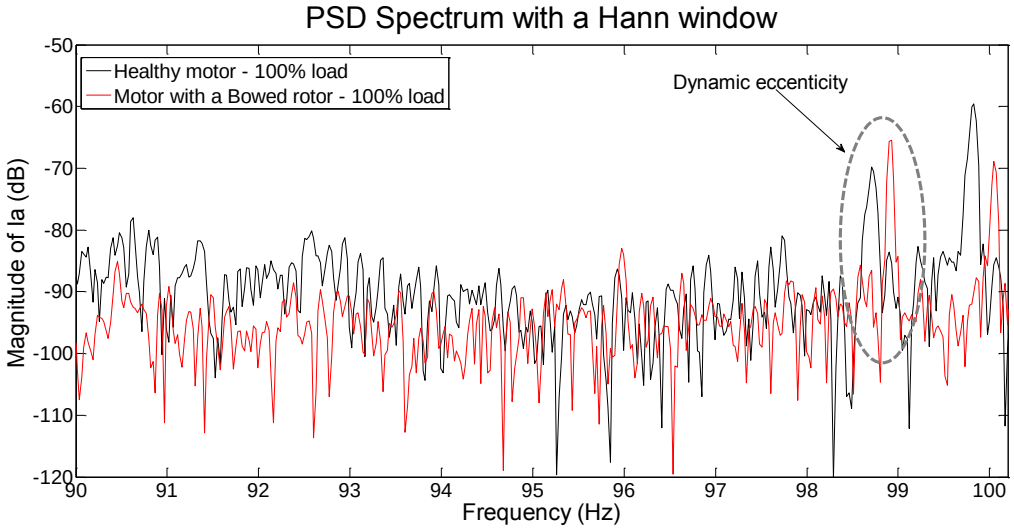

Figure 6-29: The current spectrums for healthy motor and motor has dynamic eccentricities at 100% loading conditions

The dynamic eccentricity component given by equation (4-8) appears in the current spectrum of the healthy motor and the motor with a bowed rotor. The component is revealed at $98.76Hz$ and $98.93\ Hz$ respectively for both motors where m is equal to 1. The magnitude of this component in the healthy motor and motor with the bowed rotor is $-70.44dB$ and $-65.46\ dB$ respectively, thus this component is increases by $4.98dB$.

Likewise, the vibration velocity spectrums of both motors are shown in Figure 6-30. The fault condition is indicated by an increase of twice line frequency harmonic and the dynamic eccentricity harmonic given by equation (4-9). The twice line frequency harmonics appear at $99Hz$ and $100Hz$ respectively for the healthy motor and motor with a bowed rotor. These harmonics have magnitudes of $-47.83dB$ and $-36.58dB$ respectively. Notice the drastic increase ($11.25dB$) of this component. The dynamic eccentricity harmonics appear at $148.7Hz$ and $148.9Hz$ respectively for the healthy motor and motor with a bowed rotor. The

magnitudes of these components is $-80.69dB$ and $-60.95\ dB$ respectively, thus this component increases by $19.74dB$.

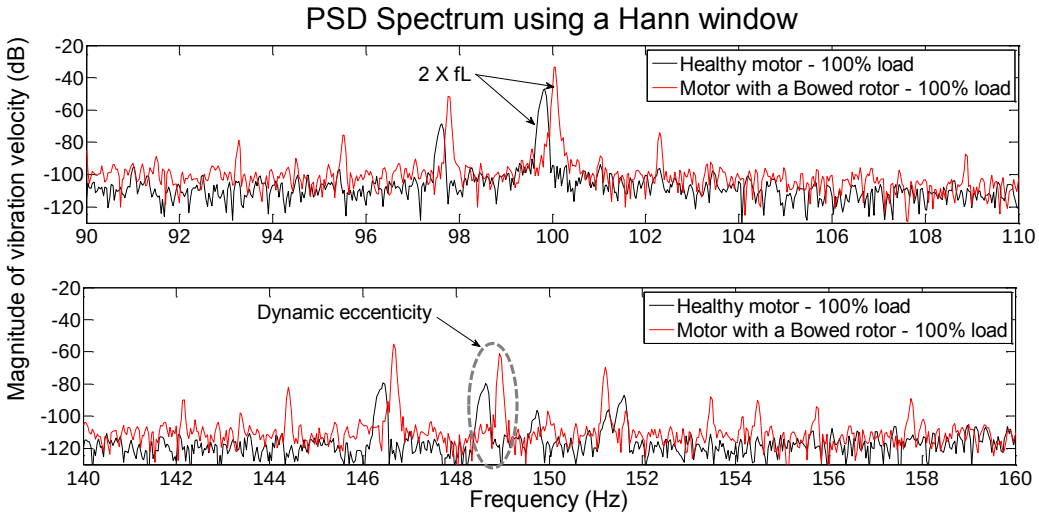

Figure 6-30: The vibration spectrums of healthy motor and a motor that has dynamic eccentricity at 100% loading conditions

6.7.1 Impact of varying the load

The results presented above showed that dynamic eccentricity is reflected more in vibration velocity spectrum compared to the current; therefore only the vibration will be considered from here on. The load was varied to explore the impact on the dynamic eccentricity component in the vibration spectrum. The vibration velocity spectrums under varying load are shown in Figure 6-31. The twice frequency harmonic in the vibration spectrum, caused by the magnetic attraction between stator and rotor, changes slightly by $0.46dB$ as the load is reduced from 100 through 50 to 0%. This is expected since the ampere-turns of the stator windings tend to balance one another, except for the excitation ampere-turns. The excitation ampere-turns created by the no load current establish the magnetic field in the motor. As the load is applied to the motor, both the stator and rotor currents increase together and balance one another, thus there is no significant change in the flux. This suggests that the magnetic forces are independent of the load current and are nearly the same at no load or full load [**90**]. As the load is reduced from full to no load, the frequency location of the dynamic eccentric increases in frequency due to change in the load, which is expected since the component is dependent on the rotor speed. The magnitude of the component decreases by $3.14\ dB$ as the load reduces from full to no load condition. This is again possibly due to the mechanical change of the air-gap attributed to the

load condition. Dynamic eccentricity fault component of the faulted motor (with the bowed rotor) is still more pronounced compared to the corresponding component in the healthy motor under no load conditions (see Appendix B)

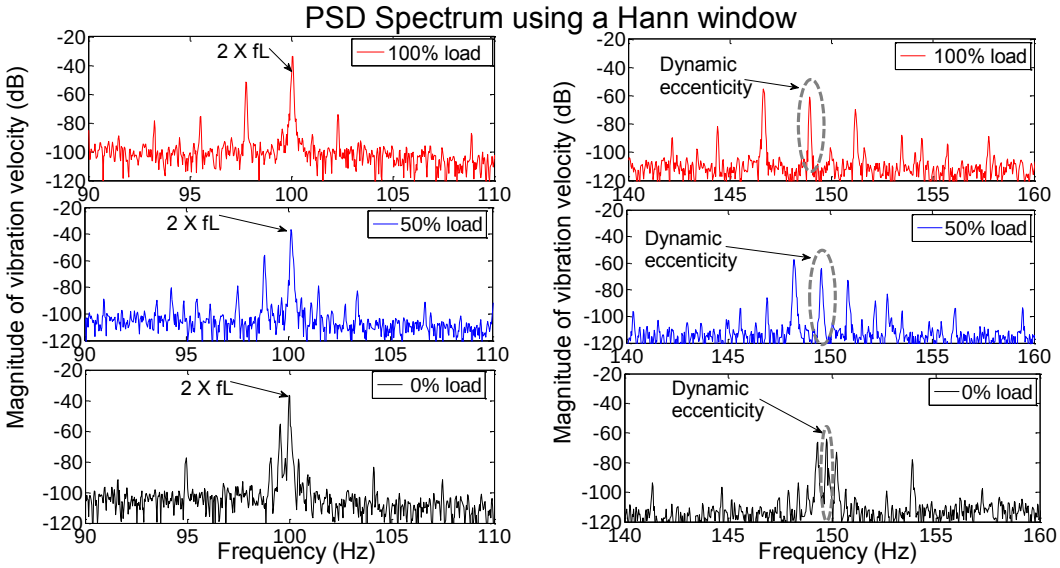

Figure 6-31: The vibration spectrums of healthy motor and a motor that has dynamic eccentricity under varying load conditions

6.7.2 The impact of the inverter

The impact of the inverter on the detection of the dynamic eccentric component was considered, the results of which are available in Appendix B. The increase of the twice line frequency and dynamic eccentricity component identified in the grid supplied motor was also evident in the vibration spectrums of the inverter-fed motor. The inverter has an insignificant effect on the detection of dynamic eccentricity on the vibration spectrum. Varying the fundamental frequency only alters the frequency location of dynamic eccentric (due to the dependency of the rotor speed) and the twice line frequency component (due to the dependency of the line frequency), and therefore the results are almost identical to that of the grid connected motor.

6.7.3 Summary of detecting dynamic eccentricities

In a grid supplied motor, under full load conditions the dynamic eccentricity component was most prominent in the vibration analysis compared to current. In the vibration, the twice frequency component also reflects a presence of the dynamic eccentricity. Varying the load did not affect the twice frequency component. However, the magnitude of the dynamic eccentricity was affected by the load due to the reasons expressed for the bearing fault in section 6.6.3. Figure 6-32 summarizes the dynamic eccentricity detection for a grid connected motor using

vibration analysis. The difference between the least extreme fault scenario (bowed rotor and 0% load) and the maximum loading condition of a healthy motor is approximately $3.3dB$ and $7.57dB$ respectively for the twice line frequency and the dynamic eccentricity component.

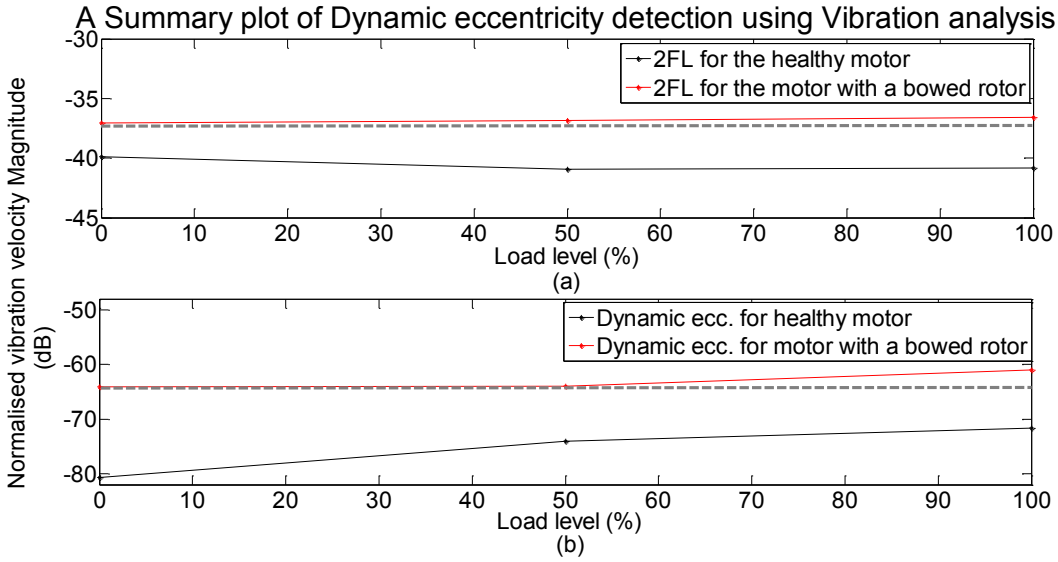

Figure 6-32: Summary of detecting dynamic eccentricity fault on a grid connected motor using vibration analysis

6.8 Concluding Remarks

The common faults experienced in induction motors were implemented under steady conditions. The frequency domain detection techniques of the strategy were applied on the stator current and vibration velocity signals to detect the faults. The resulting current and vibration spectrums were compared to establish where the fault signature was most prominent. Furthermore the impact of loading, varying fault (for the motor with an inter-turn fault), and impact of the inverter and varying the fundamental operating frequency of the inverter were explored.

The inter-turn fault signature was more prominent in the current spectrum compared to the vibration. The inter-turn fault component magnitude varied according to the load condition and fault severity, and frequency location only varied according to load. However, under the least extreme conditions (loading and fault) caution must be exercised. In an inverter-fed motor the fault harmonic components were not detected in the current spectrum. In such cases the PV and EPVA techniques complemented the detection.

The broken rotor bars' harmonics were detected in both the current and vibration spectrums. The fault harmonic magnitude and frequency location varied according to the load condition; at

light load conditions these harmonics were located closely to the fundamental frequency, which posed a challenge in the detection. In the vibration spectra, the fundamental also varied with load adding an additional variable, hence detecting the fault harmonics using current was preferred. The Hilbert technique improved the results by removing the fundamental. The fault harmonics were also detectable on the inverter-fed motor.

The bearing fault and dynamic eccentricities harmonics were more prominent in the vibration spectrum compared to the current. The outer race fault components were easier to detect compared to inner race components, in the case of the motor with the faulted bearings. The frequency location and magnitudes of these components were affected by the load. In the case of motor with a bowed rotor; the magnitude and frequency location of dynamic eccentricity component was affected by the load. The increase of the twice line frequency is also indicative of dynamic eccentricity, although it is independent of the load condition. The fault harmonics were also detectable on the inverter-fed motor.

The next chapter focuses in detecting these fault components detected under the steady state but under transient startup conditions.

7. RESULTS AND DISCUSSIONS OF DETECTING FAULTS UNDER TRANSIENT CONDITIONS: USING TIME-FREQUENCY DOMAIN SIGNAL PROCESSING TECHNIQUES

7.1 Introduction

In the previous chapter, the common faults associated with induction motors were implemented under different load conditions, power supply configurations and fault severities (only in the case of the inter-turn fault), but under steady state conditions. The electrical faults (i.e. inter-turn and broken rotor bars) were prominent in the current while the mechanical faults (faulted bearings and dynamic eccentricities) were prominent in the vibration. The startup transient regime is also an interesting phase of operation for the detection of these faults. This chapter presents the application of time-frequency fault detection techniques for the detection of faults during startup conditions. Each of the implemented fault conditions are compared against a healthy motor. most especially the fault harmonic components identified under steady state conditions, on a two dimensional time-frequency plot during transient startup for grid started (DOL) and inverter(soft) started motors.

7.2 Fault detection strategy

Similar to the steady state conditions, the transient signals were acquired using the methodology discussed in 5.8.2, all of which were sampled at frequency of $25.6kHz$ and $768k$ *Samples* were acquired. These signals were processed in *Matlab 2010* environment (see Appendix A). The drive was configured in scalar constant Volts/Hz with a linear ramp up profile. The fault detection strategy that was used is shown in Figure 7-1. The theoretical evolution representation of the frequencies contained in the analysed transient current and vibration (including the fault related) is generated as done by Pons-Llinares in [**62**]. Before the application of the DWT, the mother wavelet and number of decomposition levels is selected.

Daubechies-44 mother wavelet was selected, in this case due to the reasons expressed in section 3.8.1. As mentioned in section 3.8.1, the number of decomposition level needs to be established and the option of down sampling needs to be considered. Table 7-1 shows the different frequency bands of interest. The boundary effect of the wavelet decompositions is usually evident at the beginning and the end of the signal. To avoid the boundary effect influencing the signal integrity at the start and the end, the signals are extended to include 0.5s before motor start-up and 0.25s after startup as done in [**91**]. A two dimensional plot representing the time-frequency evolution of the harmonics present in the induction motor transient current and vibration velocity signals is generated. The characteristic evolution patterns in the time-frequency plane caused by the main fault related harmonics are identified. These are then displayed and stored. If these are not identified using DWT, then the WPD is applied for further analysis.

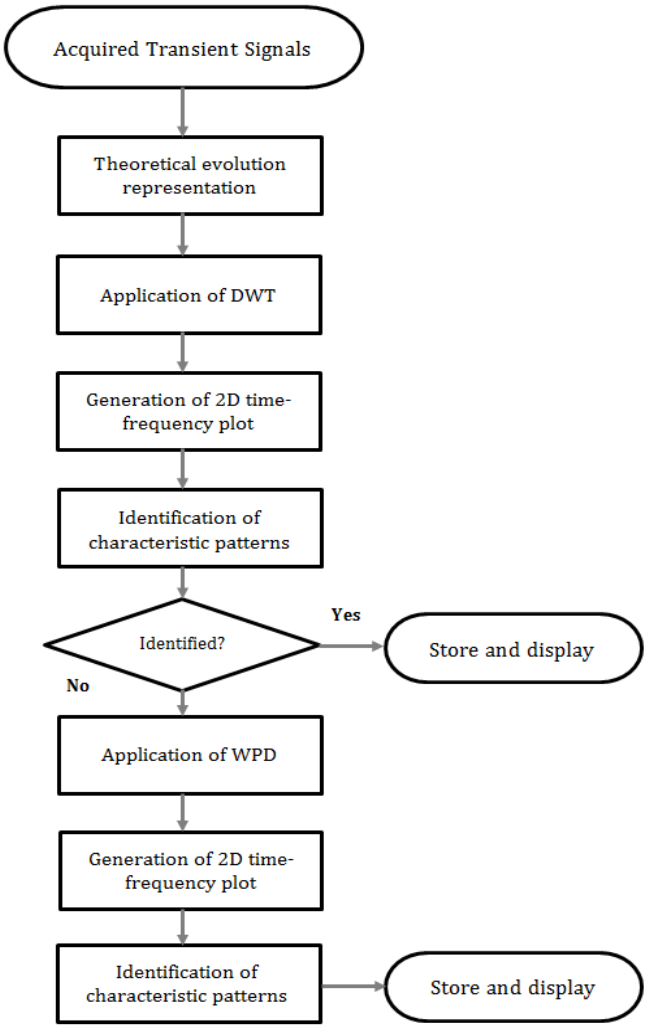

Figure 7-1: Fault detection strategy for transient conditions

Table 7-1: The twelve decomposition levels used

Level	Signals	Frequency Band Fs = 8533.4 Hz
D1	Detail Signals	2133.33 – 4266.67
D2		1066.67 – 2133.33
D3		533.33 – 1066.67
D4		266.67 – 533.33
D5		133.3 – 266.67
D6		66.66 – 133.33
D7		33.33 – 66.66
D8		16.66 – 33.33
D9		8.33 – 16.67
D10		4.17 – 8.33
D11		2.08 – 4.17
D12		1.04 – 2.08
D13		0.52 – 1.04
D14		0.26 - 0.52
D15		0.13 - 0.26

7.3 Detection of the Inter-turn fault

The results for detecting an inter-turn stator fault during start-up conditions for a motor with shorted turns are discussed in this section. Recall that in the steady-state analysis the inter-turn fault harmonic component was revealed at frequencies ranging from $196.2 - 199.1Hz$, depending on the load condition. The evolution (characteristic pattern) of this harmonic component and the other main harmonics are analysed during the startup conditions.

7.3.1 Direct on line startup

The theoretical evolution of this component anticipated during DOL startup based on equation (4-1) is shown in Figure 7-2. During startup, the slip varies from 1 to a value near 0.

This is expected since the difference between rotor speed and synchronous speed of the rotating field is reduced as expressed in section 2.2.2, when the motor startups. Notice that the dominant inter-turn fault frequency component, as detected in the steady state, moves from $150Hz$ to value close to $200Hz$, during startup conditions. Hence the component only evolves in the frequency band corresponding to *D5.* The start-up currents under full load conditions for a healthy motor and a motor with four shorted turns were considered. The characterestic evolution pattern is not observed in the band corresponding to *D5* on a 2D time-frequency when the DWT is applied, since *D5* represents a wide frequency band where the third and fifth harmonic are more dominant within this band throughout the startup; this tends to mask the evolution.

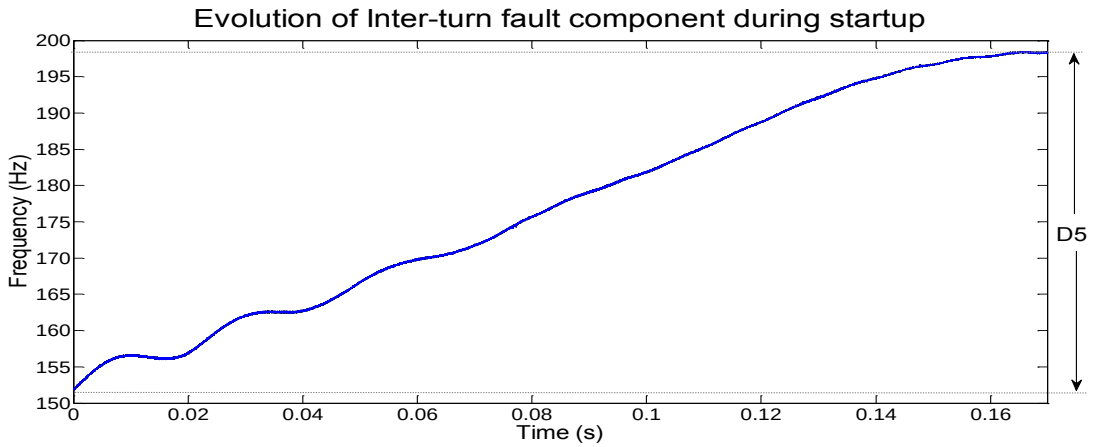

Figure 7-2: The characteristic movement of the inter-turn fault component during DOL startup

Using WPD, *D5* can be decomposed further to observe this evolution pattern, as discussed in section 3.8.1.5. The frequency bands of interest when using WPD of *D5* are shown in Table 7-2, the three bands are obtained. These bands all correspond to *depth 9* and narrower compared to *D5*; this allows the evolution of the fault component to be tracked as the motor starts up.

Table 7-2: The frequency band wavelet packets decomposition of level 5

Detail level	Frequency band
D5	183.33 -199.99 (depth 9, node 11)
	166.66 -183.33 (depth 9, node 10)
	149.99 -166.66 (depth 9, node 9)

The WPD 2D plots of the currents and the evolution of the fault component with associated nodes (bands) are shown in Figure 7-3. There is no noticeable difference between the healthy motor and faulted motor. The evolution of the fault component predicted in Figure 7-2 is not observed. The possible reason for not detecting this component is the short transient of the motor of less than $0.2s$ that results in the electromagnetic transient masking the fault component. This short transient period is typical of induction motors with low paramters such as supply voltage, machine size and driven inertia. The least amount of time required to detect the fault movement is $0.5s$, which was discussed in [**91**], [**92**]. This time allows the electromagnetic transient to settle before the movement of the fault component takes place.

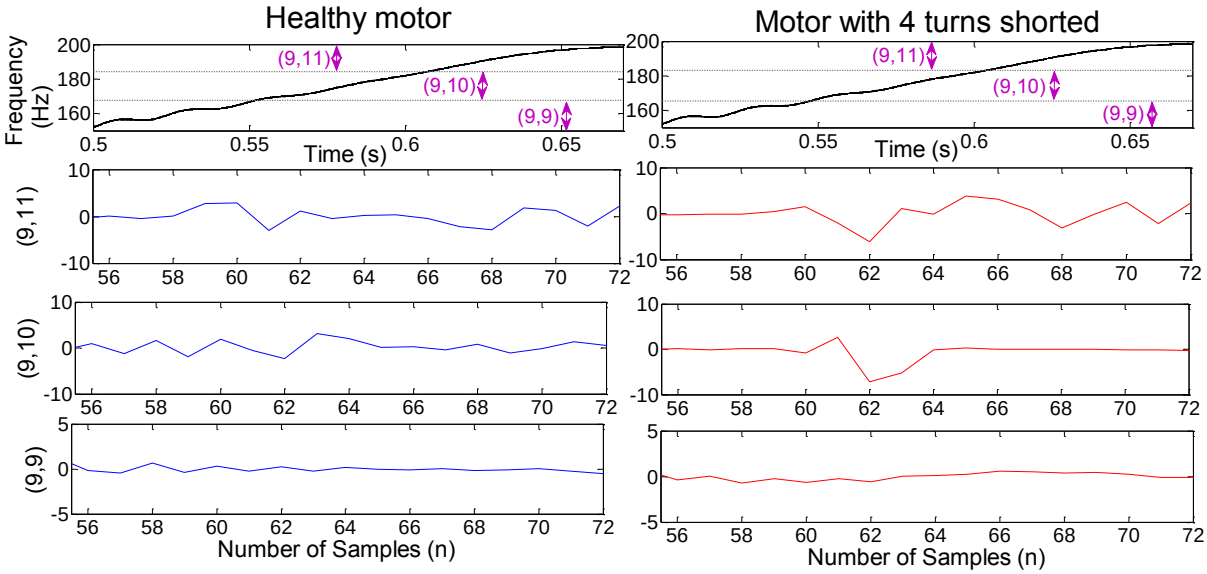

Figure 7-3: A wavelet packet decomposition of the current for a DOL started healthy motor and motor with 4 turns shorted

7.3.2 Soft starting using the inverter

In the previous section, results showed that the short transient period prevents the evolution of fault component to be observed for direct on lines startup of the motors. In this section, the startup using the inverter is considered. The theoretical evolution of the frequency components are shown in Figure 7-4. Notice that it is different from the DOL started motor since the fundamental supply frequency of the inverter is also varying with time. Since the inverter drive was configured in scalar constant Volts/Hz control with a linear ramp up profile, the fundamental frequency component is therefore assumed to vary in a linear manner. The slip remains constant during the startup at a value close to $0Hz$. This is to be expected since in

variable frequency operation, the operating speeds of the motor (i.e. $n_1 \cdots n_8$) as it startups is close to the corresponding synchronous speed as expressed by P.C Sen in [**7**]. In this method of speed control, the operating slip is low. In the stator current, the WHs and third harmonic (due to the supply voltage) appear regardless of the machine condition this was explained in section 4.2.1. The most relevant orders anticipated during the transient are: the first (the fundamental component); and fifth order harmonics. The frequency of the n order is proportional to the fundamental supply frequency as discussed in section 4.2.1. Notice now the fault frequency varies from 0 to $200Hz$, since the fundamental is also varying.

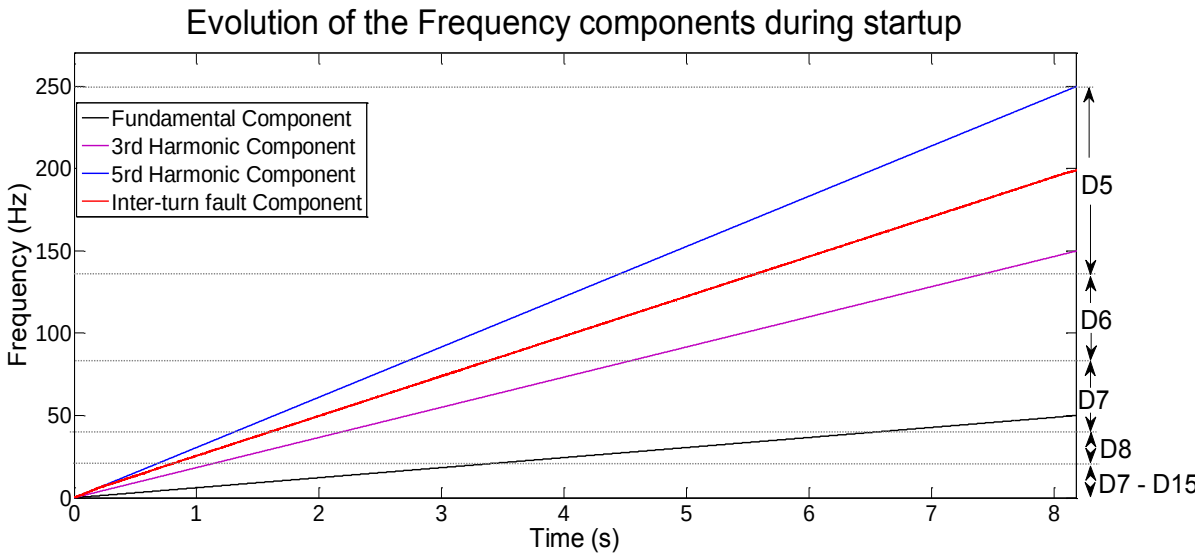

Figure 7-4: The characteristic movement of the inter-turn fault component during soft starting

Similar to the DOL started motor, the start-up currents under full load conditions for a healthy motor and a motor with 4 turns shorted were considered. In Figure 7-5, the 2D plots of the DWT of the currents of the two motors are shown. At the beginning of the startup, the evolution of the fundamental is dominant between *D11* and *D7* at times $t < 6s$ since the magnitudes of the other harmonic components are low with respect to the fundamental, thus the evolution of the other harmonics are not represented. Notice that in the absence of the fundamental component for times $t > 6s$ at *D5 and D6*, the magnitude increases. However, the increase in magnitude, especially in *D5*, is not only due to the evolution fault harmonic but also the 3rd and 5th harmonics existing in this level which can influence the increase magnitude.

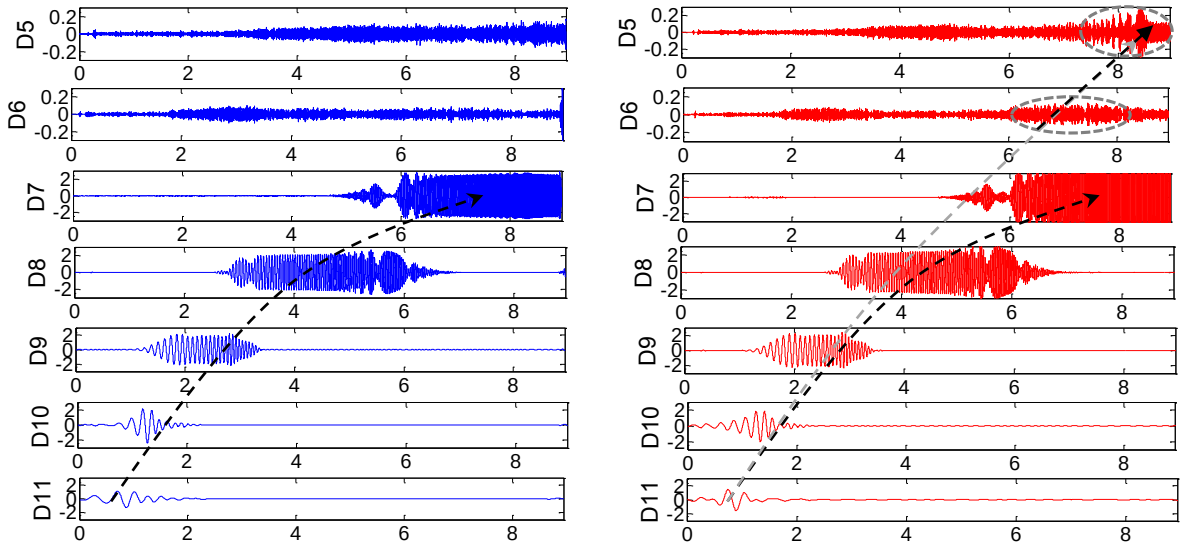

Figure 7-5: A wavelet decomposition of the current for soft started; healthy motor and motor with 4 turns shorted

These components needed to be isolated from the fault component by decomposing detail *D5* using WPD. Figure 7-6 shows the WPD 2D plot of the current. Notice at *node 9 and 11* when samples number $n > 150$ towards the end of the transient, the magnitude increases on the motor with 4 shorted turns. This is expected since at these nodes, the 3rd and 5th harmonics are eliminated, hence the increase of the magnitude is due to the inter-turn component evolving in those nodes.

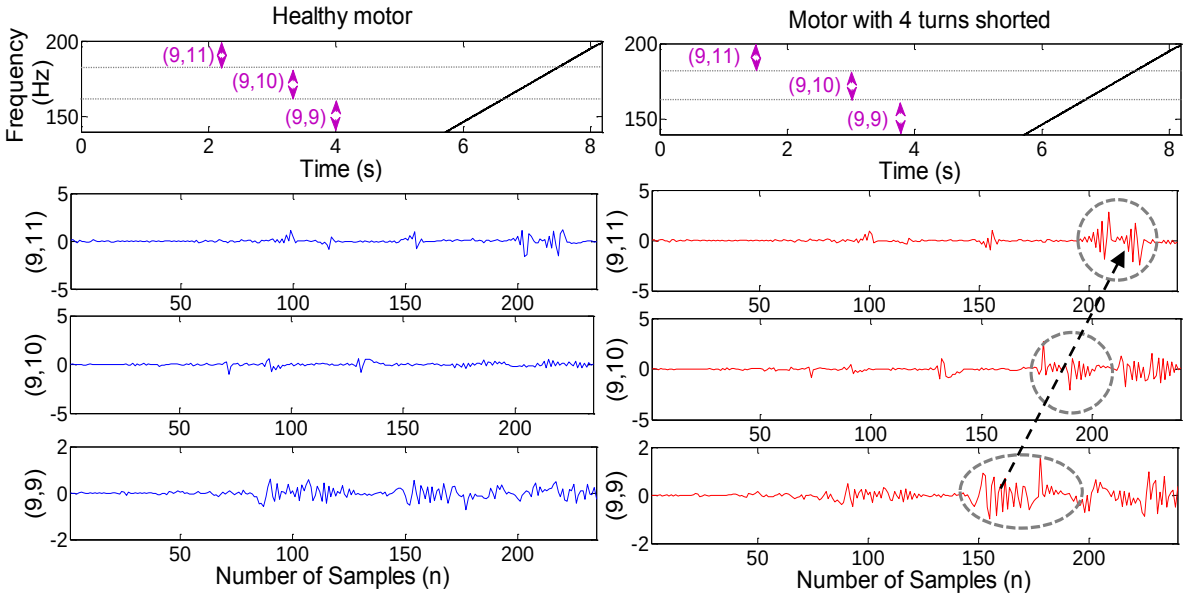

Figure 7-6: A wavelet packets decomposition of the current for soft started; healthy motor and motor with 4 turns shorted

7.3.3 Summary of inter-turn fault detection

A summary of the main findings for the preceding sections will now be presented. The ability of detecting the evolution of an inter-turn fault component during startup conditions was explored. For a DOL started motor, the application of a DWT does not decompose the frequency band of interest (*D5)*, sufficiently to observe the evolution of the fault component on the 2D plot whereas WPD yields more bands of a narrower width since the detail spaces are decomposed further as discussed in section 3.8.1.5. However, the startup transient is too short (less than $0.2s$) to observe the evolution. For a soft started motor, the fundamental and WHs components are also varying and the startup period is much longer. Applying the DWT does not provide a clear distinction of the fault component from the other components on the 2D plots; however the WPD allows the evolution of the fault component to be isolated from the other harmonic components; thus yielding more accurate and reliable results on the 2D plot.

7.4 Detection of the broken rotor bar fault

The results of detecting the left sideband harmonic (LSH) component during start-up conditions for the motor with three broken rotor bars are discussed in this section. In the steady-state analysis; the LSH was revealed at frequencies ranging from $47.29 - 49.51Hz$. The evolution (characteristic pattern) of this component is analysed during the startup conditions.

7.4.1 Direct on line startup

In Figure 7-7, the slip and theoretical evolution of the LSH component is shown. The frequency of the LSH component varies; at the beginning it is equal to the fundamental, $50Hz$ then decreases to $0Hz$ and finally moves to the steady state frequency value. This is similar to the evolution pattern obtained in [**74**] where the period was four times longer since a $1.1kW$ induction motor was used whereas, in this case a$0.25kW$ induction motor is used.

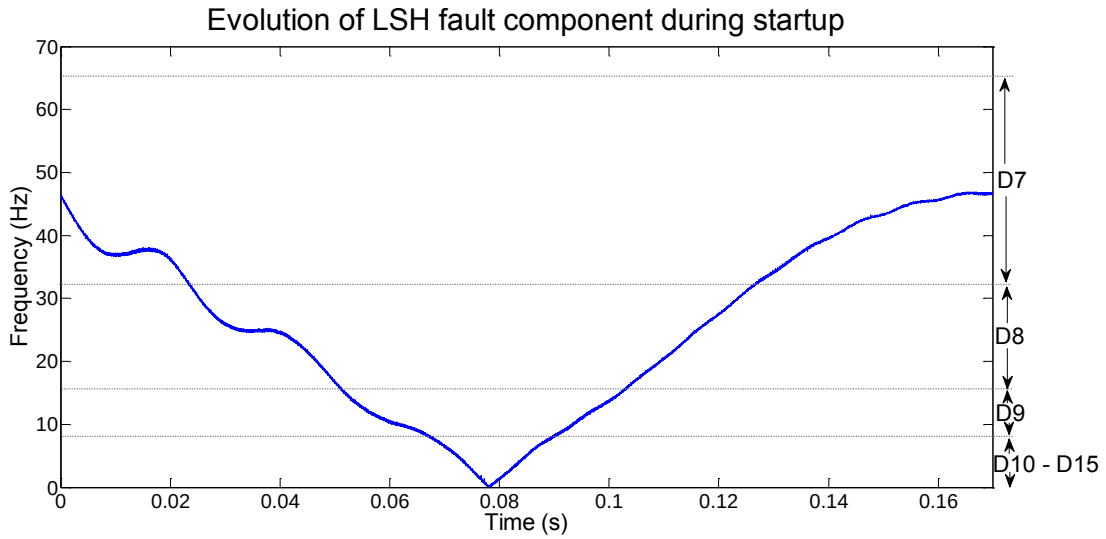

Figure 7-7: The characteristic movement of the slip and LSH component during DOL startup

The start-up currents under full load conditions for a healthy motor and a motor with 3 broken rotor bars were considered. The currents were decomposed using DWT, the 2D time-frequency plot of the current decompositions of details, *D7* to *D9* are shown in Figure 7-8. Again the characteristic evolution is not observed due to the short transient period as expressed in section 7.3.1.

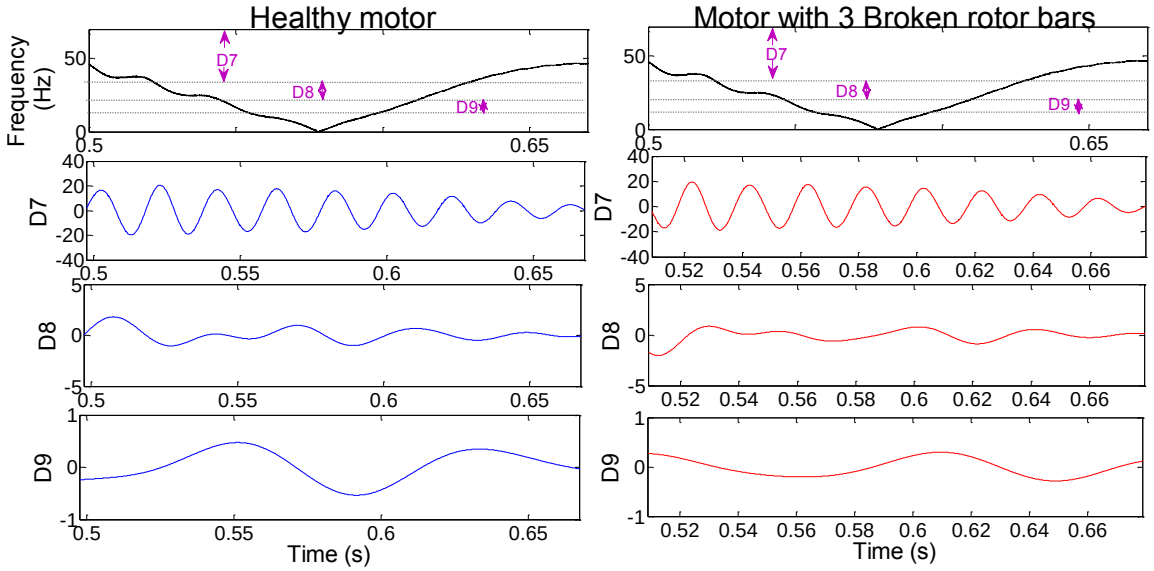

Figure 7-8: A wavelet decomposition of the current for a DOL started healthy motor and motor with 3 broken rotor bars

7.4.2 Soft starting using the inverter

In Figure 7-9, the evolution of the fundamental frequency and LSH frequency during startup is shown. Notice that now the frequency of the LSH component varies from $0Hz$ at the beginning to $50Hz$ at the end of startup. This component varies closely with respect to the fundamental component, which can mask the evolution of the LSH. This is expected since this component is closely situated to the fundamental component as illustrated in section 6.5. The Hilbert transform can remove the fundamental. The Hilbert was applied before the wavelet decomposition.

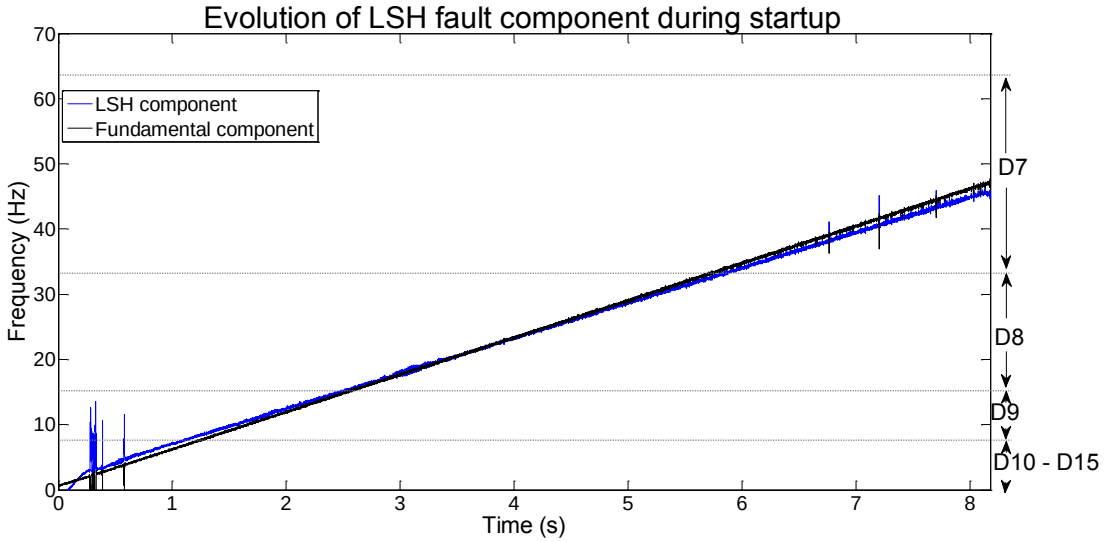

Figure 7-9: The characteristic movement of the fundamental and LSH component during a soft startup

In Figure 7-10, the evolution of the fault component in the absence of the fundamental is shown. Elimination of the fundamental component results in the fault component $2sf_1$ as illustrated in section 6.5.2. Initially, the frequency of the fault component varies from approximately $1.5Hz$, to a value close to zero at $3.5s$ where it increases to approximately $1.5Hz$.

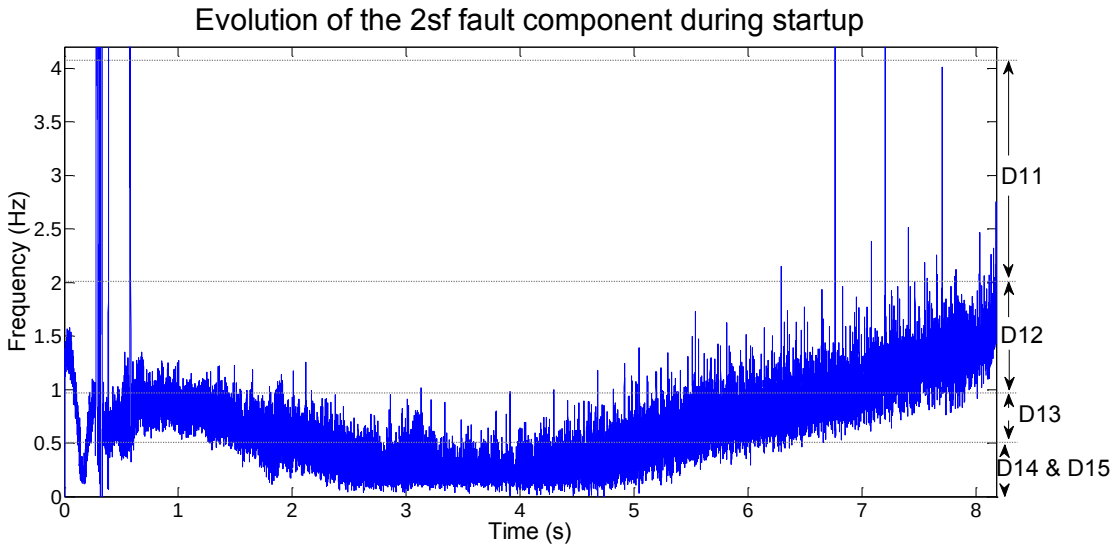

Figure 7-10: The characteristic movement of the LSH component during a soft startup

The DWT 2D plots of the current decompositions for details, *D12* to *D15* are shown in Figure 7-11. Although the fundamental component is absent, the evolution pattern of the fault is not represented at times $t < 4s$, since the influence of the other relevant components mask the fault component. However, during times $t > 4s$ at *D12* and *D13*, the magnitude increases due to the evolution of the fault component. The DWT decomposes the details sufficiently to observe the evolution pattern; hence there is no need to use WPD.

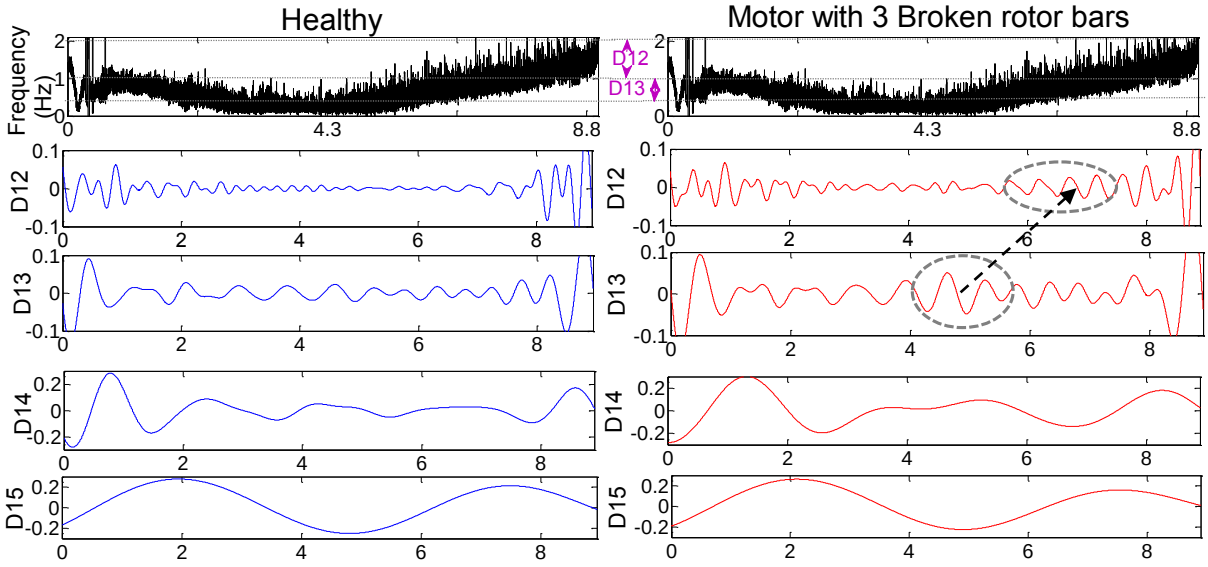

Figure 7-11: A wavelet decomposition of the Hilbert of the current for an inverter started healthy motor and motor with 3 broken rotor bars

7.4.3 Summary of broken rotor bar detection

The application of a DWT decomposes the frequency bands of interest sufficiently to observe the evolution pattern for a DOL started motor; however the transient period again is too short to observe the evolution as expressed in section 7.3.1 For the soft started motor, the fault component (LSH) varies closely with the fundamental, hence the Hilbert transform is applied to remove the fundamental component prior to the application of the DWT. The evolution of the fault component is only evident after period of 4s.

7.5 Detection of bearing faults

The detection of the outer and inner bearing fault harmonics during startup conditions will be discussed in this section. Recall that in the steady-state analysis the outer and inner race fault components were revealed at frequencies ranging from $151 - 153.8Hz$ and $241.1 - 245.7Hz$ respectively. The evolution (characteristic pattern) of these components are analysed during the startup conditions.

7.5.1 Direct on line startup

In Figure 7-12, the evolution of the rotational frequency, outer and inner race frequencies are shown. The frequency of these fault components varies from $0Hz$ to their respective values under steady state. This expected since the inner and outer race fault components are modulated by the shaft speed as discussed in section 4.4.3.

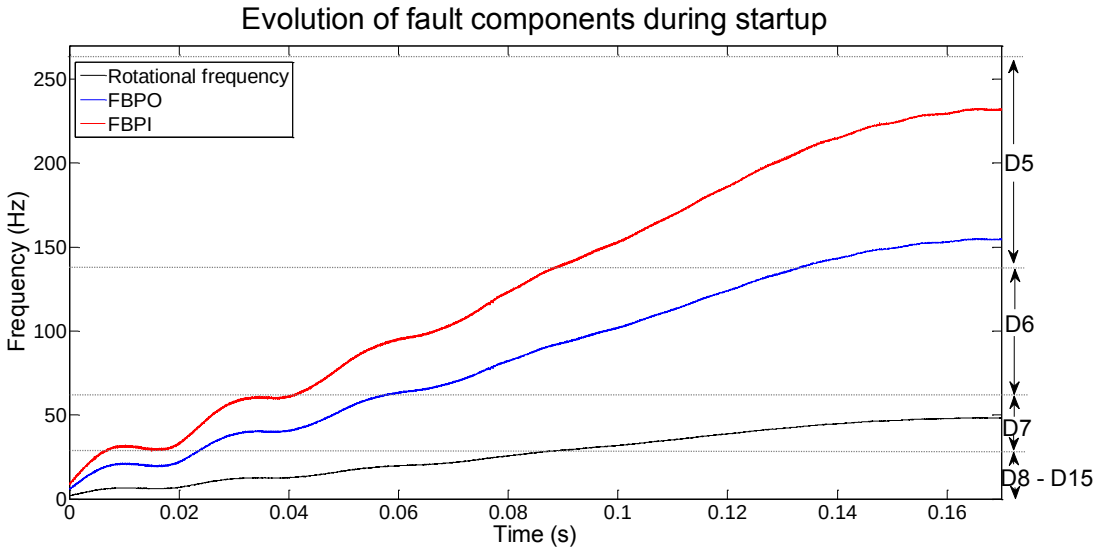

Figure 7-12: The evolution of the rotational frequency, outer and inner race fault components during startup

The DWT 2D plots of the vibration decompositions of details, *D5* and *D6* are shown in Figure 7-13. As expected at *D5,* at times $t > 0.6s$ the magnitude increases for the motor with faulted bearings due to the evolution of the outer and inner race fault components.

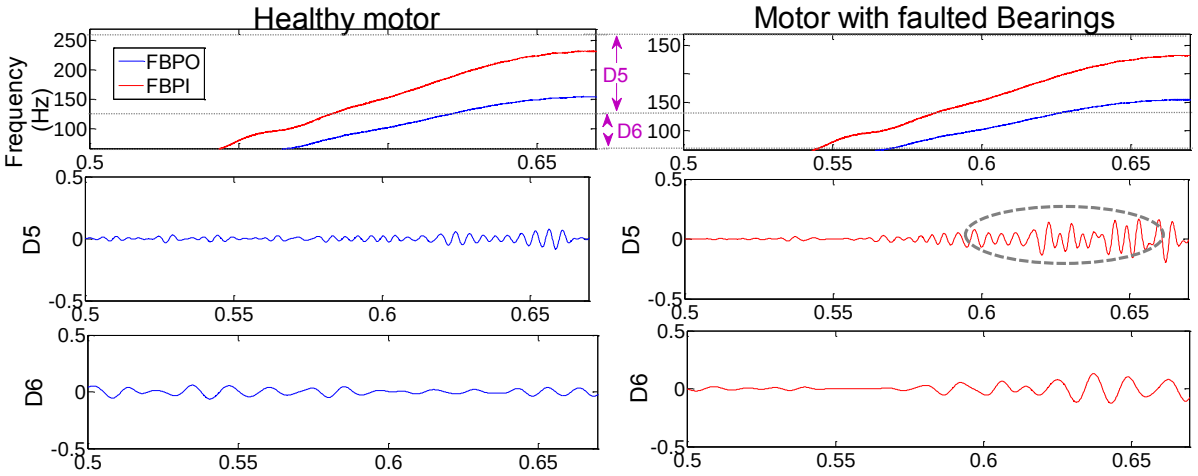

Figure 7-13: A wavelet decomposition of the vibration velocity for a grid started healthy motor and motor with faulted bearings

These components needed to be isolated from each other to distinguish the evolution patterns, by decomposing the detail further using WPD. The relevant frequency bands of *D5* and *D6* after further decomposition are shown in Table 7-3.

Table 7-3: The frequency band wavelet packets decomposition of level 5 and 6

Detail level	Frequency band (Hz)
D5	233.33 - 249.99 (depth 9, node 14)
	216.66 – 233.33 (depth 9, node 13)
	199.99 – 216.66 (depth 9, node 12)
	149.99 – 166.66 (depth 9, node 9)
	133.33 - 149.99 (depth 9, node 8)

D6	116.67 - 133.33 (depth 9, node 7)
	100.01 - 116.67 (depth 9, node 6)

The WPD 2D plots of the vibration velocities of both motors are shown in Figure 7-14. To extract the evolution of the outer race, *nodes 7* to *9* were considered. Observe the increase in the magnitude of the vibration for the motor with faulted bearings as the component evolves through *node 7 to 8* in Figure 7-14a). For the inner race evolution, *nodes 12* to *14* were considered. The increase of the magnitude for the motor with faulted bearings as the component evolves through *node 12 to 14* is shown in Figure 7-14b).

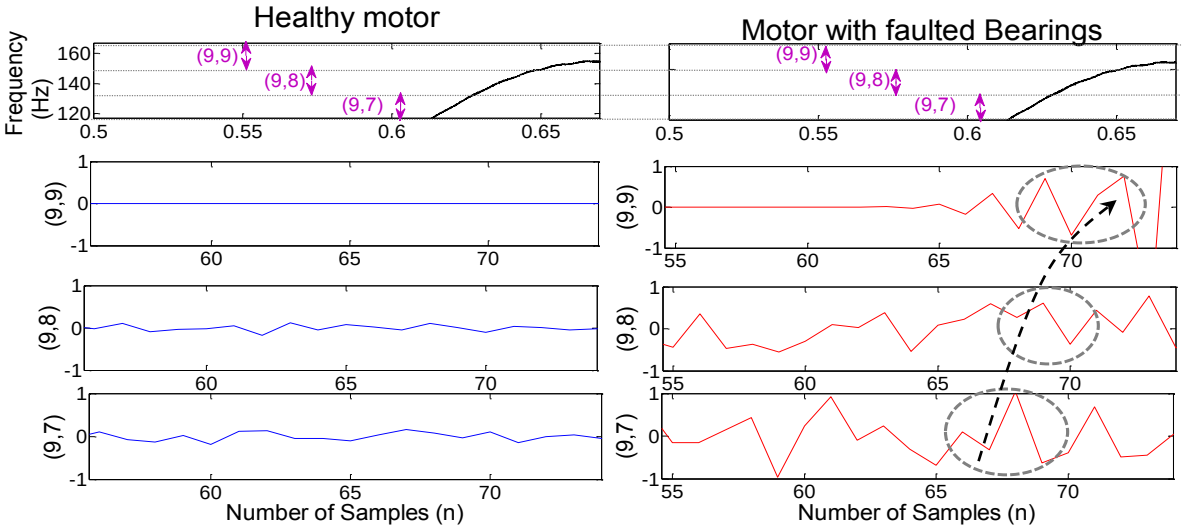

(a)

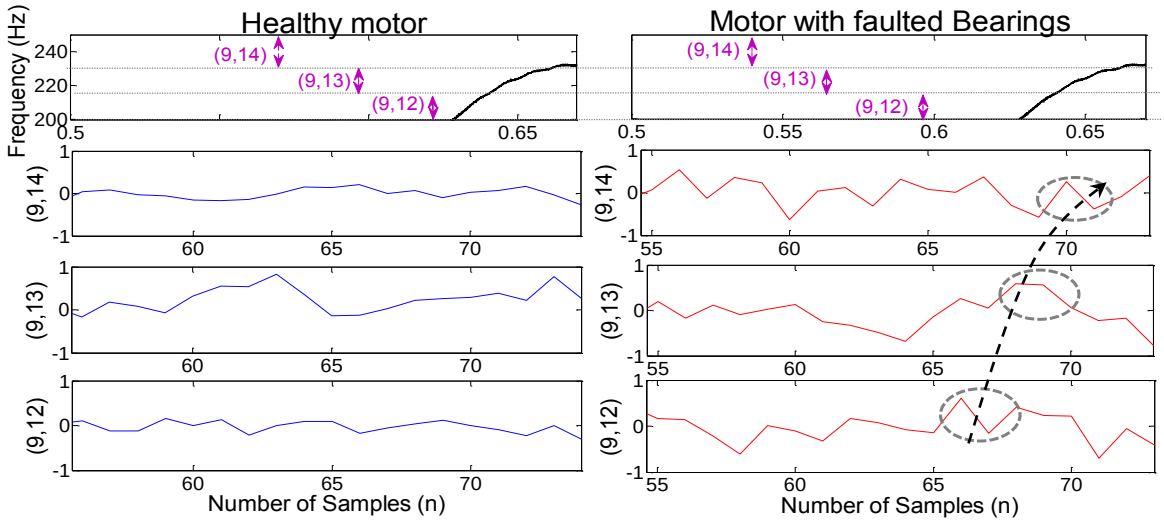

(b)

Figure 7-14: A WPD of the vibration velocity for a DOL started healthy motor and motor with faulted bearings a) Outer race b) inner race

7.5.2 *Soft starting using the inverter*

The theoretical evolution of the rotational frequency, twice line fundamental frequency outer and inner race frequencies are shown in Figure 7-15. The twice line frequency harmonic is caused by the unbalance magnetic attraction between the rotor and the stator attributed to a bearing fault, and is proportional to fundamental frequency.

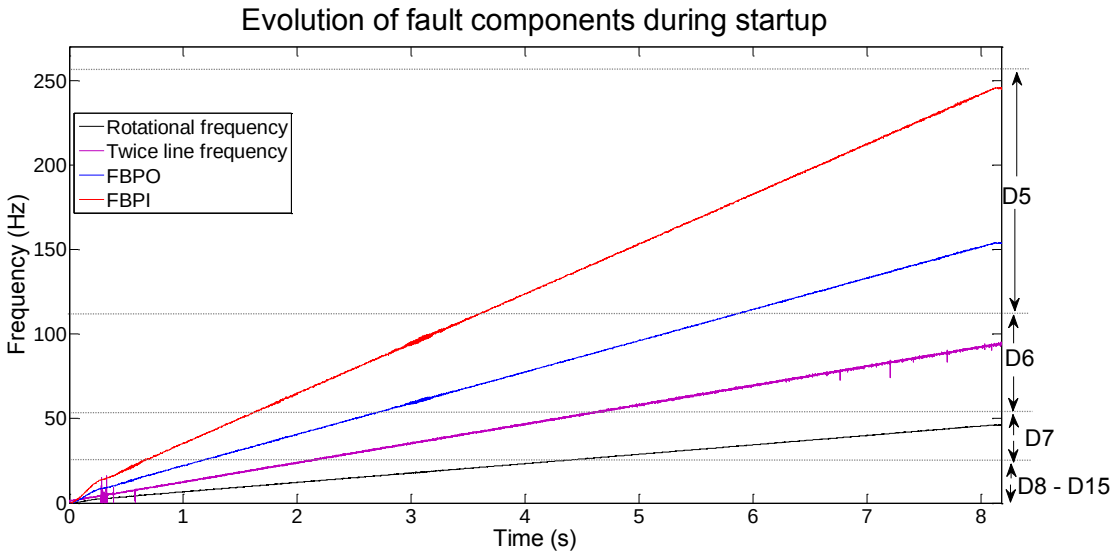

Figure 7-15: The evolution of the rotational frequency, twice line frequency outer and inner race fault components during startup

The vibration velocities were decomposed using DWT; the 2D plots of details, *D9* to *D7* are shown in Figure 7-16. At the beginning of the startup, the evolution of the rotational frequency component is dominant between *D9* and *D7*. At *D6,* at times $t > 4s$ the magnitude increases for the motor with faulted bearings, which is due to the evolution of the twice line frequency component and the outer and inner race components. As expected at *D5,* at times $t > 6s$ the magnitude increases for the motor with faulted bearings is due to the evolution of the outer and inner race fault components.

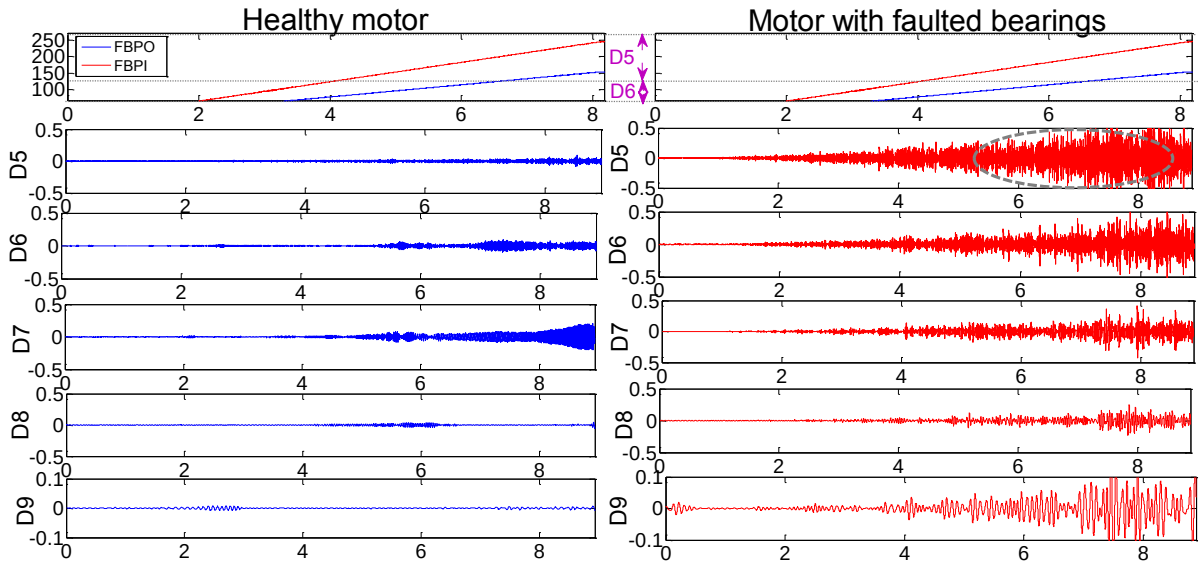

Figure 7-16: DWT 2D plots of the vibration velocity for an inverter started healthy motor and motor with faulted bearings

Similar to the grid started case; these components were separated from each other by decomposing the detail further using WPD. The *nodes 7* to *9* were considered to observe the evolution of the outer race. The WPD 2D plots of the vibration velocities of both motors are shown in Figure 7-17. The magnitude of the vibration increases for the motor with faulted bearings as the outer race component evolves through *node 7 to 9* as shown in Figure 7-17a). Similarly, the magnitude of the vibration increases as the inner race component evolves through *node 12 to 14* as illustrated in Figure 7-17b).

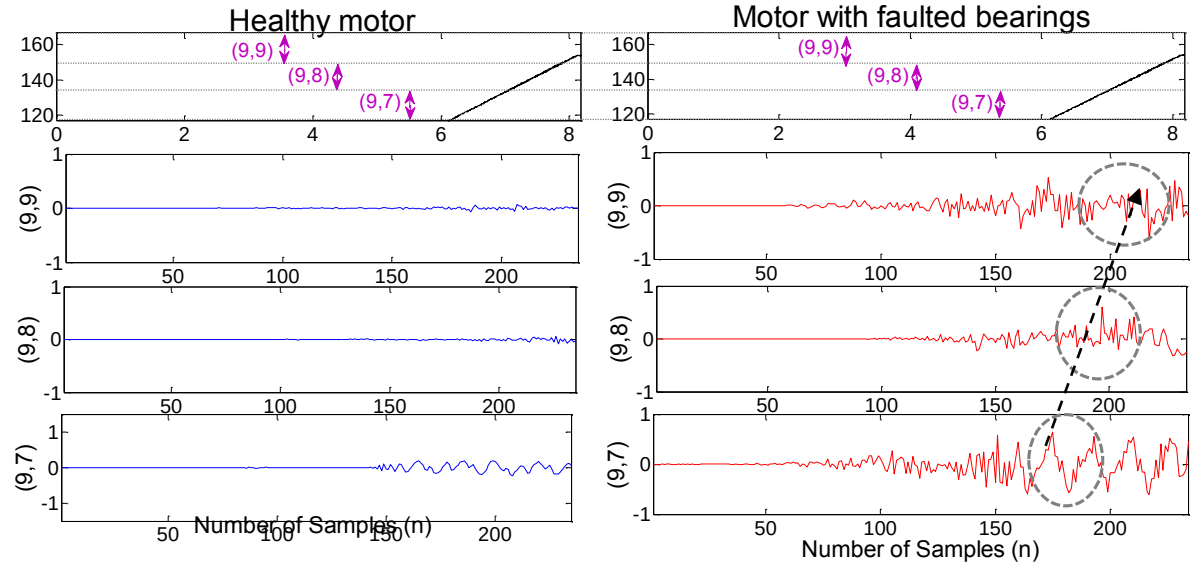

(a)

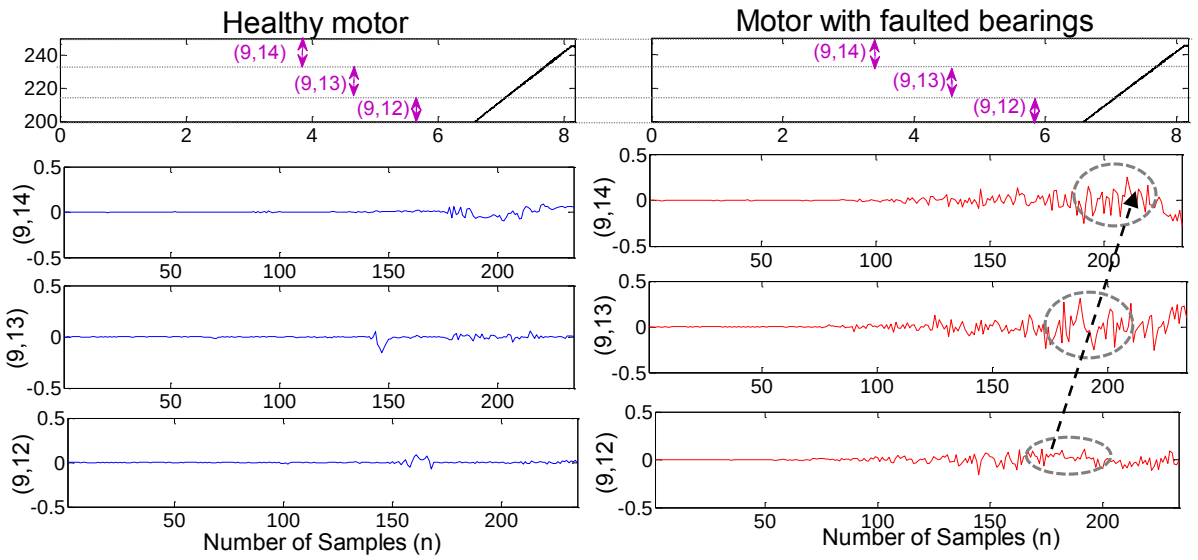

(b)

Figure 7-17: A WPD plot of the vibration velocity for a inverter started healthy motor and motor with faulted bearings a) Outer race b) inner race

7.5.3 Summary of bearing fault detection

For a DOL started motor, the fundamental (rotational) frequency component is also varying hence it dominates at the beginning. The application of a DWT does not decompose the frequency bands of interest sufficiently to differentiate the evolutions of the outer and inner race components on the 2D plot, whereas WPD decomposes the detail further. However, the evolution pattern of the inner race is less obvious compared to the outer race fault component since it is more difficult to detect as discussed earlier in section 6.6. Similarly for soft-started motor, the application of the WPD yields better results on the 2D plot compared to the application of DWT. The evolution patterns are clearer on the soft started motor using an inverter compared to the DOL started motor since the startup time is longer.

7.6 Detection of dynamic eccentricities

The results of detecting the dynamic eccentricity harmonic component during start-up conditions for a motor with a bowed rotor are discussed in this section. In the steady-state analysis, the dynamic harmonic component was revealed at frequencies ranging from $148.9 - 149.7Hz$. Although, the rise in the two line frequency component is also used for detecting dynamic eccentricities, only the evolution of the dynamic eccentricity component will be

focused on. The evolution (characteristic pattern) of this component is analysed during the startup conditions.

7.6.1 Direct on line startup

In Figure 7-18, the evolutions of the rotational frequency and dynamic eccentricity frequency are shown. The rotational frequency evolves from $0Hz$ to its respective frequency value at steady state, while the dynamic eccentricity frequency varies from $100Hz$ to its respective frequency value under steady state.

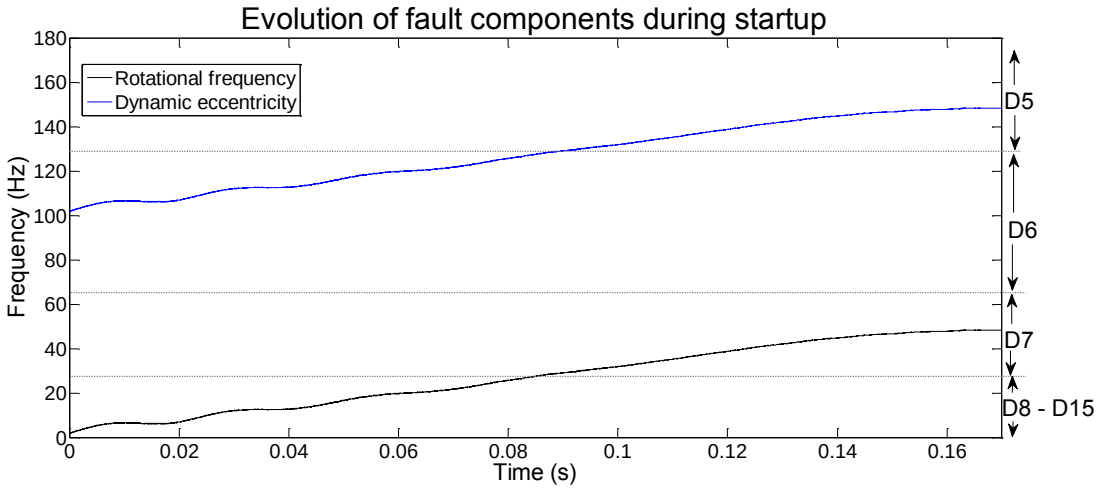

Figure 7-18: The evolution of the rotational frequency and dynamic eccentricity components during startup

The start-up vibration velocity under full load conditions for a healthy motor and a motor with faulted bearings were considered. The vibration velocities were decomposed using DWT, the 2D plot of the vibration decompositions of details, *D6* to *D5* are shown in Figure 7-19.

Notice that at *D6* the magnitude increases for the motor with a bowed rotor, which is due to the increase of the twice line frequency component that is also indicative of an eccentricity, rises in this band; the reasons of the rise are expressed in section 4.4.4.This has an influence on the evolution pattern of the dynamic eccentricity component. As expected at *D5,* the magnitude increases for the motor with the bowed rotor due to the evolution of the dynamic eccentricity component. Similarly, these components needed to be isolated from each other to observe the evolution of the dynamic eccentricity component by decomposing details; *D5* and *D6* further using WPD. The relevant frequency bands of *D5* and *D6* are shown in Table 7-3.

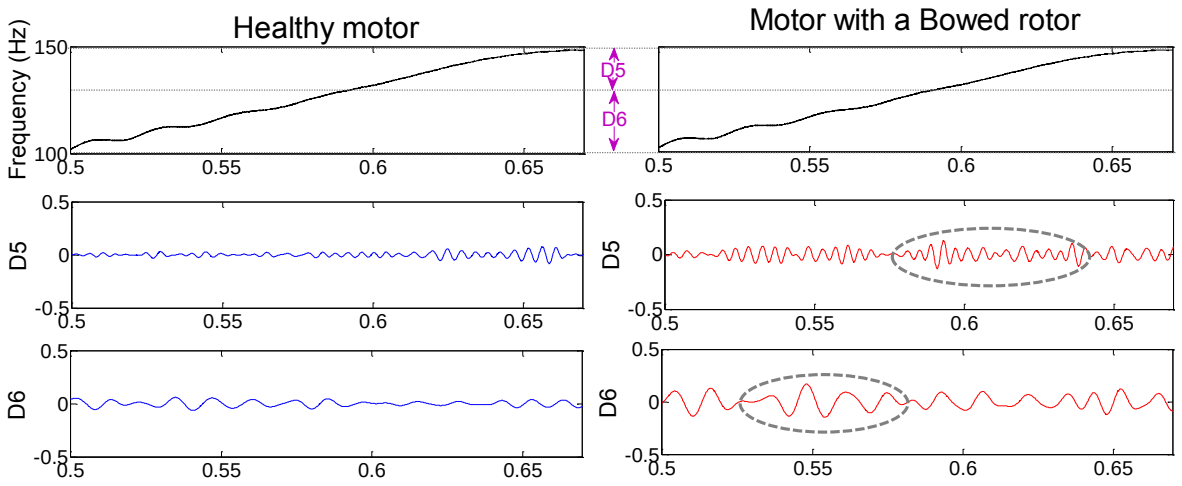

Figure 7-19: A DWT 2D plot of the vibration velocity for a grid started healthy motor and motor with bowed rotor

To observe the evolution of the dynamic eccentricity component, *nodes 6* to *8* were considered. The WPD 2D plots of the vibration velocities of both motors are shown in Figure 7-20. Observe the increase of the magnitude of the vibration for the motor with the bowed rotor as the component evolves through *node 6 to 8.*

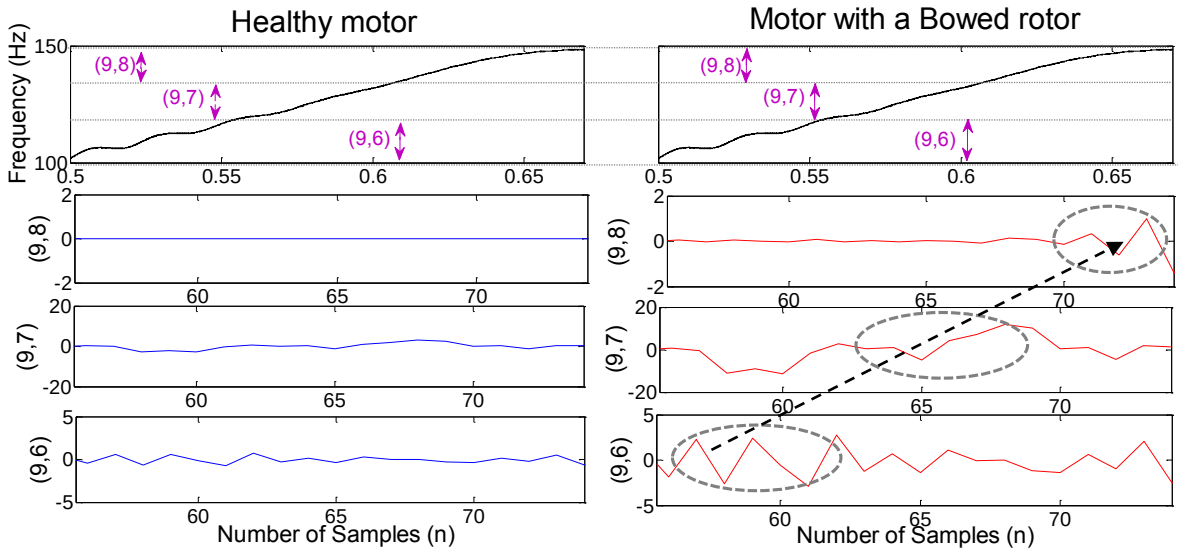

Figure 7-20: A WPD 2D plot of the vibration velocity for a grid started healthy motor and motor with bowed rotor

7.6.2 Soft starting using the inverter

The theoretical evolution of the rotational frequency, twice line fundamental frequency and dynamic eccentricity frequency are shown in Figure 7-21.

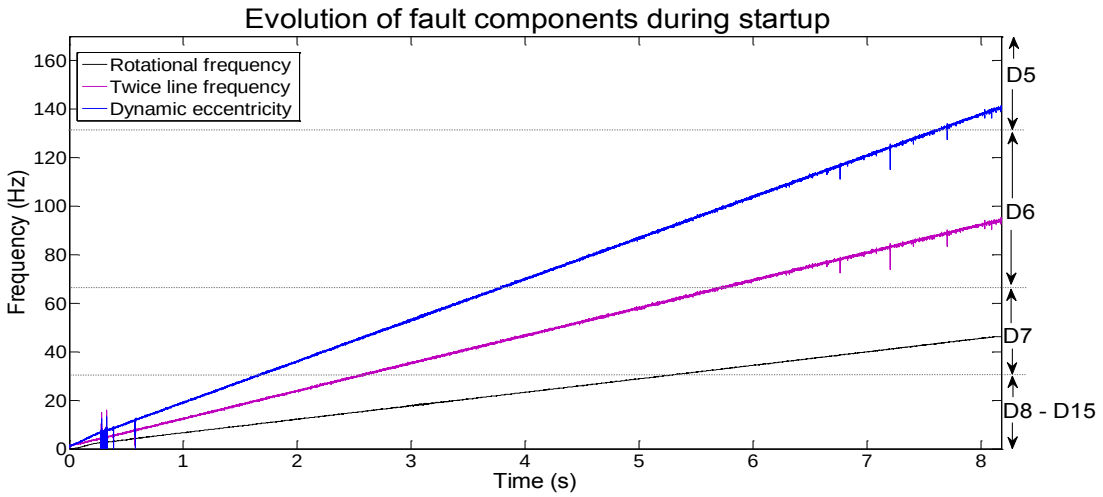

Figure 7-21: The evolution of the rotational frequency, twice line frequency outer and dynamic eccentricity components during startup

The vibration velocities were decomposed using DWT, the 2D plots of the vibration decompositions of details, *D9* to *D5* are shown in Figure 7-22.

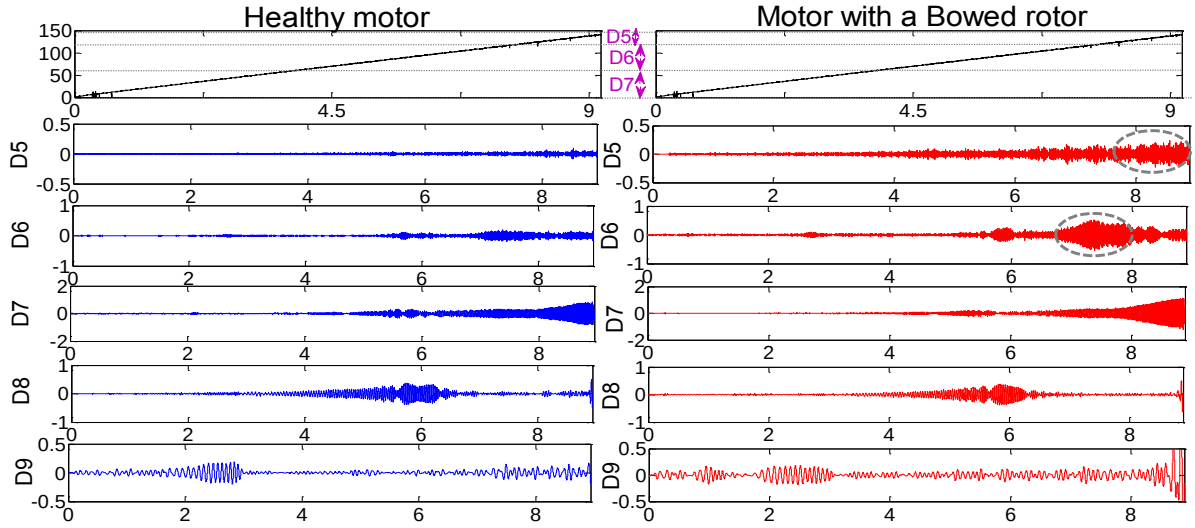

Figure 7-22: DWT 2D plots of the vibration velocity for an inverter started healthy motor and motor with bowed rotor

At the beginning of the startup, the evolution of the rotational frequency component is dominant between *D9* and *D7*. At *D6,* at times $t > 6s$ the magnitude increases for the motor with a bowed rotor, which is due to the evolution of the twice line frequency component and the dynamic eccentricity component. As expected at *D5,* at times $t > 6s$ the magnitude increases for the motor with the bowed rotor, due to the evolution of the dynamic eccentricity components.

The WPD 2D plots of the vibration velocities of both motors are shown in Figure 7-20. Observe the increase in the magnitude of the vibration for the motor with the bowed rotor as the component evolves through *node 6 to 8.*

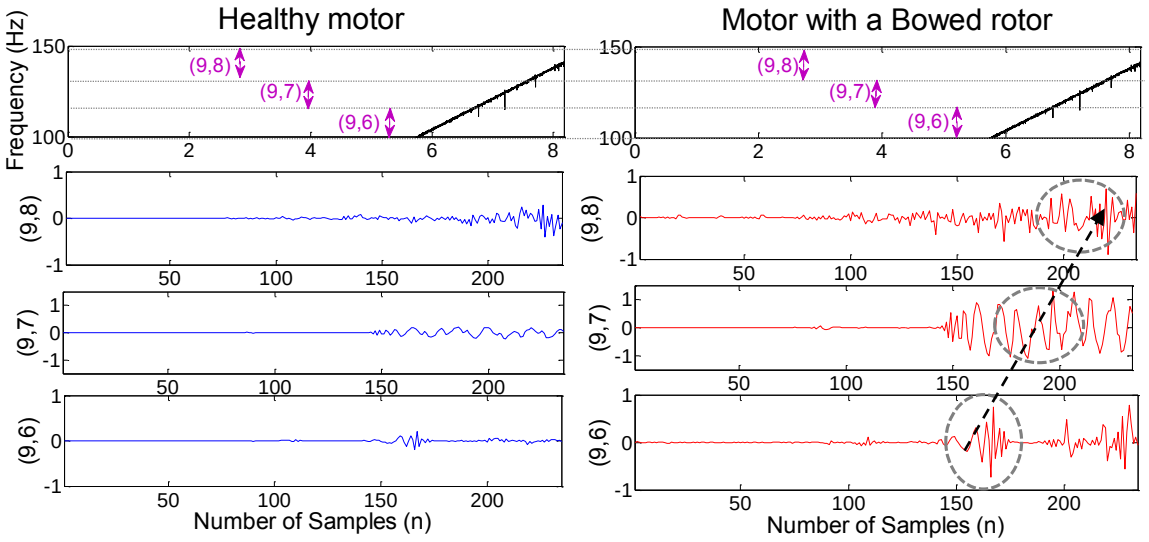

Figure 7-23: WPD 2D plots of the vibration velocity for an inverter started healthy motor and motor with bowed rotor

7.6.3 Summary of dynamic eccentricity detection

Similar to the bearing fault, the fundamental component varies for a DOL started motor, which does not influence the evolution pattern of the fault component since it varies from $100Hz$ to its respective frequency value under steady state. Applying DWT does not decompose the frequency bands of interest sufficiently to isolate the evolution of the dynamic eccentricity from resulting rise of the twice frequency component compared to WPD. Similarly, for the soft started motor, the application of WPD shows the fault evolution on the 2D plot more clearer compared to DWT. Similar to the bearing fault case, the evolution patterns are clearer on the soft started motor using an inverter compared to the DOL started motor since the startup time is longer.

7.7 Concluding Remarks

The common faults experienced in induction motors were implemented under transient startup conditions. The time-frequency fault detection strategy was applied on the stator current and vibration velocity signals to detect the characteristic evolution of the faults. Two dimensional time-frequency plots were obtained and analysed to determine the evolution patterns of the fault harmonics during startup for a grid connected and inverter-fed motor.

The startup current signals of the motor with shorted turns and the motor with broken rotor bars were analysed since the faults were more prominent in current when analysed under steady state. In the case of direct on line startups of these motors, detecting the evolution patterns on the 2D time frequency plots proved to be a challenge due to the short startup time. In the case of the soft starting them using the inverter, the evolution pattern of the inter-turn fault was only observed towards the end of the startup since at the beginning of the startup, the influences of the other harmonic components (i.e. WHs), tend to dominate in the lower frequency bands. The application of the WPD enabled a clearer distinction of the evolution pattern of the fault component towards the end of the transient period since the frequency bands were decomposed further. For the broken rotor bar fault, removal of the fundamental component using the Hilbert transform minimised the dominating effect of the fundamental in the lower frequency bands during the initial transient period.

The startup vibration signals of the motor with the faulted bearings and dynamic eccentricities were analysed since the faults were more prominent in the vibration. In the case of direct on line startups, the effect of the varying fundamental component tend to dominate in the initial periods; this posed a challenge in detecting the evolutions of the bearing fault components in the initial transient period but not for the dynamic eccentricity component. The application of the WPD enabled a clearer distinction of the evolution pattern. For the soft started motors, the evolution patterns were only evident towards the end of the startup. Again, the WPD enabled a clearer distinction of the evolution patterns. The evolution patterns were slightly detected in the case of the direct on line startups but were clearer in the case of inverter startups since the transient period was longer.

In the next chapter conclusion are drawn and recommendations are presented.

8. CONCLUSION AND RECOMMENDATIONS

8.1 Introduction

This chapter presents the conclusions that can be drawn from the results presented in the preceding chapters. These conclusions are derived with reference to the research objectives stated in section 1.4. Each objective is reviewed along with the relevant outcome of this research project. Recommendations are made based upon the conclusions presented. These include a discussion of possible improvements that can be made on the test rig, as well as some matters that may require further research to improve the signal processing.

8.2 Conclusions

8.2.1 Literature Overview

A literature review of the induction motors, condition monitoring systems and signal processing techniques used was conducted. The basic concept of the induction motor and inverter drive was reviewed. Four common types of faults associated with induction motors were identified, which are namely: stator faults, rotor cage failures, air-gap irregularities and bearing failures. These can be categorized into electrical and mechanical faults. Furthermore, the most prominent parameters used to detect these faults such as current and vibrations were identified. Frequency and time-frequency domain techniques which can be applied to these signal parameters to detect such faults were reviewed. Literature revealed that frequency domain techniques are suitable for only stationary signals while time-frequency domain techniques are suitable for non-stationary signals.

In the case of stationary signals analysis, non-parametric methods based on the Fourier transform are typically used in condition monitoring since they do not assume a specific underlying model and represent the frequency spectrum of a signal understandably. Certain techniques such as; zero padding, multiplication of the signal with a Hann window function and increasing the signal to noise by using the Welche PSD estimator, enhance the spectral estimation. In the case of non-stationary signal analysis, Wavelet Transforms are the more recently used methods to extract the time-frequency information more effectively. The

Daubechies mother wavelet is commonly used in the Discrete Wavelet Transforms to analyse signals in the field of condition monitoring.

The instrumentation typically used to measure current and vibration signals was also reviewed. For current signals, current transformers are used while for vibration signals Internal Electronic Piezoelectric accelerometers are widely used. In vibration monitoring, velocity is the preferred signal used to quantify the level of vibration since it is constant throughout all frequencies. The characteristics of the fault harmonic components in the current and vibration under steady state according to the International Standards Organization were also reviewed.

8.2.2 Development of the condition monitoring test rig

To experimentally implement these common faults in isolation to one another and to other faults in an accurate and repeatable manner, an induction motor condition monitoring test rig was developed. A Machinery Fault Simulator Magnum was used for this research. Various faults could be introduced individually or jointly in a controlled environment on this system. However, the initial setup of this system was focused to train maintenance staff in the area of predictive maintenance. The system needed to be developed further to meet the research needs. Hence the signal measuring, signal conditioning, data acquisition hardware and software, and power system configuration were developed such that signals like: current, voltage, vibration, speed, and fundamental operating frequency(for inverter-fed) could be accurately measured and captured for the fault detection of grid connected and inverter-fed motors. An experimental methodology was also developed to ensure repeatability and safe operation of the test rig.

8.2.3 Validation of conventional techniques on grid connected motors

Conventional techniques were validated to ensure that they could reliably detect faults especially during light loading. The common faults experienced in induction motor were implemented under steady state conditions. In Chapter 6, conventional fault techniques based on frequency domain methods were applied in the current and vibration signals. Each of the fault conditions were operated under different load conditions. The results pertaining to each fault condition were compared to the healthy motor which served as a baseline. In the case of a motor with an inter-turn fault, the fault component was detected in both the current and vibration spectrum, but was more prominent on the current spectrum. The magnitude of this component varied proportionally according to the load condition and fault severity, whilst the frequency location varied according to the load.

In the case of a motor with broken rotor bars, the fault component was detectable in both the current and vibration spectrums. The magnitude of the fault component and frequency location varied according to the load condition. During light load conditions, the components were

located closely to the fundamental which posed a challenge in the detection process. In the vibration spectrum, the fundamental component also varied with loading adding an additional variable, hence current was the preferred parameter. In the case of the motor with an outer and inner race bearing fault, the fault components were detected in both the current and vibration, but were more prominent on the vibration. The outer race fault component was easier to detect compared to inner component. The frequency location and magnitude were affected by the load condition.

In the case of a motor with a dynamic eccentricity, the magnitude and frequency location of the fault component was affected by the load.

8.2.4 Application of conventional techniques to inverter-fed motors

The conventional techniques were applied to inverter-fed motors in a similar manner as in the grid connected case to establish whether the fault components could be still detected. In the case of the motor with an inter-turn fault, the fault component was not detected on the current spectrum regardless of the loading condition, due to the switching operation of the inverter. In the case of the motor with broken rotors, the fault components were detected in the current spectrum. The fault components of the motors with bearing faults and dynamic eccentricities were also detected on the vibration spectrum.

8.2.5 Exploring recent time-frequency techniques

The more recent time-frequency signal processing techniques based on Wavelet transforms were examined in Chapter 7, to determine whether the fault could be detected under transient start-up conditions for grid connected and inverter-fed motors. The common faults were implemented under transient start-up conditions. The time-frequency techniques were applied to the current and vibration to detect the characteristic evolution of the fault component on a 2D time-frequency plot.

8.2.5.1 Grid connected motors

The grid connected motors were started direct on line. In the case of the motors with an inter-turn fault and broken rotor bars, detecting the evolution of the fault component in the current on the 2D time-frequency plot proved to be challenge due to the short start-up time. This was attributed to the low parameters of the induction motor such as: supply voltage, machine size, and driven inertia. In the case of the motors with bearing faults and dynamic eccentricities, the varying rotational frequency component during startup tend to dominate in lower frequency bands during the initial transient period, which posed a challenge in detecting the evolutions of

the bearing fault components during this period but not for the dynamic eccentricity fault component.

8.2.5.2 Inverter-fed motor

The inverter –fed motors were soft started using an inverter, this resulted in a longer and linear startup since the ramp profile and acceleration time could be adjusted. In the case of the motors with an inter-turn fault and broken rotor bars, the evolution patterns on the 2D plot could be observed towards the end of the startup since at the beginning of the startup, the influences of the other harmonic components tend to be dominant in the lower frequency bands. This was also the case for the motors with bearing faults and dynamic eccentricity.

Wavelet packet decompositions of the current and vibration signals resulted in clearer distinction of the evolutions patterns on the 2D time-frequency plot compared to when the Discrete Wavelet Transforms were applied since the details were decomposed further; this resulted in narrower bands of the detail levels. However, the evolutions of the other main components must also be known since the two dimensional time-frequency plot generated does not provide a clear distinction of the other harmonics evolving during initial transient phase. The time-frequency techniques can be used to complement the frequency techniques for when the induction motor is not operating under steady state.

8.3 Recommendations

Though the research objectives have been successfully accomplished, various matters have been identified that require further research. The following sections present the major aspects that can be addressed in future work.

8.3.1 Signal Processing Techniques

There is a great potential for further investigation of signal processing techniques employed in the fault detection strategy for transient conditions. The use of discrete wavelets transforms and wavelet packet decompositions in the fault detecting strategy yielded promising results, although further exploration into different types of mother wavelets is required. This may include the creation of a new mother wavelet specifically for low voltage induction motors. Since evolution pattern for direct on line started motor is dependent on the startup length, it becomes necessary for further normalization in order to obtain a uniform pattern, in the case of a fault regardless of the startup conditions or machine size. Hence a scale transform can be applied in a similar manner as Antonino-Daviu et al in [**74**]. This transform has been successfully used in order fields related to image processing and it enables scale invariant features of different signals to be obtained with high reliability. To improve the graphical

legibility of the two dimensional representation of the time-frequency plot showing the evolution of the fault components; the Analytical Wavelet Transforms (AWT) can be used to generate high detail 2D plots. These high detail 2D plots can enable clearer distinction of harmonics evolving during the transient.

8.3.2 Conditioning monitoring test rig

The very fast startup-transient of small induction motors poses challenges in detecting faults during direct on line startups. Simulation work done by Von Platen in [**89**] revealed that increasing the moment of inertia can lead to better fault detection. Future work may include the use of a fly wheel to prolong the startup time. The inverter was accelerated to rated speed in a linear manner by selecting a linear ramp profile on the drive. Other ramp profiles need to be considered to establish how the fault component evolves. Only the startup transient conditions were considered; however, load change transient needs to be considered as well. The developed test rig allows for different types of loads to be connected, which allow different transient phases and conditions to be investigated. Using different types of ramp profiles, transient conditions and loads will allow the development of a fault detection strategy that is immune to the startup condition of the inverter drive and load type.

REFERENCES

[1] L.A. Garcia-Escudero, O. Duque-Perez, and M. Perez-Alonso, "Practical Aspects of Mixed-Eccentricity Detection in PWM Voltage-Source-Inverter-Fed Induction Motors," *IEEE Transactions on Industrial Electronics*, vol. 57 , no. 1, pp. 252 - 262 , January 2010.

[2] Group Motor Reliability Work, "Report of Large Motor Reliability Survey of Industrial and Commercial Installations, Part II," *IEEE transaction of Industry Applications Society*, pp. 865-872, 1985.

[3] J.C. Appiarius , R.M. McCoy , and E.L. Owen , "Assessment of the Reliability of Motors in Utility Applications - Updated," *IEEE Transactions on Energy Conversion* , pp. 39 - 46 , 1986.

[4] A.M Da Silva, "Induction Motor Fault Diagnostic and Monitoring Methods," Wisconsin, 2006.

[5] M Blodt, "Condition Monitoring of Mechanical Faults in Variable Speed Induction Motor Drives: Application of Stator Current Time-Frequency Analysis and Parameter Estimation," Toulouse, 2006.

[6] Neelam Mehala, "Condition monitoring and fault diagnosis on induction motors using motor current signature analysis," Kurukshetra, October 2010.

[7] P.C. Sen, *Principles of Electric Machines and Power Electronic*. Kingston: John Wiley and Sons, 1997.

[8] Ned Mohan, *Power electronics coonverters, applications and design*.: John Wiley and Sons, 2003.

[9] A.T De Almeida, F.J.T.E Ferreira, and P Fonseca, "VSDs for Electric Motor Systems,".

[10] Vi-institute. [Online]. https://www.vi-institute.org

[11] M Dlamini and P.S Barendse, "The Detection of inter-turn stator faults on inverter fed induction motors," in *Power Engineering Society Conference and Exposition in Africa*

(PowerAfrica), , Johannesburg, 2012 , pp. 1 - 8.

[12] Hamid Toliyat, *Electric Machines modeling, condition monitoring and fault diagnosis*. New York: Crc Press taylor and Francis Group, 2012.

[13] Pinjia Zhang, "A Survey of Condition Monitoring and Protection Methods for Medium-Voltage Induction Motors," *IEEE Transactions on Industry Applications, vol. 47, NO. 1,* pp. 34-46, 2011.

[14] José Ignacio Terra, Terra, "Faults Detection and Remote Monitoring System for Induction Motors using MCSA Technique".

[15] N. B. Shaikh, "Online Off-Site Condition Monitoring Of Three Phase Induction Motor by Using GSM Technology," *International Journal of Emerging Technology and Advanced Engineering*, pp. 693-696, 2013.

[16] Khalaf Salloum Gaeid, "Fault Diagnosis of Induction Motor Using MCSA and FFT," *Electrical and Electronic Engineering*, pp. 85-92, 2011.

[17] Jeffrey C. Robertson, "Detecting Stator and Rotor Winding Faults in Three-Phase Induction Machines," in *ECE Technical Reports*, 1995.

[18] Arfat Siddique, "A Review of Stator Fault Monitoring Techniques of Induction Motors," *IEEE Transactions on Energy Conversion, VOL. 20, NO. 1*, pp. 106-114, 2005.

[19] Ying Xie, "Investigation of Broken Rotor Bar Faults in Three-Phase Squirrel-Cage Induction Motors," in *Finite Element Analysis – From Biomedical Applications to Industrial Developments*. Shanghai: intech, 2012, pp. 477-498.

[20] T. A Kawady, "Modeling and Experimental Investigation of Stator Winding Faults in Induction Motors," *Electric Power Components and Systems,* pp. 599-611, 2009.

[21] "Bearing failure: causes and cures,".

[22] Luceda, "diagnosis, machinery fault diagnosis a basic guide to understanding vibration analysis for machinery," 2011.

[23] ISO17359, "Condition monitoring and diagnosis of electric machines- General guidelines,"

Switzerland, April 15, 2011.

[24] M Iorgulescu, "Study relation between fault noise in Elctric motor"," *International Journal Technical and Physical Problems of Engineering*, pp. 69-73, 2010.

[25] T Assaf, H Henao, and G Capolino, "Simplified Axial Flux spectrum Method to Detect Incipient Stator inter-Turn Short Circuit in Induction Machines," in *IEEE International Symposium on Industrial Electronics* , 2004 , pp. 815-819.

[26] W Pietrowski, "Application of radial neural network to diagnostics of induction motor stator faults using axial flux," 2011.

[27] Ogbonnaya I. Okoro, "Steady and Transient States Thermal Analysis of a 7.5-kW Squirrel-Cage Induction Machine at Rated-Load Operation," *IEEE Transaction On Energy Conversion*, pp. VOL. 20, NO. 4, 2005.

[28] Ahmad Darabi, and Mahmood Chahartaghi Kaveh Sarrafan, "Comparison between Lumped-parameter Model and FEA for Steady State Temperature of an AFPM Motor," *International Journal of Research in Engineering and Technology (IJRET)* , pp. Vol. 1, No. 5, , 2012.

[29] Qiang Yu, "Improved Lumped Parameter Thermal Model and Sensitivity Analysis for SR Drives," in *Electrical Machines (ICEM), 2010 XIX International Conference on*, 6-8 Sept. 2010, pp. 1 - 6.

[30] P.H. Mellor, "Lumped parameter thermal model for electrical machines of TEFC design," in *IEE Proceedings-B*, September 1991, pp. 205-218.

[31] Thomas G. Habetler, "Online Adaptive Stator winding temperature estimator based on a hybrid thermal model for induction machines," in *2005 IEEE International Conference on Electric Machines and Drives*, 15-15 May 2005, pp. 754 - 761.

[32] R.C. Bhavsar and R.A Patel, "Various Techniques for Condition Moniotirng of Three Phase Induction Motor- A rReview," *Internation Journal of Engineering Inventions*, pp. 22-26, 2013.

[33] B.K.N Rao, *Handbook of Condition Monitoring 1st Edition*. Oxford: Elsevier Science LTD,

1996.

[34] H. D Haynes, "Electrical Signature Analysis (ESA) developments at the Oak Ridge diagnosis applied reseach center," Tennessee,.

[35] P. Phumiphak, "Induction Motor Speed Measurement Using Motor Current Signature Analysis Technique," in *International Conference on Electrical Machines and Systems*, Tokyo, 2009, pp. 1-5.

[36] M. Abdesh Shafiel Kafiey Khan, "Wavelet Based Diagnosis and Protection of Electric Motors," pp. 256-282.

[37] K. H. Ruhm, "Module: Deterministic and Nondeterministic Signals," Zurich,.

[38] Edward W Kamen, *Fundamentals of Signals and systems using the web and matlab*. New Jersey: Prentice Hall, 2000.

[39] DG Long, "Comments on Hilbert Transform Based Signal Analysis," Brigham, 2004.

[40] M Pineda-Sanchez, M Riera-Guasp , J. Roger-Folch , E Hurtado-Perez, and J. Perez-Cruz , "Improved Resolution of the MCSA Method Via Hilbert Transform, Enabling the Diagnosis of Rotor Asymmetries at Very Low Slip," *IEEE Transactions on Energy Conversion*, pp. 52 - 59 , 2009.

[41] LA Pereira, "Performance Evalution of Nonparametric, Parametric, and the MUSIC methods to the detection of rotor cage faults of induction motors," in *IECON 2006 - 32nd Annual Conference on IEEE Industrial Electronics*, Paris, 2006, pp. 5005-5010.

[42] SM Kay, *Modern Spectral Estimation theory and application*. Englewood Cliffs: Prentice Hall, 1988.

[43] S.L Marple, *Digital Spectral Analysis with Applications*. Englewood Cliffs: Prentice Hall, 1987.

[44] Mathswork. Mathworks. [Online]. http://www.mathworks.com/help/signal/ug/spectral-analysis.html

[45] G.V. Tcheslavski. (2009, June) Lecture 09: Spectrum estimation –parametric methods.

http://www.ee.lamar.edu/gleb/adsp/Index.htm.

[46] J Kusuma, "Parametric Frequency estimation: ESPRIT and MUSIC," 2002.

[47] Ashish Kumar, "A new Method for early detection of inter-turn shorts in induction motors," in *International conference on power and energy systems*, Singapore, 2012, pp. 41 - 45.

[48] Boqiang Xu, "Improvement of the Hilbert Method via ESPRIT for detecting Rotor fault in induction motors at low slip," *IEEE Transaction on Energy conversion*, pp. 225-233, 2013.

[49] I.Y-H Gu, M.H.J Bollen, and , "Estimating Interharmonics by Using Sliding-Window ESPRIT," *IEEE Transaction on Power Delivery*, pp. 13-23, 2008.

[50] G. Didier, H. Razik, O. Caspary, and E. Ternisien, "Rotor cage fault detection in induction motor using global modulation index on the instantaneous power spectrum," in *IEEE International Symposium on Diagnostics for Electric Machines, Power Electronics and Drives, SDEMPED 2003. 4th*, 2003, pp. 104 - 109.

[51] I Jaksch, "Rotor Cage Fault Detection in Induction Motors by Motor Current Demodulation Analysis," 2012.

[52] F Lindsten, "A remark on zero-padding for increased frequency resolution," November 4, 2010.

[53] A. Bellini, F. Filippetti, C. Tasson, and G.-A. Capolino, "Advances in Diagnostic Techniques for Induction Machines," *IEEE Transactions on Industrial Electronics* , pp. 4109 - 4126 , 2008.

[54] B.S Prabhu, *Dynamic Analysis of Rotating Systems and Appplications*. Brentwood: Multi-Sxience Publishing, 2008.

[55] P.S Barendse, "The application of advanced signal processing techniques to the condition monitoring of electrical machine drive systems," Cape Town, 2007.

[56] M Misiti, Y Misit, G Oppenhiem, and J-M Poggi, *Wavelet Toolbox User's Guide.*: The Mathworks, 1996.

[57] Z Ye, B Wu, and A Sadeghian, "Current Signature Analysis of induction Motor Mechanical Fault by Wavelet Packets Decomposition," *IEEE Transcation on Industrial Electronics*, pp. 1217-1228, 2003.

[58] R.N Dash, B Subudhi, and S Das, "Induction motor stator inter-turn fault detection using wavelet transform technique," in *Internation conference on industrial and information systems*, India, 2010, pp. 436 - 441.

[59] M Riera-Guasp, J Antonino-Daviu, M Pineda-Sanchez, R Puche-Panadero, and J Perez-Cruz, "A general Approach for the Transient Detection of Slip-Dependent Fault Components Based on the Discrete Wavelet Transform," *IEEE Transaction on Industrial Electronics*, pp. 4167 - 4180, December 2008.

[60] J Antonino-Daviu, M Riera-Guasp, Folch J.R, and M Pilar Molina Palomares, "Validation of a new method for Diagnosis of Rotor Bar failures via Wavelet Transform in Industrial Induction Machines," *IEEE Transaction on industrial applications*, pp. 990-996, 2006.

[61] S.H Kia, H Henao, and Gerard-Andre Capolino, "Diagnosis of Broken-Bar Fault in Induction machines using Discrete Wavelet Transform without Slip estimation," *IEEE Transaction on industrial applications*, pp. 1395 -1404, 2009.

[62] J. Pons-Llinares, J. Antonino-Daviu, J. Roger-Folch, and D. Morinigo-Sotelo, "Eccentricity diagnosis in Inverter - Fed Induction Motors via the Analytic Wavelet Transform of transient currents," in *XIX International Conference on Electrical Machines (ICEM)*, Rome, 2010 , pp. 1 - 6.

[63] W.T Thomson and R.J Gilmore, "Motor Current Signature Analysis to Detect Faults in Induction Motor Drives - Fundamentalss, Data Interpretation, and Industrial Case Histories," in *Proceedings of the thirty second Turbomachinery Symposium*, 2003, pp. 145-156.

[64] ISO/DIS20958-1, "Condition monitoring and diagnosis of machines:Electrical signature analysis," 2012.

[65] Victor Wowk, "A Brief Tutorial on Machine Vibration,".

[66] Spectra Quest, "Applied Vibration Analysis Training Manual & Laboratory Exercises,".

[67] Meggitt, "Steps to selecting the right accelerometer," 2012.

[68] ISO13373-1, "Condition monitoring and diagnostics of machines-Vibration monitoring," 2002.

[69] ISO10816-1, "Mechanical Vibration Evaluation of machine vibration by measurements of non-rotating parts," 1995.

[70] W.T. Thomson and M. Fenger, "Current signature analysis to detect induction motor faults," *IEEE Industry Applications Magazine*, pp. 26 - 34 , July 2001.

[71] James I Taylor, *The vibration analysis Handbook: A practical guide for solving rotating machinery problems*. Tampa: Vibration consultants, 1994.

[72] M.E.K Oumaamar, H razik , A Rezzoug , and A. Khezzar , "Line Current Analysis for Bearing fault Detection In Induction Motors Using Hilbert Transform Phase," in *International Aegean Conference on Electrical Machines and Power Electronics* , stanbul , 2011, pp. 288 - 293.

[73] R.R. Obaid, T.G. Habetler, and J.R. Stack , "Stator current analysis for bearing damage detection in induction motors," in *IEEE 4th International Symposium on Diagnostics for Electric Machines, Power Electronics and Drives (SDEMPED)* , Atlanta, 2003, pp. 182 - 187.

[74] J Antonino-Daviu, S. Aviyente , E. Strangas , and M. Riera-Guasp , "A Scale Invariant Algorithm for the Automatic Diagnosis of Rotor Bar Failures in Induction Motors," in *IEEE International Symposium on Industrial Electronics (ISIE)*, Gdansk , 2011, pp. 496 - 501.

[75] J Antonino-Daviu, P Jover, M Riera, A Arkkio, and J Roger-Folch, "DWT analysis of numerical and experimental data for the diagnosis of dynamic eccentricities in induction motors," *Mechanical Systems and Signal processing*, pp. 2575 - 2589, 2007.

[76] J Antonino-Daviu, S Aviyente, E Strangas, and M Riera-Guasp, "A scale Invariant Algorithm for autmomatic Diagnosis of Rotor bar failures in Induction motors," in *IEEE International Symposium on Industrial Electronics (ISIE) 2011*, Gdansk , 2011, pp. 496 - 501.

[77] M. Riera-Guasp, J.A. Antonino, J. Roger-Folch , and M.P. Molina , "The use of the wavelet approximation signal as a tool for the diagnosis of rotor bar failures," in *IEEE*

International Symposium on Diagnostics for Electric Machines, Power Electronics and Drives, SDEMPED, Vienna , 2005, pp. 1-6.

[78] S.K. Ahameda, A Sarkarb, M Mitrac, and S Senguptac, "Detection of Induction Motor Broken Bar Fault Through Envelope Analysis Using Start-Up Current," in *2nd International Conference on Computer, Communication, Control and Information Technology (C3IT)*, 2012, pp. 646–651.

[79] P. Konar and P. Chattopadhyay, "Bearing fault detection of induction motor using wavelet and Support Vector Machines (SVMs)," *Elsevier*, pp. 4203–4211, 2011.

[80] SA Adewus, "Wavelet analysis of vibration signals of an overhang rotor with a propagating transverse crack," *Journal of Sound and Vibration*, pp. 777-793, 2001.

[81] B Herndler, "Developing Methods for Implementing Faults on Induction Machines," Cape Town, 2008.

[82] R. M.H. Hefny, L. E. Kollár, and M Farzane, "Experimental Investigation of Dynamic Force on The Performance of Wet Snow Shedding," *International Journal of Mechanical and Mechatronics*, pp. 72-79, 2012.

[83] National Instruments, "Operating Instructions and specifications of NI 9215,".

[84] National Instruments, "Operating Instructions and specifications of NI 9234,".

[85] Jee-Hoon Jung, "Online Diagnosis of induction motors using MCSA," *IEEE Transaction on industrial Electronics*, pp. 1842 - 1852, 2006.

[86] R Supangat. (2014, January) Appendix A. Further Discussion and Results of the Shorted Turn Fault Test. [Online]. http://digital.library.adelaide.edu.au/dspace/bitstream/2440/50741/1/03append-ref.pdf

[87] W.T Thomson, "On-line MCSA to Diagnose Short Turns in Low Voltage stator Windings of 3-Phase Induction Motors Prior to Failure," in *IEEE*, 2001, pp. 891 -898.

[88] WR Finley , M. M. Hodowanec, and W.G. Holter, "An Analytical Approach to Solving Motor Vibration Problems," Norwood, 1999.

[89] S.J Lacey, "An Overview of bearing vibration analysis," *Maintenance and asset management*, pp. 32-42, December 2008.

[90] M.J Costello, "Understanding the vibration forces in induction motors," Houston,.

[91] P Von Platen, "Exploring Modern Signal Processing Techniques to Detect Broken Rotor Bars in Induction Motors," Cape Town, 2013.

[92] J.A Antonino, J. Roger-Folch, and M.P. Molina, "The use of the wavelet approximation signal as a tool for the diagnosis of rotor bar failures," in *IEEE International Symposium on Diagnostics for Electric Machines, Power Electronics and Drives, SDEMPED*, Vienna , 2005, pp. 1 - 6.

[93] (2010, January) circuits to day. [Online]. www.circuitstoday.com/frequency-to-voltage-converter-using-lm331

[94] Texas instruments. (2013, March) Precision voltage to frequency converters.

[95] Cheal-Sao Goo, "Condition Monitoring of Squirrel Cage Induction Motor through Torque Evaluation," *IEEE*, 2012.

[96] John S Hsu, "Monitoring of Defects in Induction Motors Through Air-Gap Torque Observation," *IEEE Transactions on Industry Applications*, pp. VOL. 31, NO. 5, September/October 1995.

[97] A Yazidi, "Improvement of Frequency Resolution for Three-phase Induction Machine Fault Diagnosis," in *Industry Applications Conference, 2005. Fourtieth IAS Annual Meeting. Conference Record of the 2005*, France, October 2005, pp. 20 - 25.

[98] Alberto Bellini, "Monitoring of Induction Machines currents by high frequency resolution analysis," in *Industry Applications Conference, 2006. 41st IAS Annual Meeting. Conference Record of the 2006 IEEE*, October 2006.

[99] V Choqueuse, "Diagnosis of Three-Phase Electrical Machines Using Multidimensional demodulation techniques," *IEEE Transaction on industrial Electronics*, vol. 59, no. 4, pp. 2014-2023, April 2012.

[100] Guillermo Jimenez, "Fault detection in induction motors using hilbert and wavelet transform," pp. 205 - 220, 2006.

[101] R Puche-Panadero, "Improved Resolution of the MCSA Method Via Hilbert Transform, Enabling the Diagnosis of rotor asymmeetries at very low slip ," *IEEE Transactions on Energy conversion, Vol 24, No.1*, pp. 52-59, March 2009.

[102] Ilias Georgakopoulos, "Detection of Induction Motor Faults in Inverter Drives Using Inverter Input Current Analysis," *IEEE Transaction on Industrial Electronics vol. 58, No.9*, pp. 4365-4373, September 2011.

[103] Sérgio M. A. Cruz, "Diagnosis of Stator Inter-Turn Short Circuits in DTC Induction Motor Drives," *IEEE Transactions on Industry Applications, VOL. 40, NO. 5, 2004*, pp. 1349-1360, 2004.

[104] Ling Feng, "Course 02453 Applied Digital Signal Processing: Zoom-FFT Spectrum Analyzer," DTU, May 2003.

[105] H Douglas, "Detection of inter-turn stator faults in doubly-fed induction generators," *International Industry applications Vol 2*, October 2005.

[106] SMA Cruz, "Stator Winding Fault Diagnosis in three-phase Synchronous and Asynchronous motors, the Extended Park's Vector Approach ," *IEEE Transactions of industrial applications vol 37, no 5*, September/October 2001.

[107] Zhenyu He, "Short-time Fourier Transform and Gabor," 2010.

[108] T. F. Quatieri, "Short time Fourier transform," in *Discrete-Time Speech Signal Processing: Principles and Practice.* Phil, 2002, pp. 1 - 17.

[109] Zbigniew Leonowicz, "Parametric methods time-frequency analysis of electric signals," Wroclawska, 2006.

[110] P Stoica and R Moses, "Lecture notes to accompany Introduction to Spectral Analysis," 1997.

[111] Qiang Miao, Cong, Lin, and Pecht, Micheal, "Identification of multiple characteristic components with high accuracy and resolution using the zoom interpolated discrete

Fourier transform," *Measurement science and technology*, 2011.

[112] Jee-Hoon Jung, Jong-Jae Lee, and Bong-Hwan Kwon, "Online Diagnosis of induction motors using MCSA," *IEEE Transaction on industrial Electronics*, pp. 1842 - 1852, 2006.

[113] Qiang Miao, "Identification of multiple characteristic components with high accuracy and resolution using the zoom interpolated discrete Fourier transform," *Measurement science and technology*, 2011.

Appendix A-

Hardware settings and software code

A1 Evaluation criteria

Table A-1: Typical evaluation criteria for determining zone vibration magnitude (severity)

<table>
<tr><th>RMS vibration velocity
mm/s</th><th>Class I
(Production of electrical motors up to 15kW)</th><th>Class II
(Medium sized electrical motors with 15kW and 75kW output)</th><th>Class III
(Large machines mounted on a relatively rigid and heavy foundation with an output above 75kW)</th><th>Class IV
(Large machines mounted on a relatively soft foundation with an output above 75kW)</th></tr>
<tr><td>0.28</td><td rowspan="3">A</td><td rowspan="4">A</td><td rowspan="6">A</td><td rowspan="8">A</td></tr>
<tr><td>0.45</td></tr>
<tr><td>0.71</td></tr>
<tr><td>1.12</td><td rowspan="2">B</td></tr>
<tr><td>1.8</td><td rowspan="3">B</td></tr>
<tr><td>2.8</td><td rowspan="2">C</td><td rowspan="2">B</td></tr>
<tr><td>4.5</td><td rowspan="3">C</td><td rowspan="3">B</td></tr>
<tr><td>7.1</td><td rowspan="5">D</td><td rowspan="3">C</td></tr>
<tr><td>11.2</td><td rowspan="4">D</td><td rowspan="3">C</td></tr>
<tr><td>18</td><td rowspan="3">D</td></tr>
<tr><td>28</td><td rowspan="2">D</td></tr>
<tr><td>45</td></tr>
</table>

A2 Inverter drive parameter settings

Table A-2: Induction motor inverter drive parameter settings

Parameter (P)	Description	Parameter setting
P100	Start source – Local keypad	0.0
P102	Minimum frequency (Hz)	0
P103	Maximum frequency (Hz)	60
P104	Acceleration time 1(s)	10.0
P106	S ramp integration time (s)- Liner ramp	0.0
P107	Line Voltage selection	01
P108	Motor overload (%)	100
P110	Start method – Normal	00
P150	TB-30 Output – Output frequency	1
P166	Carrier frequency- 6kHz	01
P300	Drive mode – Constant V/Hz	00
P302	Motor rated voltage (V)	190
P303	Motor rated current (A)	1.8
P304	Motor rated frequency (Hz)	50
P305	Motor rated speed (rpm)	2850

Table A-3: Servo motor inverter drive settings

Parameter (P)	Description	Parameter value
P1-01	Control Mode and output direction	0 x 000A
P1-02	Speed and torque limit setting	0 x 0000
P1 -04	Analogue Monitor output portion 1 (MON1)	100
P1 -05	Analogue Monitor output portion 2 (MON2)	100
P1-52	Regenerative resistor value	20
P1-53	Regenerative resistor capacity	1000
P1-72	Full-closed Loop Resolution (for CN5 terminal)	12800

A3 LabView code

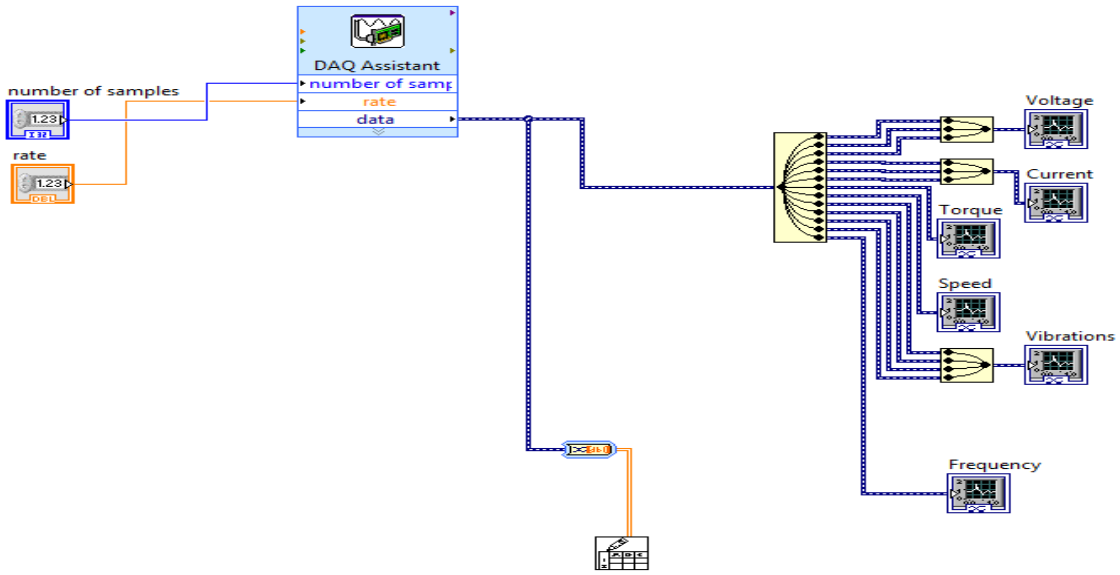

Figure A-1: LabView VI code

A4 Matlab code

A4.1 Power spectral density calculating code

```
% This code computes the PSD, with window and zero padding
%Current, voltage, and vibration signals sampled at 25600HZ and 768000samples are taken
%
Fs =25600; % Sampling frequency
N = 768000; % number of samples
 % Sum of a 50 Hz sinusoid and a 120 Hz sinusoid
 T = 1./Fs; % time step
 t = (0:N-1)*T;  % Time vector
NFFT = 2^nextpow2(N);% extend the number of samples for zero padding

%SM_Grid_Healthy_0_768kSample_25_6kHz_ss
%SM_Grid_2turns_100_768kSample_25_6kHz_ss
%SM_Grid_4turns_100_768kSample_25_6kHz_ss
%SM_100_grid_bf_768kS_25_6kHz_ss
%SM_100_grid_bow_768kS_25_6kHz_ss
%SM_100_Inv50_healthy_768kS_25_6kHz_ss
%SM_100_Inv60_2turns_768kS_25_6kHz_ss
%SM_100_Inv50_brb_768kS_25_6kHz_ss_2
%SM_100_Inv50_bf_768kS_25_6kHz_ss
%SM_100_Inv50_bow_768kS_25_6kHz_ss


data = load('SM_100_Inv50_bow_768kS_25_6kHz_startup.txt');
%data = load('SM_0_grid_brb_768kS_25_6kHz_ss_2.txt');
```

```
Iai = data(:,4);

Ia = Iai;
Sp = data(:,8); % reads the voltage
Sp1 = (Sp.*-3000)./4.73388; % scales the voltage to get speed
nr = mean(Sp1)% calculates the mean speed
disp(' Enter fundamental frequency');
fs = input(' ');% Fundamental

ns = 3000; % Synchronous speed

s = (ns - nr)./ns;% Slip

frm = nr/60; % rotor speed

fslip = fs - frm; % slip frequency
P = 2; %number of poles
fp = P.*fslip; % pole pass frequency


% to perform the hibert apply
%Iahil = abs(hilbert(Ia))-mean(abs(hilbert(Ia)));

% to multiply by the window function
%   @barthannwin   - Modified Bartlett-Hanning window.
 %  @blackman      - Blackman window.
 %  @blackmanharris - Minimum 4-term Blackman-Harris window.
 %  @bohmanwin     - Bohman window.
 %  @chebwin       - Chebyshev window.
 %  @attopwin    - Flat Top window.
 %  @gausswin      - Gaussian window.
 %  @hamming       - Hamming window.
 %  @hann          - Hann window.
 %  @kaiser        - Kaiser window.
 %  @nuttallwin    - Nuttall defined minimum 4-term Blackman-Harris window.
 %  @parzenwin     - Parzen (de la Valle-Poussin) window.
 %  @rectwin       - Rectangular window.
 %  @taylorwin     - Taylor window.
 %  @tukeywin      - Tukey window.
 %  @triang        - Triangular window.
w2 =  window(@hann,N);

% perform the PSD
[Pxx,F] = PWELCH(Iahil,w2,[],NFFT,Fs);

Pxxn = Pxx./(max(Pxx));% normalises the PSD

f=F;
% plot the freequency
figure(1)
plot(t,Sp1 , 'k'), hold on
figure(2)
semilogy(F,Pxx, 'k'), hold on

title('PSD Spectrum with a Hann window')
xlabel('Frequency (Hz)')
ylabel('Normalised Magnitude of Ia  ')
```

```
%*****************************frequency auto search**************************
% creates a vector
Freq = [];
for k = 1:2:19
   for n = 1:10
Fst = fs.*(((n.*(1 - s))./p)+ k); %
Freq(n,k) = Fst;
   end
end

Freq(Freq ==0)=[]

Freq1 = [];
for k = 1:2:19
   for n = 1:10
Fst1 = fs.*(((n.*(1 - s))./p) - k); %
Freq1(n,k) = Fst1;
   end
end
%%%%% finds the peaks
Freq1(Freq1 ==0)=[]
%Freq = round(Freq);
[PKS,LOCS]= findpeaks(Pxx, 'THRESHOLD', 0.0011)
freqfind = max(f(LOCS))./10;
```

A4.2 DWT and WPT code

```
% This code performs a discrete wavelet transform and wavelet packets
% decompositions
fs = 25600; % sampling frequency
f = 50;     % fundamental frequency
ds = 3;     % downsample value, if set to 1 no downsample takes place
fds = fs/ds;    % new sampling frequency
wlt = 'db44';   % choice of wavelet
Nf = 15       % number of decomposition levels, set to 0 for default

% Load transient signal here
%%%%%%%%%%transient%%%%%%%%%%%
%SM_100_Inv50_healthy_768kS_25_6kHz_startup
%SM_Grid_Healthy_100_768kSample_25_6kHz_startup
%SM_Grid_2turns_100_768kSample_25_6kHz_startup_v3
%SM_Inv50_2turns_100_768kSample_25_6kHz_startup_v3
%SM_100_Inv50_healthy_768kS_25_6kHz_startup
%SM_100_Inv50_brb_768kS_25_6kHz_startup_2
%SM_100_Inv50_bf_768kS_25_6kHz_startup
%SM_100_Inv50_bow_768kS_25_6kHz_startup
%SM_100_grid_bf_768kS_25_6kHz_startup
%
load('SM_100_Inv50_bow_768kS_25_6kHz_startup.mat')
%s1 = Ia;                       % set signal equal to measurand
% s1 = IM_X;
%s1 = Ia(250368:478208)%Healthy motor
%sp = Speed
%s1 = s11;
% for hilterts1 = abs(hilbert(s11))-mean(abs(hilbert(s11)));
% Possibility of downsampling
```

```
if ds~=1
   ds
   s1 = downsample(s1,ds);
end

s1_len = length(s1);
t = (0:1:s1_len-1)/fds; % generate time vector

% Calculate the frequency bands for the wavelet decomposition----------
if Nf == 0
   Nf = log(fds/f)/log(2);    % number of decomposition levels
   Nf = double(uint32(Nf));   % need an integer value
end
D = freq_bands( f, fds, Nf )   % calculate frequency bands ad display

% Wavelet decomposition
[s1_App s1_Det] = wav_analysis(s1, Nf, wlt);

% Display wavelet decomposition here
% Max of four subplots per figure and show the detail levels and last
% approximation level only

for k = 0:4:Nf-1
   figure
   for k2 = 1:min(4,Nf-k)
      hold on
      subplot(4,1,k2); plot(t,s1_Det(k+k2,:),'b');
      set(gca,'FontSize',10,'XLim',[0 t(end)]);
      title([num2str(D(1+k+k2)) '-' num2str(D(k+k2)) ' Hz']);
      k2;
   end
end

hold on
subplot(4,1,k2+1); plot(t,s1_App(5,:),'r');
set(gca,'FontSize',10,'XLim',[0 t(end)]);
title([ '0 -' num2str(D(end)) ' Hz']);
xlabel('Time(s)')

%%%%%%%%%%%%%%%%%%%%%%%%%%%%%%%%%%%%Wavelet
packages%%%%%%%%%%%%

T = WPDEC(s1,9,wlt,'shannon','norm')% Performs a wavelet decomposition

figure(1)
t1 = wptree(2,9,s1,'db44')% constructs a wavelet tree with 9 depths

plot(t1); % plots a wavelet tree with 9 depths
```

A4.3 Code for integrating acceleration

```
This code integrates acceleration to velocity
data = load('SM_100_Inv40_bow_768kS_25_6kHz_ss2.txt');
%data = load('SM_0_grid_brb_768kS_25_6kHz_ss_2.txt');
Ia_i = data(:,9);
```

```
Iai     = Ia_i;%.
datain     = Iai ;
%               1 - Displacement
 datain_type  = input('Input unit to be convert');
             % 2 - Velocity
%               3 - Acceleration
%
%               1 - t
 dataout_type =  input('output unit to be convert');
                % 2 - Velocity
%               3 - Acceleration
%
%
%%%%%%%%%%%%%%%%%%%%%%%%%%%%%%%%%%%%%%%%%%%%%%%%%%
%%%%%%%%%%%%%%%%%%%%%%%%%
%%%%%%%%%%%%%%%%%%%%%%%%%%%%%%%%%%%%%%%%%%%%%%%%%%
%%%%%%%%%%%%%%%%%%%%%%%%%
%%%%%%%%%%%%%%%%%%%%%%%%%%%%%%%%%%%%%%%%%%%%%%%%%%
%%%%%%%%%%%%%%%%%%%%%%%%%
   %   Make sure that datain_type and dataout_type are either 1, 2 or 3
   if (datain_type < 1 || datain_type > 3)
      error('Value for datain_type must be a 1, 2 or 3');
   elseif (dataout_type < 1 || dataout_type > 3)
      error('Value for dataout_type must be a 1, 2 or 3');
   end    %   Determine Number of points (next power of 2), frequency increment
   %   and Nyquist frequency

   %N = 2^nextpow2(max(size(datain)));
   NFFT = 2^nextpow2(N); % Next power of 2 from length of y
   df = 1/(NFFT*dt);
   Nyq = 1/(2*dt);    %   Save frequency array
   iomega_array = 1i*2*pi*(-Nyq : df : Nyq-df);
   iomega_exp = dataout_type - datain_type;    %   Pad datain array with zeros (if needed)
   size1 = size(datain,1);
   size2 = size(datain,2);
   if (NFFT-size1 ~= 0 && NFFT-size2 ~= 0)
      if size1 > size2
         datain = vertcat(datain,zeros(NFFT-size1,1));
      else
         datain = horzcat(datain,zeros(1,NFFT-size2));
      end
   end    %   Transform datain into frequency domain via FFT and shift output (A)
   %   so that zero-frequency amplitude is in the middle of the array
   %   (instead of the beginning)
   A = fft(datain);
   A = fftshift(A);    %   Convert datain of type datain_type to type dataout_type
   for j = 1 : NFFT
      if iomega_array(j) ~= 0
         A(j) = A(j) * (iomega_array(j) ^ iomega_exp);
      else
         A(j) = complex(0.0,0.0);
      end
   end    %   Shift new frequency-amplitude array back to MATLAB format and
   %   transform back into the time domain via the inverse FFT.
   A = ifftshift(A);
   datain = ifft(A);       %   Remove zeros that were added to datain in order to pad to next
   %   biggerst power of 2 and return dataout.
   if size1 > size2
      dataout = real(datain(1:size1,size2));
```

```
  else
     dataout = real(datain(size1,1:size2));
  end
  return

Ia = dataout;
```

Appendix B- Results

B1 Detection of an Inter-turn fault

B1.1 Current

Table B-1: The magnitude of the inter-turn fault harmonic component on the current spectrum at different load conditions for a grid connected motor

Condition	Load (%)	Speed (rpm)	Inter-turn fault frequency location and Current PSD magnitude (Hz, dB)
Healthy	100	2933.3	(196.70, -93.4)
	50	2961.5	(198.10, -93.4)
	0	2984.7	(199.20, -93.9)
2 turns Shorted	100	2936.0	(196.80, -83.6)
	50	2960.1	(198.0, -84.3)
	0	2988.9	(199.40, -89.5)
4 turns Shorted	100	2932.0	(196.60, -74.7)
	50	2960.8	(196.70, -76.7)
	0	2989.9	(199.50, -78.8)

B1.2 Vibration

Table B-2: The magnitude of the inter-turn fault harmonic component on the current spectrum at different load conditions for a grid connected motor

Condition	**Load (%)**	**2 x fL frequency location and vibration Velocity PSD magnitude in the radial direction (Hz, dB)**
Healthy	100	(99.80, -55.6)
	50	(99.9, -43.6)
	0	(99.80, -45.5)
2 turns Shorted	100	(99.93, -49.0)
	50	(99.87, -49.6)
	0	(99.93, -55.4)
4 Turns Shorted	100	(99.83, -49.64)
	50	(99.9, -49.46)
	0	(99.97, -46.48)

Table B-3: The magnitude of the inter-turn fault harmonic component on the vibration spectrum at 100% conditions for a inverter motor

Load (%)	Condition	Operating Fundamental (Hz)	Speed (rpm)	2 x fL frequency location and vibration Velocity PSD magnitude in the radial direction (Hz, dB)
100%	Healthy	60	3507.5	(120, -48.63)
		50	2939.6	(100.1, -53.52)
		40	2348.2	(80, -54.50)
	4 turns Shorted	60	3505.9	(120.0, -47.49)
		50	2938.6	(99.95, -65.89)
		40	2347.7	(79.13, -67.31)

B2 Detection of broken rotor bar fault

B2.1 Current

Table B-4: Grid connected-Broken rotor bar sidebands on the current spectrum

Condition	Load condition (%)	Speed (rpm)	1 X f_s (Hz, dB)	Broken rotor bar fault frequency location and Current PSD magnitude (Hz, dB)	
				LS	US
Healthy	100	2933.3	(49.90, 0)	(47.71, -49.96)	(52.10, -51.12)
	50	2961.5	(49.93, 0)	(48.57, -47.67)	(51.30, -47.35)
	0	2984.7	(49.90, 0)	(49.40, -47.00)	(50.37, -44.94)
Broken Rotor bars	100	2920.2	(49.88, 0)	(47.29, -42.75)	(52, -41.23)
	50	2952	(49.88, 0)	(48.32, -39.13)	(51.44, -40.09)
	0	2993.4	(50.07, 0)	(49.51, -39.85)	(50.63, -39.96)

Table B-5: Grid connected-Broken rotor bar sidebands on the current spectrum without the fundamental

Load condition (%)	Broken rotor bar 2sf fault component	
	Healthy motor	Motor with 3 broken rotor bars
0	(0.49, 3.32e-003)	(0.56, 0.018)
50	(1.37, 3.29e-003)	(1.56, 0.017)
100	(2.20, 1.59e-003)	(2.56, 0.014)

Table B-6: Inverter-fed-Broken rotor bar sidebands on the current spectrum

Condition	Fundamental (Hz)	Speed (rpm)	Broken rotor bar fault frequency location and Current PSD magnitude (Hz, dB)	
			LS	US
Healthy	40	2348.2	(38.09,-48.48)	(41.92, -50.07)
	50	2939.6	(47.75, -48.66)	(52.27, -50.35)
	60	3507.3	(56.62, -53.67)	(63.4, -54.54)
Broken Rotor bars	40	2344.6	(37.92, -41.03)	(42.09, -40.17)
	50	2934.8	(47.53, -40.8)	(52.47, -41.11)
	60	3497.8	(56.23, -44.11)	(63.79, -43.88)

B2.2 Vibration

Table B-7: Grid connected-Broken rotor bar components on the vibration spectrum

Condition	Load condition (%)	f_p (Hz)	1 X f_r (Hz, dB)	Broken rotor bar fault frequency location and velocity PSD magnitude (Hz, dB)	
				LS	US
Healthy	100	2.22	(48.80, 0)	(46.6,-53.52)	(50.13, -43.09)
	50	1.28	(49.27, 0)	(47.9, -48.8)	(50.63, -42.2)

	0	0.51	(49.67, 0)	(49.20, -44.31)	(50.13, -38.19)
Broken Rotor bars	100	2.57	(48.57, 0)	(46.00, -40.71)	(51.13, -44.04)
	50	1.57	(49.1, 0)	(47.53, -49.21)	(50.67, -39.19)
	0	0.57	(50.37, 0)	(49.20, -37.88)	(50.33, -32.14)

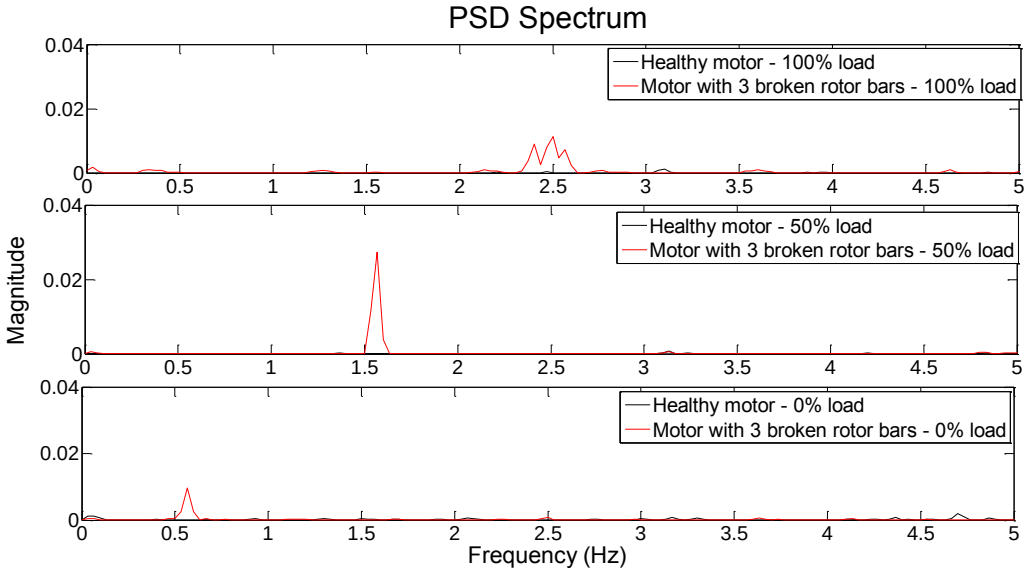

Figure B-1:The spectrums of the Hilbert transform of vibration of a grid connected motor with 3 broken rotor bars at different load conditions

Table B-8: Grid connected-Broken rotor bar sidebands on the vibration spectrum without the fundamental

Load condition (%)	**Broken rotor bar 2sf fault component**	
	Healthy motor Sideband 1	**Motor with 3 broken rotor bars Sideband 1**
0	(0.40, 1.96e-004)	(0.57, 0.96e-003)
50	(1.37, 1.96e-004)	(1.57,0.03)

100	(2.20, 2.69e-004)	(2.5, 0.01)

Table B-9: Inverter-fed-Broken rotor bar components on the vibration spectrum

Condition	Fundamental (Hz)	Speed (rpm)	1 X f_L (Hz, dB)	Broken rotor bar fault frequency location and Current PSD magnitude (Hz, dB)	
				LS	US
Healthy	40	2348.2	(39.03, -37.02)	-	(41.03, -67.43)
	50	2939.6	(48.87, -32.79)	-	(51.13, -81.08)
	60	3507.3	(58.33, -29.10)	-	(61.7, -72.94)
Broken Rotor bars	40	2344.6	(38.97, -32.66)	(36.87, -88.24)	(40.97, -79.72)
	50	2934.8	(48.77, -25.64)	(46.30, -72.21)	(51.23, -73.80)
	60	3497.8	(58.13, -20.82)	(54.33, -64.04)	(61.90, -66.16)

B3 Detection of bearing fault

B3.1 Current

Table B-10: Grid connected-bearing fault components on the current spectrum

Load condition (%)	Speed (rpm)	Bearing fault frequencies (Hz, dB)	
		FO	FI
0	2999.2	(204.70, -106.5)	(295.7, -111.90)
50	2961.5	(202.2, -94.38	(293.3, -104.40)

100	2944.5	(201.3, -83.45)	(244.1, -90.02)

B3.2 Vibration

Table B-11: Grid connected-bearing fault components on the vibration spectrum

Load condition (%)	Speed (rpm)	Bearing fault frequencies (Hz, dB)	
		FBPO	FBPI
0	2999.2	(153.8, -84.88)	(245.7, -91.22)
50	2961.5	(151.9, -75.35)	(242.6, -83.59)
100	2944.5	(151.0, -74.92)	(241.1, -78.79)

Table B-12: Inverter-fed-bearing fault components on the vibration spectrum

Load condition (%)	Speed (rpm)	Bearing fault frequencies (Hz, dB)	
		FBPO	FBPI
0	2995.8	(153.00, -83.45)	(244.1, -90.02)
50	2960.0	(150.90, -74.00)	(241.9, -82.62)
100	2946.4	(150.8, -72.94)	(240.80, -79.93)

B4 Detection of dynamic eccentricities

B4.1 Current

Table B-13: Grid connected-Dynamic eccentricities components on the current spectrum

Condition	Load (%)	Speed (rpm)	Dynamic eccentricity component frequency location and Current PSD magnitude (dB /Hz])
Healthy	100	2933.3	(98.76, -70.44)
	50	2961.5	(99.31, -67.22)
	0	2984.7	(99.675, -68.83)
Dynamic	100	2940	(98.93, -65.46)
	50	2971.6	(99.49, -62.46)
	0	2993.3	(99.76, -65.24)

Table B-14: Inverter-fed-Dynamic eccentricity components on the current spectrum

Load (%)	Condition	Operating Fundamental (Hz)	Speed (rpm)	Dynamic eccentricity component frequency location and Current PSD magnitude (dB /Hz])
100%	Healthy	60	3507.5	(118.3, -61.92)
		50	2939.6	(98.88, -64.55)
		40	2348.2	(79.05, -70.96)
	Dynamic	60	3510.5	(118.4, -62.9)
		50	2939.6	(98.97, -65.89)
		40	2351.1	(79.13, -67.31)

B4.2 Vibration

Table B-15: Grid connected-Dynamic eccentricities components on the vibration velocity spectrum

Condition	Load (%)	Dynamic eccentricity component frequency location and Current PSD magnitude (dB /Hz])	
		2 X fL	2 X fL + fr
Healthy	100	(99, -40.83)	(148.7, -71.66)
	50	(99.87, -40.96)	(149.1, -74.04)
	0	(99.8, -39.88)	(149.4, -80.69)
Dynamic eccentricity	100	(100, -36.58)	(148.9, -60.95)
	50	(100.1, -36.87)	(149, -63.95)
	0	(100, -37.04)	(149.7, -64.09)

TableB-16: Inverter-fed-Dynamic eccentricity vibration spectrum

Load (%)	Condition	Operating fundamental (Hz)	Dynamic eccentricity component frequency location and Current PSD magnitude (dB /Hz])	
			2 X fL	2 X fL + fr
100%	Healthy	60	(120, -51.16)	(178.50, -83)
		50	(100, -53.61)	(148.9, -79.79)
		40	(80, -50.01)	(119, -96.74)
	Dynamic eccentricity	60	(120, -43.09)	(178.4, -66.45)
		50	(100, -40.75)	(148.9, -66.04)

		40	(80, -45.65)	(119.1, -74.16)

B5 Baseline measurement

B5.1 Grid connected motor

Table B-17: Baseline measurements for grid connected motor

50Hz Grid
Healthy

					Induction Machine						Servo-Motor		Power		
LOAD	SPEED	TORQUE	SPEED	TORQUE	VOLTAGE			CURRENT			VOLTAGE	CURRENT	Real	Reactive	PF
					Vab	Vbc	Vca	Ia	Ib	Ic					
	rpm	A	V	V	V	V	V	A	A	A	V	A	W	VAR	
100%	2918.4	0.92	3.032	0.517	186	191.5	186.9	1.6	2.1	2.1	166.4	2.02	451.4	628.1	0.72
75%	2948.7	0.65	3.0562	0.3941	189.5	194.7	190.2	1.5	1.9	2	169	1.44	373.6	580.2	0.637
50%	2955.8	0.45	3.004	0.3	192.9	197.6	194.3	1.5	1.7	1.8	170.8	1.06	297.9	560.2	0.53
25%	2962.2	0.21	78	0.2	192.6	197.1	194	1.4	1.6	1.7	171	0.62	237	533.2	0.443
0%	2983.1	0	3.689	0.98	192.6	196.7	163.5	1.3	1.5	1.6	100	0	168.2	506.2	0.335
No Load	29838		3.099	0.009	195.8	200.2	197	1.3	1.5	1.6			112.7	512.6	0.217

B5.2 Inverter-fed motor

Table B-18: Baseline measurements for inverter-fed motor

50Hz Inverter Healthy

					Induction Machine						Servo-Motor		Power		
LOAD	SPEED	TORQUE	SPEED	TORQUE	VOLTAGE			CURRENT			VOLTAGE	CURRENT	Real	Reactive	PF
					Vab	Vbc	Vca	Ia	Ib	Ic					
	rpm	A	V	V	V	V	V	A	A	A	V	A	W	VAR	
100%	2929.5	0.74	3.033	0.507	206.6	203	203.9	2	2	1.9		2.03	456.1	700	0.643
75%	2945.1	0.57	3.047	0.386	206.7	203.5	204.6	1.8	1.8	1.7		1.43	365.3	641.3	0.568
50%	2958.3	0.37	3.062	0.285	207.1	204	205.6	1.7	1.7	1.6		1.26	232.9	574.7	0.492
25%	2969.3	0.26	3.076	0.18	208.4	204.7	205.9	1.5	1.6	1.6		0.6	232.9	574.7	0.404
0%	2982.3	0	3.089	0.069	209.3	205.5	206.9	15	1.6	1.5		0.48	161.2	558.2	0.287
No Load	2990.6		3.099		209.3	205.4	207.7	1.5	1.5	1.4			109.1	547	0.2

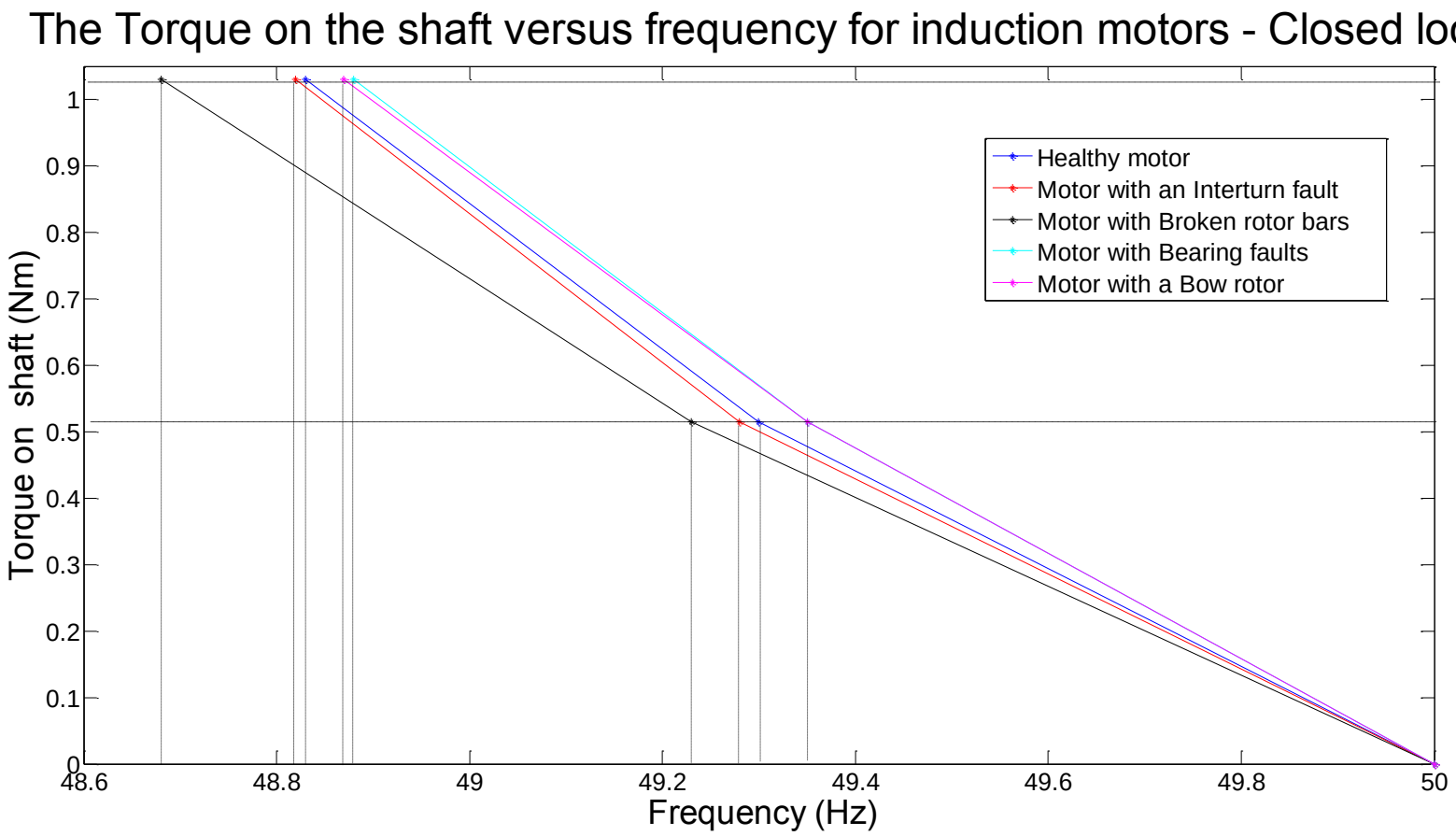

Figure B-2: Torque vs frequency for induction motor closed loop load control

Appendix C Circuit diagrams

Hazard Identification & Risk Assessment Form Date:

Conducted by: Project name: DSP techniques to detect faults in induction motor

Laboratory/area: Machines Lab Safety Officer: Sign:
Procedures used: Supervisor: Sign:
Induction training:
Logsheets:

Identified Hazard or Unsafe Work Activity	Potential Risk Assessment					Controls Required
	Major Injury	Injury	Minor Injury	Damage	Probability	Eliminate, Contain, Revise Procedure, Reduce Exposure
Rotating parts of machine		X			High	Eliminate and contain by using the plastic cover and not wearing any loose items of clothing or jewelry. Introducing a procedure to test the interlock system during start-up.
Mechanical Vibrations			X		High	Contain by having clear working area and using the safety guides (including the safety cover) built into the simulator.
Shock	X				Low	Wear correct clothing (PPE) and adhere to all lab rules to reduce exposure and contain the hazard. This includes correct wire gauge, healthy insulation, correct grounding. Making use of the protection devices available (circuit breakers and fuses). Adhere to the procedures for using the SpectraQuest fault simulator.
Fire	X				V. Low	This potential hazard can be eliminated by using correct connections. Knowledge and adherence to the fire procedures will ensure the containment of the hazard. This includes knowledge of the fire extinguisher (CO_2) locations, evacuation paths and Campus Security number (2222)

Figure C-1: Hazard identification and risk assessment form

C1 Frequency to voltage converter circuit

The frequency-to-voltage was achieved using an integrated circuit (IC) $LM331$as illustrated in the circuit diagram below. The $LM331$ output voltage has excellent linearity approximately 0.01% to the input frequency.

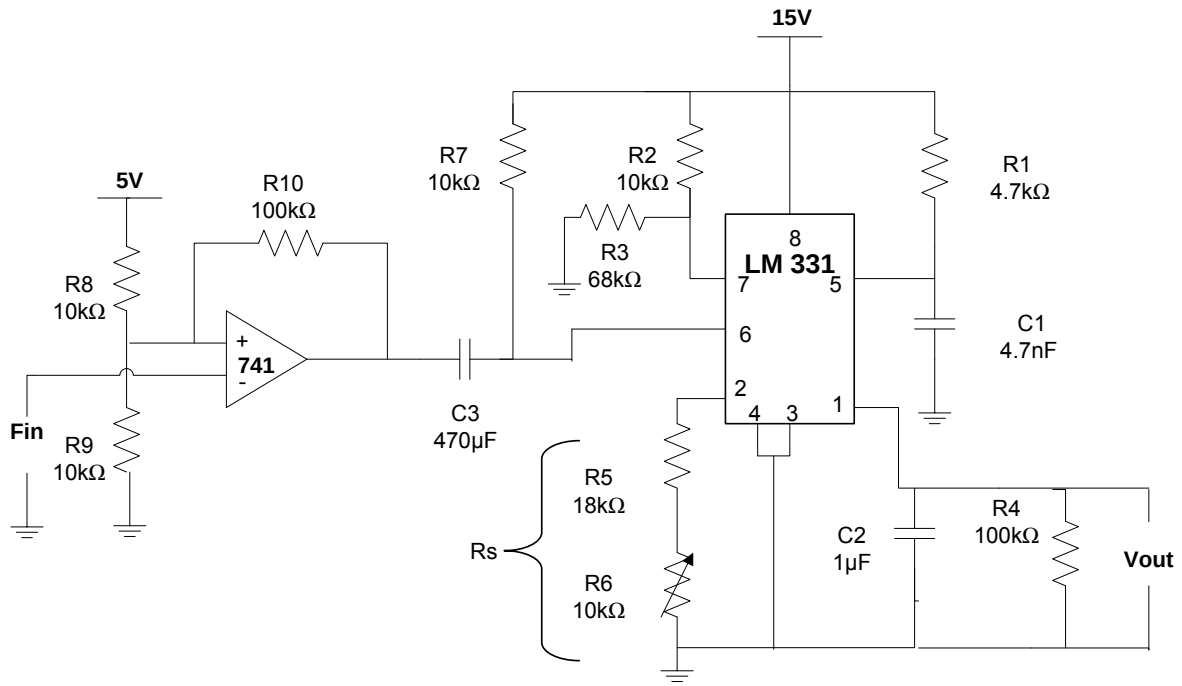

Figure C-0-2: Frequency to voltage converter circuit

The frequency to voltage conversion is attained by differentiating the input frequency using capacitor C_3 and resistor R_7 and feeding the resultant pulse into $pin\,6$ (threshold) of the $LM331$. The negative going edge of the resultant pulse train makes the built-in comparator circuit to trigger the timer circuit. At any instant in time the current flowing out of $pin\ 6$ will be proportional to the frequency and value of the timing components (R_1 and C_1). The output voltage proportional to the input frequency is available at the output across the resistor R_4. The voltage is obtained using equation below [**93**] [**94**].

$$V_{out} = \frac{R_4}{R_S} \cdot R_1 C_1 \cdot 2.09V \cdot f_{in} \qquad \text{(C-1)}$$

To stabilize the switching against rapid triggering by noise a Schmitt trigger circuit is employed in the frequency-to-voltage converter circuit. The Schmitt trigger uses negative feedback to prevent switching back to the other state until input passes a lower threshold voltage. The trigger voltage is $2.619V$ and will hold until the signal drops to $2.142V$

C2 Motor control circuit

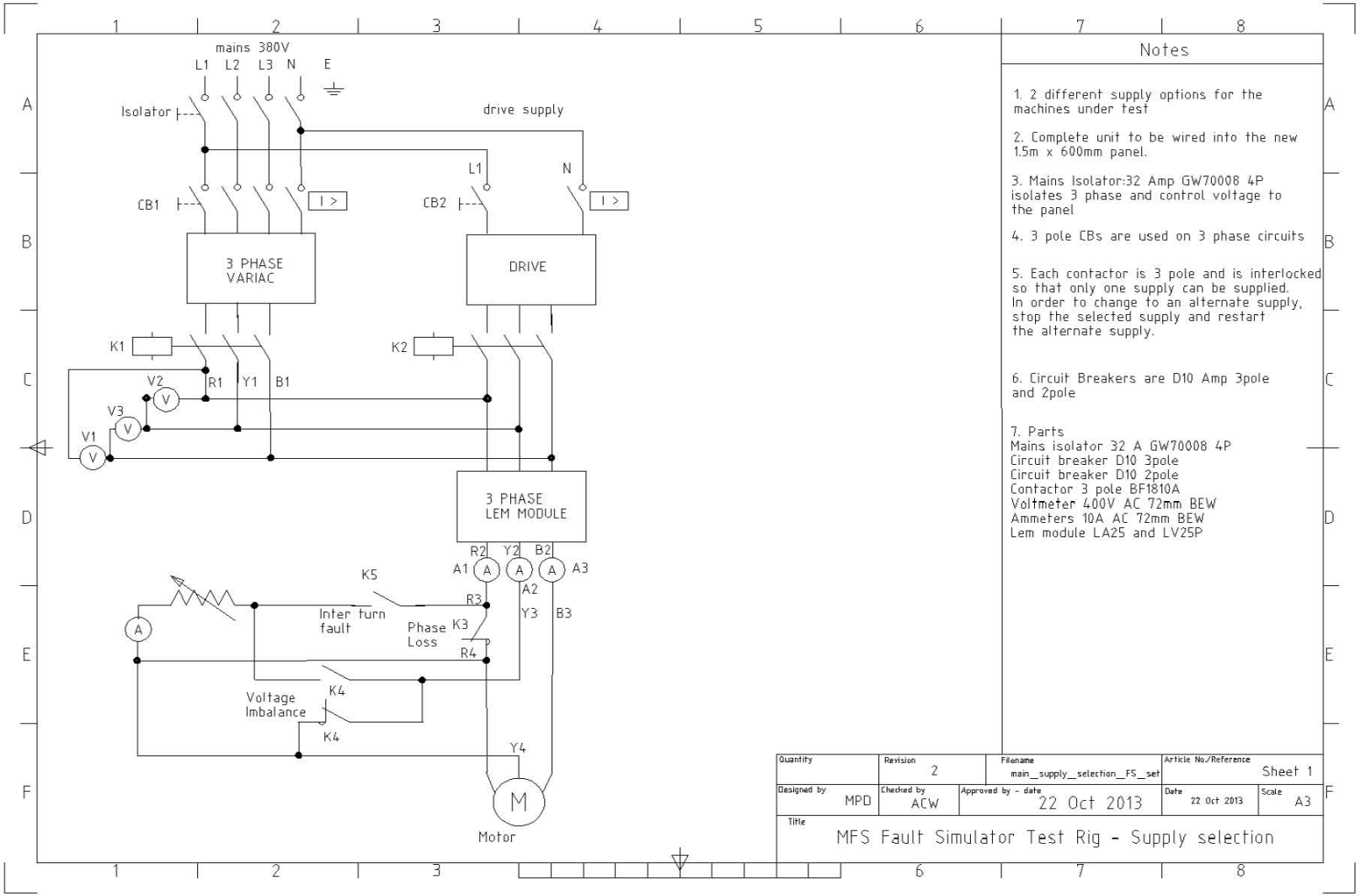

Figure C-3: MFS Fault Simulator Test - Supply voltage selection circuit

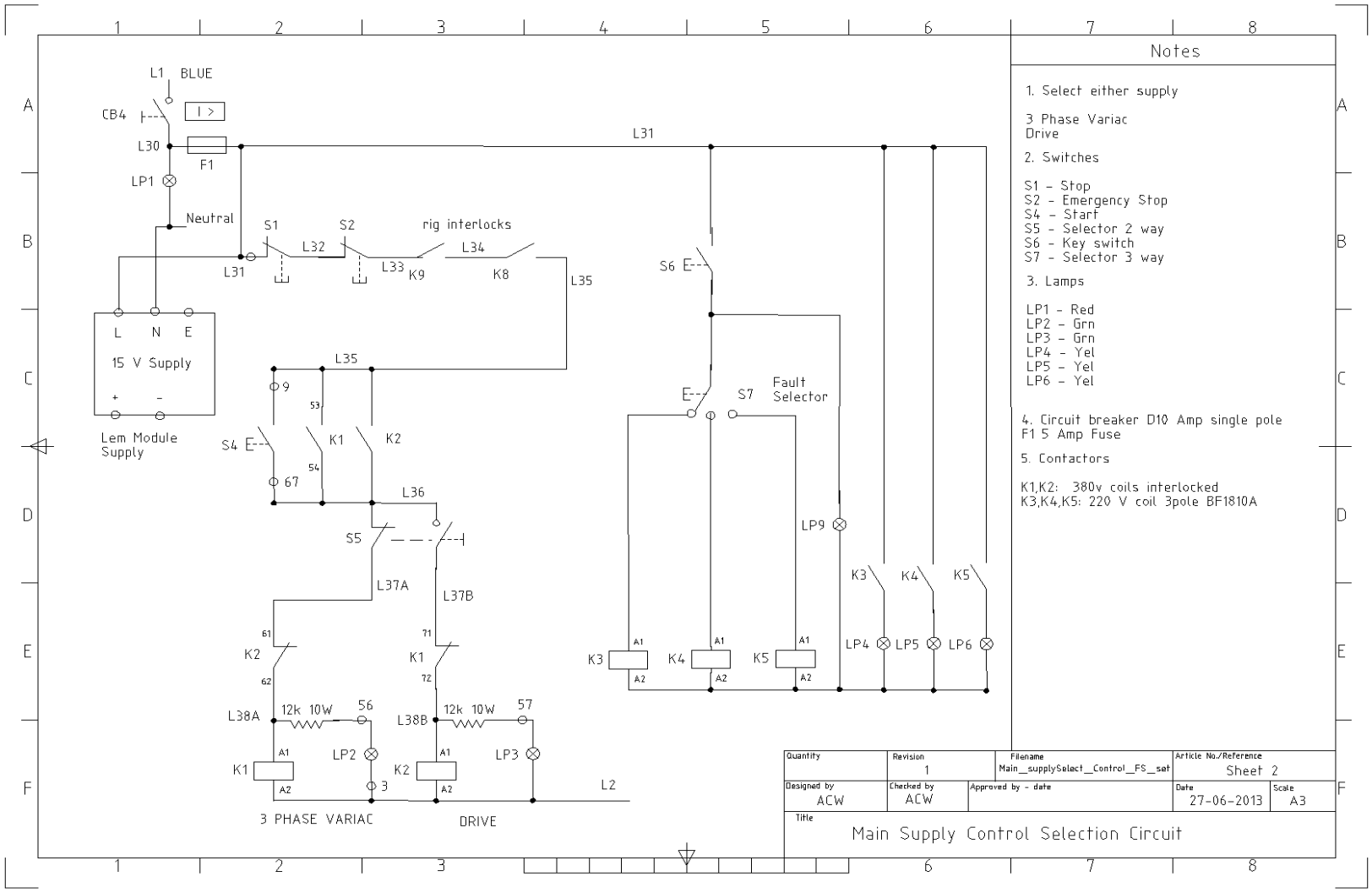

Figure C-4: Main supply control selection circuit

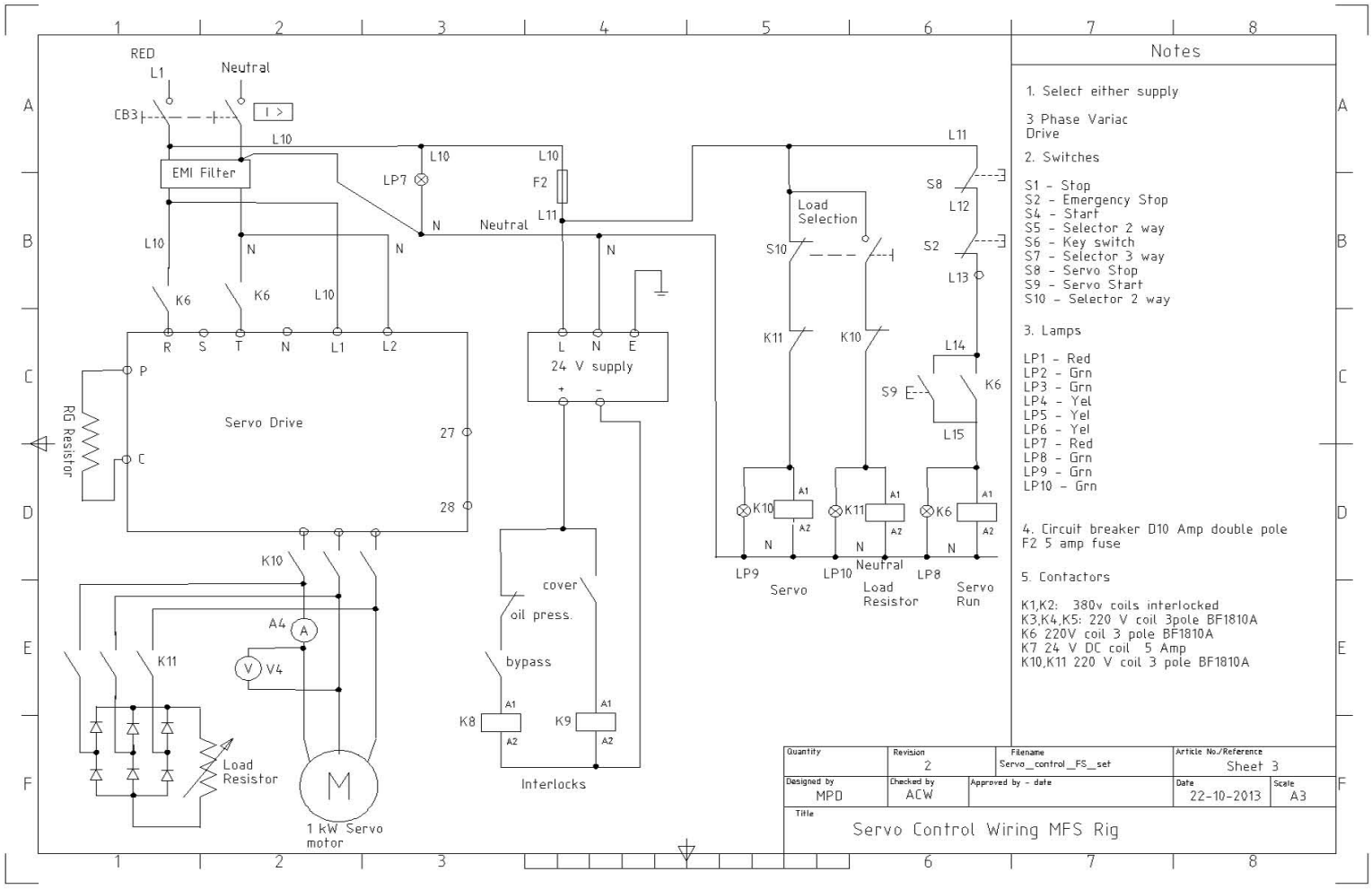

Figure C-5: Servo Control Wiring MFS rig